SISSA
Scuola
Internazionale
Superiore di
Studi Avanzati

Physics Area - PhD course in

Physics and Chemistry of Biological Systems

On the role of topological constraints in melts of ring polymers: from structure to dynamics

Candidate:

Mattia Alberto Ubertini

Advisor:

Angelo Rosa

Academic Year 2022/2023

Abstract

Ring polymers display several noteworthy properties arising from their non-linear topology, which are absent in linear chain systems. Rings are of great interest in materials science as they offer opportunities for creating new soft materials that harness topological constraints to achieve unconventional features. Moreover, they have significant implications in biology, as they connect to the physical behavior of chromosomes within cell nuclei. In this Thesis, we investigate their physics, in particular from the point of view of topological constraints, by using large-scale computer simulations.

First, we focus on melts of non-concatenated and unknotted ring polymers; in this case, theoretical models predict that the permanent topological constraints force the rings to double-fold onto compact and segregated tree-like objects. Yet, recent numerical investigations have shown that rings overlap and thread each other. We show how to reconcile these two pictures and provide new measurements that support the tree-like structure of the rings. At the same time, we provide evidence attesting to the fundamental role of threadings in the dynamics of melts of rings, which are not predicted by current theories.

In the second part of the Thesis, inspired by the recent experimental synthesis of DNA-based topological networks, we develop a computational model with which we explore how to fine-tune the topology of self-assembled polymer networks through several experimentally controllable parameters. We also consider the impact of geometric confinement on network synthesis, which we find can be exploited to bias the synthesis towards polymer networks that are softer under mechanical stress. Then, we also show how entanglements in polymer melts arise from the topological interactions in the system.

Finally, inspired by recent efforts to account for the active processes shaping both the structure and dynamics of biological filaments, we study how the role of entanglements is influenced in melts of active linear chains. We find that both the statics and dynamics of the chains are affected by the activity of the chains. Significantly, in contrast to passive systems, we do not find any sign of reptation in the chains' relaxation dynamics, which we interpret as the result of intra-chain entanglements becoming less detrimental to the relaxation of active chains.

Contents

Introduction

Polymers are ubiquitous in our daily lives, playing pivotal roles in the material industry, with plastics and rubber as paramount examples, and also in biology, where DNA, RNA, and proteins stand out as the most notable biopolymers, serving as the very foundation of life as we understand it. In many notable contexts, polymers are often found in concentrated conditions (melts) whose rheological and mechanical properties are profoundly influenced by the microscopic *entanglements* arising from the impossibility of nearby polymer filaments to cross each other. These constraints, referred to as *topological constraints*, are transient for linear chains, affecting only their dynamical properties. In contrast, there are systems where topological constraints are quenched from their initial preparation and profoundly influence the system's behavior.

A notable example is constituted by melts of non-concatenated and unknotted ring polymers, which have obtained significant attention over the past four decades. Although not a new subject, this area of research continues to draw interest for several reasons: not only do many aspects concerning the structure and dynamics remain not fully understood, but melts of ring polymers are also inherently connected to chromosome biology during interphase.

Current theories describe rings as *double-folded* tree-like objects. While these models accurately describe several properties of these systems, they fail to account for some crucial features revealed by numerical simulations. In particular, it has been shown that rings in the melt are not exactly double-folded, and even if they are compact, they overlap significantly with each other forming *threadings*, the interpenetration of a ring through the effective surface of another ring. Simulations have shown that these constraints introduce novel and significant properties absent in linear systems.

Motivated by these reasons, part of my PhD Thesis is dedicated to the studying of such systems, focusing on the complex interplay between the postulated double-folding and formation of threadings. In particular, the first part of Chapter 1 is dedicated to a careful review of the state of the art of the subject. Then, Chapter 3 is dedicated to presenting numerical simulations of melts of non-concatenated and unknotted rings with varying bending rigidity. These simulations allow us to reconcile the previously mentioned dichotomy.

On the other hand, recent advancements in the synthesis of topologically complex materials, such as polycatenanes composed of interlocked polymer rings, have demonstrated the potential of manipulating topology to fine-tune the mechanical properties of polymeric materials. In this context, inspired by biology, where topology and entanglement in DNA are commonly manipulated by a family of enzymes called topoisomerases, Olympic DNA networks have been experimentally realized. These networks consist of topologically interlinked DNA rings and are synthesized by exploiting the *strand crossing* action of topoisomerases. Remarkably, this system exhibits different viscoelastic behavior dependent on the action of the enzyme. In particular, by blocking its activity, the system assumes the characteristics of a polymer network with mechanical properties relying on the topology of the interlocked DNA rings. However, topology, arising from random strand crossings between DNA filaments, cannot be controlled and can only be indirectly inferred from rheological measurements. Therefore, in this context, the modeling and simulations of such systems can help in guiding the synthesis of networks with desired properties. For these reasons, part of this Thesis will deal with the development and the applications of a new computational model for describing and characterizing such polymer systems. In particular, in the second part of Chapter 1, we review recent experimental realizations of topologically complex ring assemblies and we frame the interest in such systems in the context of my PhD work. In Chapter 4, we introduce tools derived from *Knot Theory* which are useful when dealing with topologically complex systems. Finally, in Chapters 5, 6, and 7, we develop the computational model and apply it to study the physics of ring polymers with unconstrained topology. In these chapters, we explore various experimentally tunable parameters, such as polymer chain length, bending rigidity, system geometry, and their impact on the resulting topology of the network. Moreover, in Chapter 6, we derive an explicit relationship between the system's topology and its entanglement properties, addressing a long-standing problem in polymer physics.

The last chapter 8 deviates substantially from the rest of the Thesis, and it deals with *active polymers*. Active polymers, and in general *active matter*, represent a very active field of research in statistical physics. Active systems are out-of-equilibrium systems, consisting of units that can consume energy to move or perform mechanical work, with living systems providing a prominent example of active matter. The tight connection with biology has led to the application of active matter concepts in the description of several biological phenomena, such as cell migration, bacterial motility, and bird flocking.

More recently, significant attention has been drawn by active polymers due to their relevance in biology, since many biological filaments, *e.g.*, DNA, RNA, cytoskeleton filaments, etc., are subject to various non-equilibrium processes. To date, many of the investigations have focused on single active chain systems, while few studies, and all limited to the case of

low activity, have focused on the case of chains in melt. For this reason, the last chapter is dedicated to preliminary investigations dealing with melts of active linear chains. Here, we explore how the presence of non-conservative forces acting along the backbone of the polymer chains impacts the statics and dynamics of such systems and how the role of entanglement changes in active systems.

The material presented in this Thesis is based on the following published papers:

- Ubertini, Mattia Alberto, and Angelo Rosa. "Computer simulations of melts of ring polymers with nonconserved topology: A dynamic Monte Carlo lattice model." Physical Review E 104.5 (2021): 054503 [1].

- Ubertini, Mattia Alberto, Jan Smrek, and Angelo Rosa. "Entanglement length scale separates threading from branching of unknotted and non-concatenated ring polymers in melts." Macromolecules 55.23 (2022): 10723-10736 [2].

- Ubertini, Mattia Alberto, and Angelo Rosa. "Topological Analysis and Recovery of Entanglements in Polymer Melts." Macromolecules 56.9 (2023): 3354-3362 [3].

- Ubertini, Mattia Alberto, and Angelo Rosa. "Spatial Organization of Slit-Confined Melts of Ring Polymers with Nonconserved Topology: A Lattice Monte Carlo Study." Macromolecules (2023) [4].

The last chapter is based on an ongoing project in collaboration with Dr. Emanuele Locatelli from University of Padova.

Chapter 1

Topological effects in (linear vs ring) polymer melts: state of the art and open questions

In this chapter, we briefly introduce and review the theory of polymer melts. We will start from the established results obtained for linear chains which will be used to make the comparison for the case of interest of my PhD work: non-concatenated and unknotted rings in melt. We will comment on what is already known as well as on open problems which remain to be tackled.

In the second part of the chapter, we review a more recent area of study of polymer physics, namely, topologically complex ring assemblies. We comment on some recent experimental findings concerning this area and we frame the interest on such systems in the context of my PhD work.

1.1 Polymer melts

Polymers are large molecules consisting of many elementary units called monomers, which are connected through bonds. Monomers are characterized by excluded volume interactions which synthesize the fact that they cannot overlap. The sum of the excluded volume interactions and the typical short bond lengths make the polymer chains to be uncrossable. The *uncrossability constraints* are usually termed as *topological constraints*.

While for linear open chains, it is easy to see that these constraints are only transients, ring polymers are permanently affected by these constraints. Topological constraints influence

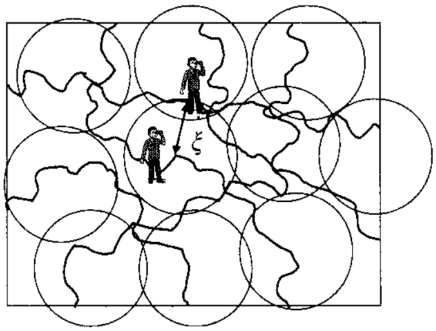

Figure 1.1: Schematic representation of the correlation length, ξ, in a polymer solution. The correlation length ξ sets the the typical scale of interpenetration between different chains. If a chain has spatial extension smaller than ξ then their properties are not affected by the presence of the other chains. Image adapted from [5]

already the behavior of diluted ring polymers [6], yet, the most notable topological effects [5] arise for both systems (for linear chains only for dynamical properties) when one considers solution of polymer chains at high concentration, *i.e.*, *polymer melts*. Polymer melts are systems at a density so high that the typical scale at which the polymer chains start to interpenetrate, the so-called *correlation length* ξ [5] (see Fig. 1.1), is smaller or equal than the scale of the typical *thermal fluctuations* [5].

1.2 Linear chains

1.2.1 Statics

As mentioned briefly in the previous section, the dynamic nature of topological constraints in linear polymer melts allows chains to relax *or disentangle* by sliding past each other, while preventing them from crossing. Notably, prior to the concept of entanglement (Sec. 1.2.2), Flory and Huggins [7, 8] developed a mean field lattice model that accurately predicted the scaling of linear chain sizes in solution. This model considers the interplay, at a mean field level, between intra-chain repulsions and inter-chain interactions. It correctly accounts for the fact that, at high concentrations, inter-chain interactions screen the intra-chain repulsions, leading to a vanishing excluded volume interaction for long chains, approximated as[1] $v_{excl} \sim 1/N$,

[1]The excluded volume parameter, v_{excl}, summarizes the net two-body interaction between monomers [5]. If $v_{excl} > 0$, monomers repel each other; $v_{excl} < 0$, monomers attract each other; $v_{excl} = 0$, the short range steric repulsion cancels exactly the attractive interactions, resulting in the chains adopting nearly ideal conformations. Typically, the value of v_{excl} is influenced by the property of the solvent in which the polymer is placed [5].

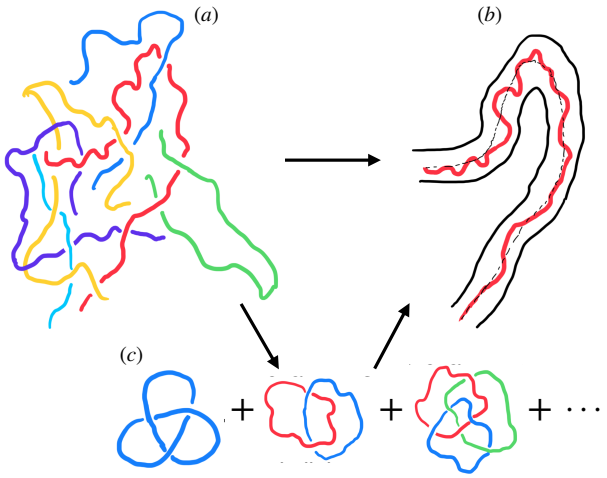

Figure 1.2: (a) Schematic representation of linear chains in the melt. (b) The effective tube of the red polymer chain according Edward's theory [13, 14]. Dotted line indicates the primitive path lying at the centre of the tube. (c) Topological approaches for the definition of polymer entanglement [13, 15–22] view the entanglements in terms of an infinite series of polymer knots or links.

where N represents the number or monomers units of the polymer chain. Consequently, under typical conditions, the equilibrium properties of linear chains are minimally affected by topology and entanglement (see Sec. 1.2.2).

Edwards [9] later provided explicit confirmation of the Flory-Huggins conjecture by demonstrating that linear polymers in the melt follow ideal statistics, with the mean size of chains, R, described by the power-law behavior:

$$R \approx \sqrt{\ell_K L}\,. \tag{1.1}$$

Here, ℓ_K [5] (see Sec. 2.2.1) represents the Kuhn length of the fiber, while $L = N\langle b\rangle$ is the contour length of the polymer, where $\langle b\rangle$ is the average bond length of the chain. These fundamental findings have been extensively validated by simulations [10–12].

1.2.2 Entanglement length

The dynamics of linear polymers in a melt can be understood as the slow reptation flow of each chain through the network of topological obstacles, known as *entanglements*, which are formed by the surrounding chains. The *tube model* [13, 14], developed by Edwards, represents the key framework for studying the rheology of polymer melts. This model summarizes the collective effects of the surrounding chains on a reference chain by confining it within an effective tube-like region (see Fig. 1.2 (b)), where the *primitive path* lies at the center line

(see Fig. 1.2 (b)). The size of the tube is determined by the *tube diameter*, denoted as d_T, which is given by

$$d_T \approx \sqrt{L_e \ell_K} \, . \tag{1.2}$$

The equation follows from Eq. 1.1 and L_e corresponds to the *entanglement length* in bond units (or N_e in monomer units, with $L_e = N_e \langle b \rangle$). L_e represents the typical length of a polymer strand with spatial span of d_T. Finally, the primitive path (see Fig. 1.2 (b)), can be thought as comprising $Z = L/L_e$ segments, each with linear size of d_T. Consequently, the average contour length of the primitive path, L_{pp}, is given by:

$$L_{pp} = d_T Z \, . \tag{1.3}$$

Thus, L_e marks the transition from the *non-entangled* to the *entangled* regime. Polymer strands below L_e are not constrained by topological obstacles and undergo random thermal motion, longer strands are heavily affected by the fact that they have to move through the tube. In principle, by knowing L_e one would be able to predict the viscoelastic properties of such entangled systems [5, 13, 14]. Consequently, extensive research has been conducted to understand the relationship between the microscopic parameters characterizing these systems and L_e.

Theoretical scaling relationships of the entanglement length L_e in terms of ℓ_K and the number density of Kuhn segments[2], ρ_K, have been derived for the two typical limiting regime of polymer melts. In the "loosely" entangled regime, $\rho_K \ell_K^3 < 1$, L_e exceeds ℓ_K resulting in a random walk behavior between entanglement points. In this case, Lin [23] and Noolandi [24] independently proposed a conjecture, for which the number of the entanglements in a cube of size d_T should be a universal constant $\rho_e d_T^3 \simeq 20$, where[3] ρ_e is the entanglement number density and $\simeq 20 \equiv O_{KN}$ is the universal *overlap number* of entanglement strands inferred from rheological experimental data, also known as the Kavassalis Noolandi overlap parameter. From this, it follows:

$$\frac{L_e}{\ell_K} \simeq \left(\frac{20}{\rho_K \ell_K} \right)^2 \, . \tag{1.4}$$

In the opposite regime of tightly entangled melts, $\rho_K \ell_K^3 \gg 1$, L_e is smaller than ℓ_K. In this regime, the relationship of L_e and $\rho_K \ell_K^3$ was determined by Semenov [25] from a geometrical argument: the area described by the transverse fluctuations of a filament of length L_e must be traversed, on average, by another filament acting as an obstacle. In particular, by definition,

[2]The number density of Kuhn segments is defined as $\rho_K \equiv \rho / N_K$, where ρ represents the monomer number density of the system, and N_K the number of monomers in a Kuhn segment. Assuming a system made up by M chains with N monomers each in a volume V, then $\rho \equiv \frac{MN}{V}$, while $N_K \equiv \frac{\ell_K}{\langle b \rangle}$.

[3]Similarly to ρ_K, $\rho_e \equiv \rho / N_e$.

two consecutive entanglement points are at polymer contour distance of L_e, then one can show that the area spanned by the deflection of a polymer filament of length L_e, along the mean primitive path, is $A \simeq L_e^{3/2}/\ell_K$ [25, 26]. Then, by requiring that the volume spanned by the tube between the two entanglement points is pierced by one filament alone, one get $\rho A L_e \simeq 1$. By combining these two relationships, the scaling of L_e in terms of $\rho_K \ell_K^3$ can be obtained:

$$\frac{L_e}{\ell_K} \simeq \left(\frac{1}{\rho_K \ell_K^3}\right)^{2/5} . \tag{1.5}$$

On the other hand, there exists a physics-motivated method known as *primitive path analysis* (PPA) [20, 27, 28] which has proved successful in the estimation of L_e and through which the two different scaling have been confirmed. PPA builds upon the core idea of the tube model [14], which suggests that linear chains can be coarse-grained down to their minimal path while still respecting the topological constraints. This approach offers an intuitive understanding of the microscopic nature of entanglements. In simple terms, PPA effectively averages out the random thermal motions that characterize the polymer chain at microscopic scales $\lesssim d_T$, allowing the polymer chain to assume the conformation of the primitive path itself.

The implementation of PPA in a modern computer simulation is quite straightforward [29, 30]. Initially, the chain ends are fixed in space. Then, by disabling the intra-chain interactions while preserving the inter-chain ones so to enforce the uncrossability constraint, the system is gradually cooled towards $T = 0$. Through energy minimization, the bond lengths decrease to zero, pulling the chains taut. By analysing the final conformations of the chains [29], it was shown that the "minimized" polymers consists of a series of straight segments sharply bending at entanglement points (see Fig. 1.3). These conformations agree with the fact that the primitive path is a random walk with $l_K \simeq d_T$ (Eq. (1.3)). Thus, PPA yields the instantaneous primitive paths, enabling the determination of the entanglement length Le from the bending statistics of paths.

Interestingly, by starting from the hypothesis, supported by extensive analysis, that PPA is a way to renormalize a loosely to a tightly entangled system, a unified view of the entanglement has been derived [31]. This concept serves as the foundation for deriving both Eq. (1.4) and Eq. (1.5) within the same theoretical framework, by simply considering opposite limits of $\rho_K \ell_K^3$. Finally, in the same work [31], a very accurate semi-empirical formula that interpolates between the two entanglement regimes have been found:

$$\frac{L_e}{\ell_K} \approx \left(\frac{1}{c_\xi \rho_K \ell_K^3}\right)^{2/5} + \left(\frac{1}{c_\xi \rho_K \ell_K^3}\right)^{2} . \tag{1.6}$$

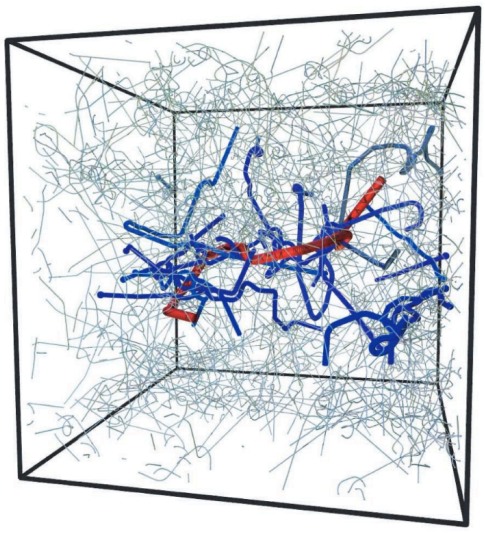

Figure 1.3: Result of the primitive-path analysis of a melt of 200 chains of $N+1=350$ beads. Here, the primitive path of one chain (red) is shown together with all of those it is entangled with (blue). The primitive paths of all other chains in the system are shown as thin lines. From the image one can notice that at the entanglement points, the red chain sharply bends while it attains straight conformations along non-entangle regions. Image adapted from [27]

Here, $c_\xi = 0.06$ is a fitted parameter. In my works, the entanglement lengths, L_e, of the different systems studied have been estimated by using Eq. (1.6).

At the same time, the notion of uncrossability and in general of topological constraints are addressed in the realm of knot theory and substantial efforts have been devoted to establishing mathematical theories that connect the topology of the melt with the effective parameters characterizing the tube model [13, 15–22]. In these works, the main idea is that one can quantify the topological constraints, to which polymers are subject in the melt, by means of suitable topological invariants (see Chapter 4), which measures the presence of knots, links and higher order topological structures (see Fig. 1.2). Then, from these topological indicators one should be able to infer the entanglement properties of the melt. However, the full characterization of entanglements in polymer melts would, in theory, require an infinite set of topological invariants [16, 18], and analytical theories are challenging to develop [32], resulting in limited applicability at present.

1.2.3 Dynamics

Building upon Edwards' tube model, de Gennes [34] developed the *reptation* model simplifying the complex motion of polymer chains in the melt, into the motion of a single chain

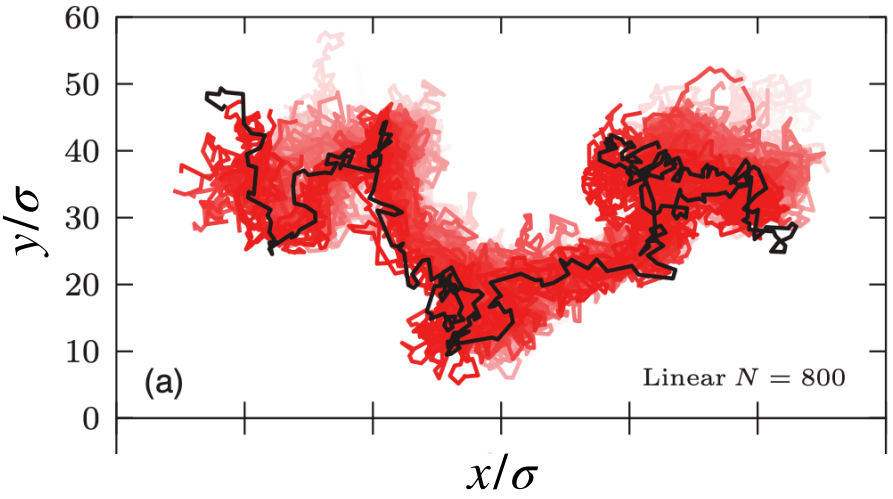

Figure 1.4: Two dimensional visualization of consecutive conformations of a linear chain with $N = 800$ in melt, sampled equidistantly on time, for a total time $\tau \ll \tau_{relax}$, obtained via molecular dynamics simulations. Chain snapshots at later times are drawn darker in color with the final chain conformation in black. From the image it is clear that, for times much smaller than τ_{relax} (Eq. (1.10)), the chain dynamics is restricted to a tube like region. Image adapted from [33]

confined within a network of fixed obstacles. In this model an entangled chain diffuses in a curved path along its confining tube (see Fig. 1.2 (a),(b) and Fig. 1.4), reminiscent of a snake's movement (and from here the name reptation).

The chain is free to diffuse up to the tube diameter, d_T, until it encounters topological constraints. The time taken to diffuse up to d_T is referred to as the entanglement time[4], τ_e.

For $\tau < \tau_e$, the chain is free to diffuse and its dynamics is described by the Rouse model [5, 14]. The Rouse model describes the dynamics of a single polymer. In its simplest form, only consecutive monomers along the polymer chain are interconnected by harmonic springs, and monomers dynamics is described by the set of coupled overdamped Langevin equations (see Sec. 2.1.1), which for the i-th monomer reads:

$$\gamma \frac{d\vec{x}_i}{dt} = -k\left(2\vec{x}_i - \vec{x}_{i+1} - \vec{x}_{i-1}\right) + \vec{\eta}_i \,. \tag{1.7}$$

Here, γ is the friction coefficient of the monomer, k represents the stiffness of the harmonic springs and $\vec{\eta}_i$ is a Gaussian noise with moments: $\langle \vec{\eta}_i \rangle = 0$, $\langle \vec{\eta}_i(t)\vec{\eta}_j(t') \rangle = 6\gamma k_B T \delta_{i,j}\delta(t-t')$ where $\delta_{i,j}$ and $\delta(t-t')$ are the Kronecker delta and Dirac delta function. The Rouse model can be solved analytically in terms of the Rouse modes which diagonalize the set of coupled

[4] τ_e is usually computed numerically as the time such that $g_1(\tau_e) \equiv 2d_T^2$ [35] (see Eq. (1.13) for the definition of the mean square displacement of single monomer g_1).

differential equations (Eq. (1.7)). Then, one can show that the first Rouse mode corresponds to the polymer's centre of mass and derive that its diffusion coefficient, D, is:

$$D = \frac{k_B T}{N\gamma} \,. \tag{1.8}$$

The longest relaxation time of the system, τ_{Rouse}, corresponds to the time the polymer take to diffuse of its own size and it corresponds to:

$$\tau_{Rouse} = \frac{R^2}{D} \sim N^{1+2\nu} \,. \tag{1.9}$$

In the present case (see Eq. (1.1)) $\nu = 1/2$ and $\tau_{Rouse} \sim N^2$.

Then, for $\tau > \tau_e$ the chain diffuses along the tube. The one-dimensional curvilinear displacement along the tube axis is unconstrained and for this reason is well described by Rouse-like dynamics. This implies that the *curvilinear* diffusion coefficient, D_c, is given by Eq. (1.8). From this, we can derive the relaxation time of the chain, τ_{relax}, which represents the time required for the chain to diffuse along the tube of length L_{pp} (Eq. 1.3) escaping from its initial topological constraints:

$$\tau_{relax} \approx \frac{L_{pp}^2}{D_c} = \frac{\gamma \langle b \rangle \ell_K}{k_B T} \frac{N^3}{N_e} = \frac{\gamma \langle b \rangle \ell_K}{k_B T} N_e^2 Z^3 \,. \tag{1.10}$$

Thus, τ_{relax} scales with the cube of the number of entanglements (Z) in contrast with Eq. 1.9, highlighting the role of topological constraints in slowing down the chain's relaxation. This slowdown is also manifest in the *asymptotic three-dimensional* diffusion coefficient of the chain, D, which can be estimated by considering that, at τ_{relax}, the chain has diffused over its own size:

$$D \approx \frac{R^2}{\tau_{relax}} \approx \frac{k_B T}{N_e \gamma} Z^{-2} \,. \tag{1.11}$$

Finally, from the reptation model, one can derive the full power-law dependencies of the mean square displacement of the centre of mass, as a function of time[5] (Eq. (2.18)), $g_3(\tau)$:

$$g_3(\tau) = \left\langle \left(\vec{r}_{CM}(t+\tau) - \vec{r}_{CM}(t)\right)^2 \right\rangle \propto \begin{cases} \tau & \tau < \tau_e \\ \tau^{1/2} & \tau_e < \tau < \tau_{relax} \\ \tau & \tau > \tau_{relax} \end{cases} \tag{1.12}$$

The $\tau^{1/2}$ dependency arises from the chain's one-dimensional diffusion along the tube, which undergoes a random walk in space.

A similar line of reasoning can be applied to derive the scaling behavior of the single

[5]We properly introduce this quantity as well as g_1 (Eq. 1.13) in the next chapter in Sec. 2.2.2

monomer mean square displacement (Eq. (2.17)), $g_1(\tau)$:

$$g_1(\tau) = \langle (\vec{r}(t+\tau) - \vec{r}(t))^2 \rangle \propto \begin{cases} \tau^{1/2} & \tau_0 < \tau < \tau_e \\ \tau^{1/4} & \tau_e < \tau < \tau_{Rouse} \\ \tau^{1/2} & \tau_{Rouse} < \tau < \tau_{relax} \\ \tau & \tau > \tau_{relax} \end{cases} \tag{1.13}$$

where τ_0 represents the microscopic time-scale of the monomer, and $\tau_{Rouse} \propto N^2$ (see Eq. 1.9).

The reptation model has been amply validated by simulations from which the tube-confined dynamics has been visualized (see Fig. 1.4). Moreover, the scaling behavior of the mean square displacements observed in simulations [35] agree with the one predicted in Eqs. (1.12) and (1.13)[6].

1.3 Joining chain ends: ring polymers

When the end monomers of the polymer chains are connected, topological interactions assume a crucial role, since the resulting topological state remains quenched for the entire course of the system. In concentrated solutions, the simplest example is represented by melts of non-concatenated and unknotted ring polymers, where the uncrossability constraint significantly restricts the conformational space accessible to the chains. As a result, unique features emerge that are absent in the linear case. The study of such systems is of great interest due to their relevance to chromosomes [37, 38]. In particular, the stability of chromosome territories during interphase [39] is in stark contrast with the mixing that chromosomes would undergo if they were well represented by an equilibrated melt of linear chains (see Fig. 1.5). Interestingly, based on an estimated time of $\simeq 500$ years a human chromosome would take to disentangle, Rosa and Everaers [37] realized that human chromosomes do not escape topological constraints, and for this reason, they can be effectively modelled as an equilibrium melt of non-concatenated and unknotted rings whose topology is, indeed, quenched and which are known to segregate forming territories. Moreover, melts of non-concatenated and unknotted rings have drawn interest due to the glassy-like behavior arising from the nonlinear topology of the chains [40–43] that causes rings to mutually thread each other (see Fig. 1.12): the importance of all this will be discussed in Sec. 1.3.3.

[6] It is worth mentioning that simulations and experiments [35, 36] revelead some deviation from the theory. An example is in the scaling $\tau_{relax} \sim Z^{3.4}$ exceeding the theoretical prediction of 3 (see Eq. (1.10)). This discrepancy can be reconciled by considering additional physical mechanisms non included in the model, such as tube-length fluctuations and constraint release effects [5].

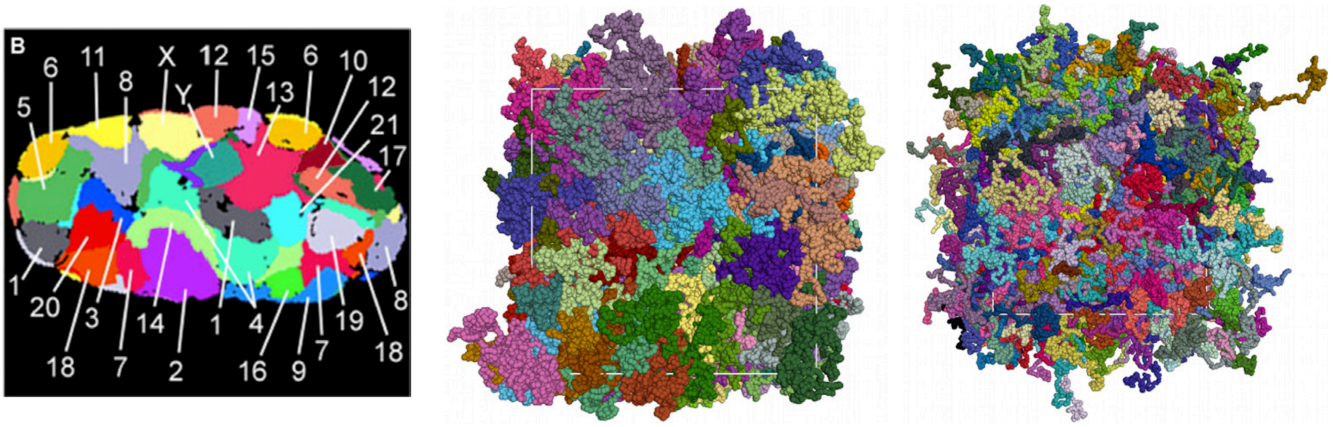

Figure 1.5: Left, experimental image of chromosome territories in a fibroblast cell nucleus reproduced from [39]. Middle, territorial segregation in an equilibrated melt of non-concatenated unknotted rings. Right, mixing of melt of linear chains at equilibrium. Middle and right images are results from molecular dynamics simulation [44]. Image adapted from [38].

The physics of ring polymer melts poses many significant challenges, and many fundamental aspects of these systems remain poorly understood. The explicit inclusion of constraints through suitable topological invariants in physical theories [45–49] proves to be mathematically arduous, if not entirely intractable, especially in the context of dense, multi-chain systems. Consequently, the existing physical models proposed thus far [50–55] employ suitable approximations to address the constraints, rendering the problem more approachable. However, these models inevitably require supplemental validation through experiments or numerical simulations.

For these reasons, in the following sections, a series of models and results will be presented and commented in light of numerical and experimental results, which have helped in the understanding and advancement of the problem.

1.3.1 Statics

Topological constraints reduce the conformation space of unknotted and non-concatenated rings and as a consequence, an effective topological exclusion volume between rings, of purely entropic origin, arises [56]. Based on this idea, Cates and Deutsch [50] were the first to tackle the problem of how rings should fold in melt. They developed a Flory theory in which the free energy of the system is given by the sum of two terms: i) the free energy cost due to topological interactions of a ring, with size R, with overlapping rings, scaling as $\sim \rho R^3/N$ (in 3-dimensions), ii) the free energy cost of for compressing a polymer in a size R, scaling as N/R^2 [5]. By balancing these two terms they obtained the scaling for the typical ring's size

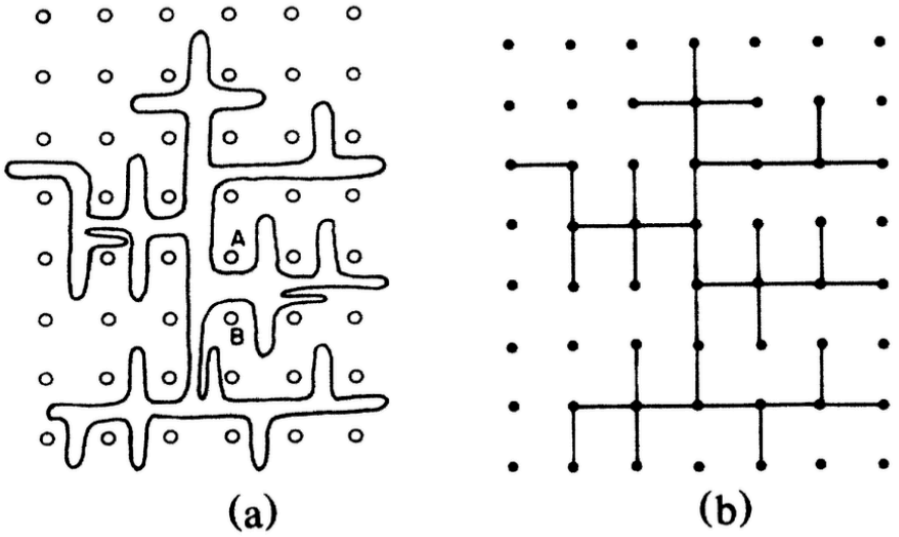

Figure 1.6: (a) Two-dimensional representation of a ring in a grid of fixed obstacles. (b) Mapping of the double-folded rings onto its corresponding lattice-tree. Image adapted from [52].

R:

$$R \sim N^{2/5} \,. \tag{1.14}$$

Thus, rings in the melt would not be ideal, $\nu = 2/5$, and they would be more compact than linear chains. The authors argued that further corrections to the free energy can considered taking into account higher order interaction terms, scaling as $\sim (\rho R^3/N)^{\alpha}$ with $\alpha \geq 1$. These corrections lead to a scaling exponent which depends on α as:

$$\nu = \frac{1+\alpha}{2+3\alpha} \tag{1.15}$$

taking any value in the interval $1/3 \leq \nu \leq 2/5$.

A distinct approach was developed later by Grosberg with his *annealed lattice-tree model* [57], which is based on earlier works [51, 52], where the problem of a ring in an array of fixed obstacle was studied (see Fig. 1.6 (a)). There, it was shown that the ring, in order to avoid crossings with the obstacles, would assume a double-folded randomly branching configuration and it can be effectively mapped to a randomly branching tree (also known as lattice animal) (see Fig. 1.6 (b)). Building upon these ideas, Grosberg assumed that non-concatenated and unknotted rings in the melt would indeed assume similarly double-folded configurations above some characteristic length scale, marking the onset of topological constraints. Assuming such length scale being the same entanglement length, N_e, valid for melt of linear chains (see Sec. 1.2.2), at scale smaller than N_e, rings are ideal $R \sim N^{1/2}$, above they assume double-folded configurations. Then, above N_e, the whole system can be mapped into a corresponding melt of annealed lattice-trees. From this assumption, he developed a Flory theory in terms of

the ring's spatial size R and the mean path length of the backbone of the corresponding tree (see thick black line in Fig. 1.7), $L_{\rm tree}$. In its model, the free energy is characterized by two terms: i) an elastic free energy $\sim R^2/L_{\rm tree}$ penalizing stretching of the tree to size R larger than the size of an ideal randomly branching tree, and ii) a second term, $\sim L_{\rm tree}^2/N$, derived in [58] corresponding to the entropic free energy of random branching. From the minimization of the free energy, one finds the scaling exponents describing the characteristic power-law behaviors as a function of $N/N_e \equiv Z \gtrsim 1$ of the following observables:

(i) The mean ring size as a function of the ring mass:

$$\langle R\rangle \sim d_T\, Z^{\nu}\,,\ \ \nu = 1/3\,; \tag{1.16}$$

(ii) The mean path length on the backbone of the tree (Fig. 1.7, thick black line) as a function of the ring mass:

$$\langle L_{\rm tree}\rangle \sim d_T\, Z^{\rho}\,,\ \ \rho = 5/9\,; \tag{1.17}$$

(iii) The mean ring size as a function of the mean path length:

$$\langle R\rangle \sim d_T^{1-\nu_{\rm path}} \langle L_{\rm tree}\rangle^{\nu_{\rm path}}\,,\ \ \nu_{\rm path} = 3/5\,. \tag{1.18}$$

Eq. (1.16) means that rings (*i.e.* the equivalent trees) behave like compact, space-filling objects while Eq. (1.18) expresses the fact that linear paths follow self-avoiding walk statistics [57]. Notice also that Eq. (1.18) follows directly from Eqs. (1.16) and (1.17), since $\nu_{\rm path} = \nu/\rho$.

Thus, to sum up, Grosberg model starts from the assumption that rings in the melt assume double-folded conformations above the entanglement length scale N_e and they can be effectively treated as annealed lattice-trees. Then, by building a Flory theory for the correspondent melt of annealed lattice-trees, he showed that rings are compact $\nu = 1/3$ and the underlying tree-backbone follows self avoiding walk statistics $\nu_{\rm path} = 3/5$.

Another very popular and accurate model is the so called *fractal loopy globule* (FLG) [55] developed by Rubinstein and co-workers. The model is based on earlier computational observations for rings in the melt showing that the overlap parameter, number of segments of a given length sharing a common volume, remains close to the Kavassalis Noolandi parameter (see Sec. 1.2.2), $O_{KN} \simeq 20$, for any subsection of the rings of length n exceeding the entanglement length, $n/N_e > 10$ [59]. From this result, the theory conjectures that the rings overlap on all scales above N_e in a self-similar manner with the the same overlap parameter $\simeq 20$. Then, being $O_{KN} = \frac{\rho}{N} R^3$, with $\frac{\rho}{N}$ representing the chain number density and R the ring's mean spatial extension, it directly follows that:

$$R \sim N^{1/3}\,, \tag{1.19}$$

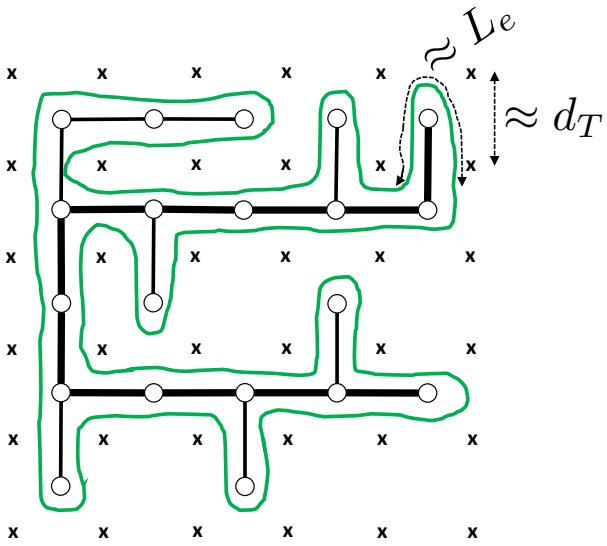

Figure 1.7: Schematic picture of a single ring polymer conformation (green line) which double-folds around its tree-like backbone (thick black line). The crosses $(\times)$ represent the lattice of topological obstacles as introduced by [51, 52]. In the theory of Grosberg [57] they represent the topological constraints created by the surrounding rings in the melt. The lattice spacing is of the order of the tube diameter d_T, and the polymer contour length inside each unit cell is $\approx L_e$.

and this holds for any subsection of the rings of length $N_e < n < N$, while below N_e, as for the Grosberg theory, $R \sim N^{1/2}$. The self similar structure of the rings (see Fig. 1.8), as loops on loops, is "somewhat analogous" to a randomly branched structure, where the loops of the FLG are viewed as the branches. The authors assert that the loops are not perfect double-folded, but do not elaborate on the double-folded structure further, except that the number of loops $n(r)$ of size r has to decrease reciprocally to their pervaded volume r^3: $n(r) \sim \left(\frac{R}{r}\right)^3$.

The difference between the FLG and the lattice-tree models, from the structural point of view is in the branching statistics, manifested in the structure of the mean (primitive) path[7]. While in the lattice-tree model the scaling of the size of a segment of the ring with the corresponding primitive path is governed by the exponent ν_{path} on scales above N_e (eq. 1.18), in the FLG, the scaling is more complicated because it takes into account "tube dilation". The tube dilation means freeing of the constraints imposed by the other surrounding segments due

[7]Note that here the terms primitive path and tree backbone are used interchangeably, because they have the same meaning for linear polymers – the shortest end-to-end path of the chain to which its contour can be contracted without crossing other chains. In rings, there are no ends and therefore such equivalence is, to say the least, not clear. The tree backbone, governing the stretching and branching of the ring is a properly weighted average of all possible path lengths in the tree structure (see [60] for details), while the primitive path of the ring is measured in [55] with a method analogous, but not identical, to primitive path analysis [29].

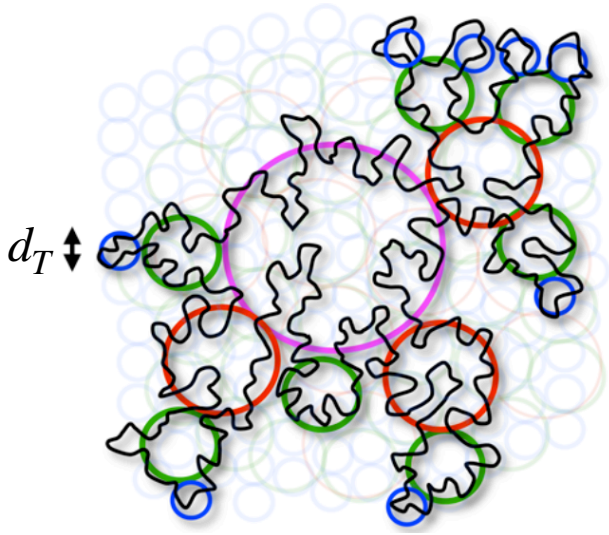

Figure 1.8: Schematic representation of a conformation of a ring (black line) in the melt according to the fractal loopy globule (FLG) model. The circles of different colors indicate the length scales where loops of various sizes overlap with similar size neighbors (dimmed in the background) at the same overlap parameter O_{KN}. Figures adapted from [55].

to their motion, hence effectively increasing the length scale between constraints, making it time-dependent $N_e(t)$. In the FLG model, if the segment is shorter than $N_e(t)$ its primitive path is just straight, hence the size of the segment scales linearly with the length. If the segment is longer than $N_e(t)$, its size scales with the exponent $\nu = 1/3$ equal to that of the whole ring. The analysis of the primitive paths in [55] reports that they do not observe the scaling of the size of the primitive path with its length with the exponent $\nu_{\text{path}} = 3/5$. Yet their analysis focuses on rather flexible system only and the reported dependence broadly and smoothly crosses over from the exponent 1 to $1/3$ (hence visiting all the intermediate exponents).

From an experimental standpoint, a few studies [61–63] have attempted to estimate the scaling behavior of ring sizes with respect to molecular weight. These studies indicate a compact structure for the rings, with scaling exponents yielding values of $\nu \simeq 0.4$. However, it is important to note that these investigations primarily focused on chains with moderate lengths corresponding to only few entanglements.

On the numerical side, early works [64, 65] supported the first theoretical estimates of $\nu \simeq 0.4$. However, simulations involving larger ring sizes [44, 66, 67] demonstrated that asymptotically, for $Z \gtrsim 15$, the exponent converges to $\nu = 1/3$. Furthermore, robust numerical evidence [59] has shown that ring polymers in a melt can be effectively mapped onto melts of interacting lattice-trees, providing support for the model proposed by Grosberg. These

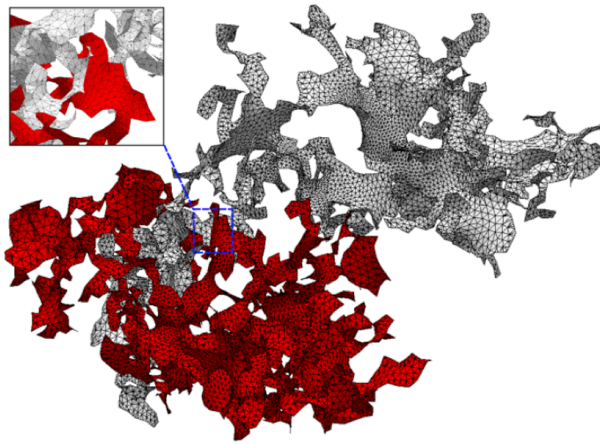

Figure 1.9: Example of the minimal surfaces spanned by two threaded rings. Image adapted from [69]

findings suggest that rings tend to adopt a compact conformation in line with the annealed lattice-tree model of Grosberg and the FLG model of Rubinstein. However, it is worth noting that direct reconstruction of a tree-like structure, which would corroborate the lattice-tree model of Grosberg, has not been reported in these studies. Detecting and quantifying the hypothesized branch structure that characterizes ring conformations in a melt remains, therefore, a challenge.

Early large-scale simulations revealed that even though rings exhibit a compact nature, they often overlap significantly with each other protruding through themselves. To this end, new observables have been developed in order to detect and quantify the openings of the rings in the melt. This is the case of the measure of loop openings proposed in [68], in which the mean-square "magnetic" radius was first introduced and defined as

$$\langle R_m^2 \rangle = \frac{1}{\pi} \langle \left| \vec{A} \right| \rangle \,, \tag{1.20}$$

where, inspired by the analogy to the classical electrodynamics of the magnetic far field generated by a loop carrying a constant electric current,

$$\vec{A} \equiv \frac{1}{2} \sum_{i=1}^{N} \vec{r}_i \times (\vec{r}_{i+1} - \vec{r}_i) = \frac{1}{2} \sum_{i=1}^{N} \vec{r}_i \times \vec{r}_{i+1} \tag{1.21}$$

is the (oriented) area enclosed by the ring. In [68], it was shown that R_m^2 obeys the same power law of the mean spatial size of the ring itself: $R_m^2 \propto Z^{2/3}$. There, they argue that one possible explanation for the scaling would be that the rings open $\mathcal{O}(1)$ loop of the same order of the rings size themselves, yet no direct evidences of this folding pattern have been explicitly shown. Another example is the minimal surface, minS, spanned by a ring polymer (see Fig. 1.9) which was introduced [69, 70] as a quantitative tool for measuring the "exposed" area that each ring

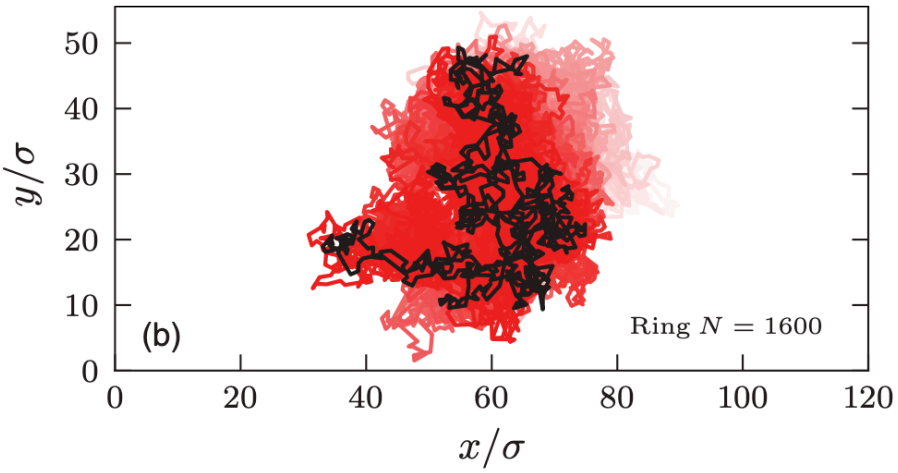

Figure 1.10: Two dimensional visualization of consecutive conformations of a ring chain with $N = 1600$ in melt, sampled equidistantly on time, for a total time $\tau \ll \tau_{relax}$, obtained via molecular dynamics simulations. Chain snapshots at later times are drawn darker in color with the final chain conformation in black. From the image, one can see that rings motion is isotropic in space and not constrained in a tube-like region as in the case of linear chains. Image adapted from [33]

offers to its neighbors. There, it was shown that $\mathrm{minS} \propto N^x$ with $x \simeq 1.03$, which would suggest that rings are, indeed, characterized by an underlying quasi double-folded structure. We recall that local opening below N_e are possible within the Grosberg model (see Fig. 1.7), then assuming that each section of rings N_e participate to a local opening of $\simeq d_T^2$, it would follow: $\mathrm{minS} \simeq d_T^2 Z$ in agreement with their analysis. Moreover, besides the absolute value of the surfaces, the pipeline developed in [69] allows to precisely triangulate the area exposed by the rings: in this way, one can precisely quantify ring-ring interpenetration (see Fig. 1.9), referred to as *threadings* (see Fig. 1.12). This has been done in [69, 71] where they have shown that threadings become increasingly present as ring size increases. In Chapter 3, we will employ such tools for the characterization of non-concatenated and unknotted ring polymers in melt.

1.3.2 Ring dynamics

Ring polymers do not posses ends, which leads to their inability to perform reptation as linear chains do. Large-scale simulations of melts of ring polymers [33] have confirmed this observation finding that at short timescales, unlike linear chains that diffuse within a tube-like region (see Fig. 1.4), ring polymers exhibit unrestricted spatial fluctuations (see Fig. 1.10).

In the next section, we recapitulate the general results for ring dynamics according to the

annealed lattice-tree model of Grosberg discussed in Refs. [53, 60] and we compare them to the ones of the FLG of Rubinstein [55]. In order to quantify chain dynamics we consider as for linear chains (see Sec. 1.2.3), the single monomer mean-square displacement (see Eq. 1.13), $g_1(\tau)$, and the mean-square displacement of the ring centre of mass (see Eq. 1.12), $g_3(\tau)$.

Dynamics in the annealed lattice-tree model For time scales $\tau \lesssim \tau_e$ and length scales $\lesssim d_T$ monomer motion is not affected by entanglements and we expect the characteristic Rouse-like [5] behavior, $g_1(\tau) \sim \tau^{1/2}$ and $g_3(\tau) \sim \tau$.

On larger time scales $\tau \gtrsim \tau_e$, mass transport *along the trunk* is, by assumption, the dominant relaxation mode of the chain (see Fig. 1.11): in particular, each one of the $\mathcal{O}(Z^\rho)$ branches (Eq. (1.17)) protruding from the trunk acts as a "reservoir" exchanging a single polymer mass of equivalent contour length $\sim L_e$ on the time scale $\sim \tau_e$ with its neighbors. The displacement associated to a single mass exchange, projected along the trunk, is of the order of $\sim \frac{d_T}{Z}$; since each of them happens randomly the curvilinear mean-square displacement of the centre of mass of the chain after τ_e is:

$$\langle (\Delta L_{\rm tree})^2 \rangle \sim \left(\frac{d_T}{Z}\right)^2 Z^\rho = d_T^2\, Z^{\rho-2}\,,$$

while the total relaxation time of the chain is given by

$$\tau_r \sim \frac{\langle L_{\rm tree}\rangle^2}{\langle (\Delta L_{\rm tree})^2\rangle/\tau_e} \sim \tau_e\, Z^{2+\rho}\,. \tag{1.22}$$

Per self-similarity of the branched structure, the mass $z(\tau)$ of ring sections which have relaxed up to time τ with $\tau_e \lesssim \tau \lesssim \tau_r$ can be obtained by inverting Eq. (1.22), *i.e.*

$$z(\tau) \sim \left(\frac{\tau}{\tau_e}\right)^{1/(\rho+2)}\,. \tag{1.23}$$

By using Eq. (1.16) this is equivalent to the mean-square displacement:

$$g_1(\tau_e \lesssim \tau \lesssim \tau_r) \sim d_T^2 \left(\frac{\tau}{\tau_e}\right)^{2\nu/(\rho+2)}\,. \tag{1.24}$$

Similarly, the mean-square displacement, g_3, of the centre of mass of the chain results from the sum of the (independent) random motions of the $z(\tau)$ ring sections which have relaxed up to time τ, *i.e.*

$$g_3(\tau_e \lesssim \tau \lesssim \tau_r) \sim \frac{g_1(\tau)}{Z/z(\tau)} \sim \frac{d_T^2}{Z}\left(\frac{\tau}{\tau_e}\right)^{(2\nu+1)/(\rho+2)}\,. \tag{1.25}$$

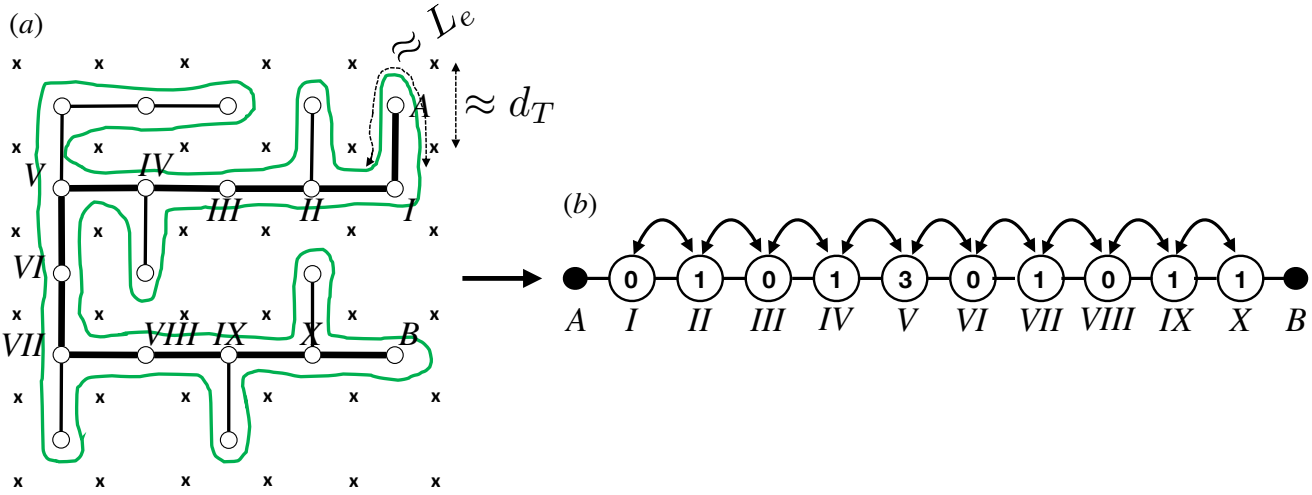

Figure 1.11: Schematic representation of the relaxation process within the annealed lattice-tree picture. (a), as in Fig. 1.7, a ring conformation in the lattice of topological obstacles is represented with its underlying lattice-tree backbone, the trunk (thick black line), which is ramified in further branches. (b), a schematic representation of the relaxation process acting via diffusion of the branches between the nodes of the trunk, the total weight of the branches for the specific conformation are reported inside the nodes.

At large times $\tau \gtrsim \tau_r$ the whole chain is simply diffusing ($g_1(\tau) \sim g_3(\tau) \sim D_{\rm ch}\,\tau$) with the chain diffusion coefficient given by $D_{\rm ch} \sim \langle R_g \rangle^2/\tau_r$, with $\langle R_g \rangle \sim d_T\, Z^\nu$ (see Eq. (1.16)). By fixing the numerical coefficients for smooth crossovers, the complete time behaviors for g_1 and g_3 are then given by the respective expressions:

$$g_1 \sim d_T^2 \times \begin{cases} \left(\frac{\tau}{\tau_e}\right)^{1/2}, & \tau \lesssim \tau_e \\ \left(\frac{\tau}{\tau_e}\right)^{2\nu/(\rho+2)}, & \tau_e \lesssim \tau \lesssim \tau_r \\ Z^{2\nu-\rho-2}\,\frac{\tau}{\tau_e}, & \tau \gtrsim \tau_r \end{cases} \tag{1.26}$$

and

$$g_3 \sim d_T^2 \times \begin{cases} \frac{1}{Z}\frac{\tau}{\tau_e}, & \tau \lesssim \tau_e \\ \frac{1}{Z}\left(\frac{\tau}{\tau_e}\right)^{(2\nu+1)/(\rho+2)}, & \tau_e \lesssim \tau \lesssim \tau_r \\ Z^{2\nu-\rho-2}\,\frac{\tau}{\tau_e}, & \tau \gtrsim \tau_r \end{cases} \tag{1.27}$$

Comparison with the fractal loopy globule As mentioned in the previous section, the FLG model [55] takes into account the tube dilation which means that the constraints imposed by the other surrounding segments vanish due to their local motion: the more the monomers diffuse over space, the more constraints cease to be present, leading to a bigger tube diameter, hence a time-dependent $N_e(t)$ increasing over time.

In particular, in the model, the time-dependent *characteristic loop* plays an important role. This is defined as the ring section containing $g(t)$ monomers such that its spatial extension is equal to the root-mean-square displacement of its centre of mass:

$$r(g,t) \equiv \sqrt{g_3(g,t)}\,. \tag{1.28}$$

Here, $g_3(g,t)$ indicates the mean square displacement of the centre of mass restricted to sections of the polymers containing g monomers. Instead, $r(g,t)$ represents the average spatial size of the characteristic loop made up by $g(t)$ monomers.

In [55], they develop a method to compute the time-dependent ring primitive paths by averaging the position of the monomers of the chains over the time interval t. From the t-dependent primitive paths, they estimate the time dependence of the tube diameter, $d_T(t)$, finding that $d_T(t)$ increases as a function of time, *i.e.*, a dilating tube diameter. They compare these results with the estimates of $r(g,t)$ conveying that $d_T(t) \simeq r(g,t)$, which implies that $N_e(t) \simeq g(t)$.

More generally, one can imagine partial dilation of the tube, which can be expressed through the relation: $N_e(t) \simeq g(t)^\theta$ with $0 \leq \theta \leq 1$. θ serves as parameter quantifying the dilation, with $\theta = 1$, there is complete dilation, while $\theta = 0$ there is no dilation $N_e(t) = N_e$ independent of time.

Besides this important difference, the theory relies on the same concept of self-similar dynamics of the annealed branching trees discussed for the Grosberg's model. Following similar reasoning as shown for the Grosberg model dynamics, in [55], they make predictions for the g_1 and g_3 as a function of the parameter θ:

$$g_1(\tau) \sim \tau^{\frac{2}{\frac{2}{\nu}+\frac{1-\theta}{\nu_{\text{path}}}+\theta}}\,, \tag{1.29}$$

and

$$g_3(\tau) \sim \tau^{\frac{2\nu+1}{\nu\left(\frac{2}{\nu}+\frac{1-\theta}{\nu_{\text{path}}}+\theta\right)}}\,, \tag{1.30}$$

for times $\tau_e \leq \tau \leq \tau_r$.

By setting $\theta = 0$, the Grosberg predictions are obtained (Eq. (1.26) and Eq. (1.27)). Setting $\theta = 1$, one finds the prediction of the FLG model. Anyhow, the predictions of the two models regarding the exponents governing the dynamics of g_1 and g_3 are quite similar to each

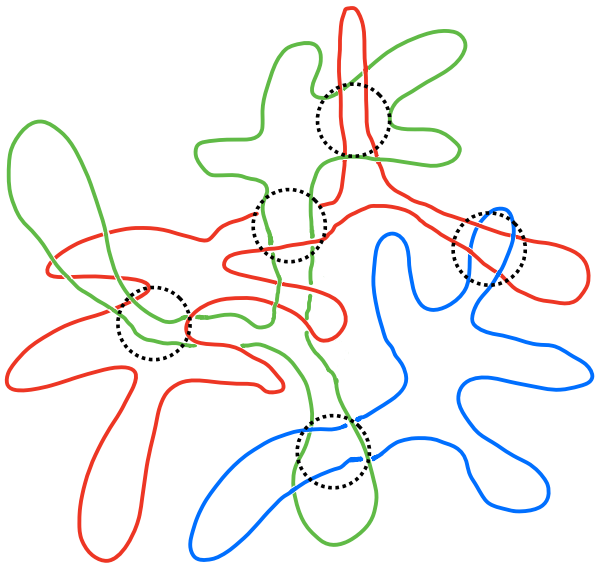

Figure 1.12: Schematic representation of ring polymers in melt. Encircled regions denote threadings. The relaxation process described schematically in Fig. 1.11 is hindered by their presence since blobs cannot diffuse anymore freely along the backbone but they have to wait for them to disappear.

other. The single monomer mean square displacement, $g_1(\tau)$, scales as: i) $g_1(\tau) \propto t^{0.26}$ for the lattice-tree model and ii) $g_1(\tau) \propto t^{0.29}$ for FLG one. Instead, the centre of mass mean square displacement, g_3, goes respectively as: $g_3(\tau) \propto 0.65$ and $g_3(\tau) \propto 0.71$.

Thus, the FLG and the annealed lattice-tree model, are very close in the predictions of the scaling of mean square displacements and these predictions are in agreement with experimental and numerical estimates [33, 55, 72].

Failure of the models Even if the two models are in good agreement with results obtained for the mean-square displacements through simulations and experiments, it turns out that both models underestimate the scaling of the diffusion coefficient, D, with N. This is computed as $D \sim R^2/\tau_{relax}$, where the relaxation time τ_{relax} can be derived as a function of the parameter θ [55]:

$$\tau_{relax} \sim \tau_e (N/N_e)^{2+(1-\theta)\nu/\nu_{\rm path}+\theta\nu}\,, \tag{1.31}$$

which gives

$$D \sim N^{-2+\nu(2-\theta-(1-\theta)/\nu_{\rm path})}\,. \tag{1.32}$$

Thus, for the annealed lattice model of Grosberg ($\theta = 0$ and $\nu_{\rm path} = 3/5$), $D \sim N^{-1.89}$, while for the FLG model ($\theta = 1$), $D \sim N^{-1.67}$. However, experimental and numerical estimates suggest that the scaling is approximately $D \sim N^{-2.34}$ [33, 55, 72]. This discrepancy might be

attributed to the fact that both systems neglect the role of threadings, penetration of a ring through the surface of another ring, in the dynamics. In both models, the ring dynamics is based on the self-similar relaxation arising from the diffusion of blobs along the rings. However, the presence of threadings (see Fig. 1.12 and Fig. 1.9) could hinder such relaxation process since the blobs cannot diffuse anymore freely along the backbone. Hence, this mechanism can slow down the dynamics and it might be the cause of the discrepancy observed in the scaling of D. However, incorporating threadings into the models is challenging, and currently, there is no straightforward method to account for their dynamic role.

1.3.3 Open questions

Upon reviewing the current state of knowledge, it is apparent that several unanswered questions persist regarding the static and dynamic properties of non-concatenated and unknotted rings in a melt. The annealed lattice-tree and the FLG model, when compared with numerical and experimental data, demonstrate accurate predictions for both the static and dynamic characteristics except for the scaling of τ_{relax} (Eq. (1.31)) and D (Eq. (1.32)). The failure in predicting such scalings may be caused by the main notable limitation of these models: the neglect of the role of inter-ring threadings in the relaxation dynamics of the rings. In particular, the annealed lattice-tree model explicitly forbids them by assuming perfect double-folding of the ring backbone. On the contrary, even if, according the FLG model, threadings are not prohibited, they are simply neglected by assuming the self-similar dynamics discussed in Sec. 1.3.2. Thus, the overlook of their dynamical implications may explain the differences registered in the scaling exponent governing the diffusion coefficient and relaxation time seen between theory and simulations/experiments.

Furthermore, studies have shown that inter-ring threadings can form a network of topological obstacles. The formation of a network of threadings seems to be responsible for the glass transition showed by melts of rings when a fraction of the rings in the system are immobilized [41, 42], a phenomenon that is completely absent in the linear counterpart. Moreover, since the fraction of rings needed to induce the transition has been shown to decrease with N, it has been conjectured that long enough rings would become a glass, yet no simulations have clearly proved this point. Moreover, threadings undoubtedly have physical implications when the melt is driven out-of-equilibrium, such as in elongation flows [73], where the spontaneous formation of supramolecular chains made up by multiple rings connected by tight threadings causes an enhancement in the viscosity of the system. Another notable example is with induced asymmetry in local monomer mobilities [43], where the mixed composition of the rings made up of monomers with different mobilities induces the formation of clusters of rings that fail to

relax due to the presence of long-lived threadings. For these reasons, it is crucial to advance our understanding of the presence and role of threadings, as well as their relationship with the possible double-folded structures assumed by the rings according to the Grosberg model.

Additionally, both the annealed lattice-tree and the FLG are models working at length-scales beyond the entanglement lengths L_e and d_T. However, it remains unclear whether these length scales are identical to those introduced for linear chains (as discussed in Sec. 1.2.2).

As part of my PhD work, I focused on the interplay between the double-folding of the ring backbone and threading-like interactions between different rings. By performing extensive large-scale simulations of systems of non-concatenated and unknotted rings with variable bending rigidity, I showed that rings are double-folded at and beyond the entanglement length scale L_e. Interestingly, we found that double folding is enhanced by the stiffness of the polymer fiber in such a way that most of the double folding features seen for stiffer rings are completely lost for the fully flexible case. This finding could explain why no indication of a tree-like structure was found in [55], where polymers comparable to the flexible ones studied in my work were examined. In addition, the analysis suggests that the tree-like backbone has a self-avoiding walk tree-backbone as for the Grosberg model [57]. At the same time, I showed that rings open their surfaces hosting numerous threadings. We reconciled this observation with the double-folded model by observing that threadings are localized at a scale of $\leq d_T$, thus causing little openings. Interestingly, all the threadings-related quantities are controlled by the entanglement length L_e, as also shown in [71]. Yet, in this work, we show that small protrusion of length $L \lesssim L_e$ are system dependent and they have to be taken into account to restore universality for quantities like the minimal surface of the rings [69]. Even if localized, threadings are numerous, they grow with the size of the ring polymers, and they can be much longer than L_e, thus relevant for the dynamics. For this reason, by analyzing the dynamical behavior of such systems, focusing on the results of numerical experiments involving partially pinned systems [41, 42], I showed that the observed dynamical features cannot be reconciled within the current models, necessitating explicit consideration of threadings in the theories.

1.4 Violating the topological constraints

In my PhD work, I also focused on characterizing the physics of the opposite system described earlier, namely, randomly knotted and concatenated rings in the melt. These studies aimed to address the question of what happens when concentrated solutions of ring polymers can perform strand-crossing, hence overcoming the topological constraints. Characterizing such systems is a challenging task because it involves introducing new observables capable of distinguishing whether ring polymers are knotted or concatenated. Mathematical topology

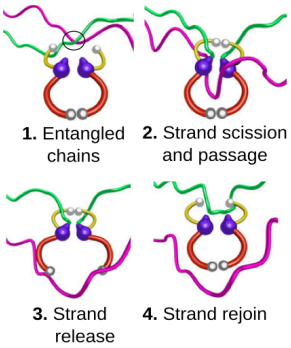

Figure 1.13: Illustration of the strand-passage mechanism between DNA filaments (green and violet filaments) mediated by the TopoII enzyme. During the reaction, the enzyme open the green chain, it makes the violet chain cross the green one, and finally the cut green segment is sealed. Image adapted from [93].

provides a natural framework for distinguishing knots and links, involving the computation of complex topological invariants. Consequently, only a limited number of analytical findings exist for simpler systems, such as the probability of knotting in a self-avoiding walk [74] or the linking of closed curves in pairs [75–77]. For a more comprehensive discussion, we refer to the reviews [77, 78]. Due to the limited applicability of analytical theories, numerical approaches have become the standard method for investigating such problems. However, most existing numerical studies have primarily focused on a couple of rings or dilute solutions of polymers [56, 79–81]. In contrast, I have focused on characterizing both the statics and the dynamics of ring polymers, which can overcome topological constraints, in melt condition, a problem also explored in [82–85]. In the following section, I will provide a brief explanation of the significance of this problem and discuss the current understanding in the field.

1.4.1 Topological polymeric materials

The synthesis of polymer materials characterized by topologically complex motif, as knots and links, has opened new routes for fine-tuning the mechanical properties of polymeric materials. This is for instance the case of the so called *smart materials* like polycatenanes and polyrotaxanes [86, 87], which consist of interlocked components resulting from precise and orchestrated ring-closure reactions. These components possess internal degrees of freedom and mobility that define the unique conformational space of the molecule. Still limited by the experimental constraints, a series of recent computational works on linear-catenanes [88–92] have shed new lights on the interesting mechanical properties of such systems arising from the "mechanical" bonding rather than the usual covalent bond.

Interlocking and topology manipulations take place also in the realm of biology occupying

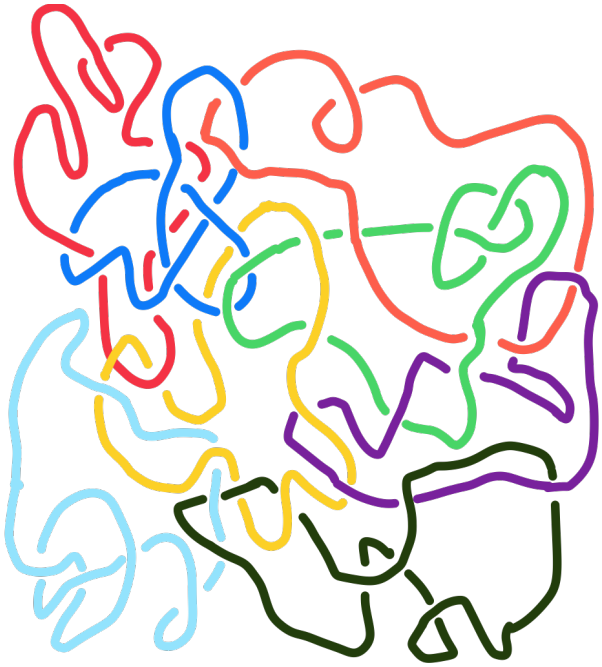

Figure 1.14: Schematic representation of a random "Olympic" gel as obtained in [93]. Here, due to the strand-crossing between nearby polymer filaments, ring polymers are randomly knotted and concatenated with neighbored chains.

a prominent role in the organization of the long DNA molecules which constitute the genomes of many organisms. For instance, in eukaryotic nuclei in normal cell conditions (interphase) the cm-long filament of DNA of each chromosome is densely packed into a corresponding μm-sized "territory" [37, 94]. In this situation, tight confinement may result in an "excess" of entanglements which may be detrimental [95] at the later stage of cell division: a specific class of enzymes, the topoisomerases [96] and in particular the type II topoisomerase (hereafter, TopoII), removes the entanglement [97] between two nearby DNA strands by cutting one strand, moving the other through the cut and ligating the broken strand back. Recently, inspired by such biological mechanism, the Spakowitz's group at Stanford [93] showed that the *strand crossing* action performed by TopoII is capable of "fluidizing" concentrated solutions of unknotted and unconcatenated DNA rings. Moreover, by blocking the activity of the enzyme, the once free rings become permanently linked with each other: under these conditions, the DNA solution becomes equivalent to a so called "Olympic" gel, a polymer material, first theorized by P.G. de Gennes [98, 99], which is maintained together by *topological bonds* and not by chemical cross-links as in the case of traditional gels [5]. Such "Olympic" gels, differently from polycatenanes which are synthesised following chemical precise routes, are characterized by an interlocking pattern that is the result of random strand-crossing of nearby DNA rings, consequently, there is no control on the topology of the resulting network. Estimates of the

linking of the network can be just indirectly inferred from rheological measurements as in [93]. For this reason, theoretical and numerical works [82–85] take an important role in the understanding of the properties of these complex systems. As a result of these investigations, a new understanding of the factors that can influence the network topology, hence the mechanical properties, has been developed. These works have also biological implications since there exist systems as the kinetoplast DNA characterizing the organization of the mitochondrial DNA of certain protozoa [100–102] which can be modeled [81] as an "Olympic" gel.

The most interesting feature showed by the material synthesised in the Spakowitz's experiment is the possibility to bend polymer topology to produce materials capable of switching from liquid-like to more solid-like behavior. From their results, it is clear that the dynamical nature of the action of TopoII plays an important role as it was shown that the fluidization of the DNA system was taking place at the typical time-scale of action of TopoII ($\simeq 1s$). Then, it seems clear that, at least for the dynamics, the kinetic features of TopoII may be relevant. Moreover, it is not known, a priori, whether or not the competition of the internal relaxation time-scales of the polymers and the time-scale of action of the enzyme can be important also for the statics, resulting in different topological networks based on their respective values. Nonetheless, studies focusing on the formation of an "Olympic" gel from a solution of polymer non-concatenated and unknotted rings [81–85], as in the case of the experiment, have always overlooked on the role of the kinetics of the enzyme within their computational models.

1.4.2 Open questions

Unlike the case of non-concatenated and unknotted rings, this area is relatively new and less explored. As mentioned earlier, there is currently no model that considers the kinetics of the enzyme responsible for strand-crossing in polymer filaments. Therefore, it appears necessary to develop a model that accounts for this aspect. For this reason, part of my work has dealt with the development of a suitable computational model that incorporates the kinetics of the strand-crossings between nearby polymer filaments. Once the model was developed, I conducted extensive computer simulations to study and characterize the dynamics and statics of the system. The interplay between the relaxation time-scale of the polymer chains and the time-scale of the enzyme was found to be crucial in understanding the overall dynamics of the system. Furthermore, I explored the influence of various parameters on the resulting network of concatenated rings. Specifically, I investigated the effects of chain length, bending rigidity, and confinement on the system's topological properties. By exploring these factors, we reached a deeper understanding of how they shape the structure and behavior of such systems. Finally, by highlighting the connection between the ensemble of randomly concatenated and

knotted rings with the one of linear chains in the melt, I addressed the long-standing problem of the definition of the entanglement length L_e from the internal topology of the melt (see Sec. 1.2.2).

Chapter 2

Materials and methods

This chapter outlines the numerical methods employed for investigating the polymer systems under study. We also present the observables we have commonly used for characterizing the statics and dynamical properties of such systems.

2.1 Polymer modeling and simulation

In my PhD work, I have focused on modelling and simulating dense polymer solutions. In particular, I have studied melts of ring polymers because of the interesting features they provide due to their non-linear topology. As discussed in the previous chapter, these systems hold significance in both the realms of biology, such as the folding of chromosomes within cells, and materials science, with the recent synthesis of topological materials composed of interlocked ring polymers: for all these reasons, rings necessitate a deeper understanding of their characteristics.

The significance of the minimal polymer modelling employed in this Thesis lies in the universal behavior exhibited by polymers, as elucidated by De Gennes [98]: despite differences in chemical composition, many polymer systems share identical properties when appropriately scaled using system-specific units. Consequently, to comprehend the macroscopic behavior of these systems, it is often unnecessary to delve into an atomistic definition of the system.

A prime example is the case of polymer chains in melt conditions, which exhibit similar rheological behaviors [103] when typical observables are expressed in terms of appropriate entanglement units: so, we express contour lengths as $Z = L/L_e$, spatial distances in terms of the "tube diameter," d_T, and time in units of the entanglement time, τ_e (see Sec.1.2.2 for details). Hence, the study of complex polymer materials can be approached by matching them with simpler polymer models possessing equivalent degrees of entanglement [103]. It is

crucial to recognize that chain entanglement arises from the inability of polymer filaments to pass through one another, resulting from both the exclusion volume of monomers and chain connectivity. As a consequence, there is no necessity for intricate and fine-grained models. Instead, suitable coarse-grained polymer models suffice, where monomers interact through a strong and short-range repulsive force, and consecutive monomers are connected in a manner that prevents neighboring polymer filaments from interpenetrating.

There are two primary families of numerical approaches that have emerged and are widely employed for the investigation of polymeric systems.

The first category is *off-lattice methods*, distinguished by the absence of a requirement for monomers to reside on a regular grid. In these approaches, monomers undergo evolution either through Monte Carlo methods or by integrating their dynamics "continuously" in time. One prominent off-lattice coarse-grained polymer model is the Kremer-Grest (KG) model [35, 104]. In this model, monomers are represented as hard spheres connected by nonlinear springs, effectively capturing the connectivity and liquid-like arrangement observed in polymer melts. The behavior of polymers in the KG model is studied through numerical integration of Langevin dynamics. The versatility of molecular dynamics simulations allows for a wide range of investigations using the KG model, spanning from the properties of synthetic polymers to their biological counterparts. We briefly discuss off-lattice dynamics and the KG model in Sec. 2.1.1, for a more detailed discussion about KG coarse-grained models and their applicability we refer to [35, 103, 105].

The second family of models employed in the study of polymeric systems consists of *on-lattice* polymer models, where monomers are located exclusively at the vertices of a conveniently chosen regular lattice (like the simple cubic, FCC, etc.). In this case, the evolution of the system is simulated using Monte Carlo methods. In these models, excluded volume effects are implemented simply by prohibiting more than one monomer from occupying the same lattice site. Chain connectivity is typically enforced by requiring consecutive monomers on the polymer backbone to occupy neighboring lattice sites, effectively preventing bond intersections and strand-crossing. As a result, the interaction between monomers typically occurs through a localized delta-like potential, which enforces the non-overlapping criterion. The locality of the interactions represents the main computational advantage of on-lattice methods over off-lattice methods, which instead require calculating inter-monomer distances, an operation that scales approximately as $(\text{number of monomers of the system})^2$.

While numerous on-lattice methods have been developed over the years (for a comprehensive discussion, we refer to the review by Kremer and Binder [106]), only a few of them exhibit numerical efficiency in simulating polymer chains at high concentrations. Most Monte Carlo methods, relying on global moves, encounter challenges when a significant portion of

lattice sites become occupied. In contrast, methods based on local displacements of individual monomers prove to be highly efficient. Moreover, since the Monte Carlo moves consist of local jumps, the motion developed during the course of the simulation can be used for studying the dynamic properties of the polymer system. The most-known models used for simulating polymers in melt conditions are: i) the "bond fluctuation model" proposed by Carmesin and Kremer [107, 108], and ii) the "elastic lattice polymer model" developed by Hugouvieux et al. [109], based on Rubinstein's Repton model [110]. Both models have been extensively utilized and have demonstrated remarkable efficiency in simulating the coarse-grained dynamics of concentrated polymer melt solutions. In Sec. 2.1.2, a detailed description of the "elastic lattice polymer model" will be provided, being the model employed in most of this Thesis.

2.1.1 The Langevin equation and the Kremer and Grest model

The polymer systems under investigations are usually immersed in a solvent. Yet, explicit simulations taking into account also the solvent molecules are computationally prohibitive as one would need to solve the equation of motions of million of atoms [104]. For this reason, in standard polymer simulations, the interactions with the solvent molecules are taken into account effectively by coupling the polymeric system to a heat bath at some temperature T. The dynamics of a system, which is coupled to a heat bath, is well described by the *Langevin dynamics*, whose equation of motion, for the generic i-th monomer, reads:

$$m\frac{d^2\vec{x}_i}{dt^2} = -\gamma\frac{d\vec{x}_i}{dt} - \nabla\mathcal{U}_{int} + \vec{\eta}_i. \tag{2.1}$$

Here, apart from the the deterministic force, arising from monomers interactions (given by $-\nabla\mathcal{U}_{int}$), the equation accounts for a viscous force, $-\gamma\frac{d\vec{x}_i}{dt}$ with γ representing the friction coefficient, and a random force, η_i, modeling implicitly the interactions with solvent molecules. Here, the stochastic spatial components of the random force $\vec{\eta}_i$ are Gaussian variables with zero mean

$$\langle\eta_{i,\alpha}\rangle = 0 \tag{2.2}$$

and variance

$$\langle\vec{\eta}_{i,\alpha}(t)\vec{\eta}_{j,\beta}(t')\rangle = 2k_BT\gamma\delta(t-t')\delta_{i,j}\delta_{\alpha,\beta}\,. \tag{2.3}$$

Then in this context, molecular dynamics simulations consist in integrating the set of coupled Langevin equations "continuously" in time. Finally, it is important to note that by integrating Langevin dynamics, the simulated trajectory samples the canonical ensemble, in which the number of monomers of the system, the volume and temperature are fixed and constant throughout the course of the simulation.

The modeling of the system resides in the choice of the functional form of the interaction potential, $\mathcal{U}_{int}$, and its parameters. A widely used model for polymer simulations is the one introduced by Kremer and Grest [35, 104], which has become the standard for studying generic polymer properties through molecular dynamics simulations. The model describes interactions between the beads as a sum of two potential: $\mathcal{U}_{int} = \mathcal{U}_{\text{LJ}} + \mathcal{U}_{\text{FENE}}$.

Excluded volume interactions are accounted for all pairs of monomers (belonging to the same chain or to two different chains) of the system via the shifted and truncated Lennard-Jones (LJ) potential, $\mathcal{U}_{\text{LJ}}$,:

$$\mathcal{U}_{\text{LJ}}(r) = \begin{cases} 4\epsilon \left[\left(\frac{\sigma}{r}\right)^{12} - \left(\frac{\sigma}{r}\right)^{6} + \frac{1}{4} \right] & r \leq r_c \\ 0 & r > r_c \end{cases} \tag{2.4}$$

where σ represents the monomer size, and ϵ is the interaction strength, and they are usually both set to 1 defining respectively the unit of length and energy. Finally, r represents the distance between the two monomers, and $r_c = 2^{1/6}\sigma$ is the cutoff distance, corresponding to the minimum of the potential. In this way, only the repulsive interaction of the LJ potential is accounted.

In addition to $\mathcal{U}_{\text{LJ}}$, consecutive monomers along the same polymer chain interact via a bonding potential defined by the *finitely extensible non-linear elastic potential* (FENE):

$$\mathcal{U}_{\text{FENE}}(r) = -\frac{1}{2}\kappa R_0^2 \ln\left(1 - (\mathrm{r}/\mathrm{R}_0)^2\right) \tag{2.5}$$

where $\kappa = 30\epsilon/\sigma^2$ is the spring constant, while $R_0 = 1.5\sigma$ is the maximum extension of the bond. It is worth noting that given the form of the FENE potential, the bond length, b, is a fluctuating quantity. In particular, with the standard parameter values $m = \sigma = \epsilon = k_B T = 1$, $b \simeq 0.97$ and fluctuations are small preventing strand-crossings [35, 104].

In Chapter 8, we employ molecular dynamics simulations to investigate systems of linear chains out-of equilibrium, and in this case simulations have been done using LAMMPS, a widely used molecular dynamics simulator [111].

2.1.2 Elastic lattice polymer model

The "elastic lattice polymer model", to which we will refer also as kinetic Monte Carlo (kMC) algorithm, developed in [109] is derived from the concept of the repton model introduced by Rubinstein [110], and it has been widely used in many domains. Its first application was for the study of block copolymers [109], later has been applied for the investigation of dense solutions of non-concatenated and unknotted rings [68, 112] and for studying the properties of the so-called fractal globule [113]. Moreover, it has been employed in biological

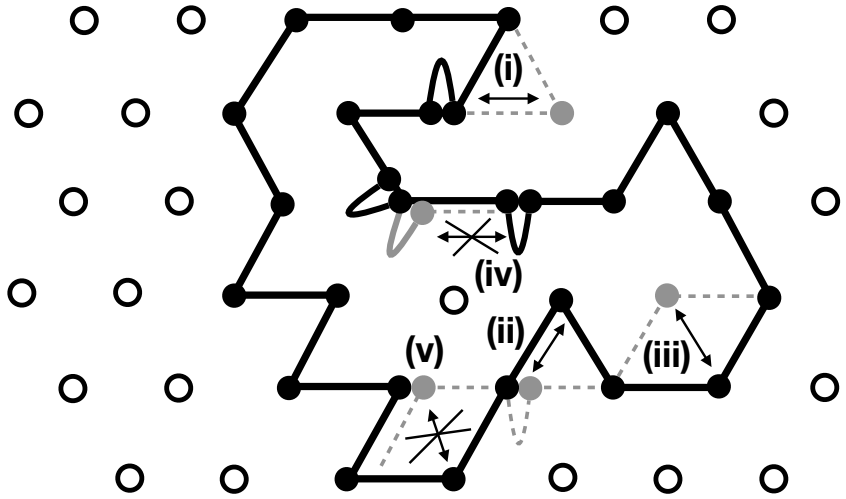

Figure 2.1: Two-dimensional illustration of the lattice polymer model with topology-preserving moves. Monomers (filled dots) occupy the spatial positions of a regular lattice (empty dots) and two nearest neighbor monomers are connected by a black line representing the polymer bond between them. For two nearest neighbor monomers occupying the same lattice site, the bond connecting them (the arcs) makes a unit of "stored length". Lattice positions connected by the double arrows are examples of MC *allowed* moves: (i) a unit of stored length unfolding to a normal bond; (ii) a bond folding into a unit of stored length; (iii) a Rouse-like move. Lattice positions connected by the double arrows with the cross are examples of MC *forbidden* moves: (iv) three consecutive monomers along the chain occupying the same lattice site; (v) two non-consecutive monomers along the chain occupying the same lattice site, hence violating the excluded volume constraint.

contexts specifically in simulating chromatin behavior within the nucleus [114–117].

The specific implementation we employ is based on the work by Hugouvieux et al. [109]. In line with the approach presented in that work, we implement the model on the three-dimensional face-centered cubic (FCC) lattice. The choice of the FCC lattice is motivated by its increased number of nearest neighbors and a smoother range of bond angles compared to the simple cubic lattice. Moreover, differently from the simple-cubic and body-centered cubic lattices, moving from one lattice point to another one can be made in an arbitrary number of steps. In this implementation, the lattice spacing corresponds to our chosen unit of length and is denoted as a.

In this model, illustrated in Figure 2.1 in two dimensions for simplicity, consecutive monomers along the polymer chain can either reside on nearest neighbor lattice sites or occupy the same lattice site. However, no more than two consecutive monomers are allowed to share the same

lattice site due to excluded volume effects. This arrangement gives rise to two possible bond lengths: $b = a$ when monomers are on neighboring lattice sites and $b = 0$ when two consecutive monomers occupy the same lattice site. The latter case is referred to as a "stored length" unit, which imparts elasticity to the polymer. The total contour length L of a polymer with N bonds is given by $L = N\langle b\rangle$, where $\langle b\rangle$ represents the average bond length. This numerical trick makes the polymer elastic.

To model polymers with varying flexibility, we introduce a bending energy term to the Hamiltonian, described by the following cosine potential term:

$$\frac{\mathcal{H}_{\rm bend}}{k_B T} = -\kappa_{\rm bend} \sum_{i=1}^{L/a} \cos\theta_i \equiv -\kappa_{\rm bend} \sum_{i=1}^{L/a} \frac{\vec{t}_i \cdot \vec{t}_{i+1}}{|\vec{t}_i||\vec{t}_{i+1}|} \,. \tag{2.6}$$

Here, $\kappa_{\rm bend}$ represents the bending stiffness which influences the Kuhn length (see Fig. 2.2), ℓ_K (see Sec. 2.2.1), of the polymer fiber, and $\vec{t}_i \equiv \vec{r}_{i+1} - \vec{r}_i$ is the oriented bond vector between monomers[1] i and $i+1$ having spatial coordinates $\vec{r}_i$ and $\vec{r}_{i+1}$. Importantly, since bond vectors are obviously ill-defined when two monomers form a stored length, the sum in eq. (2.6) is restricted to the *effective* bonds of the chains.

The dynamic evolution of the polymer chains is implemented through two types of Monte Carlo (MC) moves that preserve the chain's topology. These moves involve randomly selecting a monomer from one of the chains in the system and attempting to displace it to one of the nearest neighbor lattice sites. There are two scenarios for the destination lattice site (see Fig. 2.1):

- The destination lattice site is empty, this move is an example of *Rouse*-like move [5, 14], consisting in a local, lateral displacement of the chain.
- The lattice site is occupied by only one of the nearest neighbor monomers along the chain. This move is a *reptation*-like move [5, 14], essentially the move produces mass drift along the contour length of the chain, as occurring in reptation dynamics (see Sec. 1.2.3 in Chapter 1).

Chain connectivity is preserved by requiring that neighboring monomers along the chain either reside on nearest neighbor lattice sites or on the same lattice site (maximum 2 per lattice site). Then, by means of these MC moves, the topology of the system is rigorously preserved. Moreover, we accept the moves, based on the Metropolis-Hasting criterion [118], based on the probability associated with the bending energy term described by Eq.(2.6):

$$P(x', x) = \min\left(1, e^{-\frac{\mathcal{H}_{\rm bend}(x') - \mathcal{H}_{\rm bend}(x)}{k_B T}}\right) \,. \tag{2.7}$$

[1]For ring polymers, it is implicitly assumed the periodic boundary condition along the chain $N + 1 \equiv 1$.

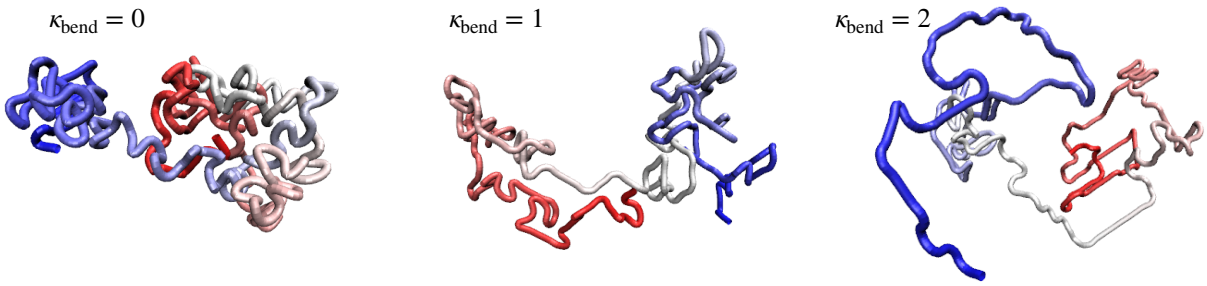

Figure 2.2: Example of melt of linear chains made up by $N = 320$ monomers and simulated according to the kMC algorithm described. The polymer's color transitions from blue to red from one chain's end to the other. As κ_{bend} grows, linear chains become more elongated, and larger sections of the filaments adopt straight conformations.

Here, x and x' denote respectively the current and proposed configurations of the polymer, which differ for the position of the monomer chosen to be moved, while $P(x', x)$ represents the probability of accepting the move. Thus, if a MC move lowers the bending energy Hamiltonian Eq. (2.6), the move is always is accepted, *i.e.*, $e^{-\frac{\mathcal{H}_{\text{bend}}(x') - \mathcal{H}_{\text{bend}}(x)}{k_B T}} > 1$, and $P(x', x) = 1$ (Eq. (2.7)). Instead, if a MC move would increase the bending energy, *i.e.*, $P(x', x) = e^{-\frac{H_{bend}(x') - H_{bend}(x)}{k_B T}} < 1$, a random number $0 \leq r \leq 1$ is generated and the move if is accepted if $r < P(x', x)$. The whole protocol assures that the MC moves are accepted with probability $P(x', x)$ and this ensures that the simulation sample the canonical ensemble [119]: $P(x) \sim e^{-\frac{\mathcal{H}_{\text{bend}}(x)}{k_B T}}$. For this reason, being the bending energy term given by Eq. (2.6), as κ_{bend} increases, straighter conformations (minimizing the bending potential) are promoted (see Fig. 2.2) enhancing the rigidity of the polymer chain.

It is useful to make the following conceptual distinction concerning how these MC moves effectively implement classical polymer dynamics [5, 14, 98]. The selected monomer which is displaced towards an empty or a single-occupation site (or, a Rouse-like move) may, in general, change the local chain curvature and, hence, depend on the bending energy term Eq. (2.6). Conversely, a unit of stored length traveling along the chain (or, a reptation-like move) is not affected by the curvature because Eq. (2.6) is, again, strictly restricted to the effective bonds of the chains. Overall, as explained in detail in [112], the stored length method ensures that the algorithm remains efficient even when it is applied to the equilibration of very dense systems.

Finally, systems in bulk can be simulated by enforcing periodic boundary conditions, then the unfolded coordinates of the polymers can evolve over the images of the primitive box. Conversely, confined systems can be simulated by restricting the polymers from crossing the walls of the unit box. In this Thesis, both bulk systems (Chapters 3, 5 and 6) and systems un-

der confinement (Chapter 7), particularly under slit-like confinement, have been investigated. For the latter case, periodic boundary conditions are enforced along the x and y directions, while the box is non-periodic along the z direction, featuring two impenetrable walls.

As already discussed, the "Rouse"-like and "reptation"-like moves strictly maintain the topology of the polymer chains and cannot implement strand-crossing events between nearby polymer filaments. For this reason, the initial part of my PhD work focused on developing a set of MC moves capable of randomly crossing nearby polymer filaments. The details of these new moves will be provided in Chapter 5, where we will describe their implementation and their impact on melts of ring polymers. In general, these moves aim to expand the capabilities of the polymer model and enable the study of more complex polymer systems with intertwining strands.

2.2 Characterizing polymer systems

In this section, I provide a concise introduction to key quantities commonly utilized for characterizing the statics and dynamics of polymer systems.

All the quantities will be defined with respect to polymers consisting of $N+1$ monomers, N bond ($N+1$ in case of rings), where the average bond length is represented by $\langle b \rangle$, and the total contour length is denoted as $L \equiv N\langle b \rangle$. The thermal or ensemble average for the generic observable $\mathcal{O}$ is denoted by $\langle \mathcal{O} \rangle$, and unless otherwise specified, is intended to be calculated across all the polymers in the system and all possible system realizations.

2.2.1 Statics

Polymer conformations and static properties are of great interest because they dictate the physical properties of the polymers. In the following, I will briefly introduce the standard static observables that I have used to characterize the polymer systems I investigated. Threading-related observables used in Chapter 3 will be directly introduced and discussed there.

Polymer size Polymer typical size, R, which, as seen in the previous chapter, is one fundamental aspect of interest in polymer physics, is usually characterized by using the end-to-end distance vector, denoted as $\vec{R}_{ee}$, defined as:

$$\vec{R}_{ee} \equiv \vec{r}_N - \vec{r}_0 \,, \tag{2.8}$$

where $\vec{r}_0$ and $\vec{r}_N$ denote the position of the chain-ends. For symmetry: $\langle \vec{R}_{ee} \rangle = 0$, and the first non-vanishing moment is the mean-square end-to-end distance, $\langle R_{ee}^2 \rangle$.

$$\langle R_{ee}^2 \rangle = \langle \vec{R}_{ee}^2 \rangle \, . \tag{2.9}$$

It is easy to show [5] that, for an ideal chain, $\langle R_{ee}^2 \rangle$ obeys the following power law:

$$\langle R_{ee}^2 \rangle = \ell_K L \, , \tag{2.10}$$

where ℓ_K is the Kuhn length [5] of the polymer fiber. The Kuhn length plays a crucial role as it represents the characteristic length scale at which the correlations between bond directions in a polymer are lost. It is important to note that the relationship expressed in equation 2.10 also holds for linear polymers in melt, as discussed in the previous chapter (refer to Sec. 1.2.1). The Kuhn length of a polymer depends on the microscopic parameter characterizing the interactions between monomers, thus, ℓ_K is not known a priori. It is usually estimated by exploiting Eq. 2.10, by examining the ratio of the mean square end-to-end distance to the polymer's contour length.

In addition to $\langle R_{ee}^2 \rangle$, another measure that is commonly used to quantify the spatial extension of a polymer is the mean square gyration radius, denoted as $\langle R_g^2 \rangle$. This quantity represents the average square distance of a monomer from the center of mass of the chain. It is defined as:

$$\langle R_g^2 \rangle = \langle \frac{1}{N+1} \sum_{i=0}^{N} (\vec{r}_i - \vec{r}_{CM})^2 \rangle, \tag{2.11}$$

where $\vec{r}_i$ represents the position of the i-th monomer and $\vec{r}_{\mathrm{CM}} \equiv \frac{1}{N+1} \sum_{i=0}^{N} \vec{r}_i$ is the center of mass of the chain.

Understanding how these quantities scale with the length of the polymer, expressed by the relation:

$$\langle R^2 \rangle \sim L^{2\nu}, \tag{2.12}$$

is of particular interest because ν identifies the specific universality class which the polymer belongs to [5, 98]. In the case of ideal chains, the exponent ν takes the value of $\frac{1}{2}$ (see Eq. (2.10)). Linear chains in the melt exhibit ideal statistics, leading to the same exponent $\nu = \frac{1}{2}$ (as discussed in sec 1.2.1). On the other hand, ring polymers in the melt are more compact than their linear counterpart with $\nu = 1/3$ (see Sec. 1.3.1).

Polymer shape In addition to the spatial extension of polymers, there is also significant interest in understanding their average shapes. Interestingly, despite the isotropy of space, polymers tend to adopt more prolate shapes due to entropic reasons [120]. Then, the anisotropy in

polymer conformations can be characterized by computing the symmetric 3×3 mean gyration tensor $Q_{ij} = Q_{ji}$ $(i, j = x, y, z)$ defined as:

$$Q_{ij} = \frac{1}{N+1} \sum_{m=0}^{N} \left(r_{m,i} - r_{\mathrm{CM},i}\right) \left(r_{m,j} - r_{\mathrm{CM},j}\right) \ . \tag{2.13}$$

Here, $r_{m,i}$ is the i-th Cartesian component of the spatial position of monomer m and $\vec{r}_{\mathrm{CM}}$ is the center of mass of the chain. The three ordered mean eigenvalues $\langle\lambda_1^2\rangle \geq \langle\lambda_2^2\rangle \geq \langle\lambda_3^2\rangle$ of the gyration tensor Q quantify the mean spatial elongation of the polymer along its principal axes. Instead, the trace of Q, $\mathrm{tr}Q = \sum_i^3 \langle\lambda_i^2\rangle$, corresponds to the mean-square gyration radius of the polymer chain (as given by Eq. 2.11). Spherical objects are characterized by:

$$\langle\lambda_1^2\rangle = \langle\lambda_2^2\rangle = \langle\lambda_3^2\rangle = \frac{R_g^2}{3} \, . \tag{2.14}$$

Thus, anisotropy is quantified by analyzing the ratios between the eigenvalues. The larger these ratios, the more anisotropic the polymers are. In [44], simulations were conducted on melts of linear chains comprising $N = 800$ monomers, resulting in[2] $\frac{\langle\lambda_1^2\rangle}{\langle\lambda_3^2\rangle} = 11.9$ and $\frac{\langle\lambda_2^2\rangle}{\langle\lambda_3^2\rangle} = 2.7$. In the same work, melts of ring chains of $N = 1600$ monomers where considered, yielding $\frac{\langle\lambda_1^2\rangle}{\langle\lambda_3^2\rangle} = 5.2$ and $\frac{\langle\lambda_2^2\rangle}{\langle\lambda_3^2\rangle} = 2.0$. The comparison of the ratios indicates that ring polymers possess a lower degree of anisotropy and are more spherical compared to linear chains.

Bond-vector correlation function The properties of polymer conformations can also be studied by examining the decay of correlations between bonds along their backbone. One common approach to analyze this is by calculating the bond-vector correlation function, $c(\ell \equiv n\langle b\rangle)$:

$$c(\ell \equiv n\langle b\rangle) \equiv \frac{\langle \vec{t}(n') \cdot \vec{t}(n'+n)\rangle}{\langle \vec{t}(n')^2\rangle} \, . \tag{2.15}$$

Here, $\vec{t}(n')$ is the n' oriented bond vector defined as: $\vec{t}(n') \equiv \vec{r}_{n'+1} - \vec{r}_{n'}$.

In the case of ideal polymers, the correlation function exhibits an exponential decay: $c(\ell) \sim e^{-\ell/l_p}$ with the decay length given by the persistence length, l_p [5]. The persistence length is associated with the polymer's bending rigidity and is directly linked to the Kuhn length as $l_p = l_K/2$. In polymer melts, the correlation hole effect[3] leads to an effective long-range coupling between the bond vectors in linear chains. This results in a power-law decay of the

[2] A random walk is characterized by $\frac{\langle\lambda_1^2\rangle}{\langle\lambda_3^2\rangle} = 12$ and $\frac{\langle\lambda_2^2\rangle}{\langle\lambda_3^2\rangle} = 3$. Linear chains in melt assume similar conformations to the ones obtained by random walks.

[3] The correlation hole indicates the fact in a melt, since density fluctuation is small, the concentration of other chains near a reference chain is reduced due to the volume taken by the reference chain. This leads to an effective repulsive interaction between monomers in melt [121, 122].

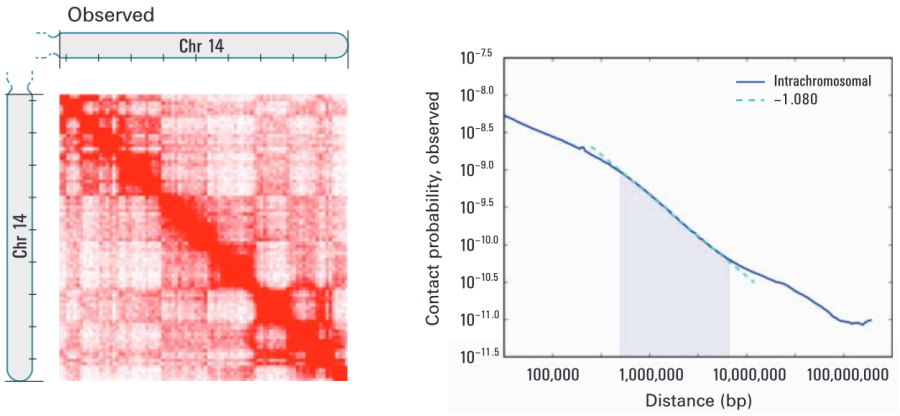

Figure 2.3: Left, HiC map of human chromosome 14 at a resolution of 1 Mb. The intensity of red indicates the probability of contact between two chromosome loci. Right, contact probability computed from HiC maps averaging over all the human chromosomes. Image adapted from [123].

correlation function: $c(\ell) \sim \ell^{-\alpha}$, with $\alpha = 3/2$ [121, 122]. On the other hand, polymer rings exhibit a distinct correlation function with a non-monotonic behavior, absent in the linear case. Specifically, it is characterized by an anti-correlation well [59, 66, 68], which is also in agreement with the concept of double folding (see Sec. 1.3.1).

Contact probability The mean contact probability, $p(\ell)$, provides access to the properties of folding and packing in polymers. It represents the probability that two monomers, separated by a contour length $\ell = n\langle b\rangle$, are within a suitable, short-range "contact distance". Mathematically, this can be expressed as:

$$\langle p_c(\ell)\rangle = \left\langle \frac{1}{N+1}\sum_{i=0}^{N}\Theta(r_c - |\vec{r}_i - \vec{r}_{i+n}|)\right\rangle . \tag{2.16}$$

Here, $\Theta(x)$ is the Heaviside step function and r_c represents the "contact distance". In all my works, $r_c = a$, with a the unit lattice distance.

Due to the fractal nature of polymers, the contact probability follows a power law decay: $\langle p_c(\ell)\rangle \sim \ell^{-\gamma}$. The exponent γ is universal, implying that polymers belonging to the same universality class share the same value γ. In the case of ideal polymers and linear chains in melts, $\gamma = 3/2$. However, polymer rings in the melt exhibit a lower exponent, approximately $\gamma \simeq 1.1$ [44]. This indicates that rings are more compact compared to linear chains in the melt.

The value of γ is of great interest from a biological point of view because it can be measured experimentally using the HiC technique [123], which determines the contacts pattern of DNA

loci within the chromosomes (see left Fig. 2.3). Based on the the chromosome's contacts, the contact probability in Eq. 2.16 has been computed (see right Fig. 2.3) and, remarkably, experimental estimates of γ for human and mouse chromosomes [123, 124] align closely with the value observed for rings. As discussed also in 1.3, this finding suggests that human chromosomes cannot be modelled as a melt of linear chains. For the time-scales of interest of chromosomes, topological constraints can be considered permanent [37], chromosomes do not disentangle and for this reason they can be effectively modelled as a melt of polymer rings which recapitulates the chromosomes main features: i) topological constraints are permanent, ii) they are segregated and iii) they form territories.

2.2.2 Dynamics

Understanding the diffusion of individual monomers and the overall polymer in space is crucial for comprehending the rheological properties of a polymer system under investigation. Here, I briefly introduce the quantities that are usually used to study the dynamical properties of polymer systems, which, in part, have already been discussed in Sec. 1.2.3 and Sec. 1.3.2.

The single monomer mean square displacement, $g_1(\tau)$, is defined as:

$$g_1(\tau) = \langle (\vec{r}(t+\tau) - \vec{r}(t))^2 \rangle \, . \tag{2.17}$$

Here, $\vec{r}(t)$ represents the position of a reference monomer at time t, and the average has to be intended over all the monomers of the systems and over time t.

The single monomer mean square displacement is usually characterized by a sub-diffusive behavior at short times $\sim t^{\alpha}$ with $\alpha < 1$ [5, 14]. This behavior arises due to the incomplete equilibration of instantaneous stresses along the entire polymer chain. The value of α depends on the specific system under investigation. For ideal polymers, $\alpha = 1/2$ [5, 14], while linear chains in the melt display two distinct sub-diffusive behaviors, with $\alpha = 1/4$ and subsequently $\alpha = 1/2$ (refer to Sec. 1.2.3). Ring polymers in the melt exhibit instead a single subdiffusive regime with $\alpha \approx 0.26 - 0.29$ (refer to Sec. 1.3.2).

The diffusion of the entire polymer in space is typically captured by the mean square displacement of the center of mass, $g_3(\tau)$:

$$g_3(\tau) = \langle (\vec{r}_{CM}(t+\tau) - \vec{r}_{CM}(t))^2 \rangle \, . \tag{2.18}$$

Here $\vec{r}_{CM}(t)$ represents the position of the polymer's center of mass at time t, and the average has to be intended over all the polymers of the system under study and over time.

Differently from $g_1(\tau)$, ideal polymers are characterized by a purely diffusive centre of mass motion, *i.e.*, $g_3(\tau) \sim \tau$, since no external forces act on the polymers. Instead, melts of linear

chains (Sec. 1.2.3) display three regimes: free diffusion up to the entanglement time τ_e, sub-diffusion with $\alpha = 1/2$ for $\tau_e < \tau < \tau_{relax}$, and subsequent diffusion. Similarly, ring polymers in the melt exhibit the same three regimes, with the intermediate regime characterized by $\alpha = 0.65 - 0.71$ (refer to Sec. 1.3.2).

Another useful dynamical quantity is represented by the single monomer mean square displacement, $g_2(\tau)$, in the frame of the centre of mass of the corresponding chain, which is defined as:

$$g_2(\tau) = \langle((\vec{r}(t+\tau) - \vec{r}_{CM}(t+\tau)) - (\vec{r}(t) - \vec{r}_{CM}(t)))^2\rangle \, . \tag{2.19}$$

As before, $\vec{r}(t)$ and $\vec{r}_{CM}(t)$ represent respectively the positions of the reference monomer and the centre of mass of the polymer chain at time t, and the average has to be taken respect to all the monomer of the system and over time.

At long timescales, when $\tau \gg \tau_{relax}$, it can be observed that $g_2(\tau) \approx 2\langle R_g^2\rangle$, where $\langle R_g^2\rangle$ is the mean square gyration radius of the polymer (see Eq. 2.11). Hence, the plateau of $g_2(\tau)$ can be utilized to quantify the relaxation of the system. In all my works, all the simulated systems display the corresponding plateaus, which demonstrates that equilibration has been reached for all the cases considered. Accordingly, the time scale to reach the corresponding plateau corresponds to the portion of the simulated trajectory that has been discarded from the computation of averages of any considered observable.

Chapter 3

Unknotted and Non-concatenated Ring Polymers in Melt

The content of this Chapter[1] focuses on a computational study of unknotted and non-concatenated ring polymers in melt conditions. The aim of this investigation is to better understand the relationship between the theoretical postulated double folding of the polymer backbone in melt (see Sec. 1.3.1) and previous conflicting numerical evidences that pair of rings thread each other (see Secs. 1.3.1 and 1.3.3). The results are discussed in light of the current theories developed to describe such system.

The chapter is structured as the following: in the brief introduction (Sec. 3.1), we will recapitulate the current understanding on the physics of unknotted and non-concatenated ring polymers in melt conditions, which is also discussed in detail in Sec. 1.3. Then, in Sec. 3.2, we will briefly present the details of the lattice polymer model employed for the simulations introduced in Sec. 2.1.2 and derive the relevant length and time scales of the investigated polymer melts. Finally, in Sec. 3.3, we will present the main results for both the statics and the dynamical properties of the rings. In Secs. 3.3 and 3.4 we will present and discuss how the tree-like models can be reconciled with the threading features. We will also indicate measurements that can help to discriminate between the different models and discuss the common deficiency of all of them.

[1]The material described in this Chapter has been published in: M. A. Ubertini, J. Smrek, and A. Rosa, Macromolecules (2022) [2]

3.1 Introduction

As already discussed in Sec. 1.3, topological constraints emerging from the mutual uncrossability between distinct chain segments dominate the viscoelastic behavior of polymer systems in high-density (melt) conditions [5, 14, 98]. In contrast to linear chains where topological constraints are transient, a significant interest lies in situations where polymers are prepared in a well-defined topological state that remains fixed as polymers diffuse and flow. The simplest example in this respect, and the central topic of the present chapter, is the case of melts of *unknotted* and *non-concatenated* ring polymers. This particular class of polymer solutions has been extensively studied for several decades, theoretically and numerically [33, 44, 50–55, 57, 59, 60, 66, 68, 69, 71, 73, 125–132] as well as experimentally [63, 72, 133–136]. Researchers have shown that there exist intriguing conceptual connections between melts of ring polymers and, for instance, chromosomes [37, 38] and a polymer glass based on the nonlinear topology of the chains [40–43]. However, due to the inherent complexity of the problem, several fundamental aspects regarding the physics of ring polymer melts remain poorly understood, primarily because of the mathematical challenges in dealing with topological constraints [45–49]. Consequently, the existing physical models proposed so far [51–55, 57] incorporate suitable approximations to address these constraints, making the problem more tractable. However, these approximations necessitate further validation from experiments or numerical simulations. As extensively discussed in Sec. 1.3, currently, the most prominent models developed for studying such system are represented by: i) the annealed lattice tree model [57] and ii) the fractal loopy globule (FLG) [55].

The lattice tree model (see Sec. 1.3.1) assumes that rings in the melt double fold on branched tree-like conformations (see Fig. 1.7). On the other hand, according to the FLG model, ring conformations are characterized by a fractal arrangement of "loops on loops," resembling a randomly branched structure where the loops of the FLG correspond to the branches. Both models predict, in agreement with numerical results [44, 66, 67], that the mean linear size or gyration radius, $\langle R_g \rangle$, scales with the total contour length of the chain, L, as:

$$\langle R_g \rangle \sim d_T \left(\frac{L}{L_e} \right)^{1/3} , \tag{3.1}$$

for L larger than the the *entanglement length*, L_e, and with d_T, the *tube diameter* of the melt (see Sec. 1.2.2 for the definitions of the quantities). As discussed in the Sec. 1.3.1, the lattice-tree model and the FLG model exhibit differences in terms of their branching statistics, which are reflected in the structure of the mean (primitive) path (see Fig. 1.7), $L_{\rm tree}$. In the lattice-tree model, on scales above L_e, the scaling of the size of a segment of the ring with its corresponding primitive path follows: $R \sim L_{\rm tree}^{\nu_{\rm path}}$ with $\nu_{\rm path} = 3/5$ (Eq. (1.18)). On the

other hand, in the FLG model, if a segment is shorter than L_e, its primitive path is a straight line, resulting in linear scaling of the segment's size with its length. For segments longer than L_e, their size follows the exponent $\nu = 1/3$, which is equivalent to the scaling behavior of the entire ring.

As for the dynamics, the predictions of the exponents of the centre of mass mean square displacement, $g_3(\tau)$, and single-monomer means square displacement, $g_1(\tau)$, are very similar to each other and close to both numerical and experimental results see Sec.1.3.2. Interestingly, as discussed in Sec. 1.3.2, both the FLG and the annealed lattice-tree model theories underestimate the exponent of the diffusion coefficient with respect to the values obtained from simulations [33, 55] and experiments [72]. Specifically, the FLG model underestimates the exponent by 0.67, while the lattice-tree model underestimates it by 0.45.

While seemingly accurate for many aspects, both models do not take into account the possibility of ring-ring interpenetrations (or, *threadings*) [68, 71]. In the lattice tree model, rings are perfectly double folded (Fig. 1.7), in the FLG, even if possible, the role of threadings is overlooked in the relaxation process of the rings. Recent studies [60, 68, 71] have quantified ring-ring interpenetrations and have shown that they become increasingly present as ring size increases. Moreover, it has been shown that threadings have physical consequences as they hinder the diffusion of the threaded rings [60] slowing down their relaxations. Finally, it has been shown that threadings give rises to a series of interesting effects when melts are driven out-of-equilibrium (see discussion in Sec. 1.3.3), such as in an elongation flow [73] or for an induced asymmetry in the local monomer mobilities [43].

From a broader perspective, it remains unclear if the entanglement scales L_e and d_T (see Sec. 1.2.2) are the only relevant ones for melts of rings or if, and up to what extent, they are influenced by the local bending rigidity or Kuhn length [5] ℓ_K of the chain. In fact, the value of L_e is measured from a linear melt (*e.g.* by primitive path analysis [29]) and the length scale is only *assumed* to be applicable for rings (with the same polymer model) as well, although no *direct* method to find the value explicitly from the rings is known. Recent theoretical works [59, 68, 126] seem to suggest that both systems are characterized by *the same* L_e. Some recent comparison of crazing in linear and ring glasses suggests [137, 138] that $L_e(\text{rings})/L_e(\text{linear}) \approx 4$, but its role in equilibrium ring melts, as well as its connection to ℓ_K, has not been thoroughly investigated.

All these aspects (double-folding/branching, threadings, entanglement scales) are clearly all related to each other and, yet, how they mutually influence each other remain poorly understood.

In this chapter, we will show results concerning these questions.

3.2 Polymer model and numerical methods

3.2.1 Melts of rings: simulation details

Bulk properties of dense solutions of M closed (ring) polymer chains made of N monomers or bonds per ring have been studied. By construction, rings are *unknotted* and *non-concatenated*. We simulated values

$$N \times M = [40 \times 1000, 80 \times 500, 160 \times 250, 320 \times 125, 640 \times 62] \ ,$$

with fixed total number of monomers $= 40,000$ (for computational convenience, the total number of monomers for $N = 640$ is slightly less). All these systems have been studied for the bending stiffness parameters $\kappa_{\rm bend} = 0, 1, 2$ (Eq. (2.6)). In addition, we have also simulated melts with $N \times M = [234 \times 171, 236 \times 58]$ for $\kappa_{\rm bend} = 1$ and $N \times M = [104 \times 385, 104 \times 64]$ for $\kappa_{\rm bend} = 2$: once rescaled in terms of the corresponding entanglement units, $Z \equiv N/N_e$, these two set-up's have the same number of entanglements per chain $Z \approx 8$ of $N = 640$ with $\kappa_{\rm bend} = 0$.

Bulk conditions are implemented through the enforcement of periodic boundary conditions in a simulation box of total volume $V = L_{\rm box}^3$. Similarly to previous works [68, 112], melt conditions correspond to fix the monomer number per fcc lattice site to (i) $\rho_{\rm site} = \frac{5}{4} = 1.25$ for $N \leq 320$ and (ii) $\rho_{\rm site} = \frac{31}{25} = 1.24$ for $N = 640$: respectively, since the volume occupied by the fcc lattice site is $= \frac{a^3}{\sqrt{2}}$ [139], the monomer number per unit volume are given by (i) $\rho = \frac{5}{4}\sqrt{2} \simeq 1.77 a^{-3}$ for $N \leq 320$ and (ii) $\rho = \frac{31}{25}\sqrt{2} \simeq 1.75 a^{-3}$ for $N = 640$. Accordingly, we fix $L_{\rm box} = 20\sqrt{2}a$ for all N's.

Finally, our typical runs amount to a minimum of 7×10^6 up to a maximum of 3×10^8 kMC time units where one kMC time unit is $\tau_{\rm MC} = NM$: these runs are long enough that the considered polymers have attained proper structural relaxation measured by monitoring the plateau of the single monomer time mean square displacement, $g_2(\tau)$ (Eq. 2.19), in the frame of the centre of mass of the corresponding chain (see Fig.3.1).

In table 3.1, relevant quantities of the polymer systems simulated are reported as a function of $\kappa_{\rm bend}$.

Finally, it is worth noticing that the introduction in our polymer model of the bending energy term in the kinetic Monte Carlo algorithm, described in Sec. 2.1.2, is inspired by the work of Cates [66]. There it is shown that by simulating stiffer polymers a significant enhancement in the interchain overlap occurs, this enables the attainment of the asymptotic regime Eq. (3.1), even with relatively moderate chain sizes and, consequently, reasonable computational times.

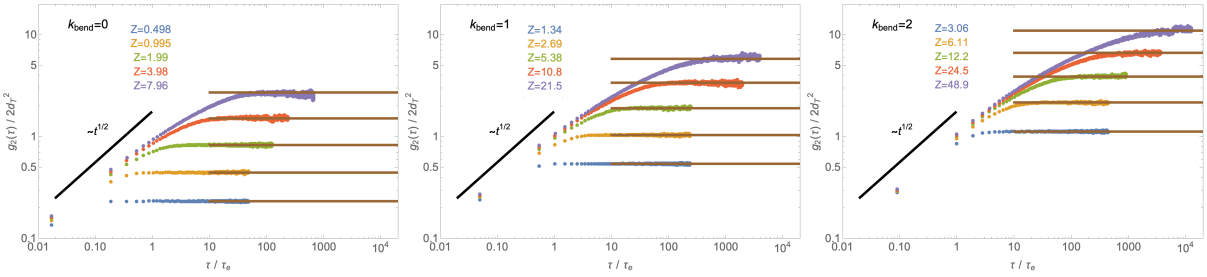

Figure 3.1: Single monomer time mean-square displacement, $g_2(\tau)$ (Eq. (2.19)), in the frame of the centre of mass of the corresponding chain. The horizontal lines are for the stationary values, $= 2\langle R_g^2(N)\rangle$ reported in Table 3.2. The dashed black lines correspond to the initial Rouse behavior where $g_2(\tau) \sim g_1(\tau)$ (see Sec. 2.2.2 for more details).

3.2.2 A closer look to the bending stiffness

It is worth discussing in more detail the consequences of the energy term, Eq. (2.6). On the fcc lattice, the angle θ between consecutive chain bonds is restricted to the five values $= 0°, 45°, 90°, 135°, 180°$. For ideal polymers (*i.e.*, in the absence of the excluded volume interaction), the angles θ_i in Eq. (2.6) are obviously not correlated to each other. This implies that the distribution function $P_{\rm ideal}(\kappa_{\rm bend}; \cos\theta)$ of the variable $\cos\theta$ follows the simple Boltzmann form:

$$P_{\rm ideal}\left(\kappa_{\rm bend}; \cos\theta\right) = \frac{1}{\mathcal{Z}} \mathcal{N}(\cos\theta)\, e^{\kappa_{\rm bend}\cos\theta}\,, \tag{3.2}$$

where $\mathcal{N}(\cos\theta)$ represents the total number of lattice states for two successive bonds with given $\cos\theta$ and $\mathcal{Z}$ is the normalization factor. In polymer melts, excluded volume interactions induce an effective long range coupling between bond vectors and the distribution function $P_{\rm melt}(\kappa_{\rm bend}; \theta)$ is expected to deviate from Eq. (3.2): for instance, one can immediately see that the angle $= 180°$ (*i.e.*, $\cos\theta = -1$) is possible for ideal polymers but strictly forbidden in the presence of excluded volume interactions.

The distributions $P_{\rm melt}(\kappa_{\rm bend}; \theta)$ for the different $\kappa_{\rm bend}$'s and in comparison to $P_{\rm ideal}(\kappa_{\rm bend}; \theta)$ are given in Fig. 3.2 (square-solid *vs.* circle-dashed lines, respectively). Corresponding mean values $\langle\cos\theta\rangle$ for the different $\kappa_{\rm bend}$'s and for open linear chains and closed rings are summarized in Table 3.1: the values for the two chain architectures are very similar, with differences in the range of a few percent.

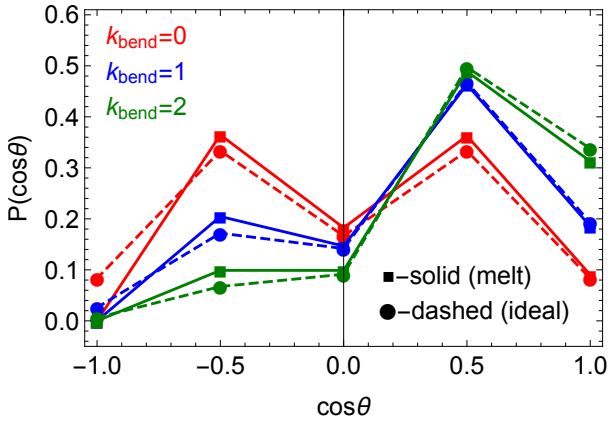

Figure 3.2: Distribution functions $P_{\rm melt}\left(\kappa_{\rm bend};\cos\theta\right)$ (square-solid lines) of the cosine of the angle θ between consecutive bonds along the polymer chain in ring melts for different values of the bending stiffness parameter $\kappa_{\rm bend}$. The curves are compared to the results for ideal rings, $P_{\rm ideal}\left(\kappa_{\rm bend};\cos\theta\right)$ (Eq. (3.2), circle-dashed lines).

3.2.3 Polymer length and time scales

In this section, a detailed derivation of the relevant length and time scales characterizing our polymer melts is provided (they are summarized in Table 3.1). Being the system simulated at fixed monomer density ρ, the values of these parameters depend only on the bending stiffness parameter $\kappa_{\rm bend}$.

Average bond length, $\langle b\rangle$ – One can observe that $\langle b\rangle$ is slightly decreasing with $\kappa_{\rm bend}$: arguably, this is the consequence of the progressive stiffening of the polymer fiber on the fcc lattice which privilege less kinked conformations through the reduction of the effective total contour length of the chain.

Kuhn length, ℓ_K – By modulating the bending constant $\kappa_{\rm bend}$, it is possible to fine-tune the flexibility of the polymers (Eq. (2.6)). The latter is quantified in terms of the *Kuhn length* ℓ_K, namely the unit of contour length beyond which the chain orientational order is lost [5, 14] (see Sec. 2.2.1 for more details). For *linear chains*, ℓ_K is defined by the relation [5, 14]:

$$\ell_K \equiv \lim_{\ell\to\infty} \frac{\langle R^2(\ell)\rangle}{\ell}\,, \tag{3.3}$$

where $\langle R^2(\ell)\rangle$ is the mean-square end-to-end distance between any two monomers along the chain at monomer number separation n or contour length separation $\ell \equiv n\langle b\rangle$. In order to determine the Kuhn length of our polymer chains, we have simulated melts of $M = 125$ linear chains with $N = 320$ monomers per chain at the same monomer density $\rho = \frac{5}{4}\sqrt{2} \simeq 1.77a^{-3}$ and for $\kappa_{\rm bend} = 0, 1, 2$ and, after equilibration, we have computed numerically Eq. (3.3). As shown in Fig. 3.3 (symbols), the chains become increasingly stiffer with $\kappa_{\rm bend}$ as expected by

$\kappa_{\rm bend}$	acc. rate	$\langle\cos\theta\rangle^{\rm lin}$	$\langle\cos\theta\rangle^{\rm ring}$	$\langle b\rangle/a$	ℓ_K/a	$\rho_K\ell_K^3$	L_e/a	N_e	d_T/a	$\tau_e/\tau_{\rm MC}(\times10^4)$
0	0.069	0.187	0.171	0.731	1.440	2.679	58.738	80.379	3.755	15.0
1	0.048	0.476	0.447	0.696	2.194	5.920	20.708	29.764	2.752	5.2
2	0.036	0.670	0.635	0.669	3.393	13.620	8.759	13.088	2.226	2.8

Table 3.1: Values of physical parameters characterizing the melts of polymers studied in this paper. a is the unit distance of the fcc lattice and the monomer number per unit volume is $\rho a^3 \simeq 1.77$ (Sec. 3.2). (i) $\kappa_{\rm bend}$, bending stiffness parameter (Eq. (2.6)); (ii) acceptance rate of the kMC algorithm; (iii, iv) $\langle\cos\theta\rangle^{\rm lin/ring}$, mean value of the cosine of the angle between two consecutive bonds along the linear/ring polymer (Eq. (2.6)); (v) $\langle b\rangle$, mean bond length; (vi) ℓ_K, Kuhn length (Eq. (3.3)); (vii) $\rho_K\ell_K^3$, number of Kuhn segments per Kuhn volume [140]; (viii) L_e, entanglement length (Eq. (1.6)); (ix) $N_e \equiv L_e/\langle b\rangle$, number of bonds per entanglement length; (x) $d_T = \sqrt{\ell_K L_e/6}$, diameter of the effective tube confining polymer chains in melt; (xi) τ_e, entanglement time.

displaying plateau-like regions for large ℓ's. The heights of these plateaus are obtained by best fits to corresponding constants on the common interval $\ell \in [150, 200]$ (Fig. 3.3, dashed lines), they provide the values of the corresponding ℓ_K's which are used in this work (see Table 3.1).

Entanglement length, L_e, and *tube diameter*, d_T – The entanglement length L_e marks the crossover from entanglement-free to entanglement-dominated effects in polymer melts (see Sec. 1.2.2 for a detailed discussion). The entanglement lengths L_e, for the different $\kappa_{\rm bend}$, are directly estimated from Eq. 1.6, from which we extract extract L_e/ℓ_K and the corresponding number of monomers per entanglement length, $N_e \equiv L_e/\langle b\rangle$. One can observe (see Table 3.1) that N_e decreases by approximately one order of magnitude by the apt fine-tuning of $\kappa_{\rm bend}$. This means that rings with the same contour length but stiffer will become increasingly entangled [66]. Finally, by using the definition (Eq. (1.2)) for d_T one can compute the tube diameters of polymers of different bending stiffnesses. Notice (Table 3.1) that, by changing chain stiffness, d_T moves from smaller to comparable to ℓ_K meaning that we are effectively able to explore the mentioned crossover from loosely to tightly entangled melts (see discussion in 1.2.2).

Unless otherwise said, we will express chain contour lengths L in units of the entanglement length L_e and, to this purpose, we introduce the compact notations [59, 68]:

$$Z \equiv \frac{L}{L_e} \equiv \frac{N}{N_e}, \tag{3.4}$$

$$z \equiv \frac{\ell}{L_e} \equiv \frac{n}{N_e}, \tag{3.5}$$

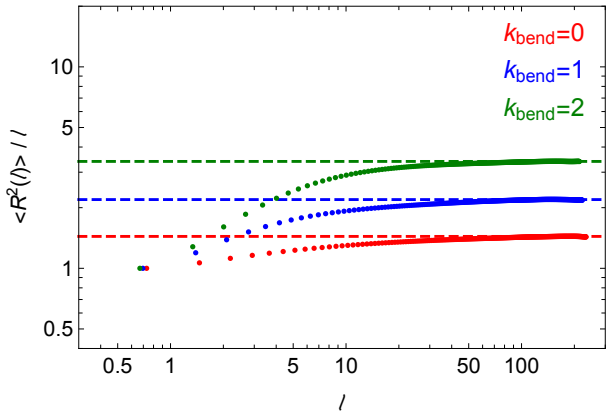

Figure 3.3: (Symbols) Ratios of the mean-square end-to-end distance, $\langle R^2(\ell)\rangle/\ell$, to the corresponding monomer contour length separation ℓ for linear chains in melt and for the different bending stiffness parameters $\kappa_{\rm bend}$ (see legend). (Dashed lines) Best fits of the plateau-like behaviors on the contour length interval $\ell \in [150, 200]$ (see Eq. (3.3) and the text for details).

where N_e corresponds to the number of monomers $L_e/\langle b\rangle$ of an entanglement length and Z and z are the number of entanglements of the polymer chain and the polymer sub-chain of contour lengths L and ℓ, respectively. Accordingly, variables such as the polymer mean-gyration radius $\langle R_g\rangle$ or the mean-magnetic radius $\langle R_m\rangle$ (see definitions eqs. (2.11) and (1.20), respectively) are expressed in units of the tube diameter d_T (Eq. (1.2)).

Entanglement time, τ_e – Entanglements affect the motion of the chains on time scales τ larger than a the entanglement time, τ_e, which can be computed numerically from simulations (see Sec. 1.2.3), as $g_1(\tau_e) = 2d_T^2$, where $g_1(\tau)$ is the monomer time mean-square displacement (Eq. (2.17)) and d_T is the tube diameter (Eq. (1.2)). For consistency with the definitions for L_e and d_T, notice that $g_1(\tau)$ has been calculated on the same dynamic simulations of melts of *linear* chains used for calculating ℓ_K. Moreover, in this work, as L_e and d_T being the main units respectively of polymer lengths and distances, τ_e is the main unit of time.

3.2.4 Computing the ring minimal surface

As discussed at the end of Sec. 1.3.1, the minimal surface spanned by a ring [69, 70] represents a powerful tool to measure the openings of the rings surfaces, which has been used to quantify deviations of the ring's conformation from the double folded picture of Grosberg. Moreover, this observable allows to precisely detect interpenetration between couple of rings.

Here, we briefly summarize the salient numerical aspects of the procedure used to obtain the minimal surface, the interested reader will find a complete overview on minimal surfaces

for melts of rings in the mentioned references and also in [71].

The search for the minimal surface of a ring polymer is based on a suitable minimization algorithm which works as the following. Essentially, the algorithm is based on successive iterations of triangulations evolving under surface tension by moving the free vertices: each triangle in the initial triangulation is made of two successive monomer positions and the center of the mass of the ring, then it is refined (by subdividing each edge into two edges, creating therefore four triangles out of one) and the surface area minimized by the surface tension flow with restructuring of the mesh. Finally, the algorithm stops when the relative surface area does not change by more than 0.1% over a few tens of additional steps of the minimization procedure. Similarly to the eye of a needle pierced by a thread, the single minimal surface of a given ring can be pierced or *threaded* by the other surrounding polymers in the melt: in particular, once the minimal surfaces of the rings in the melt are determined, it is possible to define in a precise and robust manner what amount of the total contour length of any given ring passes through the minimal surface of another ring.

Notice that the computation of the minimal surfaces have been performed by Jan Smrek co-author of the work.

3.3 Results

3.3.1 Ring structure

Ring size In order to characterize the ring structure, we consider the more standard chain mean-square "gyration" radius (see Eq. (2.11)), $\langle R_g^2 \rangle$, and the mean-square "magnetic" radius (see Eq. 1.20), $\langle R_m^2 \rangle$, which, as discussed in Sec. 1.3.1, has been introduced in [68] as a measure of the oriented area enclosed by one ring. Both quantities are an expression of the average (square) ring size, yet they have different meaning: in particular, Eq. (1.20) was introduced to detect and quantify the presence of open loops inside the ring (see discussion in Sec. 1.3.1).

Numerical values of $\langle R_g^2 \rangle$ and $\langle R_m^2 \rangle$ for melts of rings with different flexibilities are summarized in table 3.2. Fig. 3.4 (l.h.s panel) shows these quantities, rescaled (filled symbols) by the corresponding tube diameters d_T and as a function of the total number of entanglement $Z = L/L_e$, see Table 3.1 for specific values of d_T and L_e. For further comparison, we have also included the results for $\langle R_g^2 \rangle$ obtained from Monte Carlo simulations (bond-fluctuation model) of melts of rings by Müller *et al.* [66] (open symbols) and the universal curves (solid

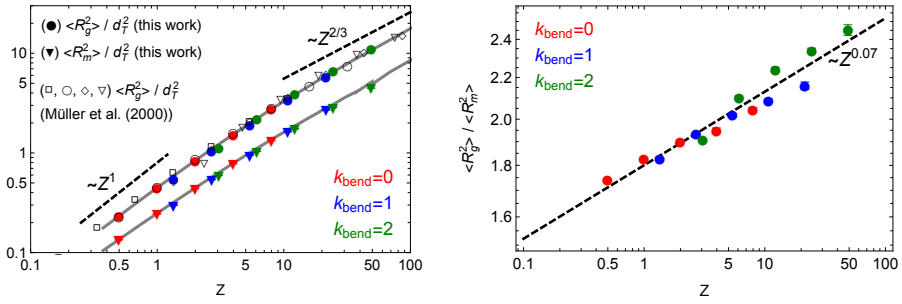

Figure 3.4: On the left, the scaling behavior of the mean-square gyration radius, $\langle R_g^2 \rangle$, and the mean-square magnetic radius, $\langle R_m^2 \rangle$, of ring polymers as a function of $Z = L/L_e$, of the chain. Error bars are smaller than the symbols size. The empty symbols reproduce the ring data by Müller *et al.* [66], with different symbols for the different Kuhn lengths used in that work (by employing their notation: $\sigma/\kappa_B T = 0(\square), 1(\circ), 2(\diamond), 3(\triangledown)$, from flexible to increasingly stiffer chains). The solid grey lines are for the on-lattice rings on the fcc lattice studied in [68]. On the right, $\langle R_g^2 \rangle / \langle R_m^2 \rangle$: ratio of the mean-square gyration radius to the mean-square magnetic radius as a function of Z of the chain. Notice the *weak* increasing of the ratio with Z (the straight line is obtained by best fit of the data to a simple power-law).

grey lines) from the "hierarchical crumpling" [2] method by Schram *et al.* [68]. The excellent matching between these old data sets and the present new data validates our methodology: the average ring size covers the full crossover from Gaussian ($\sim Z^1$) to compact ($\sim Z^{2/3}$) behavior. This is particularly evident for the stiffest rings ($\kappa_{\rm bend} = 2$) whose reduced flexibility "helps", in agreement with Müller *et al.* [66], reaching the asymptotic behavior.

The data for the mean-square magnetic radius $\langle R_m^2 \rangle$ rescale equally well and, as noticed in [68], with the same large-Z behavior $\sqrt{\langle R_m^2 \rangle} \sim d_T\, Z^{1/3}$. However a closer look to the ratio $\langle R_g^2 \rangle / \langle R_m^2 \rangle$ (see Fig. 3.4 r.h.s panel) reveals significant, albeit extremely slow ($\mathcal{O}(Z^\gamma)$ with $\gamma \approx 0.07$), power-law corrections which *were not* noticed in the previous study [68]: instead, a similar result was already described in [66] where, however, the authors employed a different definition for the area spanned by a ring which was based on the $2d$ projection of the chain onto a random direction.

Minimal surfaces The universal behaviors of the two quantities $\langle R_g^2 \rangle$ and $\langle R_m^2 \rangle$ characterize the chain as a whole yet, in principle, there could be other length scales below L_e which produce no effect on these quantities but affect and become visible in others. We look then at the average behavior of the ring minimal surface (hereafter, minS), a concept introduced [69–

[2] "Hierarchical crumpling" consists on a two step process: first equilibrated conformation of ring polymers in the melt are made to grow in a fractal manner, and then are locally relaxed at a time-scale τ_e.

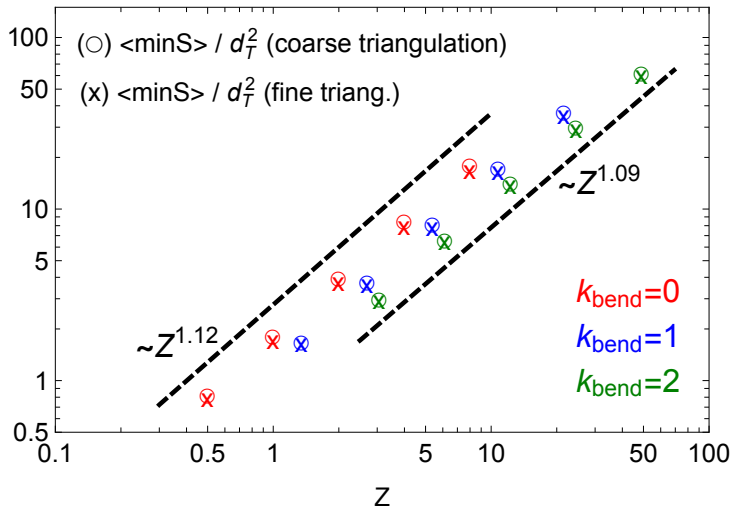

Figure 3.5: Mean minimal surface area, $\langle \mathrm{minS} \rangle$, of ring polymers as a function of the total number of entanglements, Z, of the chain. The ○- and ×-symbols (see legend) are for the two chosen resolutions in the triangulation procedure at the basis of the calculation of the ring minimal surface (see Sec. 3.2.4 for details). For the higher resolution, we take two additional refining steps before the minimization procedure stops. Error bars are smaller than the symbols size. The power laws (dashed lines) correspond to best fits to the data.

71] to quantify the "exposed" area that each ring offers to its neighbors (see Sec. 3.2.4 for technical details). Surprisingly, our data (collected in table 3.2) demonstrate that this is not the case (see Fig. 3.5): in fact $\langle \mathrm{minS} \rangle \sim Z$ for the different flexibilities in agreement with previous results [69] for off-lattice simulations, but the three data sets – contrary to $\langle R_g^2 \rangle$ and $\langle R_m^2 \rangle$ (Fig. 3.4) – do not collapse onto each other after rescaling in terms of entanglement units Z and d_T^2. Notice that this finding – which looks even more surprising given that both, $\langle R_m^2 \rangle$ and $\langle \mathrm{minS} \rangle$, are in the end two measures of the ring effective area – is robust and independent of the triangulation resolution employed to calculate the minimal surface of the rings ("○-symbols" vs. "×-symbols" in Fig. 3.5). Note also that $\langle \mathrm{minS} \rangle$ is normalized by d_T^2 which should correct for the different "elementary areas" due to different local structure of the polymer model[3].

Threadings statistics We tried to find the reason for this discrepancy. In an earlier paper [71] it was shown that the minimal surface of each ring can be pierced (threaded) a certain number of times by portions of surrounding rings, but that it is necessary to distinguish care-

[3]Note also that normalization by the other microscopic length scale, ℓ_K, would not imply a collapse either, in fact it would make it even worse as ℓ_K grows with κ_{bend} (see table 3.1).

N	M	$\langle R_g^2 \rangle$	$\langle R_m^2 \rangle$	$\langle \mathrm{minS} \rangle$	$\langle \Lambda_1^2 \rangle$	$\langle \Lambda_2^2 \rangle$	$\langle \Lambda_3^2 \rangle$
			$\kappa_{\mathrm{bend}} = 0$				
40	1000	3.3007 ± 0.0007	1.8937 ± 0.0008	11.60 ± 0.05	2.1160 ± 0.0007	0.8280 ± 0.0003	0.35669 ± 0.00008
80	500	6.304 ± 0.004	3.447 ± 0.004	25.6 ± 0.2	4.052 ± 0.004	1.560 ± 0.001	0.6912 ± 0.0003
160	250	11.76 ± 0.02	6.19 ± 0.02	55.6 ± 0.4	7.56 ± 0.02	2.891 ± 0.005	1.310 ± 0.001
320	125	21.48 ± 0.08	11.0 ± 0.1	119.7 ± 1.2	13.74 ± 0.07	5.29 ± 0.02	2.447 ± 0.005
640	62	38.6 ± 0.2	18.9 ± 0.2	256.2 ± 2.8	24.7 ± 0.2	9.37 ± 0.05	4.47 ± 0.01
			$\kappa_{\mathrm{bend}} = 1$				
40	1000	4.133 ± 0.001	2.262 ± 0.002	12.82 ± 0.07	2.772 ± 0.001	0.9778 ± 0.0004	0.38363 ± 0.00008
80	500	7.915 ± 0.008	4.09 ± 0.01	28.6 ± 0.2	5.220 ± 0.006	1.893 ± 0.002	0.8028 ± 0.0004
160	250	14.52 ± 0.02	7.19 ± 0.05	61.9 ± 0.6	9.43 ± 0.02	3.506 ± 0.007	1.573 ± 0.002
234	171	19.97 ± 0.06	9.70 ± 0.04	94.3 ± 0.8	12.95 ± 0.03	4.834 ± 0.008	2.223 ± 0.002
320	125	25.8 ± 0.1	12.38 ± 0.07	132.3 ± 1.4	16.67 ± 0.08	6.28 ± 0.02	2.936 ± 0.006
640	62	44.3 ± 0.5	20.5 ± 0.3	279.7 ± 3.3	28.1 ± 0.4	10.73 ± 0.09	5.20 ± 0.03
			$\kappa_{\mathrm{bend}} = 2$				
40	1000	5.600 ± 0.006	2.935 ± 0.005	14.8 ± 0.1	3.998 ± 0.004	1.199 ± 0.002	0.4030 ± 0.0003
80	500	10.82 ± 0.02	5.15 ± 0.03	33.0 ± 0.3	7.45 ± 0.02	2.426 ± 0.007	0.946 ± 0.002
104	385	13.56 ± 0.02	6.27 ± 0.02	44.1 ± 0.4	9.21 ± 0.01	3.092 ± 0.004	1.261 ± 0.001
160	250	19.4 ± 0.2	8.66 ± 0.06	70.7 ± 0.7	12.87 ± 0.07	4.50 ± 0.02	1.943 ± 0.006
320	125	33.2 ± 0.3	14.2 ± 0.1	148.7 ± 1.8	22.0 ± 0.3	7.90 ± 0.07	3.65 ± 0.02
640	62	54.9 ± 1.4	22.4 ± 0.4	308.8 ± 3.5	35.6 ± 1.3	12.9 ± 0.2	6.36 ± 0.06

Table 3.2: Conformational properties of melts of ring polymers with bending stiffness κ_{bend}. N: number of monomers per chain; M: number of chains in the melt; $\langle R_g^2 \rangle$: mean-square gyration radius Eq. (5.1); $\langle R_m^2 \rangle$: mean-square magnetic radius Eq. (1.20); $\langle \mathrm{minS} \rangle$: mean minimal surface; $\langle \Lambda_\alpha^2 \rangle$: mean value of the α-th eigenvalue ($\alpha = 1, 2, 3$) of the gyration tensor $\mathcal{G}_{\alpha\beta}$ Eq. (3.10); The reported values with the corresponding error bars have been rounded to the first decimal digit. The data for $\langle \mathrm{minS} \rangle$ are for a coarse resolution of the triangulation procedure adopted to calculate the minimal surface of a ring polymer (see Ref. [69] for the technical details). A finer triangulation gives essentially the same values ("$\circ$-symbols" vs. "$\times$-symbols" in Fig. 3.5) which we have not reported explicitly in this Table.

fully the contributions from chain contour lengths $z = \ell/L_e \lesssim 1$ (*shallow threadings*) from the others. For each ring piercing the minimal surface of another ring, we define [71] the threading contour length L_{t_i} as the contour length portion of the ring comprised between the two consecutive penetrations i-th and $i+1$-th which allow us to assign L_{t_i} *unambiguously* to either "side" of the other ring's minimal surface. Based on L_{t_i}, we consider the following observables:

1. The mean number of rings threaded by a single ring, $\langle n_t \rangle$.

2. The mean relative amount of contour length of a ring on one side of another ring's minimal surface with respect to the other side:

$$\langle Q \rangle \equiv \left\langle \frac{L_{\rm sep}}{L - L_{\rm sep}} \right\rangle , \tag{3.6}$$

   where the so called *separation length* [69, 71],

$$L_{\rm sep} = \min \left(\sum_{i={\rm even}} L_{t_i}, \sum_{i={\rm odd}} L_{t_i} \right) , \tag{3.7}$$

   quantifies for the total contour length of one of the two complementary portions (the other has contour length $L - L_{\rm sep}$) obtained by the passage of the *penetrating* ring through the minimal surface of a *penetrated* ring: *i.e.*, $Q = 1$ simply means that the penetrating ring is half split by the penetrated surface.

3. The mean number of times any ring penetrates the minimal surface of any other ring, $\langle n_p \rangle$.

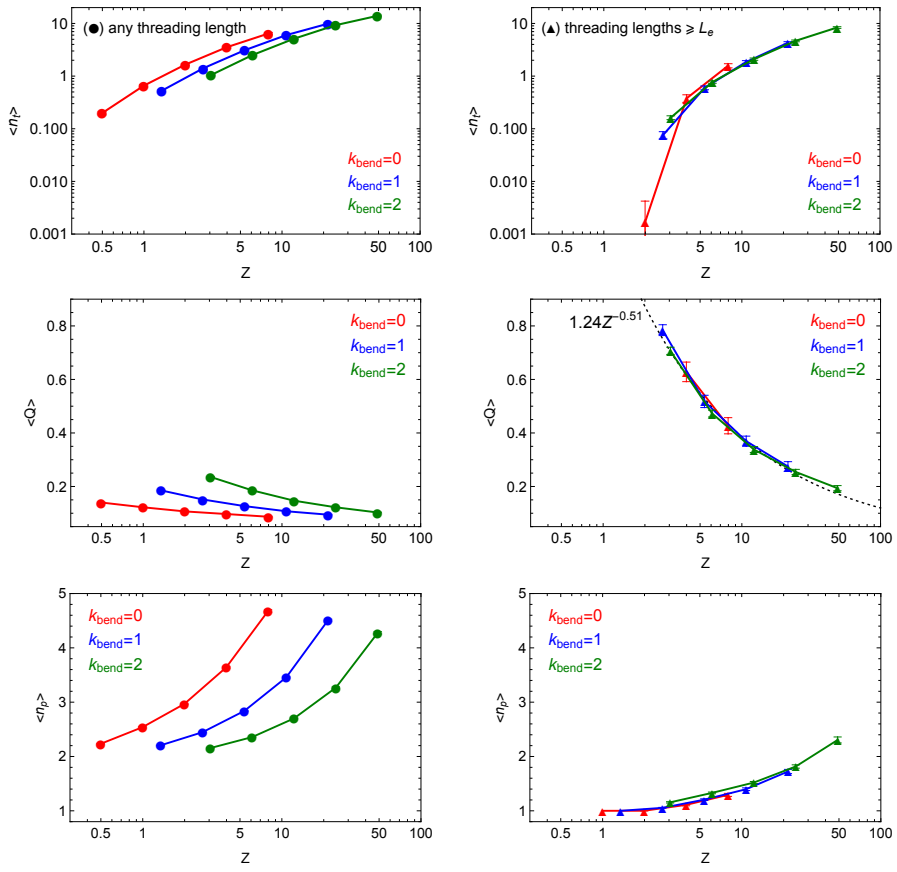

Figure 3.6: Statistics of threadings by minimal surfaces as a function of the total number of entanglements, Z, of each ring in the melt. The data (circles) shown in the l.h.s panels (respectively, (up-triangles) in the r.h.s panels) have been obtained by including threading lengths L_t of any size (resp., $L_t \geq L_e$). Error bars represent the error of the mean calculated from 100 uncorrelated snapshots. (Top) $\langle n_t \rangle$: mean number of rings threaded by a single ring. (Middle) $\langle Q \rangle$: mean relative amount of contour length piercing one ring minimal surface side with respect to the other (Eq. (3.6)). The dashed (black) line on the r.h.s. panel corresponds to the best fit to the data. (Bottom) $\langle n_p \rangle$: mean number of times a ring penetrates the minimal surface of any other single ring.

These different quantities may be computed by taking into account all possible threading segments or by excluding the shallow ones namely, as said, those whose contour lengths are shorter than the entanglement length L_e. Noticeably, in the first case there is no evidence for universal collapse (Fig. 3.6, l.h.s. panels) in any of these quantities. On the contrary (Fig. 3.6, r.h.s. panels), universal collapse is observed after removing the contribution of the short threading filaments: this points to the fact that the same shallow threadings are responsible for the lack of universality observed for $\langle \mathrm{minS} \rangle$ (Fig. 3.5).

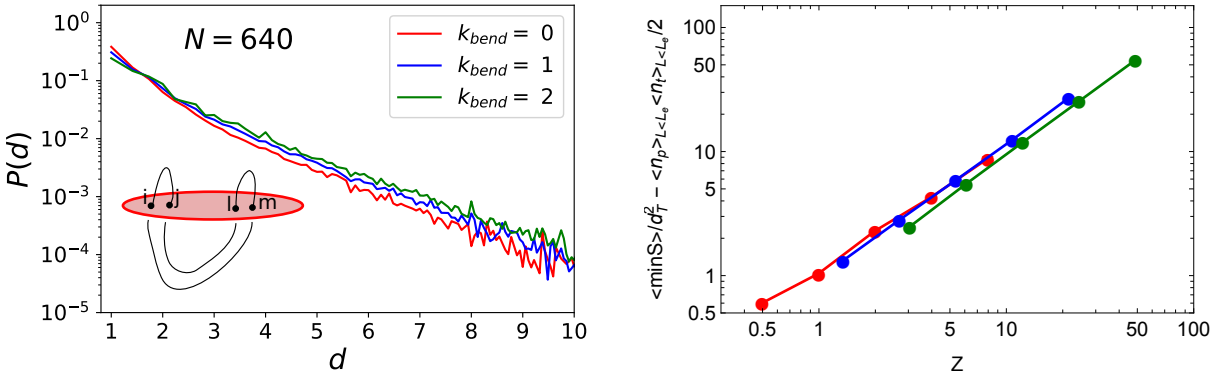

Figure 3.7: On the left, distribution functions of distances, d, between subsequent piercings on the minimal surfaces of rings with $N = 640$ and different flexibilities. Clearly the distributions are exponential. The mean values are $\langle d \rangle = 1.87$, 2.1 and 2.33 (in units of lattice site a) for $k_{\rm bend} = 0$, $k_{\rm bend} = 1$ and $k_{\rm bend} = 2$ respectively. Interestingly, in contrast to the tube diameter d_T, $\langle d \rangle$ grows with the stiffness. On the right, mean minimal surface area, $\langle \mathrm{minS} \rangle$, of ring polymers as a function of the total number of entanglements, Z, of the chain after subtracting the "contribution" to the area by short (or, *shallow*) threadings with contour length $L < L_e$.

To support this idea, we measured the mean distance $\langle d \rangle$ between two bonds involved in the threading. We find that $\langle d \rangle \lesssim d_T$ (see the values, the corresponding distribution functions in Fig. 3.7 l.h.s. panel), which strongly supports the fact that threadings occur on scales below the entanglement scale. We still find some cases when $\langle d \rangle > d_T$, but these are exponentially rare (see Fig. 3.7 l.h.s. panel). Moreover, based on this observation, it is reasonable to assume that each shallow threading contributes $\sim d_T^2$ to the average $\langle \mathrm{minS} \rangle$. Consequently, one can estimate the non-universal contribution to $\langle \mathrm{minS} \rangle$ by assuming that each shallow threading span an area $\sim d_T^2$ and there are on average[4] $\sim \langle n_p \rangle_{L<L_e} \langle n_t \rangle_{L<L_e}/2$ of such threadings spanning the minimal surface of each ring. As expected, the removal of the non-universal contribution to $\langle \mathrm{minS} \rangle$ restores universality almost completely (see Fig. 3.7 r.h.s. panel).

Additionally, restricting the discussion to the universal behaviors, we see that $\langle Q \rangle$ decreases with Z, *i.e.* less material enters the minimal surface of a ring. Yet, the mean number of times, $\langle n_p \rangle$, any ring penetrates the minimal surface of any other single ring increases: notice that these two apparent contradictory features can be easily reconciled by supposing that while retracting from each other (*i.e.* decreasing $\langle Q \rangle$), rings may at the same time pierce each

[4] $\langle n_t \rangle_{L<L_e}$ and $\langle n_p \rangle_{L<L_e}$ are (as in Fig. 3.6 but here restricted to shallow threadings) the mean number of rings threaded by a single ring (which equals the mean number of threadings received by a single ring) and the mean number of times a ring penetrates the minimal surface of any other ring, while the "$1/2$"-factor takes into account the fact that a single threading loops counts as twice in terms of contacts on the minimal surface.

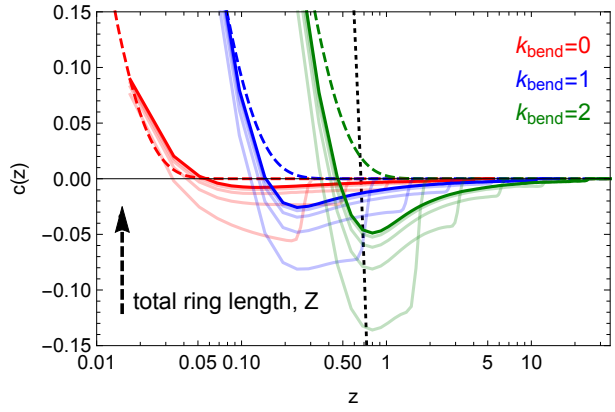

Figure 3.8: Bond-vector orientation correlation function (Eq. (3.8)), $c(z)$, as a function of the number of entanglements $z = \ell/L_e$ along the chain. Lines of equal color are for the same chain stiffness (see legend), full colors are for the longest rings ($N = 640$) while lines in fainter colors are for chains of shorter contour lengths (see arrow's direction). The long-dashed lines correspond to the exponential decay typical of linear polymers with local stiffness, namely $c(\ell) = (\langle\cos\theta\rangle^{\rm ring})^{\ell/\langle b\rangle}$, where the values for $\langle\cos\theta\rangle^{\rm ring}$ are reported in table 3.1. The short-dashed line is the analytical function for an exactly double-folded polymer filament of contour length $= 2L_e$ (see the text for detail).

other more frequently by the increased propensity to form branches at the entanglement scale. Overall, this agrees with the results in [71] for off-lattice dynamic simulations of melts of rings[5].

Double folding signatures According to the lattice-tree model (Sec. 1.3.1), the contour length of each ring above the entanglement length L_e should double-fold along a branched (*i.e.*, tree-like) backbone. We seek now specific evidences of this peculiar organization.

As the first of these signatures, we look at the bond-vector correlation function [59, 66, 68], which has been introduced in Sec. 2.2.1, and defined as:

$$c(\ell) \equiv \frac{\langle \vec{t}(\ell') \cdot \vec{t}(\ell' + \ell)\rangle}{\langle \vec{t}(\ell')^2\rangle} \,. \tag{3.8}$$

Contrary to the known monotonous decaying behavior typical of linear polymers (solid lines *vs.* long-dashed lines in Fig. 3.8) $c(\ell)$ is manifestly non-monotonic, showing an anti-correlation

[5]Notice, however, that in [71] the scaling behavior for Q follows: $\langle Q\rangle \sim Z^{-0.31}$, distinct from the one measured here ($\langle Q\rangle \sim Z^{-0.51}$, see middle right panel in Fig. 3.6). This apparent discrepancy is due to the fact that in [71] the mean value $\langle Q\rangle$ includes the contribution of the shallow threadings: in fact, their removal gives identical results to the ones of the present work (data not shown).

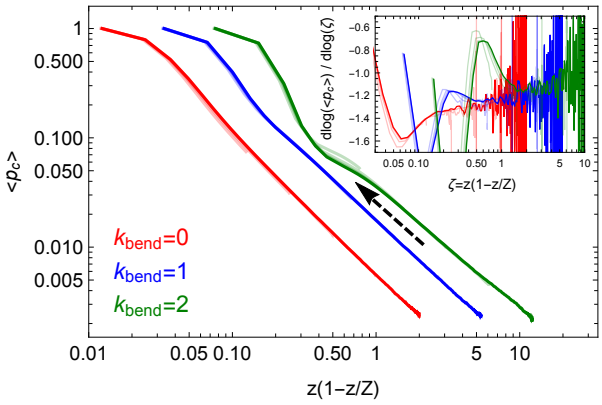

Figure 3.9: Mean contact probabilities, $\langle p_c(\ell)\rangle$ (see Eq. (3.9)), as a function of the "effective" ring contour length $\zeta \equiv z(1-z/Z)$. The arrow points at the levelling of the curves around $z \approx 1$. Inset: local differential exponent $\equiv \frac{d\log\langle p_c\rangle}{d\log\zeta}$. Color code is as in Fig. 3.8.

well whose minimum becomes more pronounced and locates around $z = \ell/L_e \approx 1$ with the increasing of the chain stiffness. By using the function $\vec{t}(\ell) = (0, +1, 0)$ for $0 < \ell < L_e$ and $\vec{t}(\ell) = (0, -1, 0)$ for $L_e < \ell < 2L_e$ as a toy model for an exactly double-folded polymer filament of contour length $= 2L_e$, it is easy to see that $c(z = \ell/L_e) = (1 - 3/2z)/(1 - z/2)$ for $0 < z < 1$ and $c(z) = -1$ for $1 \leq z < 2$, *i.e.* $c(\ell)$ displays an anti-correlation minimum at $z = 1$ or $\ell = L_e$ (short-dashed line in Fig. 3.8). A deep anti-correlation well is particularly visible in short rings (at given $\kappa_{\rm bend}$) while in larger rings the effect is smoothed, arguably because thermal fluctuations wash out such strong anti-correlations.

As a second signature, we look at the mean contact probability [123], $\langle p_c(\ell)\rangle$, between two monomers at given contour length separation ℓ, introduced in Sec. 2.2.1, and defined as:

$$\langle p_c(\ell)\rangle = \left\langle \frac{1}{N+1}\sum_{i=0}^{N} \Theta(r_c - |\vec{r}_i - \vec{r}_{i+n}|) \right\rangle , \tag{3.9}$$

where $\Theta(x)$ is the usual Heaviside step function and the "contact distance" r_c between two monomers is taken equal to one lattice unit, a.

Reducing finite ring size effects by plotting $\langle p_c\rangle$ in terms of the variable [130] $\zeta \equiv z(1 - z/Z)$, the data, from the different rings, form three distinct curves according to their Kuhn length (Fig. 3.9). Notably these curves display the asymptotic power-law behavior $\sim \zeta^{-\gamma}$ with scaling exponent γ close to 1, as reported in the past [38, 44, 59]. At the same time, the stiffer chains with $\kappa_{\rm bend} = 2$ display a short, yet quite evident, levelling of the contact probability curves around $z \approx 1$ (see arrow's direction) which is clearly compatible with double-folding on the entanglement scale.

However, we show now that the most compelling evidence for double-folding comes from

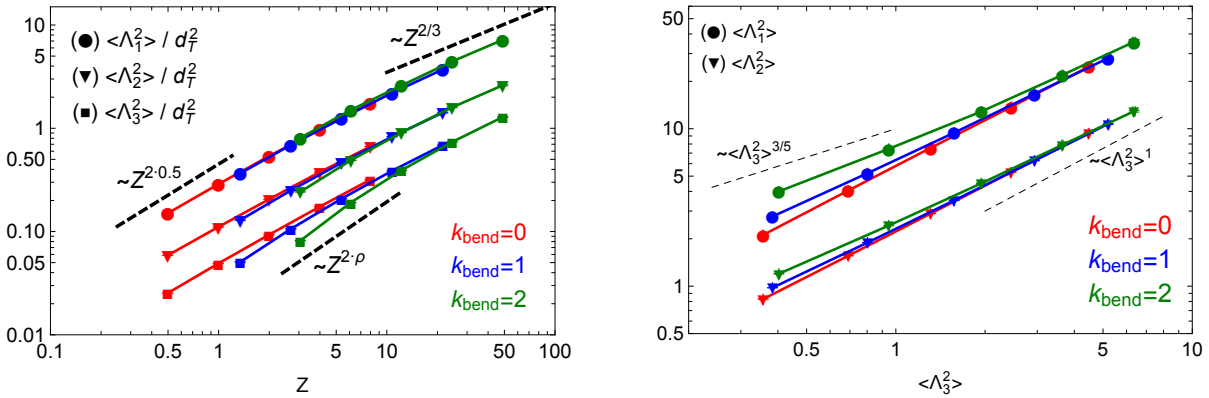

Figure 3.10: Left panel, scaling behavior of the mean-square eigenvalues $\langle \Lambda^2_{\alpha=1,2,3} \rangle$ of the gyration tensor as a function of the total number of entanglements, $Z = L/L_e$, of the chain. Notice the large finite-size corrections to scaling for the smallest eigenvalue $\langle \Lambda^2_3 \rangle$ and its behavior $\sim Z^{2\rho} \sim \langle L_{\rm tree} \rangle^2$. Error bars are smaller than the symbols size. Right panel, mean eigenvalues, $\langle \Lambda^2_1 \rangle$ and $\langle \Lambda^2_2 \rangle$, of the gyration tensor Eq. (3.10) as a function of the smallest eigenvalue $\langle \Lambda^2_3 \rangle$. The dashed lines are the predicted limits of small and large length scales.

examining the average polymer *shape*. To this purpose, we introduce the 3×3 symmetric gyration tensor $\mathcal{G}$, discussed in Sec. 2.2.1, whose elements are defined by:

$$\mathcal{G}_{\alpha\beta} = \frac{1}{2N^2} \sum_{i=1}^{N} \sum_{j=1}^{N} \left(r_{i,\alpha} - r_{j,\alpha} \right) \left(r_{i,\beta} - r_{j,\beta} \right) \, , \tag{3.10}$$

where $r_{i,\alpha}$ with $\alpha = x, y, z$ are the Cartesian components of the spatial position of monomer i. The three order eigenvalues, $\Lambda^2_1 \geq \Lambda^2_2 \geq \Lambda^2_3$, quantify the spatial variations of the polymer along the corresponding principal axes, *i.e.* the instantaneous shape of the chain. Since, these quantify the spatial variation of the polymer we expect, similarly to $\langle R^2_g \rangle$ (Fig. 3.4), a scaling curve for each $\langle \Lambda^2_\alpha \rangle$ in universal units Z and d_T and, for $Z \gg 1$, $\langle \Lambda^2_{\alpha=1,2,3} \rangle \sim \langle R^2_g \rangle \sim d^2_T Z^{2\nu}$.

In general our data (see Fig. 3.10 l.h.s. panel) reflect well this trend, except for the smallest mean eigenvalue $\langle \Lambda^2_3 \rangle$ which displays systematic deviations from the asymptotic behavior which persist for chain sizes well above the entanglement threshold $Z \approx 1$. Interestingly, these deviations are *quantitatively* consistent with the scaling properties of rings being double-folded on an underlying tree-like structure (Sec. 1.3.1): in fact, according to Fig. 3.10 (l.h.s. panel) and for the given mean path length $\langle L_{\rm tree} \rangle \sim Z^\rho$ (Eq. (1.17)) of the "supporting" tree, we can write the expressions:

$$\langle \Lambda^2_{i=1,2} \rangle \sim Z^{2\nu} \sim \langle L_{\rm tree} \rangle^{2\nu_{\rm path}} \, , \tag{3.11}$$

$$\langle \Lambda^2_3 \rangle \sim Z^{2\rho} \sim \langle L_{\rm tree} \rangle^2 \, , \tag{3.12}$$

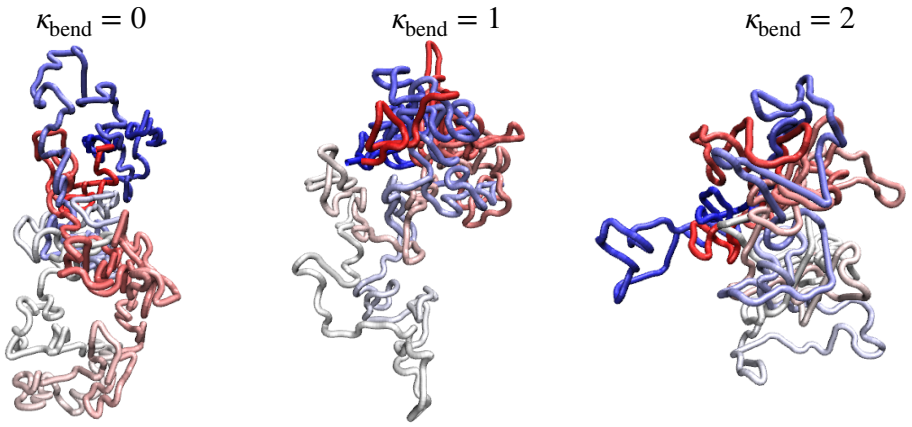

Figure 3.11: Example of ring's conformations in melt with $N = 640$ for the different $\kappa_{\rm bend}$ studied. The polymer's color transitions from blue to red from one chain's end to the other, which are joined to form the rings. For the flexible case, $\kappa_{\rm bend}$ large openings are visible, these openings starts to close as $\kappa_{\rm bend}$ increases. Double folded like conformations are clearly visible for $\kappa_{\rm bend} = 2$.

where the latter is equivalent to assuming local stiff behavior at small contour length separations. Eqs. (3.11) and (3.12) are just equivalent to:

$$\langle \Lambda^2_{i=1,2} \rangle \sim \langle \Lambda^2_3 \rangle^{\nu_{\rm path}} , \tag{3.13}$$

with $\nu_{\rm path} = 3/5$ (Eq. (1.18)). Our data are well described by Eq. (3.13), see Fig. 3.10 (r.h.s panel), before the crossover to the asymptotic regime, $\langle \Lambda^2_{i=1,2} \rangle \sim \langle \Lambda^2_3 \rangle$, takes finally place. Notice that the value of $\nu_{\rm path}$ agrees well with that of the annealed tree model [57]. Note also that here we observe the exponent clearly only for the stiffest system. This might explain why the work [55] that analyzed only simulations [44] with low stiffness (roughly, between our $\kappa_{\rm bend} = 0$ and $\kappa_{\rm bend} = 1$ in terms of L_e) reports that they do not see $\nu_{\rm path}$ (there measured as the scaling of the chain *primitive path* with the contour length).

In conclusion, the *universal* scaling features of the static quantities and the bond correlations reveal double-folded tree-like structure on scales above L_e (see Fig.3.11), with indications ($\langle \Lambda^2_3 \rangle$) that the trees are of the annealed tree type [57]. Conversely, the *non-universal* features ($\langle {\rm minS} \rangle$) and threading analysis show that the trees are threaded on scales smaller than the tube diameter d_T, hence reconciling the tree picture with that of the threaded conformations. At the same time the "depth" of threadings can be (Fig. 3.6) longer than L_e, giving hints on its relevance for the dynamic features. Therefore, in the next section we explore the consequences of the double-folding and threadings on the dynamic properties of the melts.

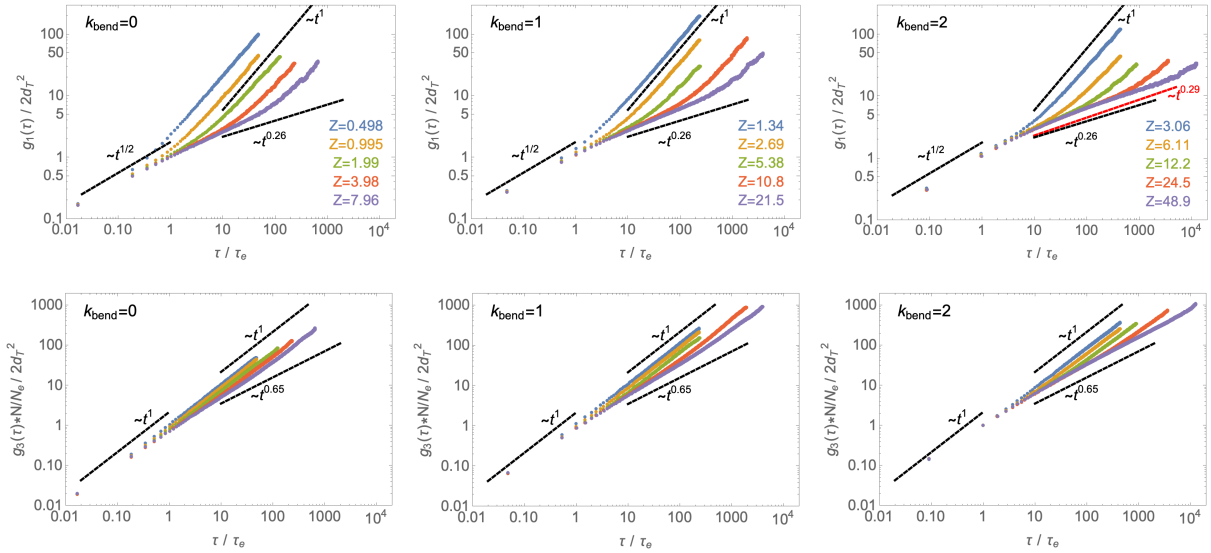

Figure 3.12: Monomer time mean-square displacement, $g_1(\tau)$ (Eq. (2.17)), and chain center of mass time mean-square displacement, $g_3(\tau)$ (Eq. (2.18)). Symbols of the same color are for the same number of monomers N, and the corresponding number of entanglements Z per chain is indicated in the legends. The dashed black lines correspond to the dynamic predictions of the lattice tree model, eqs. (1.26) and (1.27) with $\nu = 1/3$ (Eq. (1.16)) and $\rho = 5/9$ (Eq. (1.17)). The dashed red line in the top-right panel corresponds to the theoretical prediction of the FLG model [55] by Ge *et al.*.

3.3.2 Ring dynamics

Comparison with the models As briefly discussed in Sec. 1.3.2, the lattice-tree model predicts universal dynamic chain behavior for length scales $\gtrsim d_T$ and time scales $\gtrsim \tau_e$. Recent numerical works employing off-lattice molecular dynamics simulations [33] and lattice models [132] agree well with these predictions.

In order to compare the dynamic behavior of the present systems to the results of the lattice-tree model (namely, Eqs. (1.26) and (1.27) with $\nu = 1/3$ (Eq. (1.16)) and $\rho = 5/9$ (Eq. (1.17))), we look then at the monomer mean-square displacement, $g_1(\tau)$, and the center of mass mean-square displacement, $g_3(\tau)$, and plot them in properly rescaled length and time units by using the values of the parameters d_T and τ_e reported in table. 3.1.

Fig. 3.12 demonstrates the correctness of the rescaling procedure and, in line with previous works [33, 132], the good agreement between our simulations (symbols) and the lattice-tree predictions (dashed black lines), in particular for melts of rings with $\kappa_{\rm bend} = 2$ and $Z \approx 50$. Notice though that our data match well also the predictions of the FLG model [55] by Ge *et al.* (dashed red line in the top-right panel), since the two scaling exponents (0.29 *vs.* 0.26,

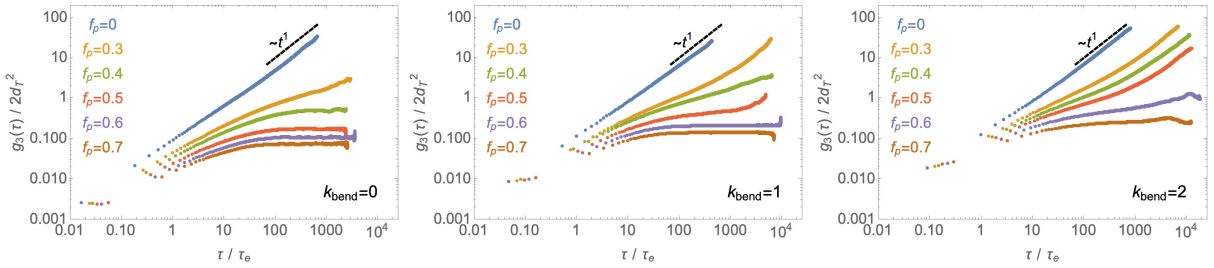

Figure 3.13: Effects of random pinning on chain dynamics. Chain center of mass time mean-square displacement, $g_3(\tau)$ (Eq. (2.18)), at different pinning fractions, f_p, and chain flexibilities, $\kappa_{\rm bend}$ (see legends). Results correspond to melts with the same number of entanglements, $Z \approx 8$, per individual chain.

respectively) are within 10% of each other and, hence, beyond the present accuracy of our data.

The role of threadings in the dynamics Finally, we investigate the implications of threading and double-folding for ring dynamics.

The formation of topological links via threadings has been hold responsible of the unique rheological properties of melts of rings as, for instance, the unusually strong extension-rate thickening of the viscosity in extensional flows [73]. Notably, it was conjectured [40] that inter-ring threadings should form a network of topological obstacles which, by percolating through the entire melt, should sensibly slow down the relaxation of the system, not dissimilar from what happens in those materials undergoing the glass transition.

While direct proof of this *topological glass* is currently missing, recently Michieletto and others [41, 42] gave indirect evidence of this through the following numerical experiment: they froze (pinned) a certain fraction f_p of rings in the melt and reported that the dynamics of the remaining ones is considerably reduced if not frozen at all. In corresponding melts of linear chains this effect is not seen, so they attributed the observed slowing down to the presence of threadings present in rings but absent in linear chains.

In the numerical experiments discussed here, while double-folding is "enhanced" (Sec. 3.3.1) by the chain local stiffness, long threadings, with $L_t > L_e$, which should be the ones affecting the dynamics of the system, result to be universal. At this level, it is unclear what is the impact of these features on the dynamics and whether or not they can be distinguished.

To get some insight into this question, we have taken inspiration from the mentioned pinning numerical experiments [41, 42] and performed additional simulations of melts of rings for $\kappa_{\rm bend} = 0, 1, 2$ with the same number of entanglements $Z = 8$ (to ensure the same large-scale behavior, see Fig. 3.4) and for ring pinning fractions f_p from 0 (*i.e.* no pinning) to 70%. Then

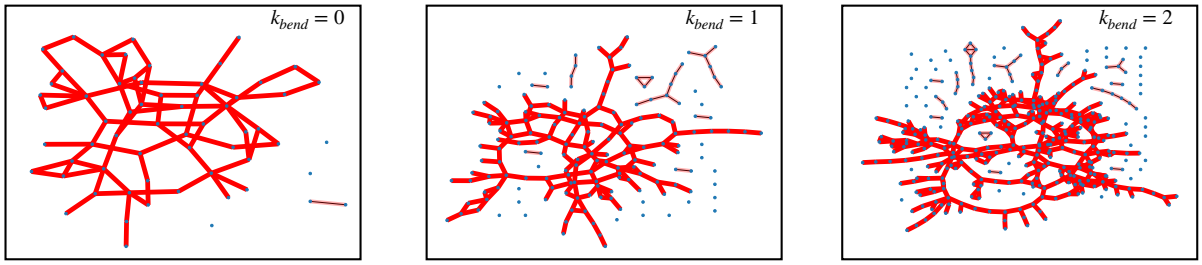

Figure 3.14: Network representation of ring melts with the same number of entanglements, $Z \approx 8$, per individual chain and for different chain flexibilities $\kappa_{\rm bend}$ (see legends). Each node of the network represents a given ring of the melt and the bond between two nodes means that one of the two ring is threading the (minimal surface of the) other (see the discussion in Sec. 3.2.4). For constructing the networks, we have included threading lengths $L_t > L_e$ for which universal scaling behavior emerges (see Sec. 3.3.1).

we monitored the mean-square displacement, $g_3(\tau)$, of the center of mass of the non-pinned rings.

As shown in Fig. 3.13, our results are consistent with the proposed picture: more flexible rings ($\kappa_{\rm bend} = 0$, left panel) which we have interpreted as less double-folded are already completely frozen at $f_p \simeq 30 - 40\%$ while the stiffer (and comparably more double-folded) rings ($\kappa_{\rm bend} = 2$, right panel) require $f_p \simeq 60 - 70\%$.

Finally, we see that this is compatible with a network of percolating topological constraints. To this purpose, we represent the melts as networks where each node corresponds to a ring and we draw a link between two nodes (*i.e.*, rings) whenever the minimal surface of one of the two rings is pierced by a threading segment of the other ring of contour length $L_t > L_e$ (*i.e.*, we neglect the shallow threadings). A picture of these networks is shown in Fig. 3.14: it is seen that, at increasing chain stiffness, the fraction of rings globally connected through threadings sensibly decreases with chain stiffness, from[6] $\sim 93\%$ for $\kappa_{\rm bend} = 0$ to $\sim 74\%$ for $\kappa_{\rm bend} = 1$ and $\kappa_{\rm bend} = 2$, *i.e.* the network of threadings is percolating less through the stiffer melts. Notice that this decrease corresponds roughly to the fractional amount ($\approx 20\%$) of rings which need to be additionally pinned in the stiffer systems compared to $\kappa_{\rm bend} = 0$ in order to get complete freezing (Fig. 3.13).

To summarize, flexible melts showing higher propensity to shallow threadings (Fig. 3.6) are more strongly affected by the pinning, pointing to a possible dynamical role of the shallow threadings. In contrast – yet consistent with the pinning fraction – the deep threadings

[6] In principle, these percentages may be affected by finite-size effects due to the limited number of chains of our melts. Nonetheless, runs with smaller (and, arguably, more finite-size dependent) systems give similar values (data not shown here). Consequently, our conclusions should be fairly robust.

in flexible melts form more connected networks in comparison to the stiffer melts seemingly suggesting that these alone are the relevant ones in the pinning experiment. The latter result is however surprising, because the deep threadings were found to behave universally for the systems with different stiffness (see Fig. 3.6).

Another view on the results of our pinning experiments shows that the threading constraints are a relevant physical feature that needs to be taken into account to refine models for the ring dynamics. As discussed in Sec. 1.3.2, the ring relaxation time with ($\theta = 1$, FLG model) or without ($\theta = 0$, lattice tree model) the tube dilation can be written [55] as

$$\tau_{relax} \sim \tau_e (N/Ne)^{2+(1-\theta)\nu/\nu_{\rm path}+\theta\nu} .$$

Notably, the pinning of a large fraction f_p of rings must stop the dilation, because the pinned chains around a mobile ring cannot move, hence impose constraints at all times. The plateau of the g_3 that we observe indicates a divergence of the relaxation time, but the FLG as well as the lattice models give a finite prediction for the relaxation time even for inhibited dilation $\theta = 0$. Indeed this is the consequence of neglecting of the threadings. Although the FLG model is built on the full tube dilation in the melt, and therefore, its comparison to the pinning with a limited dilation is problematic, its general formulation (see Eq. (1.31)) allows to consider a partial ($\theta < 1$) or no tube dilation. Last but not the least, the fact that both the lattice-tree and the FLG model underestimate the scaling exponent of the diffusion coefficient with N in comparison to simulations and experiment: a similar underestimation of the scaling exponent of the diffusion coefficient is found in *linear* melts when compared to a naïve reptation theory [14]. The agreement between the theory and the experiment is restored when contour length fluctuations and tube dilation are incorporated (see discussion at the end of Sec. 1.2.3). In the rings, the FLG model already includes the tube dilation, yet the prediction of the exponent does not agree with the experiment, which indicates that this is due to the neglect of the threadings. Another explanation of the discrepancy might be the correlation hole effect as indicated in [72]. Whether this is independent of threadings remains to be elucidated.

3.4 Discussion and conclusions

The conformational properties of unknotted and non-concatenated ring polymers in dense melts represent one of the remaining unsolved challenge in polymer physics.

In this chapter, in particular, we have focused on which properties of the rings can be interpreted as signatures of the hypothesis proposed long ago [51–53] that the polymer fiber double-folds around a branched (lattice-tree) path. In this respect, global observables like the

polymer mean-square gyration radius or the mean-square magnetic radius ($\langle R_g^2 \rangle$ and $\langle R_m^2 \rangle$, Fig. 3.4) are very useful for model validation but otherwise offer little insight.

On the contrary, robust evidence for double-folding comes by exploiting the mean polymer shape (Fig. 3.10). The 3 principal axes of the polymer are very different in size and, for relatively moderate polymer lengths, they are not at the same "point" of the crossover to asymptotic behavior: in particular, on the studied range where the largest and the smallest axes are not proportional to each other, we have shown that their functional relation is in *quantitative* agreement with the lattice-tree model. This argument is proposed here for the first time, and it could be useful to revise data relative to other polymer models at its light.

Additional signatures of double-folding on polymer contour lengths $z = \ell / L_e \lesssim 1$ become manifested also in the characteristic negative well of the bond-vector orientation correlation function (Fig. 3.8) and in the "softer" slope of the mean contact probability $\langle p_c(\ell) \rangle$ (Fig. 3.9) displayed before the asymptotic $\sim \ell^{-1}$ power-law behavior takes effectively place. Intriguingly, the reported $\langle p_c(\ell) \rangle$ for chromatin fibers measured in conformation capture experiments [123] displays the same systematic two-slope crossover [141] for $\ell \lesssim 10^5$ basepairs, *i.e.* below the estimated [37] entanglement length of the chromatin fiber. Notice that, in this respect, the formulated hypothesis that such "shoulder" in the contact probability derives from active loop-extrusion [141] provides a dynamic explanation about how (double-folded) loops can form, otherwise it is not needed *per se* in order to explain the observed trend in the contact probabilities.

Overall it is worth stressing that these features, that we interpret as manifestations of double-folding, can be made explicit only by introducing some (even if only moderate) bending penalty to the polymer elasticity (see Fig. 3.11).

Using minimal surfaces we confirm (Fig. 3.5) that rings may reduce their threadable surfaces via double-folding on the entanglement scale and that the piercings of the minimal surface occur only on the scale below the entanglement tube radius. Yet, the threading loops can be numerous and their length can exceed the entanglement length, but these threading features (Fig. 3.6 and Fig. 3.7) evaluated on length scales larger than one entanglement length behave universally. The universal behavior shows the applicability and the relevance [137] of the (linear) entanglement scale to ring polymer melts.

From the point of view of ring dynamics, we have reported that single monomer and global chain motions are in good agreement (Fig. 3.12) with the theory stating that the dominant mode of relaxation is mass transport along the mean path of the underlying tree. Yet the threading constraints can cause divergence of the relaxation time if a fraction of rings is immobilized – a feature not predicted by the theories. On this point, in a recent work [142], thanks to a new experimental techniques which allows the preparation of topologically pure,

high molecular weight ring polymers, first hints on the possible breaking of the self-similar dynamics have been shown. In the work, experiments and simulations of highly entangled ring chains up to $Z = 229$ show slow, non-power law stress relaxation dynamics contrasting the power-law behavior predicted by both the lattice tree and FLG models. Thus, revisiting the theories to incorporate threading constraints might also help to get full understanding on the ring polymer dynamics and clarify if the conjecture on the existence of topological glass in equilibrium is valid.

Chapter 4

A brief review on Knot Theory

In the previous chapter, we have investigated systems with "trivial" topology, *i.e.*, non-concatenated and unknotted rings. However, as discussed in the introductory Chapter 1, a significant portion of my work focused on systems of topologically concatenated and knotted polymer rings. In this context, an important part of the work involved characterizing these systems from a topological standpoint. Specifically, one of the goals was to determine the propensity of the chains to form knots and, if so, what type of knots they exhibited, as well as the nature and arrangement of the ring concatenations.

The study of topology in polymer systems is a long-standing problem, as knotting is a naturally arising phenomenon in sufficiently long polymers for both closed and open chains[1]. Unfortunately, due to the complexity of the problem, only a limited number of analytical findings exist. One of the main results is represented by the probability of knotting in a self-avoiding walk [74], which was proved to tend to 1 exponentially fast with the length of the polymer, implying that long enough polymers become surely knotted. Besides the mathematical charm knots possess, they are important as they affect the statics and dynamical properties of the hosting polymers [143, 144]. Moreover, knots are relevant in the realm of biology, as biopolymers such as DNA are sufficiently long to become self-entangled and form knots [143] and experimental works proved this point, as in the case of DNA in some viruses [145] or in the case of yeast circular chromosomes [146] which were found to be knotted. Regarding linking and concatenations, it has been shown that these rule the mechanical properties of entangled polymer systems,[15–17, 147]. Even in this case, these concepts are biologically relevant as the mitochondrial DNA of some protozoa, the kinetoplast DNA is organized in terms of a

[1]In this regard, we need to specify that rigorous definitions of knots exist only for closed structures and in the rest of the chapter this will be the case of interest. However, in general, spontaneous formation of knots can arise also for open chains, but while for closed chains a knot is permanent, for open chains the knot can diffuse towards the end-chains and consequently can disappear.

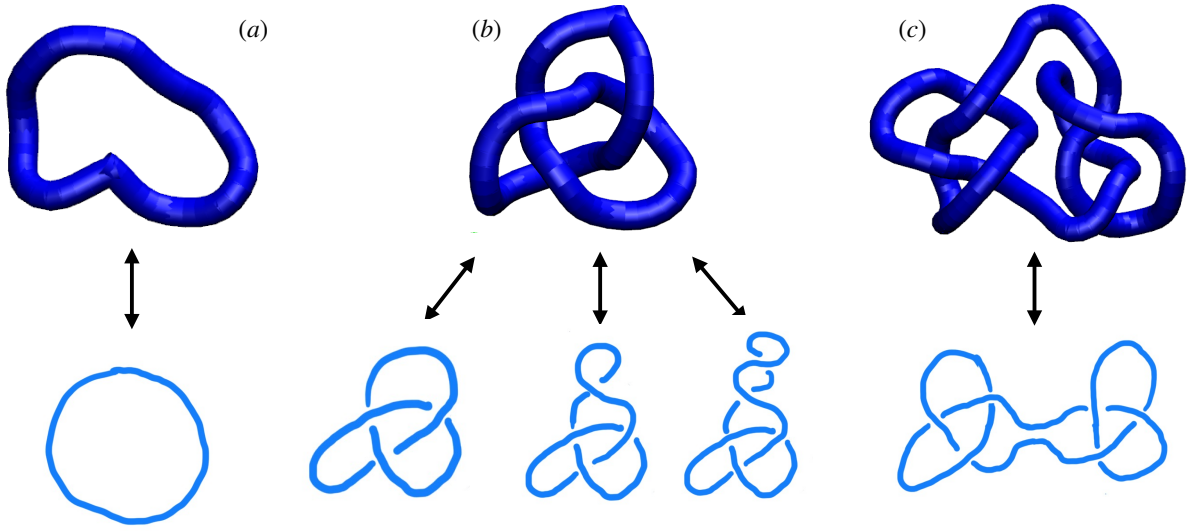

Figure 4.1: Examples of unknotted and knotted polymer configurations extracted from simulations presented in Chapter 6 and their corresponding possible diagram representations. (a) Top, an unknotted polymer ring, bottom, corresponding knot diagram representation. (b) Top, an example of polymer configuration displaying the *trefoil* knot (3_1 in Rolfsen convention [149]); bottom, equivalent diagrammatic representations of a *trefoil* knot: left, minimal representation with $K = 3$, the other two present a higher number of crossing points which can be removed by using the type-1 Reidemeister move (see Fig. 4.2). (c) Top, an example of polymer configuration displaying a composite knot ($3_1\#3_1$ according to Rolfsen convention) formed by two *trefoil* knots; bottom, its diagrammatic representation.

network of thousands of concatenated circular DNA molecules [100].

For all these reasons, it is clear the need for a detailed topological characterization of systems of concatenated and knotted polymer rings to understand their dynamical and mechanical properties. However, this task is not straightforward and relies on tools derived from *Knot Theory*. In the following sections, I introduce and comment briefly on concepts and quantities that have proven useful for my work, while for a detailed account of this topic, I refer the interested reader to [148].

4.1 What is a knot?

Mathematically, a knot is an embedding of a circle in the Euclidean space, $\mathbb{S}^1 \rightarrow \mathbb{R}^3$. Two knots are considered equivalent if one can be transformed into the other through smooth deformations that do not involve cutting or self-intersecting the knot itself. Knots are typically studied through their two-dimensional projections (see Fig. 4.1), or *knot diagrams*, onto

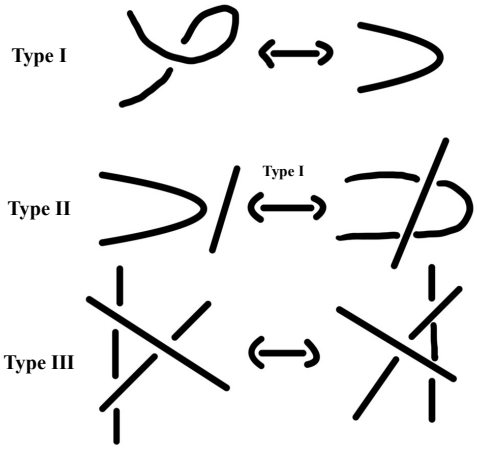

Figure 4.2: Representation of the three Reidemeister moves.

a plane. A knot diagram represents a closed two-dimensional curve characterized by a finite number of intersection points called *crossings*. However, it is important to note that multiple planar diagram representations can correspond to the same knot, differing only by smooth deformations known as *Reidemeister Moves* [148] (see Fig. 4.2). Then, a fundamental problem in knot theory is to determine when different planar diagrams represent the same knot.

Notably, for the same reason above, a knot may exhibit various knot diagrams with different numbers of crossings, some of which can be eliminated through smooth deformations (see Fig. 4.1 (b)), while others cannot. Thus, an essential concept in knot representation is the knot's *minimum crossing number*, K, which represents the smallest number of crossings in any planar diagram of the considered knot that cannot be removed. The simplest knot, known as the *trefoil* knot, has $K = 3$ (see Fig. 4.1 (b)). On the other hand, the unknot, or trivial knot, has $K = 0$, as any of its planar diagram representations can be transformed into a simple non-self-intersecting circle (see Fig. 4.1 (a)). Moreover, knots can be distinguished in *irreducible* or *composite*. While irreducible knots are indecomposable (see Fig. 4.3 for the list of irreducible knots up to $K = 7$), composite knots are just the sum of two or more irreducible knots, (see Fig. 4.1 (c)).

In this work, knots are named following the Rolfsen convention [149], where a knot is denoted as K_i, with K representing the minimum crossing number and the subscript i serving as an enumerative index to distinguish different knots at the same crossing number. For instance, the trefoil knot is represented as 3_1. Composite knots are expressed as a collection of their constituent prime knots: for instance, the composite knot formed by two trefoil knots is written as $3_1\#3_1$.

All the aforementioned concepts also apply to multicomponent systems known as links. A

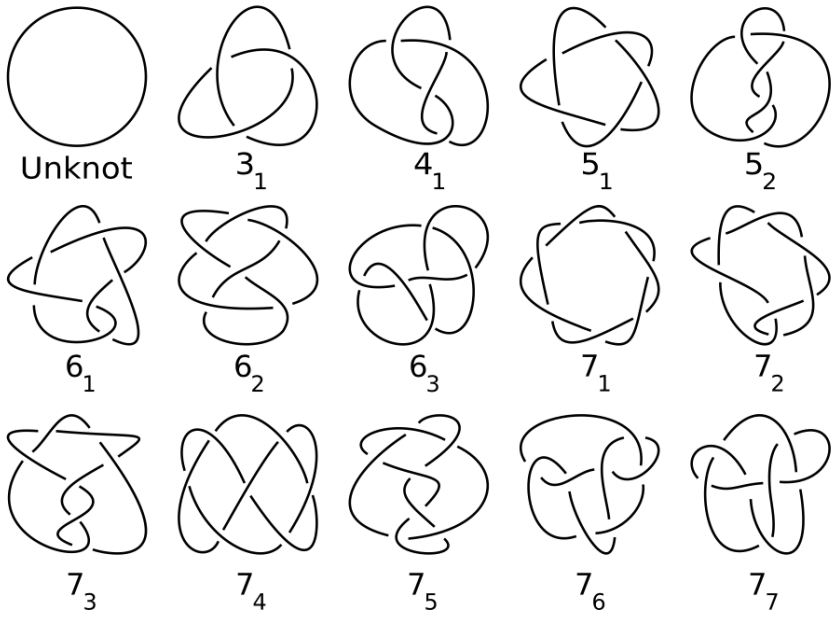

Figure 4.3: List of all irreducible knots up to $K = 7$ named following Rolfsen convention [149]. Image adapted from List of Knots".

link is characterized by the number of individual components it comprises. An n-component link consists of n circles. Then, an n-component link is considered equivalent to the unlink if, through smooth deformations, its planar diagram can be transformed into a collection of non-mutually crossing knots.

Similar to knots, links are distinguished based on their *minimum crossing number*, K. The link with the smallest number of crossing is the 2-chain link with $K = 2$ also known as the *Hopf* link (see Fig. 4.4 (a)).

Additionally, links can be classified as irreducible (Fig. 4.4 (a),(c)) or composite (Fig. 4.4 (b)). Irreducible links cannot be expressed as a sum of lower-order chain links, while an n-chain composite links can be written in terms of a sum of m-chain irreducible links with $m < n$, *e.g.* a 3-chain link made up by two *Hopf* links (Fig. 4.4 (b)).

As for knots, links are named following the Rolfsen convention. According to the convention, an n-chain link is denoted as K_i^n, where K represents the minimum crossing number, the superscript n represents the number of components of the link, the subscript i is an enumerative index to differentiate between different n-chain links at the same crossing number. Composite links are written as a collection of their constitutive irreducible links. The simplest composite link is the 3-chain link formed by two Hopf links $2_1\#2_1$ (see Fig. 4.4 (b)).

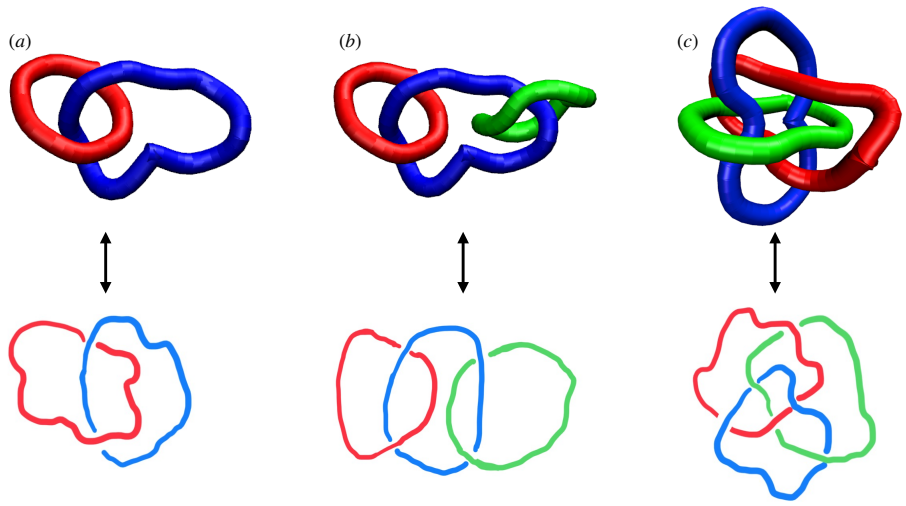

Figure 4.4: Examples of concatenated polymer configurations extracted from simulations presented in Chapter 6 and their corresponding diagram representations. (a) Top, a Hopf link, 2_1^2 in Rolfsen convention, bottom, corresponding diagrammatic representation. (b) Top, a composite link, $2_1^2 \# 2_1^2$, formed by two successive Hopf links, bottom, its diagrammatic representations. (c), Top, an example of an irreducible 3-chain link known as the Borromean rings, bottom, its diagrammatic representation.

4.2 Polynomial invariants

As stated before, knot theory aims to find a way to distinguish inequivalent knots or links (for the rest of the section we will use generically knots for both, if needed, we specify). To this end, a set of *polynomial invariants* have been developed in the course of the last 100 years. These quantities correspond to knot invariants in the form of polynomials whose coefficients encode properties of the corresponding knot. From the knot-diagram representation, one can compute the associated polynomial which, most importantly, is invariant under Redemeister moves. Ideally, each different knot would correspond to a different polynomial, in this situation the polynomial is said to be *complete*.

4.2.1 Alexander polynomials

The first polynomial to be discovered in 1928 was the *Alexander polynomial* [77, 148, 150, 151]. For each given closed curve featuring a knot (see Fig. 4.5) the correspondent Alexander polynomial $\Delta(t)$ of the variable t can be obtained as the following:

- Give an orientation to the curve.
- Classify the crossings as positive or negative by a right-hand rule.

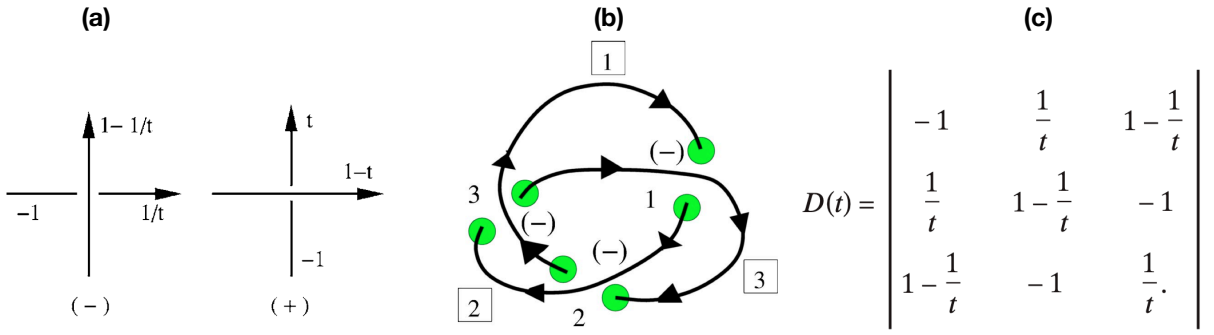

Figure 4.5: (a) Arcs values for computation of the Alexander polynomial. (b) Labelling of the crossings and the arcs for a trefoil knots, 3_1. (c) Corresponding Alexander matrix. In the illustrated case, by taking as the principle minor the one at the bottom-left corner and multiplying by t^2, one obtains $\Delta(3_1, t) = t^2 - t + 1$. Image adapted from [77].

- The crossings divide the curve into four arcs. At each crossing, there is an overcrossing arc, an incoming arc, and an outgoing arc. Number the arcs and the crossings.
- Write the matrix with rows corresponding to the crossings and columns corresponding to the arcs, with arc parameters as shown in Fig. 4.5 (a).
- The Alexander polynomial $\Delta(t)$ can be computed by taking any principal minor and multiplying or dividing it by suitable powers of t and $1 - t$ to obtain a polynomial that does not contain any negative powers and which has a constant term.

For its simplicity, the Alexander polynomial is widely used for distinguishing different knots; however, it is not a complete invariant [148]. Namely, there exist different knots sharing the same Alexander polynomial, such as the 8_{20} knot and the composite $3_1\#3_1$ knot. Moreover, the Alexander polynomial does not distinguish the *unknot* [148], meaning that there are known examples of nontrivial knots with the trivial Alexander polynomial equal to 1.

4.2.2 Jones polynomials

In 1969, approximately 40 years after the discovery of the Alexander polynomial, Conway proved that the Alexander polynomial satisfies a so-called *skein relation* (see Eq.(4.2) for the case of Jones polynomial): this consists in an equation that relates the polynomial of a link with polynomials of other links obtained by changing the crossings of the original knot diagram. In 1984, Vaughan Jones discovered a new kind of polynomial, which after him was named *Jones polynomial* [152]. The Jones polynomial can be constructed by exploiting the skein relation

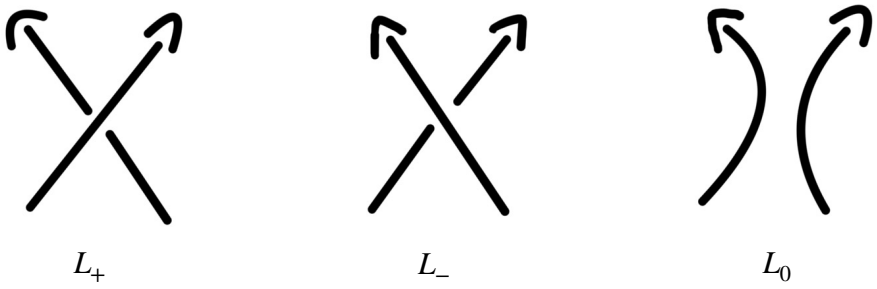

Figure 4.6: Three knot diagrams that are identical except at this crossing obeying the skein relation Eq. (4.2).

expressed in Eq. (4.2). In particular, the Jones polynomial, V, is a polynomial in the variable t and is defined in terms of two properties:

- the Jones polynomial of the *unknot* is 1:

$$V(unknot) = 1 \tag{4.1}$$

- the Jones polynomials of three diagrams that are identical except for one crossing of two lines (see Fig. 4.6) satisfies the skein relation:

$$t^{-1}V(L_+) - tV(L_-) + (t^{-1/2} - t^{1/2})V(L_0) = 0\,. \tag{4.2}$$

  Here, $V(L_+)$, $V(L_+)$ and $V(L_0)$ are the Jones polynomials corresponding to the three different knot diagrams which are identical except in one crossing point where they appear as in Fig. 4.6.

Through the skein relation, the Jones polynomial of any knot can be iteratively defined as in Fig. 4.7. The Jones polynomial is more powerful in *distinguishing* knots compared to the Alexander polynomial, but it is not a complete invariant as well. Moreover, it is not known whether the Jones polynomial distinguishes the *unknot*, but for links, there are known families of nontrivial links with a trivial Jones polynomial.

In my works, I have used both polynomials. In Chapter 5 to detect knots (not links) in the configurations of randomly concatenated and knotted polymers, I have computed the corresponding Alexander polynomials using *Kymoknot* [153], a software developed for this purpose. In all the others, we have resorted to the Jones polynomials, which have been computed using the python package *Topoly*. In this case, the Jones polynomials have been computed to detect and categorize knots, 2-chain links, and 3-chain links.

It is worth stressing two points. First, computing these polynomials is computationally

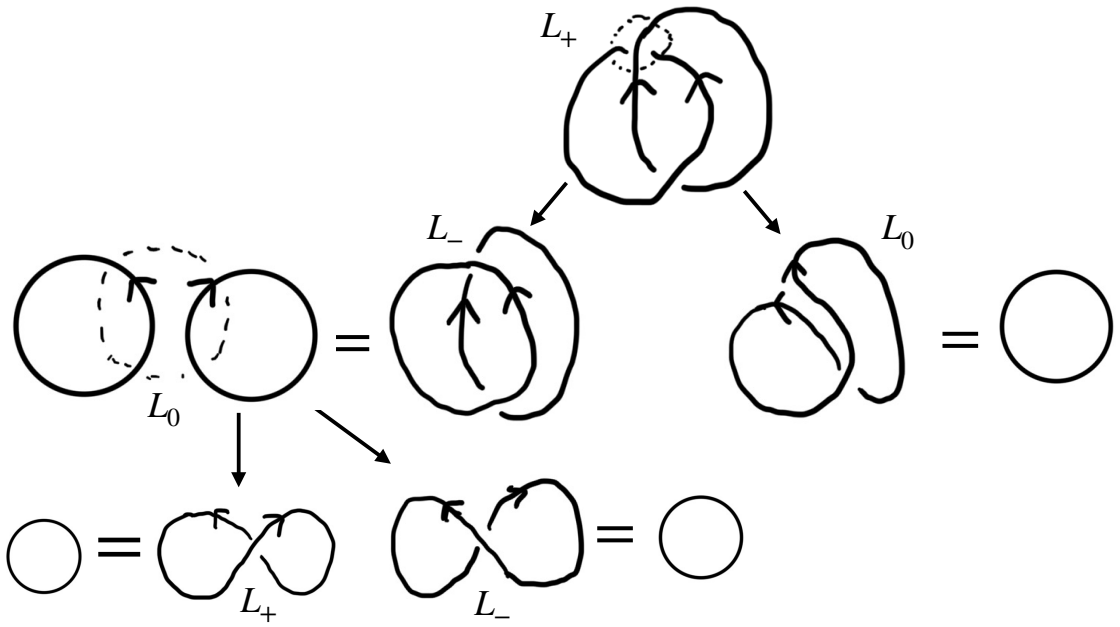

Figure 4.7: Illustration of the calculation of the Jones polynomial for the Hopf link. We start by exploiting the skein relation focusing on the L_+ encircled crossing. The diagram with the substituted L_0 crossing corresponds to the *unknot*, $V(unknot) = 1$. Instead, the one with L_- corresponds to the 2-chain unlink diagram, $V(\text{unlink})$ has to be calculated. By applying again the skein relation, one obtains $V(\text{unlink}) = -\left(t^{-1/2} + t^{1/2}\right)$. It follows that the Jones polynomial of the Hopf link is $V(\text{Hopf}) = -t\left(t\left(t^{-1/2} + t^{1/2}\right) + (t^{-1/2} - t^{1/2})\right) = -t^{5/2} - t^{1/2}$.

Figure 4.8: Positive and negative crossing patterns. Based on this labeling, the GLN of any link diagram can be computed.

expensive and not so straightforward. For Jones polynomials, the computation involves recursively applying the skein relations on knot diagrams as in Fig. 4.7, and the complexity increases with the complexity of the diagram. Alexander polynomials are relatively easier to obtain since they can be computed as the determinant of a matrix (see example in Fig. 4.5) [77, 151]. Second, one would like to associate the computed polynomial with a known knot, which can be done by comparing the computed polynomial with the table of the polynomials of the known knots. In the case of *Topoly*, knots up to 12 crossings and links up to 9 crossings have been tabulated. Therefore, more complex structures cannot be distinguished using this tool.

4.3 Gauss linking number

One of the most well-known and widely used invariants for 2-chain links is the *Gauss linking number* (GLN). The GLN quantifies the linkage between two closed curves $\mathcal{R}_1$ and $\mathcal{R}_2$ and can be computed as [77, 78]:

$$\mathrm{GLN} \equiv \frac{1}{4\pi} \oint_{\mathcal{R}_1} \oint_{\mathcal{R}_2} \frac{(\vec{r}_2 - \vec{r}_1) \cdot (d\vec{r}_2 \wedge d\vec{r}_1)}{|\vec{r}_2 - \vec{r}_1|^3} \,, \tag{4.3}$$

where, respectively, $\vec{r}_1$ and $\vec{r}_2$ represent the spatial coordinates for points on the oriented contour lines formed by $\mathcal{R}_1$ and $\mathcal{R}_2$ and $d\vec{r}_1$ and $d\vec{r}_2$ are the corresponding infinitesimal increments. For a closed curve, GLN is always an integer number and returns the semi-sum of the signed crossings of the diagram [78] (see Fig. 4.8). Thus, once given an orientation to the link diagram, one can associate value $c = 1$ or $c = -1$ to each crossing based on the right-hand rule (see Fig. 4.8 and Fig. 4.9), then

$$\mathrm{GLN} = \frac{1}{2} \sum_{\mathrm{i}=1} \mathrm{c_i} \,. \tag{4.4}$$

Therefore, the GLN represents the number of times (with a positive or negative sign, depending on the orientations of the curves) that each curve winds around the other. However, since

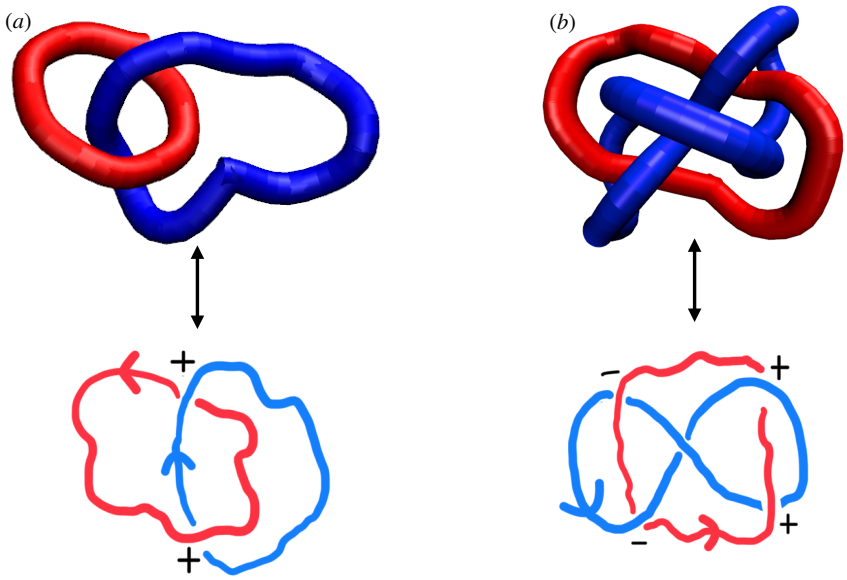

Figure 4.9: Illustration of the calculation of the Gauss linking number using the signed crossings for two non-equivalent links. (a) Top, a Hopf link realization, bottom, its diagrammatic representation with signed crossings based on the labelling in Fig. 4.8. Hence, the GLN of a Hopf link is $= 1$. (b) Top, a Whitehead link realization; bottom, its diagrammatic representation with signed crossings. In this case, the GLN is $= 0$ as the unlink.

it just deals with crossings, many 2-chain links share the same GLN, hence, it is less sensitive with respect to the polynomials previously presented. Furthermore, while it is true that 2-chain links with GLN $\neq 0$ are concatenated, the converse is not necessarily true. For example, the Whitehead link (see Fig 4.9 (b)) has GLN $= 0$.

Despite its limitations, the GLN has found extensive use in detecting concatenations between polymer rings. This is primarily because of its computational convenience when compared to polynomial invariants [77, 78, 81, 154]. Moreover, topological approaches to the definition of the entanglement properties in melts [15–17, 147] have employed the GLN. This is because GLN is an explicit function of polymer conformations (see Eq. 4.3), which makes it more amenable for analytical computations with respect to the other topological invariants.

In this work, we have numerically computed Eq. (4.3) for polymer rings, which are modeled as discretized closed paths on a 3d face-centered cubic (FCC) lattice (see Sec. 2.1.2), by employing the algorithm developed by Klenin and Langowski [155]. The algorithm exploits the fact that the oriented contour lines $\mathcal{R}_1$ and $\mathcal{R}_2$ in Eq. 4.3 consists of a collection of straight segments[2] $\mathcal{R}_1 = \bigcup_{i=1}^{N} \gamma_i$ and $\mathcal{R}_1 = \bigcup_{i=1}^{N} \gamma_i'$. In this situation, Eq. 4.3 turns into a double sum

[2]Here N is the number of bonds of the polymer.

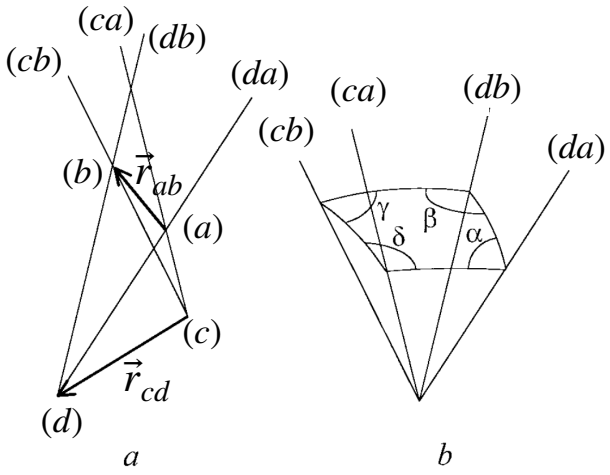

Figure 4.10: (a) Illustration of the observation directions that limit the solid angle needed to compute the Gauss integral Ω_{ij}. (b) The corresponding solid angle. Image adapted from [155].

over the segments of the paths:

$$\mathrm{GLN} = \frac{1}{4\pi}\sum_{i=1}^{N}\sum_{j=1}^{N}\int_{\gamma_i}\int_{\gamma'_j}\frac{(\vec{r}_2-\vec{r}_1)\cdot(d\vec{r}_2\wedge d\vec{r}_1)}{|\vec{r}_2-\vec{r}_1|^3} = \sum_{i=1}^{N}\sum_{j=1}^{N}\frac{\Omega_{ij}}{4\pi}\,. \tag{4.5}$$

Here, $\vec{r}_1$ represents a point belonging to the segment γ_i while $\vec{r}_2$ belongs to γ'_j, Ω_{ij} is the Gauss integral contribution coming from segment γ_i and γ'_j. Then, labelling the end points of the segment γ_i a and b, and the one of the segment γ'_j c and d, these corresponds to the vectors $\vec{r}_{ab}$ and $\vec{r}_{cd}$ (see Fig.4.10 (a)). Ω_{ij} has to be computed and this is done by realizing that its absolute value, $|\Omega_{ij}|$, corresponds to the solid angle which includes all the observation directions such that $\vec{r}_{ab}$ and $\vec{r}_{cd}$ form an apparent crossing [155] (see Fig.4.10 (a,b)). The solid angle $\tilde{\Omega}_{ij}$ is delimited by the planes (c,d,a), (c,d,b),(a,b,d) and (a,b,c) and its value is equal to the area of the quadrangle on the unit sphere having the centre in the origin of the solid angle. The area of the quadrangle can be directly computed as a sum over its angles:

$$|\Omega_{ij}| = \alpha+\beta+\gamma+\delta-2\pi\,. \tag{4.6}$$

To compute the angle, one defines the versor:

$$\vec{n}_1 \equiv \frac{\vec{r}_{ac}\wedge\vec{r}_{ad}}{|\vec{r}_{ac}\wedge\vec{r}_{ad}|} \qquad \vec{n}_2 \equiv \frac{\vec{r}_{ad}\wedge\vec{r}_{bd}}{|\vec{r}_{axd}\wedge\vec{r}_{bd}|} \qquad \vec{n}_3 \equiv \frac{\vec{r}_{bd}\wedge\vec{r}_{bc}}{|\vec{r}_{bd}\wedge\vec{r}_{bc}|} \qquad \vec{n}_4 \equiv \frac{\vec{r}_{bc}\wedge\vec{r}_{ac}}{|\vec{r}_{bc}\wedge\vec{r}_{ac}|}$$

and then:

$$\begin{cases} \alpha = \frac{\pi}{2} + \arcsin\left(\vec{n}_1 \cdot \vec{n}_2\right) \\ \beta = \frac{\pi}{2} + \arcsin\left(\vec{n}_2 \cdot \vec{n}_3\right) \\ \gamma = \frac{\pi}{2} + \arcsin\left(\vec{n}_3 \cdot \vec{n}_4\right) \\ \delta = \frac{\pi}{2} + \arcsin\left(\vec{n}_4 \cdot \vec{n}_1\right) \end{cases} \tag{4.7}$$

As final step, to introduce the crossing sign, since $\Omega_{ij} = |\Omega_{ij}|$ if the two segments form a right-handed crossing, *i.e.* $(\vec{r}_{cd} \wedge \vec{r}_{ab}) \cdot \vec{r}_{ac} > 0$, and $\Omega_{ij} = -|\Omega_{ij}|$ otherwise, Ω_{ij} is defined as:

$$\Omega_{ij} = |\Omega_{ij}| \text{sign}\left((\vec{r}_{cd} \wedge \vec{r}_{ab}) \cdot \vec{r}_{ac}\right) . \tag{4.8}$$

Chapter 5

Monte Carlo method for lattice polymers with non-conserved topology

In this chapter[1], we present the work aimed at the development of a suitable computational polymer model which take into account the dynamical topological rearrangement of melts of ring polymers through a generic strand-crossing mechanism.

The chapter is organized as follows. In Sec. 5.1, we explain the significance of the problem. In Sec. 5.2, we describe the polymer model, the numerical details of the algorithm, its computational cost and summarize the relevant length scales of the polymer melts. In Sec. 5.3, we present the main results of the work. Finally, in Sec. 5.4, we discuss an effect related to the efficiency of the strand crossing mechanism that may be tested in experiments employing DNA rings. The material presented here is complemented by additional figures in the Appendix A.

5.1 Introduction

In dense polymer liquids and melts, the local Brownian motion of each polymer chain is subject to long-lived topological constraints (a.k.a. entanglements) imposed by the presence of the other chains (see Sec.1.2.2). Polymer chains under typical dense conditions become mutually entangled because they are effectively uncrossable to each other [5, 14]. In recent years, direct "manipulation" of entanglements in single chain molecules has opened new routes to fine-tune the mechanical properties of polymeric materials. This is for instance the case of the so called *smart materials* like polycatenanes and polyrotaxanes [86, 87], which are made of interlocked components whose internal degrees of freedom and mobility shape the unique conformational space of the molecule, which can be artificially synthesised following precise

[1]The material described in this Chapter has been published in: M. A. Ubertini and A. Rosa, Physical Review E (2021) [1]

chemical routes [86, 87].

Interestingly, a similar system has been recently synthesised following a complete different approach. This is the case of the work of the Spakowitz's group at Stanford [93], which represents the first synthesis of a so-called *Olympic* hydrogel (see Fig. 1.14), consisting of a polymer network made up by interlocked polymer rings, and first theorized by de Gennes [98, 99]. In the experiment, the synthesized Olympic hydrogel is made up by DNA plasmid rings [93], which interlock to each other through the action of the enzyme[2] *topoisomerase-II* (TopoII). There, it was showed that the "strand crossing" mechanism induced by the continuous action of TopoII relaxes ("fluidizes") the topological constraints dominating the viscoelastic behavior of concentrated solutions of entangled DNA rings. Moreover, by blocking the activity of the enzyme, the once free rings become permanently linked with each other and under these conditions the DNA solution becomes equivalent to an *Olympic gel*.

Olympic gels constitute a fascinating class of soft materials due to their remarkable theoretical [82–85], biological (the kinetoplast DNA of certain protozoa [100, 102] can be modeled [81] as an Olympic gel) and even pharmacological [156] applications. The fundamental difference between an Olympic gel and a traditional gel is that the former is maintained together by topological bonds and not by chemical cross-links [5].

Undoubtedly, one of the most interesting feature of the synthesised Olympic gels of Spakowitz's experiments is the possibility to control polymer topology and entanglements to switch from liquid-like to more solid-like features. As discussed in Sec 1.4.1, the dynamical nature of the action of TopoII plays an important role for the definition of these effects, yet all polymer models developed for dealing with topological complex polymer assemblies have overlooked this feature. For this reason, in this chapter, I present a new computational model, which generalizes the efficient Monte Carlo scheme for lattice polymers described in Sec. 2.1.2 taking into account the kinetic nature of the strand-crossing mechanism. Then, building on this, I present the results of extensive numerical simulations describing the formation of linked networks of ring polymers in melt conditions.

[2] *Topoisomerase-II* [96] is an enzyme which act between two nearby DNA filaments (see Fig. 1.13, by cutting one strand, moving the other through the cut and ligating the broken strand back, effectively producing "strand-crossing" events.

5.2 The polymer model: simulation protocol, length scales, methods

5.2.1 The kinetic Monte Carlo algorithm

We employ the kinetic Monte Carlo (MC) algorithm described in 2.1.2 on the three-dimensional FCC lattice with lattice spacing $= a$ corresponding to our unit of length, and we model solutions of ring polymers with *excluded volume* interactions.

The core of the algorithm is based on the elastic lattice polymer model inspired by the Rubinstein's [110] repton model and developed in [109, 112] which has been described in Sec. 2.1.2. The model is sketch in Fig. 2.1. Here, we just recall that the bond length b between nearest neighbor monomers takes then two possible values, $= a$ or $= 0$: in the latter case the bond is said to host a unit of *stored length*. For a polymer with N bonds, the total contour length $L \equiv N\langle b\rangle < Na$ where $\langle b\rangle$ is the average bond length.

The dynamic evolution of the chains is implemented by combining two kinds of MC moves, which we classify based on the effects they produce on the global topology of the chain: (i) topology-preserving moves, and (ii) topology-changing by stochastic strand crossing moves.

5.2.2 Topology-preserving moves

The first set of MC moves is as in the original lattice model [109, 112]: by construction, these moves preserve the overall topological state of the system and they have been discussed in Sec. 2.1.2. These moves are also summarized in Fig. 2.1.

5.2.3 Topology-changing (strand crossing) moves

Here, we are interested in studying melt of ring polymers where topology changes are induced over time. In particular we consider the basic mechanism of *strand crossing* (hereafter, SC) involving a pair of nearby polymer filaments, similar to the action triggered by the enzyme TopoII in DNA rings solutions [93]. The original [109, 112] lattice model does not include such feature: we show here that it is however possible to remove this "constraint" and we describe the simplest possible MC move capable of inducing a single crossing between two nearby polymer strands. These polymer strands may either belong to the same chain (*intra-chain* SC) or they can stay on two distinct chains (*inter-chain* SC).

The new move (which is also one of the main contributions of this work[3]) is explained

[3]A similar move was introduced in [113] with the purpose of accelerating the equilibration of long polymer chains on the FCC lattice and investigating the structural stability of the so called *fractal globule* [123]. The

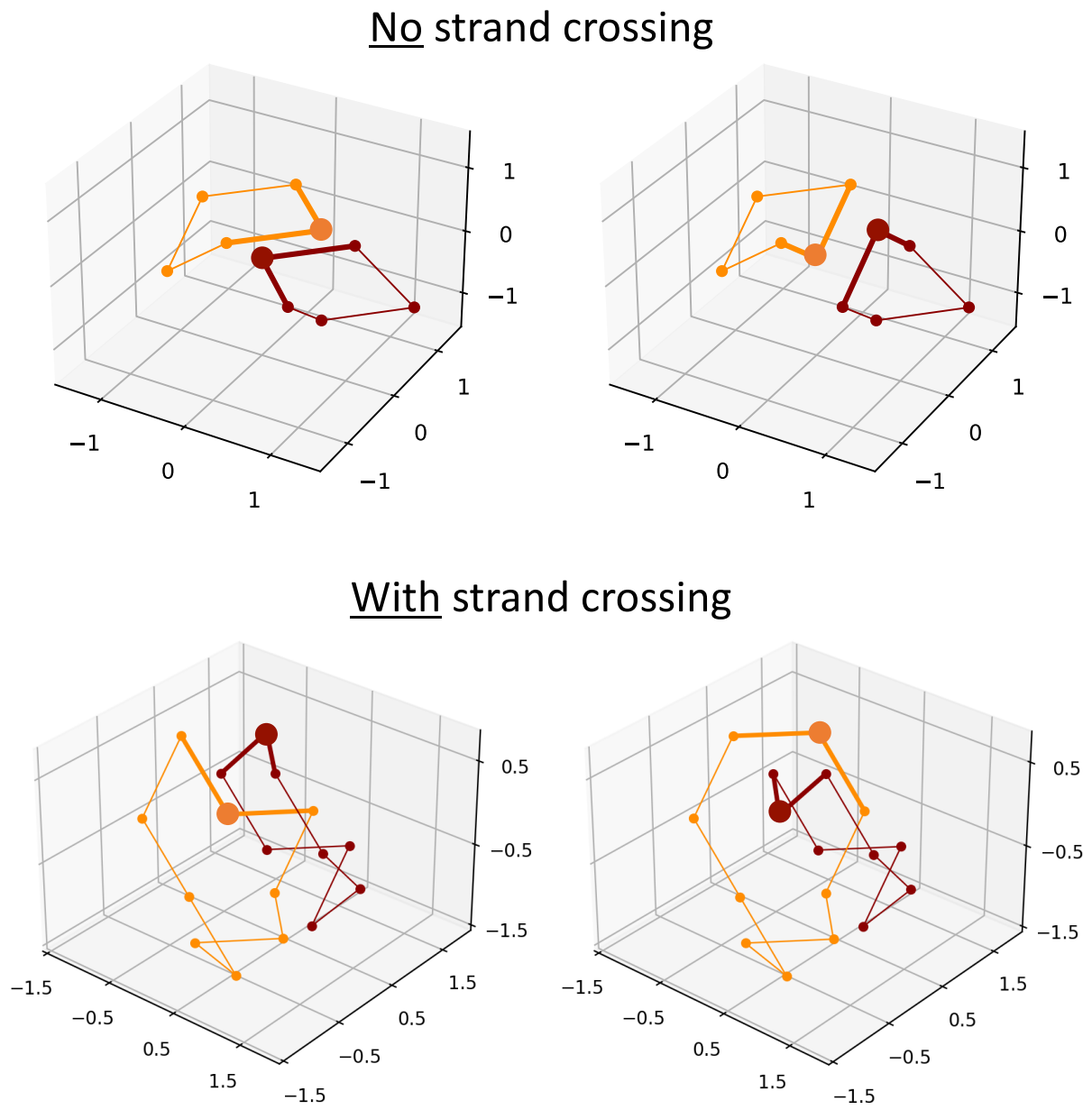

Figure 5.1: Illustration of Monte Carlo moves for strand crossing. On each pair (red/orange (color) or dark/light gray (b/w)) of ring polymers we identify those portions (the thicker strands) of contour length $= 2a$ whose central monomers (the bigger dots) are one lattice site far apart. The two strands can be "transformed", such that the original central monomer of one strand turns into the central monomer of the other strand (l.h.s. panels *vs.* r.h.s. panels) and viceversa, without violating the chain connectivity constraint. In some cases (*e.g.*, as in the top row) this operation does not lead to strand crossing, in others (*e.g.*, as in the bottom row) it does. We list all cases (12 in total) leading to strand crossing and implement them in our MC algorithm. The configurations in the bottom row constitute an example of a linking (left $\rightarrow$ right) or an unlinking (right $\rightarrow$ left) event.

with the help of the two examples in Fig. 5.1. Take the two distinct polymer strands, each of effective contour length $= 2a$, which are illustrated, in each panel of the figure, as the thicker portions of the two closed curves. The two segments are chosen with the constraints that the corresponding central monomers (the bigger dots): (i) are positioned at lattice site distance $= a$ and (ii) one can switch position with the other and be then reconnected to the other chain with no violation of polymer connectivity and preserving the contour length. By exhaustive search, we have then compiled the list of all possible (36 in total) swapping moves compatible with these constraints. By closer examination, we verify that 24 of them do not produce SC (essentially the two chain strands remain on parallel planes even after swapping, see the polymer configurations in the top row in Fig. 5.1), while the remaining 12 moves effectively lead to a single SC (as in the polymer configurations in the bottom row in Fig. 5.1). The successful SC has been verified by looking at the *variation*, $|\Delta \mathrm{GLN}| = +1$, of the *Gauss linking number* GLN (see definition, Eq. (4.3)) relative to the piecewise closed curves formed by the triplets of monomers involved in the MC swapping move.

The implementation of this move in the kinetic MC algorithm is as the following. We pick randomly two polymer strands of effective contour length $= 2a$, then check whether they belong to the set compatible with a SC and, if so, we swap the corresponding central monomers. When the two involved strands belong to the same ring the move is introducing *knots* in the chain (Sec. 6.3.1), while on two separate rings it will induce the formation of *links* (Sec. 5.3.2).

5.2.4 Simulation details

We have considered bulk solutions of M closed (ring) polymer chains, each chain made of N monomers or bonds. With values $N \times M = [40 \times 5120, 80 \times 2560, 160 \times 1280, 320 \times 640, 640 \times 320]$ each system contains a fixed number of monomers $= 204800$. In this work, we have considered flexible chains ($\kappa_{\mathrm{bend}} = 0$ in Eq. (2.6)).

Bulk conditions are implemented through the enforcement of periodic boundary conditions in a simulation box of total volume $V = L^3$, where the linear sizes of the box, L, has been fixed based on the monomer number per fcc lattice site $= 1.23$ corresponding to melt conditions [68, 112]. As specified in Chapter 3, the volume occupied by the fcc lattice site is $= \frac{a^3}{\sqrt{2}}$ [139], hence, the monomer number per unit volume of the system is $= 1.23\sqrt{2} \simeq 1.74 a^{-3}$.

We have studied and compared structure and dynamics for different set-up's as in the exper-

authors' choice, however, does not necessarily modify topology (which is, instead, the main concern here) and the paper did not address questions like the physical consequences of using different strand crossing rates (Sec. 5.2.4).

$\langle b\rangle/a$	ℓ_K/a	$\rho_K\ell_K^3$	L_e/ℓ_K	N_e
0.74	1.48	2.82	36.95	73.9

Table 5.1: Values of physical parameters for melts of ring polymers on the FCC lattice with unit distance $= a$ and monomer number per unit volume $= 1.74$ derived as in Sec. 3.2.3: (i) $\langle b\rangle$, mean bond length; (ii) ℓ_K, Kuhn length (Eq. (3.3)); (iii) $\rho_K\ell_K^3$, number of Kuhn segments per Kuhn volume [140]; (iv) L_e, entanglement length (Eq. (1.6)); (v) $N_e \equiv L_e/\langle b\rangle$, number of bonds per entanglement length.

iment of Spakowitz:

- Ring polymer melts with *non-conserved* chain topology. Here, the topological state of the system changes in time according to the SC mechanism. Therefore, the MC scheme includes the whole set of dynamic moves described in Sec. 5.2.2 and Sec. 5.2.3.

- Ring polymer melts with *conserved* chain topology. Here, only topologically preserving moves (Sec. 5.2.2) are included. Since now topology can not relax the choice of the initial state is crucial. The following two options have been considered: (i) Equilibrated melts of *unknotted and non-concatenated* or (for brevity and as in Ref. [68]) *untangled* rings. (ii) Equilibrated melts of *permanently catenated* rings, corresponding to the equilibrated polymer conformations obtained at the end of the simulations with non-conserved chain topology. The name anticipates some properties of the rings (catenation and linking) that will be discussed in depth in Sec. 5.3.2.

- For additional comparison, we have also considered ideal (*i.e.*, no excluded volume and no topological interactions) rings.

At each MC time step, monomers are picked at random and time is measured in MC units of $\tau_{\rm MC} \equiv N \cdot M$. For polymer solutions with non-constrained topology (Sec. 5.2.3) one needs to specify also the *rate*, $\lambda_{\rm SC}$, at which SC's occur. In principle, this rate is a free parameter of our model that we must tune. For the typical experimental conditions described in the work by Spakowitz *et al.* [93], it was estimated that the action rate of TopoII on DNA rings is close to its *intrinsic* rate of $\mathcal{O}(1{\rm s}^{-1})$ and $\approx 10^4$ times slower than the mean diffusion time of a single DNA persistence length[4].

Then, by considering that our polymers are flexible (see table 5.1), we take here one SC

[4]We estimated such time from the experimentally reported curves of the frequency dependent shear modulus $G^*(\omega)$ [93] of the system. In particular, from the scaling behavior, $G^*(\omega) \sim \omega^\alpha$, it is possible to locate the crossover between the regime in which the system's relaxation process is dominated by the thermal bend

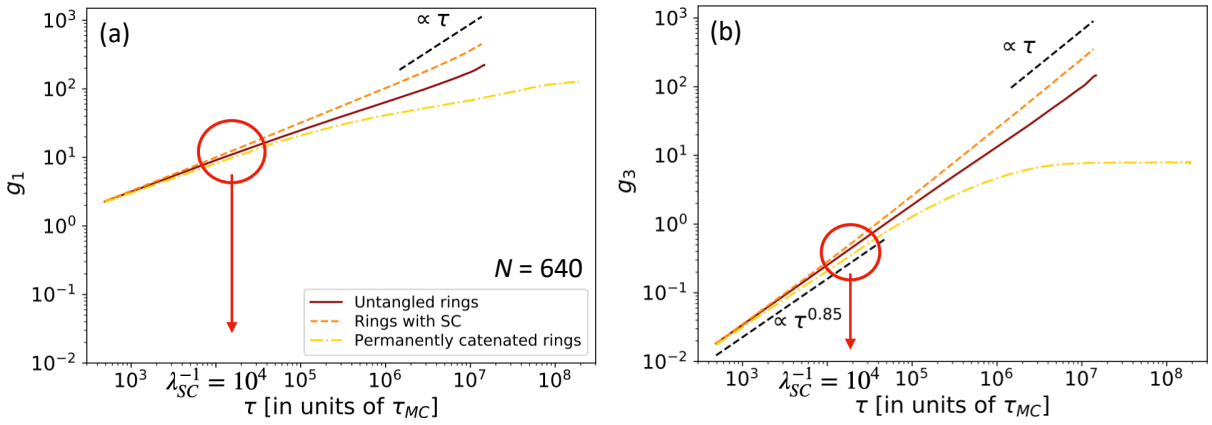

Figure 5.2: Time mean-square displacements of (a) single chain monomers (Eq. (2.17)), g_1, and (b) the chain center of mass (Eq. (2.18)), g_3, for rings with $N = 640$ monomers. In both panels, the lines for (i) melts of untangled rings (red, solid), (ii) rings with active SC's (orange, dashed) and (iii) permanently catenated rings (yellow, dot-dashed) visibly depart (circle) from each other at the imposed SC time scale $\lambda_{\rm SC}^{-1}/\tau_{\rm MC} = 10^4$ (see Sec. 5.2.4).

move (modeled according to Sec. 5.2.3) each 10^4 MC time steps (*i.e.*, $\lambda_{\rm SC}^{-1} = 10^4\,\tau_{\rm MC}$) with only topology-preserving moves. Notice that the algorithm makes the implicit assumption that the enzyme TopoII is immediately available for the reaction, *i.e.* the SC process is intrinsically *reaction-limited*. Nonetheless, we will also discuss (see Sec. 5.4) smaller values of $\lambda_{\rm SC}$ corresponding to "less efficient" TopoII.

Fig. 5.2 shows that the algorithm generates the correct dynamics. By taking the longest rings with $N = 640$, the diffusive monomer (panel (a)) and chain (panel (b)) motions for the three cases of melts of (i) untangled rings, (ii) rings with active SC's and (iii) permanently catenated rings nicely superimpose on each other on time scales shorter than the SC time scale $\lambda_{\rm SC}^{-1}$, *i.e.* ring dynamics on these time scales is not sensitive to SC's, and deviate above $\lambda_{\rm SC}^{-1}$. Importantly, this test confirms that the local segment dynamics is not significantly altered by the presence of SC's (see Sec. 5.2.5 for more details on this point).

5.2.5 Comparison to other simulation methods

In this section, we review some computational work having significative overlap with (i) our method of creating strand crossings and (ii) the consequent formation of linked gels from melts of entangled rings.

---

fluctuations of individual semiflexible chains, for which $G^*(\omega) \sim \omega^{3/4}$ [5], to the one dominated by the fluctuations of a flexible Rouse polymer, $G^*(\omega) \sim \omega^{1/2}$ [5]. Since such crossover is in correspondence with the mean diffusion time of a single DNA persistence length, one can easily estimate such time from $G^*(\omega)$.

In two papers [157, 158], Schaffer introduced and studied the physical properties of a Monte Carlo model for polymer dynamics where monomers have distinct positions on the simple cubic lattice and bonds are allowed to fluctuate by inclusion of the first, second and third nearest neighbors of each monomer. Chain dynamics proceeds by random monomer displacements which respect bond constraints and excluded volume. Then, topological constraints between different chains are switched on/off by allowing/forbidding chain conformations with bonds which may cross at their midpoints. Using these simple rules, the model was applied first to melts of linear chains [157, 158] and later on to melts of untangled rings and rings with SC's [159]. Our results for ring structure (see Sec. 5.3.1) and dynamics (see Sec. 5.3.2) substantially confirm the results reported in [159].

An approach very similar to Schaffer's was then employed by Lang and coworkers in a series of more recent papers [82–85]: specifically, the authors complemented the *bond fluctuation* model on the FCC lattice [160, 161] with a set of *diagonal* moves (the so called "x-traps" [162]) which enforce the temporary overlap of polymer bonds and hence possible SC's. The model was used to study the conformational properties of Olympic gels, however the dynamics of the gel was not discussed.

The philosophy at the basis of these two models is the same: letting random overlaps between bonds as the first, necessary, step for strand crossings to occur. However (quoting Schaffer [157]) this procedure suffers from the inconvenience that "the local density is not guaranteed to be the same ... because the noncrossing simulations exclude a small fraction of configurations (those in which bond midpoints overlap) that are included in the crossing simulations". At the same time, albeit small, the chain local mobility changes in moving from noncrossing to crossing simulations (see [157], Fig. 5) and the corresponding single-mononomer time mean-square displacements $g_1(\tau)$ do not coincide at short time scales (see [157], Fig. 8) where we expect the effects of SC's to be small.

For the completeness of the discussion, it is worth mentioning that the preservation of the local density may indeed be a problem that one has to deal with also in classical off-lattice simulations. Related to that, in Ref. [81] Michieletto and coworkers used classical Brownian dynamics simulations of a bead-spring polymer model to construct model Olympic gel conformations for the DNA kinetoplast. In this study, entanglements were removed by (i) switching off the non-bonded monomer-monomer interactions of the system, (ii) letting the system to equilibrate and (iii) slowly turning interactions on again. However, as demonstrated by Auhl *et al.* [163], this procedure must be performed with extreme care, especially when applied to dense polymer solutions as it may lead to considerable artifacts if the system is not let to equilibrate properly.

Clearly both the above discussed problems (the non preservations of the local density *and*

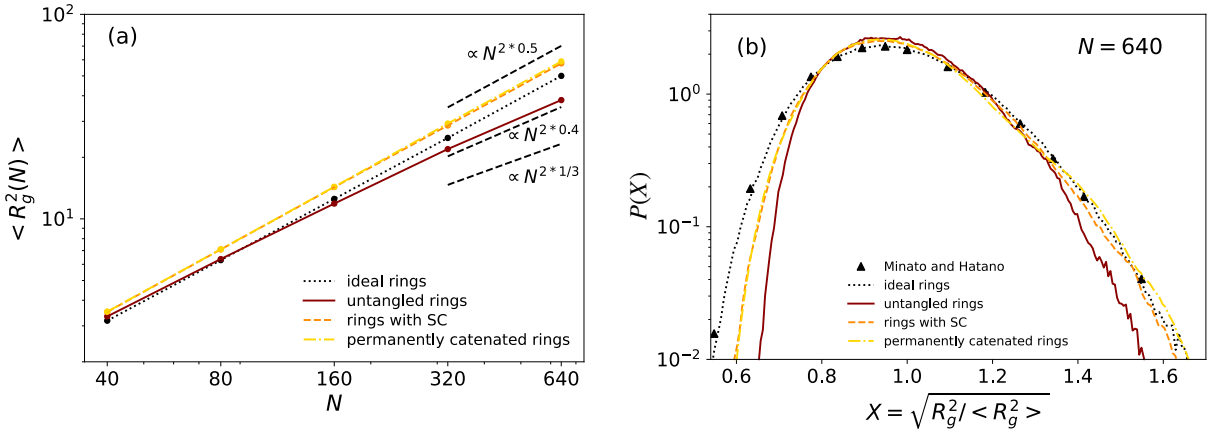

Figure 5.3: (a) Mean-square gyration radius of ring polymers, $\langle R_g^2(N)\rangle$, as a function of the number of bonds, N (for detailed values at each N, see Table A.2 in Appendix A). Different colors / line styles are for different polymer ensembles (color code / line style for untangled rings, rings with SC and permanently catenated rings are as in Fig. 5.2), and dashed lines correspond to theoretical asymptotic behaviors. (b) Distribution functions of gyration radius, $P(R_g/\sqrt{\langle R_g^2\rangle})$, in the different ring ensembles and for the largest chains ($N = 640$). The up-triangles correspond to the Minato and Hatano's exact analytical result for ideal rings [164].

chain mobility) are absent in our work, see Figs. 5.1 and 5.2(a). At the same time, the protocol allows for easy calibration of the relevant SC parameter $\lambda_{\rm SC}$ (Sec. 5.2.4) whose effects, to our knowledge, are considered here (see Discussion, Sec. 5.4) for the first time.

5.3 Results

5.3.1 Single-chain structure

Ring size

We have studied first how the polymer mean-square gyration radius Eq. 2.11, $\langle R_g^2(N)\rangle$, scales as a function of N:

$$\langle R_g^2(N)\rangle \sim N^{2\nu} . \tag{5.1}$$

The results for the different ensembles are summarized in Table A.2 in Appendix A and plotted in Fig. 5.3(a). As discussed in the chapter 3 and in agreement with refs. [44, 59, 68], topological constraints in untangled melts are ineffective below $N \lesssim N_e$ where $N_e \approx 74$ is the total number of monomers per entanglement length (see Sec. 3.2.3). Above N_e, the mutual topological constraints between nearby rings let the chains to deviate from the ideal behavior $\langle R_g^2(N)\rangle \sim N^{2\cdot 1/2}$ and to become more compact: in particular here we report

the scaling $\langle R_g^2(N)\rangle \sim N^{2\cdot 0.4}$, which describes [50] the slow crossover to the asymptotic compact regime $\langle R_g^2(N)\rangle \sim N^{2\cdot 1/3}$ [57, 59]. In the presence of active SC's the rings swell again, $\langle R_g^2\rangle \sim N^{2\cdot 1/2}$, and reach a steady state which does not change further after the SC mechanism is switched off and rings become permanently catenated (overlying dashed and dot-dashed lines in Fig. 5.3(a)).

It is interesting to point out that, while the reported scaling exponent $\nu = 1/2$ is the same of ideal chains, rings structure remains nonetheless non-ideal. To show that, we have computed the complete distribution function, $P(\frac{R_g}{\sqrt{<R_g^2>}})$, of the gyration radius and compared their shapes in the different ensembles (see Fig. 5.3(b)). First, ideal rings (dotted line in Fig. 5.3(b)) are remarkably well described by the analytical expression (up-triangles in Fig. 5.3(b). Second, untangled rings (solid lines in Fig. 5.3(b)) show systematic deviations from the ideal behavior which are especially visible for small and large R_g's. Third, rings with active SC's and permanently catenated rings have, as expected, the same $P(\frac{R_g}{\sqrt{<R_g^2>}})$ (dashed and dot-dashed lines in Fig. 5.3(b)): the curves are consistent with ideal behavior only for large R_g's, while for small R_g's they confirm the non-ideal nature of rings and highlight the incomplete screening of excluded volume at short scales.

Contact probabilities

We investigate the physics of polymer self-interactions, and consider the mean contact probability, $\langle p_c(\ell)\rangle_L$ Eq. (2.16), between pairs of monomers separated by n bonds (equivalent to the mean contour length $\ell = n\langle b\rangle$, see Table 5.1) for rings of total mean contour length $L \equiv N\langle b\rangle$.

In agreement with Ref. [130], finite-chain effects can be reduced and the universal shape of $\langle p_c(\ell)\rangle_L$ in the large-L limit can be demonstrated by plotting the curves for different L's in terms of the variable $\Lambda = \ell(1-\ell/L)$. It is then useful to discuss the scaling behavior of $\langle p_c(\ell)\rangle_L$ by introducing the local exponent:

$$\gamma(\ell) \equiv \frac{d\log\langle p_c(\ell)\rangle_L}{d\log\Lambda}\,. \tag{5.2}$$

Fig. 5.4 shows results for $\langle p_c(\ell)\rangle_L$ (main) and the corresponding $\gamma(\ell)$ (inset) for rings with $N = L/\langle b\rangle = 640$ in the different ensembles. Asymptotically, ideal rings, rings with SC's and permanently catenated rings converge all to the ideal value $\gamma = -\frac{3}{2}$ while untangled rings show $\gamma \simeq -1.2$ consistent with the mean filed prediction : $\gamma = \nu d$ [38] with $\nu \simeq 0.4$ (Fig. 5.3) for these systems. On the contrary, and quite interestingly, the small scale behavior of $\gamma(\ell)$ (see inset in Fig. 5.4 for $\Lambda \lesssim 100$) for rings with SC's is strongly *non ideal*, in agreement with the similarly non ideal behavior seen for the corresponding chain size distributions (Fig. 5.3(b)).

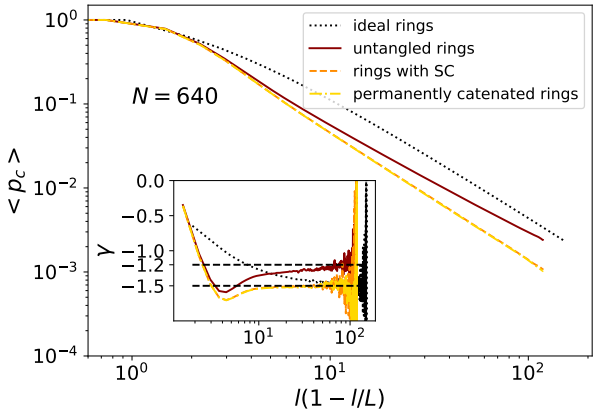

Figure 5.4: Monomer-monomer mean contact probability $\langle p_c(\ell)\rangle_L$ as a function of $\ell(1-\ell/L)$ and for the largest simulated rings ($N \equiv L/\langle b\rangle = 640$) in the different ensembles. We define two monomers to be in contact if their distance is $\leq$ one lattice unit. (Inset) Local scaling exponent $\gamma(\ell)$, defined as the logarithmic derivative of $\langle p_c(\ell)\rangle_L$ (Eq. (5.2)). Dashed horizontal lines correspond to theoretical asymptotic behaviors. Color code / line style are as in Fig. 5.3.

Knot statistics in ring polymers with SC's

Topological constraints in untangled melts make the chains more compact with respect to the ideal case, a situation which is radically altered in the presence of active SC's (Fig. 5.3(a)). SC's act in the same way regardless the two strands are on the same or on different rings (see Sec. 5.2.3): for this reason they change both, single-chain topology by forming *knots* and inter-chain topology by forming *links* (studied in Sec. 5.3.2).

As explained in Chapter 4, knotted curves can be classified based on the number of *irreducible* crossings, K, they present when one tries to smoothly deform the curve so as to force it to lie on a plane. However, as discussed in Chapter 4, a more detailed classification of knots can be carried out by means of suitable *topological invariants*. Here, we employ the so called Alexander polynomial of knots discussed in Sec. 4.2. In particular, we have used the open package KymoKnot [153] to detect and classify the knots which form in our polymer chains through SC. Then, for simplicity, we have used the sole number of irreducible crossings, K, for knot classification. An example of a model ring conformation entrapping a trefoil knot is given in Fig. 5.5(a).

Fig. 5.5(b) shows the probability, $P(N;K)$, that N-monomer rings have given knot type $K = 0$ (the unknot), $K = 3$ (the trefoil, *i.e.* the simplest non trivial knot) and so on for knots of increasing complexity. Knots of complex shapes are in general rare (the trefoil dominates), yet their frequency increases [77, 151] steadily with N and for $N = 640$ we are even able to

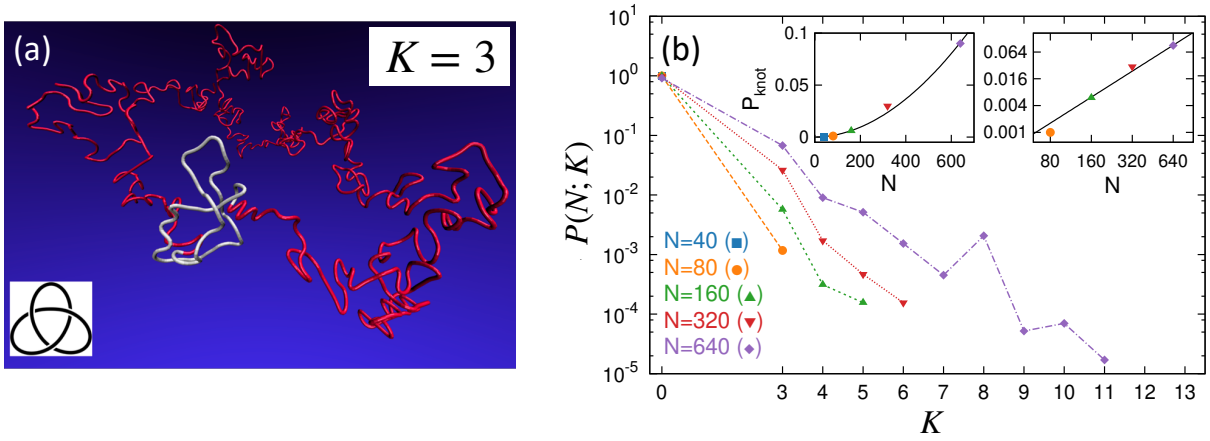

Figure 5.5: (a) Model conformation of a ring polymer (in red) entrapping a trefoil ($K = 3$) knot (highlighted in white). (b) Probability distribution function, $P(N;K)$, of knots with K crossings in N-monomer rings (different symbols and line styles correspond to different N's) undergoing continuous SC's. Rings with $N = 40$ do not knot during the simulation. The two insets show plots (in lin-lin (left) and log-log (right) representations) of the knotting probability $P_{\rm knot}$, Eq. (5.3), as a function of N (symbols) and the corresponding best fit to power-law behavior (line, Eq. (5.4) with Eqs. (5.5) and (5.6)).

detect a few, and quite complex, knotted structures up to 11 crossings.

Then we consider the cumulative knotting probability, defined as

$$P_{\rm knot}(N) \equiv \sum_{\rm K=3,4,...} P(N;K) = 1 - P(N;K=0)\,. \tag{5.3}$$

In [82], Lang and coworkers showed that for catenated N-monomer rings in solution $P(N;{\rm kt} = 0_1) \simeq \exp(-N/N_0)$, where N_0 is some characteristic (and model dependent [165]) polymer length scale. The exponential character of $P(N;K=0)$ matches the known mathematical result [77, 165] that the probability of the unknot in *ideal*, closed lattice polygons decays exponentially with the chain contour length, and it implies that $P_{\rm knot}(N)$ has a *concave* shape when displayed in a lin-lin plot. Our data for $P_{\rm knot}(N)$ do not seem to reflect this behavior, they are better described instead by the simple power law (see symbols *vs.* line in the l.h.s. inset (lin-lin plot) and r.h.s inset (log-log plot) of Fig. 5.5(b)):

$$P_{\rm knot}(N) = \left(\frac{N}{N_{\rm knot}}\right)^{\alpha_{\rm knot}}\,, \tag{5.4}$$

with[5]

$$N_{\rm knot} = 2203 \pm 433\,, \tag{5.5}$$

$$\alpha_{\rm knot} = 1.9 \pm 0.2\,. \tag{5.6}$$

Of course it is possible that the quadratic behavior, Eqs. (5.4) and (5.6), is just a cross-over to the "$\sim 1-\exp(-N/N_0)$" behavior and that we can not detect the latter because polymers of higher N's need to be considered. Yet, it is interesting to notice that the value $\alpha_{\rm knot} \approx 2$ (Eq. (5.6)) has a simple interpretation: it mirrors the enforced mechanism where knots form "cooperatively" due to random SC's between pairs of polymer strands.

In conclusion, to assess the validity of Eq. (5.4) systematic (and computationally much more expensive) simulations of polymers of higher N's need to be done: in particular, since $P_{\rm knot}(N) \to 1$ for large N, we expect rings with $N \gtrsim N_{\rm knot}$ to be always knotted on average.

5.3.2 Structure and dynamics of ring polymers with SC's

Physical links

The physical links between any given pair of rings have been quantified in terms of the corresponding *Gauss linking number* defined in Eq. (4.3), GLN. In particular, we employ the efficient algorithm by Klenin and Langowski [155] for the evaluation of Eq. (4.3) (see Sec. 4.3). We recall that physically GLN represents the number of times (with "+" or "−" sign, depending on the reciprocal orientations of the curves) that each curve winds around the other. An example of a pair of linked rings (with $\mathrm{GLN} = 1$) is given in Fig. 5.6(a).

First, we compute the probability to find a pair of rings with given $|\mathrm{GLN}|$, $P(N;|\mathrm{GLN}|)$, as a function of the polymer length N. Here, we focus just on $|\mathrm{GLN}|$, because $P(N;\mathrm{GLN})$ is symmetric around $\mathrm{GLN} = 0$ (see Fig. A.1 in Appendix A). Results are plotted in Fig. 5.6(b). We find[6] that for $|\mathrm{GLN}| \geq 1$, $P(N;\mathrm{GLN})$ follows the exponential decay:

$$P(N;\mathrm{GLN}) \sim e^{-|\mathrm{GLN}|/\mathrm{GLN}_0(N)}\,. \tag{5.7}$$

The "decay length" $\mathrm{GLN}_0(N)$ as a function of N (for the specific values, see Table A.3 in Appendix A) is well described by the power law behavior (see symbols *vs.* line in the l.h.s inset

[5]Here, mean values and corresponding error bars for $N_{\rm knot}$ and $\alpha_{\rm knot}$ are calculated by averaging distinct estimates of these parameters. These estimates were obtained by separate best fits of the data to Eq. (5.4) in the linear-linear and log-log representations. The same procedure was used for $N_{\rm link}$ and $\alpha_{\rm link}$ (Eq. (5.8)).

[6]Notice that since GLN has been computed between all possible ring pairs. For this reason, the value for $P(N;\mathrm{GLN}=0)$ does depend on the total number of chains in the sample (in an infinite system, there is an infinite number of unlinked chains). Conversely, two chains are linked only if they are spatially close to each other and so each value $P(N;\mathrm{GLN}\geq 1)$ is expected to correspond to "bulk" properties.

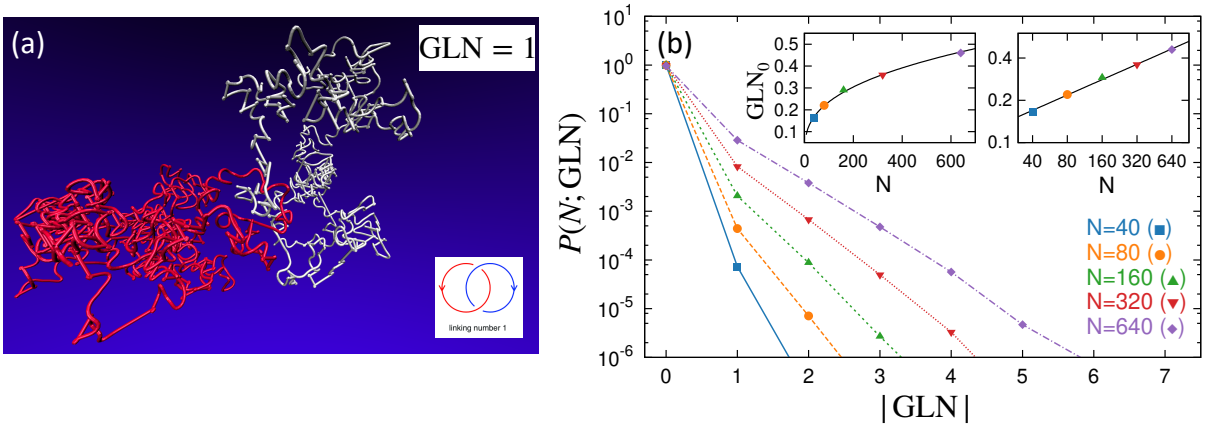

Figure 5.6: (a) Pair of model ring conformations connected by a link with Gauss linking number (Eq. (4.3)) $\mathrm{GLN} = 1$. (b) Probability distribution function, $P(N;|\mathrm{GLN})$, of the absolute value, $|\mathrm{GLN}|$, of the Gauss linking number between pairs of N-monomer rings. The two insets show plots (in lin-lin (left) and log-log (right) representations) of the decay length GLN_0 *vs.* N (symbols, Eq. (5.7)) and best fit to power-law behavior (line, Eq. (5.8) with Eqs. (5.9) and (5.10)). Color code, line styles and symbols are as in Fig. 5.5(b).

(lin-lin plot) and r.h.s. inset (log-log plot) of Fig. 5.6(b)):

$$\mathrm{GLN}_0(N) = \left(\frac{N}{N_{\mathrm{link}}}\right)^{\alpha_{\mathrm{link}}} , \tag{5.8}$$

with

$$N_{\mathrm{link}} = 5277 \pm 239 , \tag{5.9}$$

$$\alpha_{\mathrm{link}} = 0.363 \pm 0.005 . \tag{5.10}$$

The reported value for α_{link}, close to the scaling exponent ν of the gyration radius of the ring (Fig. 5.3(a)), is consistent with the intuitive picture that two rings link to each other if the spatial distance between the corresponding centers of mass is of the order or smaller than $R_g(N) \sim N^{\nu}$ (Eq. (5.1)). Since $\mathrm{GLN}_0(N \approx N_{\mathrm{link}}) \approx 1$, N_{link} is intuitively close to the polymer length scale N^* described in Ref. [82] which physically marks the crossover to the regime in which any ring is concatenated with all the overlapping rings. Although the polymer model adopted here and the one by Lang *et al.* are not the same and a quantitative comparison is difficult, our N_{link} (Eq. (5.9)) and Lang *et al.*'s N^* [82] are similarly large, in particular of the order of a few thousands bonds.

By using the results on the Gauss linking number, we consider (i) the *mean number of chains linking to a single ring*, $\langle \mathcal{L}(N) \rangle$, and (ii) the mean ring fraction, $\langle M_{\mathrm{cc}}(N) \rangle / M$, belonging to the largest *connected component* of chains in the melt. The results are shown

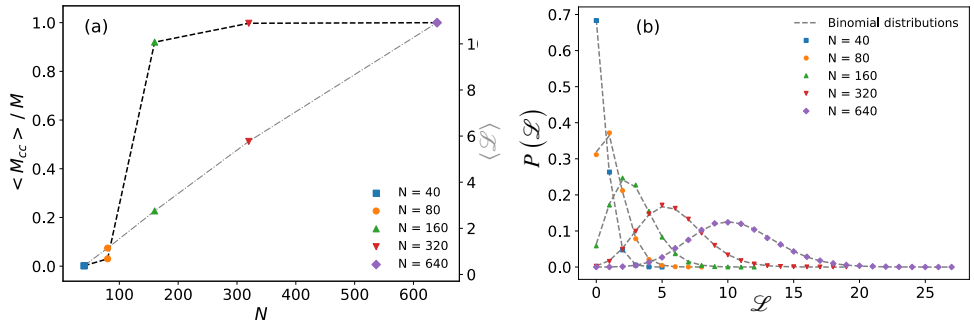

Figure 5.7: (a) Mean ring fraction in the largest *connected component*, $\langle M_{\rm cc}(N)\rangle/M$ (black line, left y-axis), and mean *linking degree*, $\langle \mathcal{L}(N)\rangle$ (grey line, right y-axis) as a function of N. (b) Frequency of observing a ring linking to, respectively, $\mathcal{L} = 0, 1, ..., M-1$ other rings (symbols) in comparison to the binomial function (lines, Eq. (5.11)) for random graphs. Color code and symbols are as in Fig. 5.5(b).

in Fig. 5.7(a). $\langle \mathcal{L}(N)\rangle$ increases linearly [82] with N and the largest (≈ 10) attained value is consistent with the characteristic number of $10-20$ chains [55, 59] protruding the volume occupied by a single ring in melt. We see that for $\langle \mathcal{L}(N)\rangle \gtrsim 2$, *i.e.* when one ring is connected on average to two (or more) other rings, a single giant network is obtained (see also Fig.A.2 in Appendix A for instantaneous snapshots of the networks for different N's).

It is interesting to notice that, in agreement with previous studies [81, 85], the network of connections has the structure of a *random graph*, hence the frequency of observing a ring linking to, respectively, $\mathcal{L} = 0, 1, ..., M-1$ other rings is accurately described (symbols *vs.* lines in Fig. 5.7(b)) by the binomial function:

$$P(M, p_{\rm link}; \mathcal{L}) = \binom{M-1}{\mathcal{L}} p_{\rm link}^{\mathcal{L}} \left(1 - p_{\rm link}\right)^{M-1-\mathcal{L}}. \tag{5.11}$$

Eq. (5.11) is equivalent to the probability that a single node in a random graph made of M nodes is connected to $\mathcal{L}$ other nodes, with $p_{\rm link}(N) = \langle \mathcal{L}(N)\rangle/(M-1)$ (see values in Table A.3 in Appendix A) representing the *linking probability* or the fraction of distinct node-to-node links out of the $M(M-1)/2$ total possible combinations. As in [81], the onset of a single fully connected polymer network can be then interpreted as the *percolation transition* on the graph, signifying that on average each node can be reached from any other node by walking on the graph.

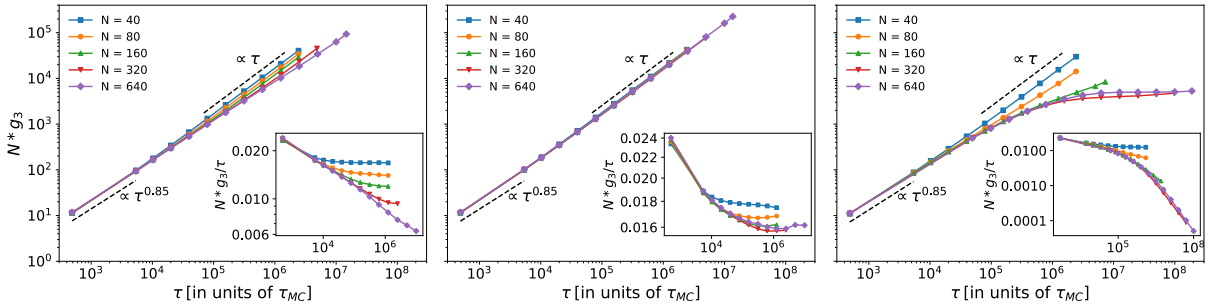

Figure 5.8: Time mean-square displacement, $g_3(\tau)$, of the center of mass of N-monomer rings in melt. (a) Melts of untangled rings. (b) Melts of rings in the presence of SC's. (c) Melts of permanently catenated rings. The insets display $Ng_3(\tau)/\tau$ as a function of τ. Curves of different colors and with different symbols (color code and symbols are as in Fig. 5.5(b)) are for different N's (see legends).

Single chain and network dynamics

We analyze first polymer dynamics in the different ensembles. To this purpose, as in the previous chapter, we consider the mean-square displacement of the centre of mass of the chain (Eq. (2.18)), g_3, as a function of time τ. Unconstrained motion implies that $g_3(\tau) \propto \tau/N$ in the long-time regime. Fig. 5.8(a) shows that this is not the case for untangled rings, in agreement with the original simulations by Schram and Barkema [112]. Conversely, introducing SC's into the system (Fig. 5.8(b)) removes the constraints and accelerates the dynamics to the extent that $g_3(\tau)$ is now proportional to $1/N$ (Fig. 5.8(b)). Then, by the right amount of SC's, it is possible to "fluidize" [93] the entanglements induced by the presence of uncrossable strands and in this way to enhance the dynamics of the polymer system.

In agreement with that, by again turning off the SC activity and then "quenching" the topology, polymer dynamics slows down dramatically (Fig. 5.8(c)) up to the complete arrest (evident in the saturation of $g_3(\tau)$ at large times). Slow-down for $N = 40$ and $N = 80$ is due to the the fact that rings have linked into multi-chain structures (Fig.A.2(a, b) and Fig.A.3(a, b) in Appendix A) which tend to move slower. Starting from $N = 160$ (Fig.A.2(c, d, e) and Fig.A.3(c, d, e) in Appendix A) rings are locked together into a single, giant structure and, therefore, unable to perform large scale diffusion, hence the reported saturation. This effect confirms experimental reports [93] of a rubber-like plateau in the storage modulus of TopoII-inactivated solutions of catenated DNA rings. Accordingly, the relative motion displayed by rings with $N = 160$ (line with "▲" symbols, Fig. 5.8(c)) is the consequence of the fact that a non negligible amount of unconcatenated rings is still undergoing random diffusion (see Fig.A.2(c) and Fig.A.3(c) in Appendix A). Notice that these dynamic effects appear on time

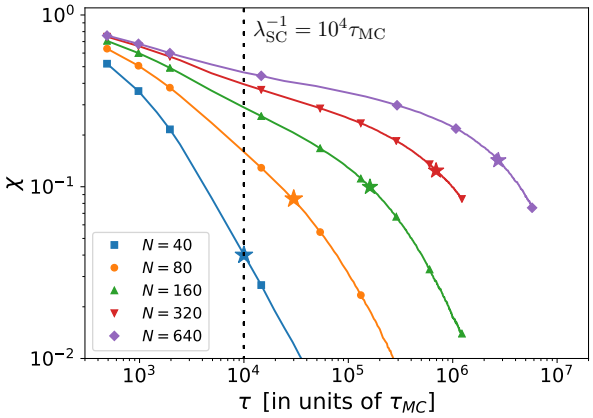

Figure 5.9: Time auto-correlation function $\chi(\tau)$ for two rings remaining linked on time scale $= \tau$ in the presence of SC's (Eq. (5.12)). The vertical dotted line corresponds to the time scale $\lambda_{SC}^{-1} = 10^4 \tau_{MC}$ for SC. The "$\star$'s" mark the positions of the polymer self-diffusion times $\tau_d(N)$ (see Table A.1 in Appendix A). Color code and symbols are as in Fig. 5.5(b).

scales larger than the imposed (Sec. 5.2.1) time scale $\lambda_{SC}^{-1} = 10^4 \tau_{MC}$ for SC's: on time scales $\tau \lesssim \lambda_{SC}^{-1}$, the three ensembles show the same subdiffusive behavior $\sim \tau^{0.85}$ characteristic [112] of untangled rings.

To complement the analysis on ring dynamics (Fig. 5.8) in the presence of active SC's, we characterize now the interplay between ring motion and the "fluidization" [93] process induced by the SC mechanism from the point of view of the formed polymer network. To this purpose, we introduce the characteristic function $C_{ij}^{\rm link}(t) = 1/0$ between the pair of rings i and j being linked/unlinked at time t, and calculate the corresponding time auto-correlation function:

$$\chi(\tau) \equiv \frac{\langle C_{ij}^{\rm link}(t+\tau)\, C_{ij}^{\rm link}(t)\rangle}{\langle C_{ij}^{\rm link}(t)^2\rangle}\,, \tag{5.12}$$

where the average is taken over all possible pairs i and j.

The results for rings made of N monomers are shown in Fig. 5.9. Qualitatively, we identify three regimes: (i) Below the SC time scale $\lambda_{SC}^{-1} = 10^4 \tau_{MC}$, $\chi(\tau)$ displays power law decay. (ii) This is followed by a second regime which, by increasing N, becomes slower than the first one and attains a quasi-plateau. Intuitively, this is due to the fact that on such time scales both linking and unlinking events may happen, while at times $\tau < \lambda_{SC}^{-1}$ we expect on average only a single unlinking event. (iii) Finally, on time scales larger than the ring self-diffusion time $\tau_d(N)$ (corresponding to the time scale for the polymer to spread over a distance the size of its own mean gyration radius, $g_3(\tau_d(N)) \equiv \langle R_g^2(N)\rangle$, see Table A.1 in Appendix A), the two rings occupy, on average, distinct regions in space and $\chi(\tau)$ decays as an exponential. The "persistent" regime (ii) valid for long chains is particularly noteworthy, because it suggests

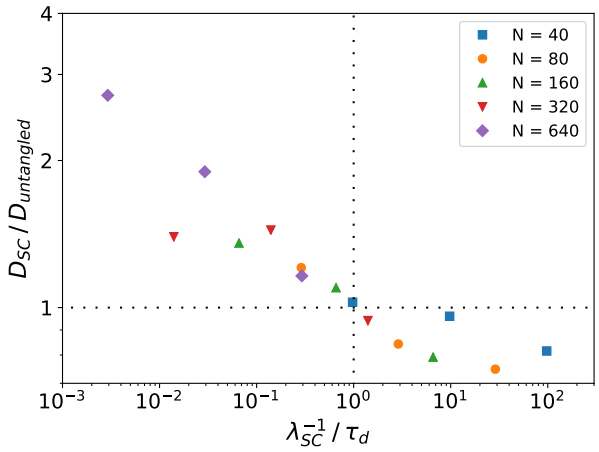

Figure 5.10: Asymptotic diffusion coefficient of rings with active SC's normalized to the corresponding values in untangled melts as a function of the inverse of the SC rate, $\lambda_{\rm SC}^{-1} / \tau_d(N)$, normalized to the ring self-diffusion time in untangled melts (see Table A.1 in Appendix A). Color code and symbols are as in Fig. 5.5(b).

that with SC's at work rings coalesce into a "dynamic" gel-like structure.

5.4 Discussion

Our melts of rings with active SC's form transient networks (Fig. 5.9) which, in spite of the non negligible amount of introduced linking (Fig. 5.6), move faster than in the untangled case (Fig. 5.8, panel (a) vs. panel (b)). Physically this happens because SC's operate at a reasonably fast rate ($\lambda_{\rm SC}^{-1} = 10^4\,\tau_{\rm MC}$, see Sec. 5.2.1), guaranteeing rapid linking/unlinking events which maintain rings only "loosely" entangled with each other.

By the same argument one may imagine that, by opportunely slowing down the SC rate $\lambda_{\rm SC}$, it ought to be possible to create systems of interlocked rings where topologically constraints are temporary yet long-lived [166]: as a consequence, now chain dynamics is expected to be *slower* than in untangled melts [7]. Intuitively this situation can be realized by choosing $\lambda_{\rm SC}^{-1}$ to be of the same order or larger than the self-diffusion time τ_d of rings in untangled melts since, supposedly, during this time scale a single polymer has interacted with the chains to which it is effectively able to link.

To validate this idea, which may be also tested experimentally, for instance by resorting to DNA rings [93], we performed new simulations for the same melts of rings but with the two

[7] Notice that since, in the absence of the SC mechanism, rings must follow untangled dynamics, this is equivalent to say rings diffusivities display non-monotonous behavior as a function of $\lambda_{\rm SC}$.

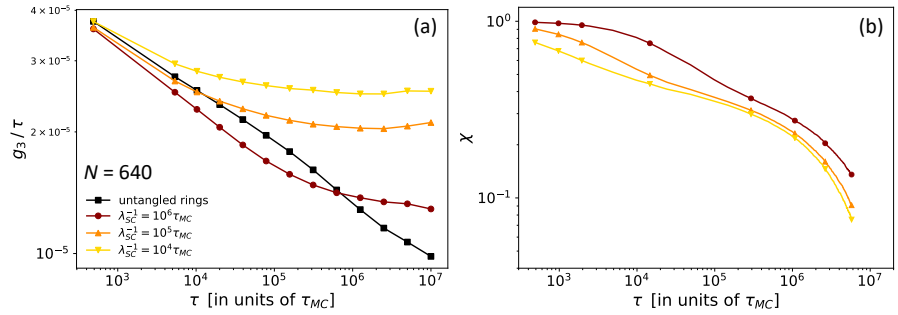

Figure 5.11: (a) $g_3(\tau)/\tau$: time mean-square displacement of the centre of mass of rings with $N = 640$ monomers normalized to time τ. (b) $\chi(\tau)$: time correlation function for two rings remaining linked on time span τ in the presence of SC's (Eq. (5.12)). Different colors and symbols are for different SC rates $\lambda_{\rm SC}$ (see legend).

different rates $\lambda_{\rm SC}^{-1} = 10^5\,\tau_{\rm MC}$ and $\lambda_{\rm SC}^{-1} = 10^6\,\tau_{\rm MC}$, *i.e.*, ten and one hundred times slower than the previous one. We have then estimated the asymptotic diffusion coefficients of the rings, $D_{\rm SC}$, by best fits of the terminal behaviors of the corresponding mean-square displacements, $g_3(\tau)/\tau$ (see Fig.A.5 in Appendix A), normalized to time τ.

The results (normalized to the corresponding values for untangled melts, $D_{\rm untangled}$) *vs.* the inverse of the SC rate, $\lambda_{\rm SC}^{-1}\,/\,\tau_d(N)$, normalized to the polymer self-diffusion times in untangled melts are shown in Fig. 5.10. The plots confirm our expectations: slow SC rates result in melts with slower relaxation dynamics compared to the untangled case. Notice that while the precise value of the SC rate affects the dynamics of the melt, static quantities like the gyration radius of the ring or the Gauss linking number (see, respectively, Figs.A.5 and A.6 in Appendix A) do not change for the different set-up's.

It is also worth noticing that, even in those cases where SC accelerates the asymptotic chain dynamics w.r.t. the untangled case, detailed analysis of $g_3(\tau)/\tau$ shows a regime where the action of SC's makes the rings temporarily slower (Fig. 5.11(a), the "$\lambda_{\rm SC}^{-1} = 10^6\tau_{\rm MC}$"-curve *vs.* the untangled case for $N = 640$ and on time scales $\tau/\tau_{\rm MC} \lesssim 10^5$). On the same time scales, the time auto-correlation function $\chi(\tau)$ for link dynamics (Eq. (5.12), see corresponding lines in Fig. 5.11(b)) becomes increasingly slower with $\lambda_{\rm SC}^{-1}$, demonstrating that the observed polymer slow down compared to the untangled case is the consequence of persistent links between rings.

5.5 Conclusions

In this chapter, we have presented part of my PhD work, which was primarily motivated by recent experiments [93] employing the enzyme TopoII to induce "fluidization" of the topological constraints arising in entangled solutions of DNA rings. To this end, we have developed of a new dynamic Monte Carlo computational scheme for polymer chains which takes explicitly into account the action of the enzyme by controlling the rate at which two nearby polymer strands are able to cross through each other. Interestingly, the strand-crossing scheme, as developed here, has been applied recently in [117] to model chromatin organization in cell nuclei.

In this chapter, after the detailed description of the model, we have presented its first application to ring polymers made of N monomers and in melt conditions, and we discuss how the strand crossing mechanism influences both the static and the dynamic properties of the chains.

At stationary conditions ring polymers swell with respect to the untangled (*i.e.*, unknotted and unconcatenated) case and stay non-ideal (Fig. 5.3). On the other hand, they tend to become increasingly knotted (Fig. 5.5) and to form a macroscopic network of linked chains (Fig. 5.6 and Fig. 5.7).

On the dynamics side, we show (Fig. 5.8) that the ability to produce strand crossings make polymers faster and that large rings tend to "glue" together into a permanent gel as soon as crossings are not let anymore. Yet an acceleration of the dynamics is not true *in general*, but only when the rate for strand crossings is fast enough. In the opposite case the dynamics of the melt may be even slower than the untangled case (Fig. 5.10), a prediction which might be tested by using, again, DNA rings in the presence of TopoII.

We conclude on a technical remark. Notice that the model presented here is for flexible chains (Sec. 3.2.3) while polymers in general, and DNA in particular [167], are typically semi-flexible *i.e.* locally stiff [5]. In the next chapter, we will discuss on how the bending penalty term, under the form of eq.(2.6) can change the properties of the polymer network.

Chapter 6

Topology and entanglement in dense polymer systems

In this chapter[1], we investigate the microscopic nature of the entanglement in dense polymer systems. We prove in particular, that entanglements in polymer systems arise from the topological interactions between polymers under the form of knots and links. One of our key contributions is establishing a precise relationship between the entanglement length, N_e, the phenomenological parameter at the basis of the *tube model* by Edwards (see Sec. 1.2.2), and the overall topology of the polymer melt. Interestingly, our findings reveal that the entanglement properties of the system can be accurately captured by considering 2-chain links exclusively.

The chapter is structured as the following: in Sec. 6.1 we introduce and frame the interest of the problem. In Sec. 6.2 we present the details of the simulated polymer systems and we explain the shrinking algorithm developed for the calculation of the ring minimal path coupled to the topological characterization of the systems and finally we illustrate the idea behind the Z1-algorithm used for the calculation of the entanglement length. In Sec. 6.3 we present the main results of our work, while in Sec. 6.4 we provide some discussion and conclusions regarding the fundamental connection between knots, 2-chain and 3-chain links and the entanglement length of the polymers. Additional figures have been included in the Appendix B.

[1]The material described in this Chapter has been published in: Ubertini & Rosa, Macromolecules (2023) [3]

6.1 Introduction

As already discussed in the first chapter, the viscoelastic behavior of concentrated solutions or melts of *linear* polymer chains can be understood assuming [5, 14, 98] slow reptative flow of each chain through the network of topological obstacles (entanglements) formed by the surrounding chains. According to this picture, entanglements confine each chain within an effective tube-like region of diameter $d_T \approx \langle b \rangle \, n_K \sqrt{N_e/n_K}$ where $\langle b \rangle$ is the mean bond length, n_K is the Kuhn length of the polymers (in monomer units [2]) accounting for the fiber stiffness while the *topological* entanglement length N_e is the characteristic, material-dependent [168–170], length scale marking the crossover from *non-entangled* to *entangled* polymer behavior. Then, the mean size or gyration radius $\langle R_g \rangle$ of polymer chains with contour length $N \gtrsim N_e$ follows the power-law behavior

$$\langle R_g \rangle \sim d_T \left(\frac{N}{N_e} \right)^{1/2} \sim \langle b \rangle \, n_K \left(\frac{N}{n_K} \right)^{1/2} , \tag{6.1}$$

and all the essential structural and dynamical information on the melt can be understood in terms of the single parameter N_e. As discussed in Sec. 1.2.2, estimating N_e is a challenging problem [25, 168, 171], although considerable progress has been made (at least in numerical simulations) in terms of *primitive path analysis* [20, 27, 28, 30] (PPA).

Alternatively, polymeric entanglements may be also modeled as *physical links* between chains [13, 15–22]. Specifically, the idea is "to map" the system of entangled chains to an equivalent one of randomly entangled (namely, self-knotted and linked) ring polymers and employ suitable *topological invariants* [143] in order to identify and then classify – in a mathematically rigorous manner! – the total amount of entanglements of the melt and connect them to the macroscopic viscoelastic behavior.

The connection between the two pictures is, however, not that straightforward: mainly, the reason is that the complete statistical-mechanical classification of a polymer melt would require an *infinite set* [16, 18] of topological invariants in terms of pairs, triples, etc... of loops. At the same time, efforts have been put towards the development of analytical theories [32] which turned out to be mathematically hard, involving the mapping of the polymer systems into complex field theories. Unfortunately this approach has demonstrated feasibility only for two polymers systems.

Motivated by these considerations, in this chapter we rethink the problem of characterizing a melt of entangled polymer chains in terms of topological invariants and outline, in a quanti-

[2] In this chapter, polymer contours are measured in monomer units and termed (for compactness and with abuse of language) "lengths": so, n_K and N_e are, respectively, the Kuhn and the entanglement length of the polymer. Conversion to "true" length is obtained by multiplying for the mean bond length $\langle b \rangle$

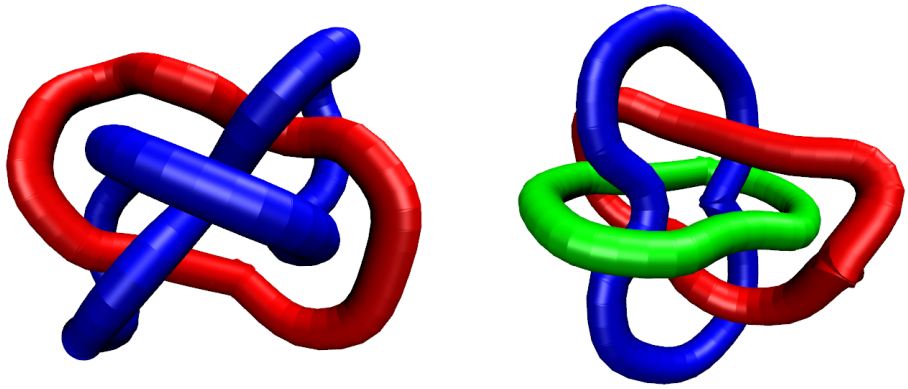

Figure 6.1: Examples of ring polymer structures with Gauss linking number (GLN, see Eq. (4.3)) equal to 0. (a) Two rings intertwined in the Whitehead link 5_1^2. (b) Three rings clustered into the Borromean conformation 6_2^3. Both conformations have been extracted from numerical simulations of ring polymer melts after the minimization procedure described in Sec. 6.2.2. To name the conformations here and in the rest of the text, we have used the classical nomenclature introduced in Rolfsen's book (see Secs. 4.1 and 6.2.3).

tative manner, the connection between the latter and the topological entanglement length of the chains. More specifically, we perform extensive computer simulations of *randomly knotted* and *randomly concatenated* ring polymers at dense conditions and different values of the bending stiffness of the polymer fiber as models for entangled polymer systems.

Then, we get inspiration by PPA and by the recent work of Bobbili and Milner [22], where melts of randomly linked and knotted ring polymers were simulated and then, trough a "shrinking" algorithm, the instantaneous primitive paths of the polymer rings were visualized and entanglement properties of the systems were studied. Similarly, we construct an algorithm for *contracting* on lattice the contour length of each ring in the melt to its "primitive" or "minimal" length which does not violate the topological constraints with the other rings. The conformational properties of the primitive ring structures are thus explored at the single-ring level (knots), between any rings' pair (see the Whitehead link in Fig. 6.1 (a)) and between any rings' triplet (see the complex Borromean configuration in Fig. 6.1 (b)). By looking at the relative abundance of these topological structures as a function of the bending stiffness of the polymers, we combine them into a proxy for the quantitative prediction of the number of entanglement lengths, N/N_e, of the polymers.

$\kappa_{\rm bend}/(k_BT)$	$\langle b\rangle/a$	$\langle\cos\theta\rangle$	n_K
0	0.733	0.186	1.965
1	0.695	0.455	3.157
2	0.663	0.638	5.118

Table 6.1: Values of physical parameters for the ring polymer melts investigated in this paper. a is the unit distance of the fcc lattice and the monomer number per unit volume is $= \frac{5}{4}\sqrt{2}a^{-3}$, as in Chapter 3. (i) $\kappa_{\rm bend}$, bending stiffness parameter in stat. mech. thermal units k_BT, where k_B is the Boltzmann constant and T is the temperature; (ii) $\langle b\rangle$, mean bond length; (iii) $\langle\cos\theta\rangle$, mean cosine value between two consecutive bonds along the chain; (iv) n_K, Kuhn length.

6.2 Model and methods

6.2.1 Polymer model

Model systems of M *randomly knotted* and *concatenated* ring polymers of N monomers each were prepared based on the kinetic Monte Carlo (kMC) algorithm illustrated in Sec. 2.1.2 complemented with the strand-crossing moves introduced in Chapter 5. Ring conformations were equilibrated through long runs at the average monomer number per lattice site $= \frac{5}{4} = 1.25$ or unit volume $= \frac{5}{4}\sqrt{2}a^{-3}$ corresponding to melt conditions (the same of Chapter 3). As in Chapter 3, we module the Kuhn segment n_K through the bending penalty Hamiltonian $\mathcal{H} = -\kappa_{\rm bend}\sum_i^{N\langle b\rangle/a}\cos\theta_i$, consequently chains become locally stiffer with $\kappa_{\rm bend}$. Table 6.1 summarizes (i) the mean bond length $\langle b\rangle$, (ii) the mean cosine value $\langle\cos\theta\rangle$ between two consecutive bonds along the chain[3], (iii) the Kuhn length n_K, as a function of[4] $\kappa_{\rm bend}$.

The simulation box of linear size $L_{\rm box}$ has periodic boundaries for the enforcement of bulky melt conditions. By fixing the *total* number of monomers to the convenient value $= 134,400$, we have that $L_{\rm box}/a = 30\sqrt{2}$. In this paper, we have studied polymer melts with $N \times M = (40\times 3360, 80\times 1680, 160\times 840, 320\times 420, 640\times 210)$.

As in Chapter 5, we introduce random strand crossing between nearby polymer strands at the fixed rate of one per 10^4 kMC elementary steps. In this way, we induce the violation of the

[3]The values for $\langle b\rangle$ and $\langle\cos\theta\rangle$ (see Tab. 6.1) are in excellent agreement with the ones for melts of unknotted and non-concatenated rings studied in Chapter 3 (see Table 3.1). The local properties of the polymer fiber are hence not affected by the different topological states of the chains.

[4]The values in Tab. 6.1 for n_K are extracted from corresponding dynamic simulations of *linear* polymers, see Chapter 3 for details.

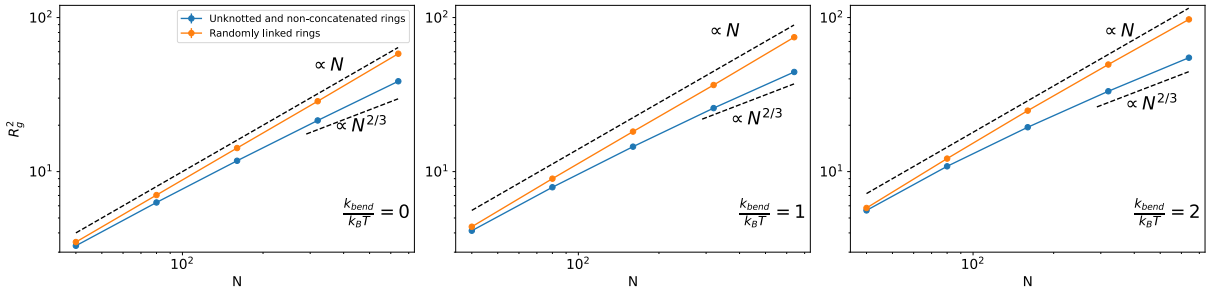

Figure 6.2: Mean-square gyration radius $\langle R_g^2 \rangle$ for melts of unknotted and non-concatenated rings (data from Chapter 3) and randomly linked rings as a function of the total number of monomers per ring, N. Panels from left to right are for bending stiffnesses $\kappa_{\rm bend}/(k_BT) = 0, 1, 2$ (see label).

topological constraints and obtain equilibrated melts of rings with intra-chain (*i.e.*, knots) and inter-chain (*i.e.*, links) non-trivial and randomly-generated topologies. By construction then, the algorithm generates rings with *annealed* topologies, in other words our ring conformations represent a thermodynamic ensemble of melts of randomly knotted and concatenated rings at the given density for different polymer lengths N and bending rigidities $\kappa_{\rm bend}$.

As for the other Chapters, to ensure proper system equilibration as well as accurate polymer statistics, we wait for the systems to reach the plateaus in the single monomer mean square displacement in the reference frame of the centre of mass (Eq. (2.19)), g_2. Accordingly, the time scale to reach the corresponding plateau corresponds to the portion of the trajectory that has been discarded from the computation of the relative observables (see Fig. B.1 in Appendix B). The total computational cost of the simulations goes from $2 \times 10^6 \tau_{\rm MC}$ for $N = 40$ and $\kappa_{\rm bend}/(k_BT) = 0$ to $7 \times 10^7 \tau_{\rm MC}$ for $N = 640$ and $\kappa_{\rm bend}/(k_BT) = 2$. As in the previous chapters, here, $\tau_{\rm MC}$, the MC "time" unit, is equal to $N \times M$ kMC elementary steps.

Violation of topological constraints by random strand crossing induces a massive reorganization of the statistics of polymer chains. As studied in Chapter 5, while unknotted and non-concatenated rings remain compact with asymptotic mean gyration radius following the power-law

$$\langle R_g \rangle \sim N^{1/3} ,$$

randomly knotted and randomly linked melt of rings swell as

$$\langle R_g \rangle \sim N^{1/2} ,$$

i.e., locally they become equivalent to melts of linear chains (see Eq. (6.1) and Fig. 6.2). Furthermore, the distinctive anti-correlation of the bond-vector correlation function (see Eq. (2.15)),

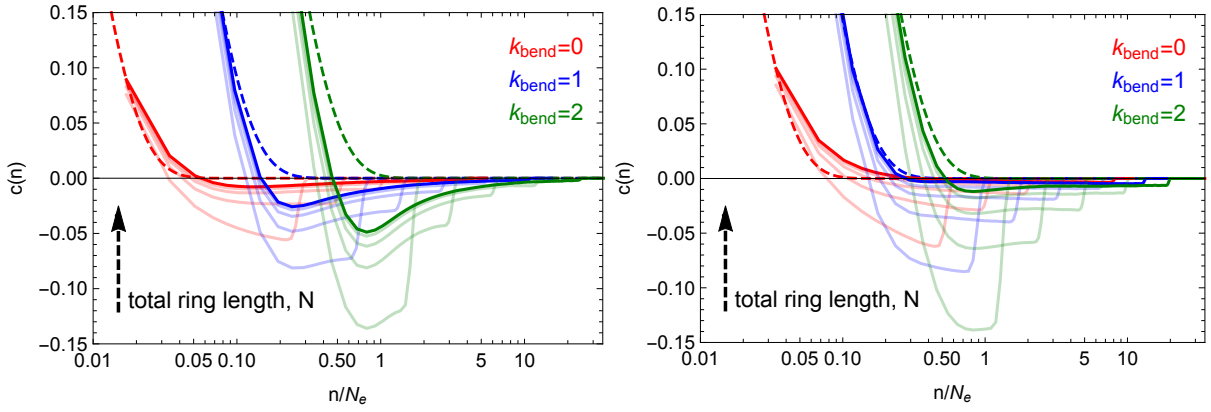

Figure 6.3: Bond-vector correlation function $c(n)$ (see Eq. (2.15)) as a function of the effective monomer length, n/N_e, normalized with respect to the entanglement length N_e. The l.h.s. panel corresponds to melts of unknotted and non-concatenated rings (data from Chapter 3). R.h.s. panel corresponds to randomly linked rings studied in this chapter. Lines of equal color are for the same chain stiffness ($\kappa_{\rm bend}$ in units of k_BT, see legend), full colors are for the longest rings ($N = 640$), while lines in fainter colors are for chains of shorter contour lengths (see arrow's direction). The long-dashed lines correspond to the exponential decay typical of linear polymers with local stiffness, *i.e.* $c(n) = \langle \cos\theta \rangle^n$.

$c(n)$, as a function of the effective monomer length separation, n, along the chain reported in melts of unknotted and non-concatenated rings (see Fig. 3.8), disappears in randomly linked systems (see Fig. 6.3), whose behavior is close to the one for linear chains (see dashed lines).

Overall, we may conclude that randomly linked rings reproduce the essential features of entangled linear polymer chains in melt. In the next, we will use these systems to investigate the microscopic nature of entanglements by means of the rigorous language of topological invariants.

6.2.2 Algorithmic pipeline to rings minimal paths

In order to detect and classify topological interactions in equilibrated melts of entangled rings, we introduce a simple "shrinking" algorithm which takes explicit advantage of the presence of stored lengths along the contour length of each chain. Specifically, the algorithm consists in iterating the following steps:

1. We remove away all the stored lengths from the polymers. Of course, this excision process leads to a reduction of the total contour length of each chain. Notice that – by construction – this does not lead to violations of the topological constraints, neither intra-chain ones (such as knots, for instance) nor between different chains (*i.e.*, links).

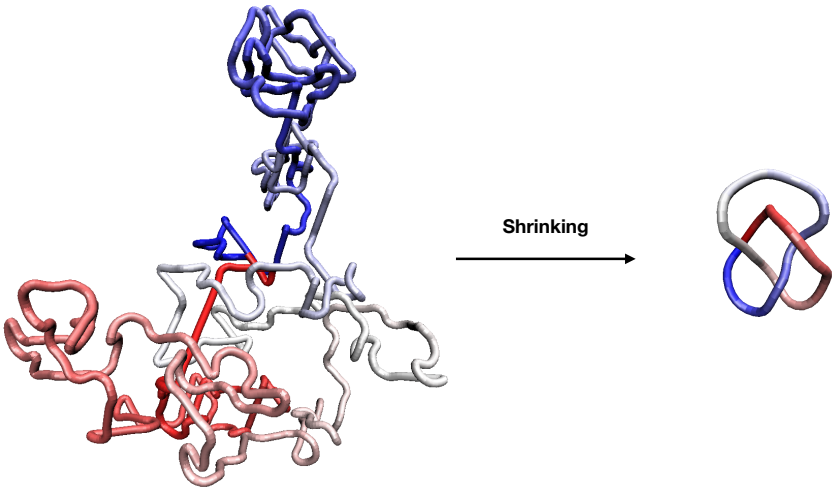

Figure 6.4: Left, knotted conformation of a ring with $N = 640$ monomers before applying the "shrinking" algorithm. Right, correspondent minimized conformation, here, it is clear that the knot corresponds to a trefoil (see Sec. 4.1). The polymers color transitions from blue to red from one chain's end to the other.

2. After the excision, we perform a short MC run (of the order of $10-100\tau_{\mathrm{MC}}$) under global preservation of topological constraints (*i.e.*, without strand crossing). In general, this step leads to formation of new units of stored length which, in turns, will be removed by the next implementation of step (1), and so on.

We apply then these operations, individually, to single chains (Sec. 6.3.1 and see Fig. 6.4), pairs of chains (Sec. 6.3.2) and triplets of chains (Sec. 6.3.3). In all these cases, the procedure stops when the number of monomers of each shrinking chain has not changed for 300 consecutive iterations: in this case, we assume that each chain has reached its *minimal* shape.

To validate the algorithm, we have tested it first on the "trivial" case of unknotted and non-concatenated ring polymers in melt. We have thus verified that shape minimization of rings taken one by one or simultaneous application of the procedure on the whole melt leads to what is expected based on intuition: that individual rings shrink to single points. Then, by our algorithm, we may isolate unknotted and non-concatenated configurations from those with non-trivial topologies.

6.2.3 Classification of knots and links

Following the contour length simplification outlined in Sec. 6.2.2, we have investigated the statistical abundance of the following topological objects: (i) knots in single ring poly-

mers (Sec. 6.3.1); (ii) links between pairs of ring polymers (2-chain topological structures, Sec. 6.3.2); (iii) links between triplets of ring polymers (3-chain topological structures, Sec. 6.3.3). We do not proceed beyond (iii) because, although in principle the procedure can be applied to even larger groups of rings, the factorial growth of possible combinations makes the analysis tediously lengthy from the computational point of view. On the other hand, it will be shown (Sec. 6.3.4) that this is perfectly adequate to capture the entanglement length N_e.

Notation

In referring to a given knot or link we follow the standard Rolfsen convention [149] as explained in the Chapter 4. Namely, a knot or a link is defined by the symbol K_i^p where: K represents the number of irreducible crossings of the knot (or the link), p is the number of rings which takes part in the topological structure (*e.g.*, $p = 2$ for links between two rings) and i is an enumerative index assigned to distinguish topologically inequivalent structures with the same K and p. For knots in single rings $p = 1$ is tacitly assumed and, as an example, the simple trefoil knot is identified by the Rolfsen's symbol 3_1.

Topological invariants

As discussed in Chapter 4, non-trivial knots and links can be detected and hence classified by means of suitable *topological invariants* [78, 143]. In this chapter, we resort to the *Jones polynomials* [172] (see Sec. 4.2) which assign to each knot a distinctive algebraic polynomial. Specifically, we use the implementation of the Jones polynomials featured in the Python package *Topoly* [173] in order to recognize and categorize knots within single ring polymers and, in this way, benchmark the simplification algorithm of Sec. 6.2.2. Moreover, and as for links alone [5], we also consider the simpler Gauss linking number (GLN), introduced in Sec. 4.3 Eq.(4.3): As discussed in Sec. 4.3, while intuitive and easier to compute with respect to the Jones polynomials, the GLN has nonetheless severe limitations [78]. It is in fact widely known that, while $\mathrm{GLN} \neq 0$ means that the two rings are linked, the opposite ($\mathrm{GLN} = 0$)

[5] The shrinking algorithm can be used to isolate structures of linked rings, yet it is easy to realize that some care has to be taken due to the fact that two or more shrinking rings may be stuck in non-trivial shapes either because they are effectively linked or because, although not linked, they are both non-trivially knotted. To remove such a possible ambiguity, we assign two rings a link if the spatial distance between their centers of mass is $< 2R_g$ where R_g is the mean gyration radius of the chain. For 3-ring link detection, this same criterion has been applied to each ring pair in the triplet. We also mention that – and only for the purpose of the detection – before minimization each of the examined structures should be placed at the center of a large box ensuring that no spurious entanglements emerge as a consequence of the periodic boundary conditions introduced in the model.

is not necessarily true. Take for instance the example shown in Fig. 6.1(a), *i.e.* the so called Whitehead link 5_1^2, constituted by two irreducibly linked rings and yet $\mathrm{GLN} = 0$. On top of that, one may imagine even more complex situations such as the one displayed in Fig. 6.1(b) (the so called Borromean conformation 6_2^3) where 3 rings, which are two-by-two non-concatenated, are irreducibly linked: such structures are, obviously, also not detected by Eq. (4.3). In the course of the paper (Sec. 6.3), we will show how these structures (which elude Eq. (4.3)) can be properly detected and, then, how to quantify their impact on the entanglement properties of the melt.

6.2.4 Calculation of the entanglement length

By following the approach by Bobbili and Milner [22] for molecular dynamics simulations of a melt of seemingly shrunk and randomly linked ring polymers, we estimate N_e by applying the recent version (Z1+ [174]) of the Z1-algorithm [28, 175–177]. The Z1-algorithm is based on the same idea of PPA (see Sec. 1.2.2), but differently from PPA, the minimal paths of polymer melts are recovered by the implementation of a series of geometrical operations which transform the entangled polymer chains in a collection of straight segments which are sharply bent at the entanglement points, then one may estimate N_e as the average length of these straight segments. In particular, the Z1+ version takes explicitly into account the role of chain self-entanglements (knots) during the determination of N_e. The effects of it will be discussed in Sec. 6.3.4.

6.3 Results

In the next, we will describe results concerning the appearances of knots (Sec. 6.3.1) and links (Secs. 6.3.2 and 6.3.3) in melts of entangled randomly linked rings of different chain length and bending stiffness. Then (Sec. 6.3.4), we will show how to establish a direct connection between the topology of links and the entanglement length of the chains. While we have considered different chain lengths (Sec. 6.2.1), covering the full crossover from loosely to strongly interpenetrating polymers, for brevity we will present many results only for the most representative and longest chains with $N = 640$.

6.3.1 1-chain topological structures, knots

First, we have applied our algorithm (Sec. 6.2.2) to detect knots in single rings and, to prove its reliability, we have applied the *Topoly* tool (Sec. 6.2.3) to the simplified ring shape

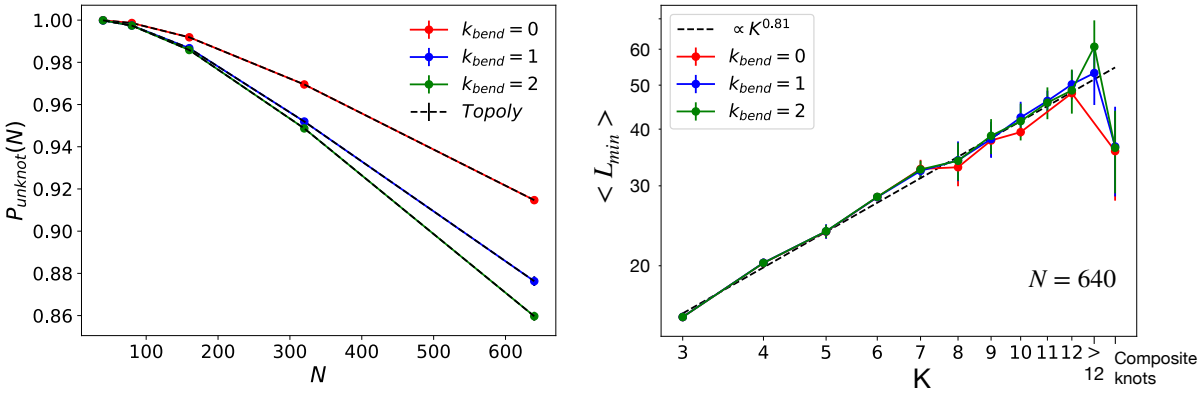

Figure 6.5: (Left) $P_{\rm unknot}$, probability that a ring is unknot as a function of the number of monomers, N, and for different bending stiffness, $\kappa_{\rm bend}$. The shrinking algorithm (solid lines) and *Topoly* (dashed lines) are in perfect agreement. (Right) $\langle L_{\rm min}\rangle$, average minimal contour length of rings with $N = 640$ monomers as a function of the knot crossing number, K, and for different bending stiffness, $\kappa_{\rm bend}$. Each error bar corresponds to the standard deviation calculated for the ring population at the respective crossing number K. The data are well described by the simple power-law behavior $\sim K^{0.81}$ (dashed line). The generic label "> 12" follows from the fact that *Topoly* is unable [173] to recognize properly knots with > 12 crossings.

in order to classify the relative knot type.

As a result, we have always found a non-trivial Jones polynomial in correspondence of those rings which do not shrink to a point, in other words the shrinking algorithm recovers knots successfully and map one-to-one to the results obtained by *Topoly*, see Fig. 6.5 (l.h.s. panel) for the probability $P_{\rm unknot}$ that a ring is unknot as a function of the monomers number N and at different bending stiffness $\kappa_{\rm bend}$.

Overall $P_{\rm unknot}$ is always a decreasing function of the polymer length N, a result in line [178, 179] with other generic polymer models. At the same time, for fixed N, $P_{\rm unknot}$ decreases as a function of $\kappa_{\rm bend}$ or stiffer rings are more likely to form knots with respect to more bendable ones and this difference appears growing with N: this feature seems also quite general having been reported recently in the context of computer simulations of isolated semiflexible ring polymers [180] and for linear polymers in melt [181]. Notice, however, that the probability to observe a knot remains small (for $\kappa_{\rm bend}/(k_BT) = 2$ and $N = 640$, this is only $= 1 - P_{\rm unknot} \approx 14\%$). Again, this is in qualitative accord with [180] although knots here seem slightly more likely in the range of values ($1 - P_{\rm unknot} \lesssim 5\%$ in [180]): arguably, this is the consequence of considering polymers at melt conditions and not isolated chains.

While Jones polynomials (as well as any other topological invariant) inform us on the knot

type "trapped" within the ring, by our shrinking algorithm we may also quantify the "amount" of topological entanglement "stored" within a non-trivial knot in terms of the corresponding "minimal" contour length: in particular, rings hosting "simpler" knots (*i.e.*, low-crossing knots) shrink more and occupy less primitive length in comparison to more complicate knots.

To show this, we have computed the mean value, $\langle L_{\rm min} \rangle$, of the ring minimal contour length as a function of the crossing number K characterizing the hosted knot. In principle the ring minimal contour length is a random quantity because the shrinking procedures goes stochastically, on the other hand we see that the fluctuations are, for each knot type, comparably small (Fig. B.2 in Appendix B), *i.e.* the minimization procedure converges to a well defined minimal shape, which is connected to the "ideal" knot concept developed in [182]. Notably $\langle L_{\rm min} \rangle$ is a genuine topological signature, it is almost insensitive to the bending stiffness $\kappa_{\rm bend}$ (see Fig. 6.5 (r.h.s. panel)) and it grows with the characteristic power-law K^{α} with $\alpha \simeq 0.81$ (dashed line). Interestingly, the same power-law behaviour in relation to the scaling of the minimal rope length required to tie a non-trivial knot into a flexible rope has been reported recently [183]: we conclude then that, for a given knotted ring, our minimization algorithm converges to the corresponding minimal knot structure. Moreover, and again in agreement with [183], we find that the so called *alternating* knots, namely knots where crossings alternate under/over when moving along the filament, display bigger $\langle L_{\rm min} \rangle$ and are less frequently seen (Figs. B.2 and B.3 in Appendix B), respectively, for $K \geq 8$ only [6]) than the *non-alternating* ones for the same number of crossings.

6.3.2 2-chain topological structures, links

After having investigated the amount of knots, we turn our attention to the topological interactions between *pairs* of rings.

To this purpose, we have devised the following way to distinguish between those links which have Gauss linking number (Eq. (4.3)) $\mathrm{GLN} \neq 0$ and links with $\mathrm{GLN} = 0$ (such as the Whitehead link, see Fig. 6.1(a)). A link between two closed chains with $\mathrm{GLN} = 0$ can be unlinked by performing a certain number of crossings between strands of the *same* chain, while the ones with $\mathrm{GLN} \neq 0$ can not be simplified and would remain linked. According to that, we have applied the shrinking procedure to the two rings in the two distinct manners: (i) straightforwardly as described in Sec. 6.2.2; (ii) with *intra*-chain crossing allowed. In this way, the *excess* of links between pairs of rings with $\mathrm{GLN} = 0$ can be measured as the "difference" between (i) and (ii). In order to test the robustness of this procedure, we have computed the corresponding Jones polynomial for the linked rings which display $\mathrm{GLN} = 0$. In the end, it

[6] As known from Rolfsen [149], the non-alternating knots start with *at least* 8 crossings.

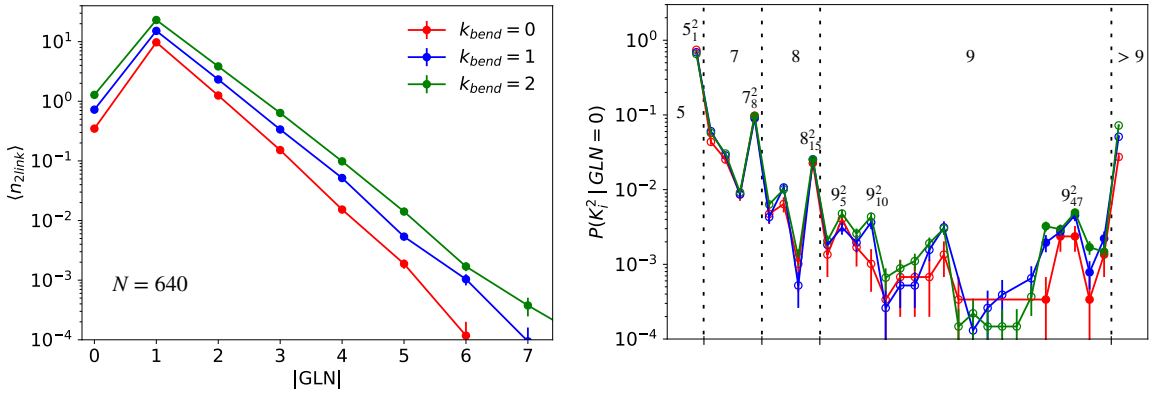

Figure 6.6: (Left) $\langle n_{2\text{link}}(|\text{GLN}|)\rangle$, mean number of 2-chain links per ring with absolute Gauss linking number $|\text{GLN}|$. (Right) $P(K_i^2|\text{GLN} = 0)$, fractional population of 2-chain links K_i^2 (termed according to the Rolfsen's convention [149]) having $\text{GLN} = 0$. Here, as well as in the r.h.s. panel of Fig. 6.7 and Fig. B.3 in Appendix B, error bars are estimated by assuming the formula for simple binomial statistics for the probability of observing a given link (knot, in Fig. B.3 in Appendix B) type in the total population. Empty/full circles are for alternating/non-alternating links while vertical dotted lines separate link classes with the same number of crossings. The displayed link labels correspond to those links appearing with the highest frequency in their class of number of crossings K. The generic label "> 9" follows from the fact that *Topoly* is unable [173] to recognize properly links with > 9 crossings. In both panels, data refer to rings with $N = 640$ and different bending stiffness κ_{bend}.

turns out that only the pairs of rings which emerge as non-trivially linked feature non-trivial Jones polynomials as well.

The mean number of links per chain with absolute Gauss linking number $|\text{GLN}|$, $n_{2\text{link}}(|\text{GLN}|)$, for rings with $N = 640$ and different bending stiffness is shown in the l.h.s. panel of Fig. 6.6 and in Fig. B.4 in Appendix B for the other polymer lengths. We find that links are mainly simple Hopf links (*i.e.*, $|\text{GLN}| = 1$), while links with $\text{GLN} = 0$ are rare and have frequency in between that for $|\text{GLN}| = 2$ and $|\text{GLN}| = 3$. More complex links follow an exponentially-decaying distribution, in agreement with Chapter 5 (see Fig. 5.6).

Finally, there exist many possible types of non-equivalent links for $\text{GLN} = 0$ and we have further investigated, by the Jones polynomials, which structures emerge and their relative abundance (Fig. 6.6, r.h.s. panel). As one may see, polymer conformations are dominated by the Whitehead link (Rolfsen's symbol: 5_1^2) which, of course, is the simplest one in terms of crossings. Nonetheless, we report a remarkably complex spectrum of link types which is very little affected by the bending stiffness of the chains. In particular, at number of crossings ≥ 7, we find that the most abundant links result to be the non-alternating ones with probabilities

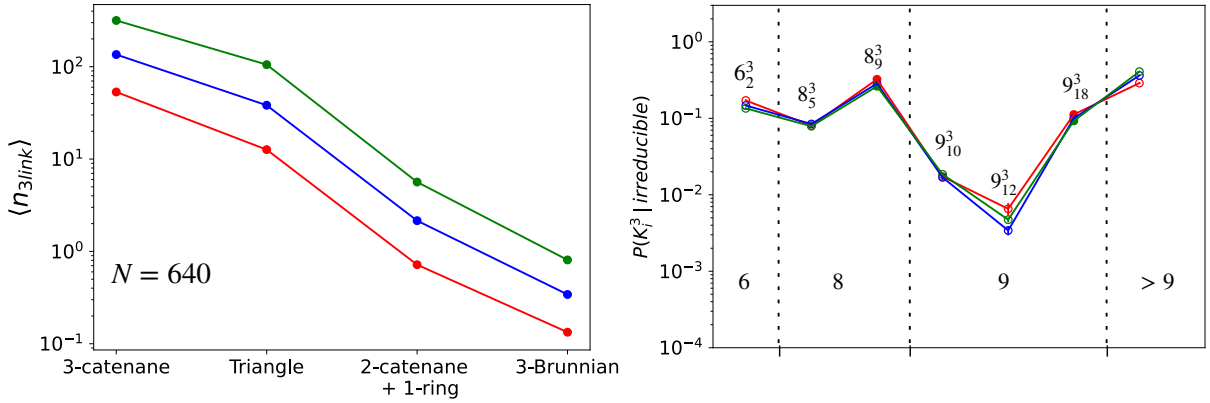

Figure 6.7: (Left) $\langle n_{3\text{link}} \rangle$, mean number of different 3-chain structures per ring. (Right) $P(K_i^3|\text{irreducible})$, fractional population of 3-chain links K_i^3 (termed according to the Rolfsen's convention [149]) belonging to the poly(2)catenane+1-ring and Brunnian classes (see text for details). These are "irreducible" with respect to the simpler compositions of 2-chain links. As in Fig. 6.6, empty/full circles are for alternating/non-alternating links while vertical dotted lines delimit link classes with the same number of crossings. Similarly, the generic label "> 9" follows from the fact that *Topoly* is unable [173] to recognize properly links with > 9 crossings. In both panels, data refer to rings with $N = 640$ and different bending stiffness κ_{bend}.

significantly higher than the alternating ones. The only notable exception is for 9 crossings where the non-alternating 9_{47}^2 occurs with the same frequency of 9_5^2 and 9_{10}^2 which are indeed alternating: overall, though, all these links are very rare.

6.3.3 3-chain topological structures, links

We consider now topological structures between ring triplets. To fix the ideas, we notice that 3-chain links can be grouped as the following: in one group those links that can be "reduced" in terms of the "composition" of simpler 2-chain structures as those seen in Sec. 6.3.2, while in the second group we place all the others which can be then called *irreducible* (see Fig. 4.4 in Sec. 4.1).

Those belonging to the first group are: (a) *poly(3)catenanes*, chains made of three rings in which two non-concatenated rings are connected to a common ring and (b) *triangles*, triplets of rings which are two-by-two concatenated. Thanks to the detection of pairwise links (Sec. 6.3.2) their presence can be efficiently assessed. The presence of these structures has been amply documented in melts of concatenated rings [81], in particular they can be identified – subject to the limitations discussed in Sec. 6.3.2 – via the summation of pairwise concatenations and the relative GLN. On the other hand, irreducible three-chain links – which fail detection by decomposition into pairwise links – can be divided further in two classes: (c)

poly(2)catenane+1-ring, structures made of a poly(2)catenane (*i.e.*, a pair of concatenated rings) plus another ring which is not directly concatenated (in a pairwise manner) with any of the two's, and (d) *Brunnian* links, non-trivial links which become a set of trivial links whenever one component ring is unlinked from the others (the Borromean conformation in Fig. 6.1 (b) constitutes the easiest example).

In order to characterize the relative abundance of each of these structures, we have studied the mean number of different 3-chain links per ring, $\langle n_{3\text{link}} \rangle$. We find (Fig. 6.7, l.h.s. panel) that links take part maximally to poly(3)catenane and triangle structures, yet, although rarer, the other two classes appear in detectable amounts. Notably, as for single knots and 2-chain links (l.h.s. panels of Fig. 6.5 and Fig. 6.6), abundance of 3-chain structures increases with chain stiffness. As for the links, within the (c) and (d) classes we have analyzed the different topological inequivalent concatenated structures with *Topoly*. Due to the complexity of the analyzed structures, *Topoly* is unable to classify them properly in about 50% of the cases after 9 crossings. As for the successfully determined links (Fig. 6.7, r.h.s. panel), we get that the most abundant links are 6_2^3 (*i.e.*, the Borromean rings) and 8_9^3 (which belongs to class (c)). Again, at fixed number of crossings, the most abundant structures are the non-alternating ones (8_5^3, 9_{10}^3 and 9_{12}^3 are all alternating), thus highlighting the preference towards non-alternating linked structures.

6.3.4 Quantitative connection to the entanglement length N_e

By applying the shrinking algorithm to the whole melt, topological interactions of any order are taken into account and, finally, we can assess their contribution to the topological entanglement length N_e (Eq. (6.1)).

In general, the process of shrinking reduces the contour length of each ring inasmuch the topological constraints allow. Thus, if a ring is unknotted and non-concatenated it will shrink to a point and it will be not taken into account since it is assumed to not contributing to the entanglement length of the chains [7]. Conversely, the more the rings are entangled the less they will shrink. Then we apply (see Sec. 6.2.4 for details) the Z1-algorithm [28, 174–177] on the shrunk structures and estimate N_e by that.

Fig. 6.8 (main panel, solid lines) shows the values of N_e as a function of N and for the different bending stiffness κ_{bend}. In all cases $N_e(N)$ tends to an asymptotic value ($N_e = [40.(2), 24.(5), 16.(5)]$ for $N = 640$ and for $\kappa_{\text{bend}}/(k_B T) = 0, 1, 2$, respectively): interestingly, by rescaling both x- and y-coordinates by the corresponding asymptotic value the distinct curves collapse onto each other (Fig. 6.8, inset). Notice also that the characteristic large

[7] A similar assumption was made in [30] regarding the PPA analysis of polymer networks.

values of N_e measured at small N are due to the fact that rings are loosely linked, in contrast at larger values of N rings result to be concatenated into a *single* percolating network of concatenated rings (see Fig. B.5 in Appendix B).

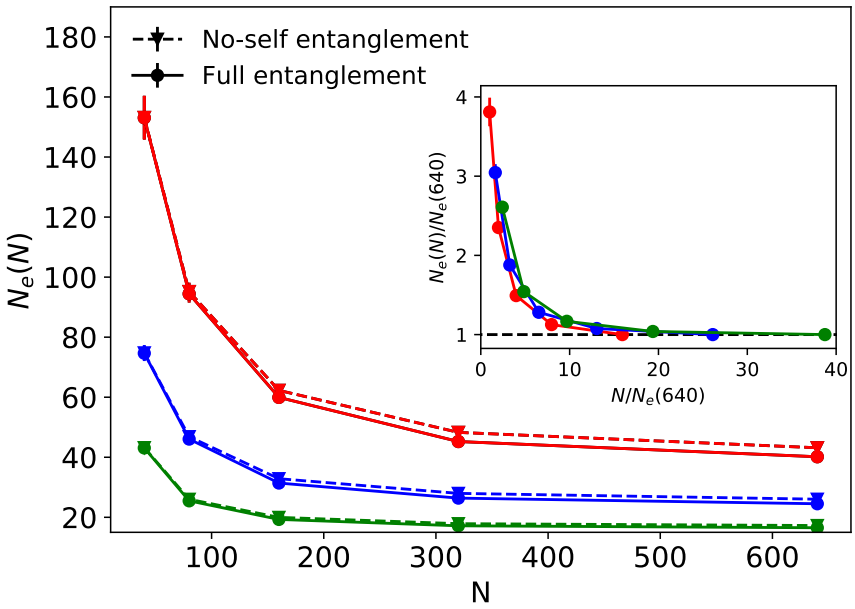

Figure 6.8: Entanglement length, N_e, as a function of the number of monomers per chain, N, and for different bending stiffness, $\kappa_{\rm bend}$. Solid and dashed lines are, respectively, after including/removing self-entanglements (knots) through the Z1-algorithm (see technical details in Sec. 6.2.4). Inset: x- and y-coordinates of data with self-entanglements normalized by the corresponding *asymptotic* value, $N_e(N = 640)$, of the entanglement length.

While, as in Chapter 3, N_e decreases as polymers become stiffer, it is worth comparing these values to the ones ($N_e = [80.37(9), 29.76(4), 13.08(8)]$) obtained in Chapter 3 by applying Eq. 1.6 which is based on theoretical results based on PPA. For $\kappa_{\rm bend}/(k_BT) = 0$ the Z1 value is twice the PPA one: this discrepancy was already noticed in previous works [177, 184, 185] and explained as the consequence of *orientational correlations* between subsequent primitive path segments. Interestingly the discrepancy almost disappears in semiflexible melts with $\kappa_{\rm bend}/(k_BT) = 1, 2$, suggesting that the corresponding correlations are limited to polymer chains which are quite flexible on the entanglement scale (*loosely entangled* [31]).

As for the possible role of self-entanglements (*i.e.*, knots), they influence N_e only marginally (compare solid and dashed lines in Fig. 6.8), in agreement with the result (Sec. 6.3.1) that only a small fraction of the rings ($\approx 10\%$) display knots. Nonetheless, when compared to the similar analysis published in [30] on the role of knots in entangled melts of *linear* polymers, the differences reported by us here appear (especially for the more flexible case $\kappa_{\rm bend}/(k_BT) = 0$)

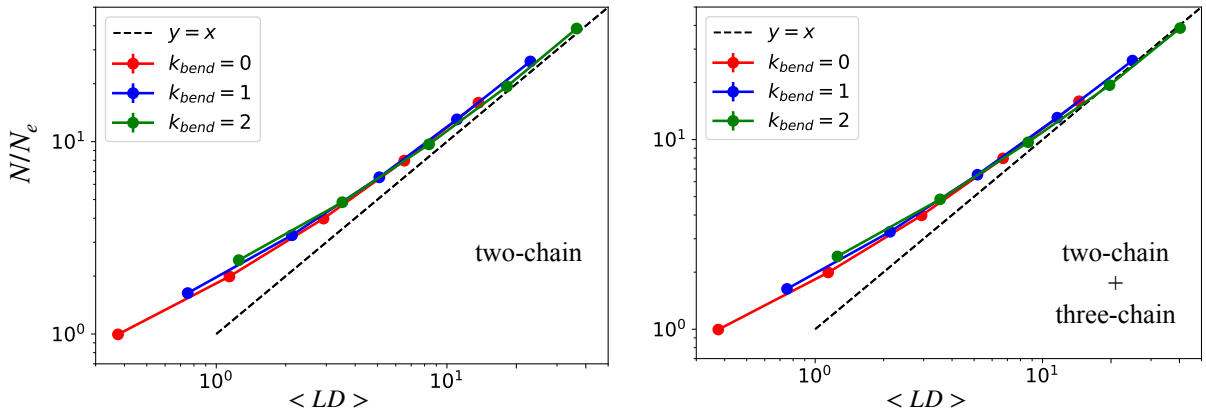

Figure 6.9: Number of entanglements per ring, N/N_e, as a function of the mean linking degree, $\langle \mathrm{LD} \rangle$, computed (see Eq. (6.2)) by taking into account the contribution from 2-chain links solely (left) and after including (right) also the contribution of 3-chain links.

slightly stronger. A likely explanation for this result is the possible role of the ring closure: in fact, we will see (read the discussion in Sec. 6.4) that linear chains of comparable length are significantly less knotted than their ring counterparts.

Finally we show how to connect, in a quantitative manner, N_e to the linking properties of the rings (see Secs. 6.3.2 and 6.3.3). To this purpose, we define the ring mean linking degree $\langle \mathrm{LD} \rangle$ as:

$$\langle \mathrm{LD} \rangle = \langle \frac{1}{M} \sum_{i=1}^{M} \sum_{j=1}^{M} \chi_{ij} \, C_{ij} \rangle \,, \tag{6.2}$$

where each sum runs over the total number of chains (M, see Sec. 6.2.1) in the melt and the average is over the sampled configurations of randomly concatenated and knotted rings. C_{ij} is the $M \times M$ matrix expressing the concatenation status between rings i and j, and it is defined as

$$C_{ij} = \begin{cases} 0 \,, & \text{if } i = j \\ 1 \,, & \text{if } i \neq j \textit{ and} \text{ form a 2-chain} \\ & \text{or a 3-chain irreducible link} \\ 0 \,, & \text{otherwise} \end{cases} \tag{6.3}$$

The "weight" factor χ_{ij} takes into account the "complexity" of the 2-chain (Sec. 6.3.2) and the 3-chain (Sec. 6.3.3) links: (i) for 2-chain links, $\chi_{ij} = |\mathrm{GLN}|$ or $= \frac{K}{2}$ depending on whether $\mathrm{GLN} \neq 0$ or $\mathrm{GLN} = 0$ respectively; (ii) for 3-chain links, $\chi_{ij} = \frac{K}{6}$. Here, K is the number of crossings characterizing the link or, in other words, each crossing of the link contributes $1/2$

to an entanglement point.

Fig. 6.9 (l.h.s. panel) shows that, by only taking into account the contribution of 2-chain links and in the large-chain limit, Eq. (6.2) accounts remarkably well for the number of entanglements, N/N_e, of each chain. Further inclusion (r.h.s. panel) of 3-chain links adds only a small contribution, otherwise it does not improve the agreement significantly.

This is probably the most important result of this chapter: it says that 2-chain links alone capture almost completely the nature of the entanglement length N_e and that, through Eq. (6.2), a true quantitative connection between them can be established.

6.4 Discussion and conclusions

Understanding the microscopic nature of topological constraints in melts of polymer chains is a long-standing, classical [15, 16, 168, 171] problem in soft matter physics. In this chapter, we have characterized accurately the topological state of melts of randomly knotted and concatenated ring polymers used as models for (long) linear polymer systems and, then, show its relationship with the entanglement length N_e of the chains which is *the* central quantity of any rheological theory [5, 14, 98]. In particular, we have demonstrated (Fig. 6.9) that the ring mean linking degree $\langle \mathrm{LD} \rangle$, which accounts for the mean number of entanglement points of each chain in the melt, is a prior for the number of entanglements N/N_e which points to a non-trivial connection between the topology of the chains and the rheological entanglement of the system. Interestingly, the quantitative matching between $\langle \mathrm{LD} \rangle$ and N/N_e is already remarkably accurate only by including the contributions up to the simplest 2-chain linked structures suggesting that, at least for the chain lengths examined here, links of higher orders contribute negligibly.

We wish to conclude by discussing more carefully our assumption (see Introduction 6.1) that *ring* melts can be used to understand entanglement in *linear* melts. To this purpose, we have analyzed the occurrence of knots and links in melts of linear chains with[8] $N = 320$ and for the same physical parameters (*i.e.*, density and bending stiffness) employed for ring melts. The comparisons for the unknot probability (P_{unknot}), and the mean number of 2-chain links with absolute Gauss linking number $|\mathrm{GLN}|$ ($\langle n_{2\mathrm{link}}(|\mathrm{GLN}|) \rangle$) are reported in Fig. 6.10 (top and bottom row panels, respectively).

For the same $N = 320$, knots are clearly less abundant in linear than in ring melts and we ascribe it to the closure constraint that may enhance knots' formation in rings compared

[8] We have considered melts of linear chains with $N = 320$ and compared their properties to those of ring melts with $N = 640$ (see Fig. 6.10). The rationale being that, for contour lengths $\lesssim N/2$, the effect of ring closure should be less impacting on the properties of the chains.

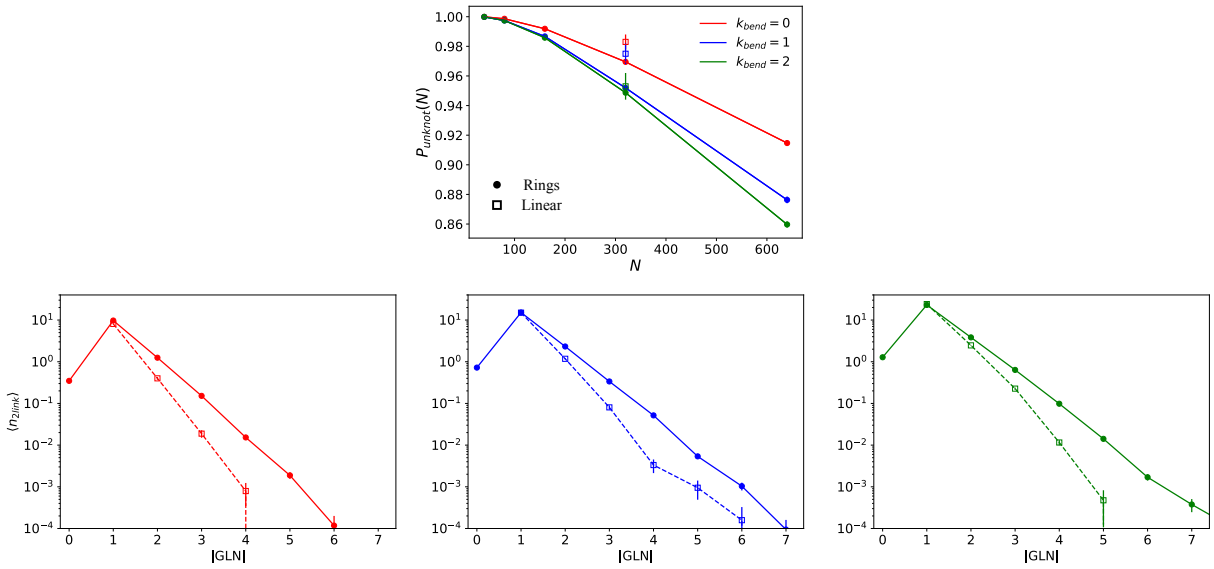

Figure 6.10: (Top row) Comparing the unknot probability, P_{unknot}, for *ring* melts (circles / solid lines, same as in Fig. 2 (left panel) in the main text) *vs.* the one for *linear* melts with $N = 320$ monomers per chain (open squares, details on the simulation runs can be found in 3). The abundance of knots in linear melts have been quantified by using *Topoly* [173], with the following prescription: (i) each of the two free end monomers of a single linear chain is connected to a randomly chosen point on a large spherical surface containing the whole chain; (ii) those added points are joined together through an arc on the sphere; (iii) the Jones polynomial associated to the now closed curve is calculated. This (stochastic) procedure is repeated several times, then the knot associated to the chain is the one corresponding to the *most probable* Jones polynomial between those calculated for the distinct random closures. (Bottom row) Comparing the mean number of 2-chain links per polymer with absolute Gauss linking number $|\mathrm{GLN}|$, $\langle n_{2\mathrm{link}}(|\mathrm{GLN}|)\rangle$, for the same linear melts (open squares / dashed lines) and for ring melts with $N = 640$ monomers per chain (circles / solid lines, same as in Fig. 6.6 (left panel). Notice that the measured GLN (Eq. 4.3) between two linear chains is, typically, a *real* – instead of an *integer* – number: then, to ensure a fair comparison to the rings' result, we round the GLN of linears to the corresponding *nearest integer*.

to linear chains. On the other hand, 2-chain links with $|\mathrm{GLN}| = 1$ (*i.e.*, the responsible ones for the topological entanglement length N_e, see Fig. 6.9) are completely equivalent for the two architectures. Together with the finding (Fig. 6.8) that knots play a marginal role in determining N_e, this result reinforces the important result of this chapter: that the physics of the polymer entanglement length N_e can be captured by 2-chain links solely.

Finally, while this chapter is mostly focused on understanding the relation between the rheological entanglement of the melt and the microscopic topological state of its constituent chains, model conformations of randomly knotted and concatenated rings can be adopted as in Chapter 5 to understand the mechanisms of synthesis of so called Olympic gels, namely polymer gels made of randomly linked rings like the ones now realized by using DNA and cutting restriction enzymes [93].

In particular, the possibility to perform fine tuning of the fiber parameters allow to foresee in great detail how one can benefit from the topological properties of the gel and design materials with certain specificities. For instance, a by-product of the present chapter concerns how the polymer length, combined with the bending stiffness of the chain, influence the topology of the resulting structure. Depending on κ_{bend}, there is a different critical N for which a percolating network of concatenated rings appears (Fig. B.5 in Appendix B), in particular longer and stiffer rings typically produce more robust networks. Moreover, depending on N and κ_{bend} the networks are constituted by a complex zoo of catenation motifs: Hopf links, which are the most abundant for all considered N and κ_{bend} (Fig. 6.6 (l.h.s. panel) and Fig. B.4 in Appendix B), some more complex links with $\mathrm{GLN} = 0$ (*e.g*, the Whitehead link) and $|\mathrm{GLN}| > 1$ or links involving 3-chain structures whose abundances grow with N and κ_{bend} (see Fig. 6.6 (r.h.s. panel) and Fig. 6.7).

These considerations highlight the topological complexity which may arise in Olympic gels made up by strand-crossing rings as in [93] and how topology can be fine regulated by controllable external parameters such as N and κ_{bend}.

Chapter 7

Olympic networks under slit-confinement

In this chapter[1], we investigate how the geometry of the box, under the form of slit-like confinement, can influence the properties of systems of randomly knotted and concatenated polymer rings used for modelling Olympic polymer networks as in Chapters 5 and 6. The results suggest that confinement can be used to fine-tune the mechanical properties of the polymer network. In particular, confinement biases the synthesis of networks that are softer to mechanical stress.

The chapter is structured as the following. After a brief introduction in Sec. 7.1, in Sec. 7.2 we describe the polymer system under study, introducing the relevant length-scales with respect to the slit-confinement applied to the system. Then, in Secs. 7.3 and 7.4, we present and comment the main results of the work providing discussion regarding the role of slit confinement in shaping both single-chain and inter-chain properties of the resulting polymer networks. Additional figures have been included in the Appendix C.

7.1 Introduction

As already discussed in Sec. 1.4.1, recent years have witnessed a growing interest in the design of so called *smart* materials, such polycatenanes and polyrotaxanes [186, 187], whose microscopic components are constituted by ring polymers interlocked to each other by topological links that can be artificially synthesised following precise chemical routes.

In this regard, part of my PhD work, summarized in Chapter 5, was motivated by the recent synthesis [93] of an *Olympic* hydrogel, prepared by employing DNA plasmid rings which

[1]The material described in this Chapter has been published as a preprint: Ubertini, Mattia Alberto, and Angelo Rosa. Macromolecules (2023) [4].

interlock to each other through the action of the enzyme TopoII. As discussed in Chapter 5, the preparation of topological materials with well designed properties is a delicate balance between many parameters: indeed, several numerical studies [188, 189] as well as the ones contained in the Chapters 5 and 6 have characterized the topological state of systems made up of randomly concatenated and knotted polymer rings, and have shown that the resulting networks can be controlled using experimentally tunable parameters such as the length of the polymer chain, the density of the polymer solution, and the bending stiffness of the polymer fiber. So far though, *geometric confinement* as a way to drive the synthesis of concatenated ring networks has received considerable less attention. Yet, recent experiments [190] performed on kinetoplast DNA [191] at varying degree of *slit confinement* have foreseen the possibility of exploiting geometric constraints to bias the synthesis of a DNA-based network, similarly to the one discussed in Ref. [93].

In this chapter, we explore how geometric constraints, under the form of slit confinement, can affect the structural properties of systems of strand-crossing rings. To this purpose, we perform extensive dynamical simulations of highly entangled systems of randomly concatenated and knotted rings employing the kinetic Monte Carlo algorithm introduced in Sec. 2.1.2 complemented by the strand-crossing moves introduced in Chapter 5, which were used so far for studying systems at bulk conditions. In this chapter, by varying the degree of confinement, we quantify its influence on the metric properties of the rings, which present interesting non-monotonous behaviour, as well as topological ones; in particular, knotting probability is highly enhanced by reducing the height of the slit, while the linking between the rings is diminished. These findings suggest that geometric confinement can be used as a powerful tool to control the topology of the resulting networks and their elastic properties.

7.2 Model and methods

7.2.1 Polymer model

We employ the same lattice polymer model used in the previous chapters. Here, in particular, we consider polymer melts made of M randomly concatenated and randomly knotted semiflexible ring polymers of $N = 320$ monomers each. Polymer semiflexibility is taken into account with the bending potential Hamiltonian (see Eq. 2.6) with $\kappa_{bend} = 2$. We fixed the monomer number per fcc lattice site equal to $\frac{5}{4} = 1.25$ as in the previous chapters, and with the chosen bending parameter, the chain Kuhn segment corresponds, in bulk, to $\ell_K/a = 3.4$ (see Table 3.1) which is high enough to guarantee that distinct polymers are in an effective highly entangled state.

H/a	$\hat{\mathrm{H}}$	M	$\langle b\rangle/a$
2.12	0.30	420	0.656
3.53	0.50	422	0.658
4.95	0.70	420	0.659
6.36	0.90	427	0.659
7.78	1.10	420	0.660
10.61	1.51	420	0.660
13.43	1.91	422	0.660
17.68	2.51	430	0.660
20.51	2.91	433	0.660
bulk	–	420	0.663

Table 7.1: Values of physical parameters for the ring polymer melts investigated in this work. a is the unit distance of the fcc lattice and the monomer number per fcc lattice site is equal, as in the previous chapters, to $\frac{5}{4} = 1.25$. (i) H, height of the slit. (ii) $\hat{\mathrm{H}} = \frac{\mathrm{H}}{\sqrt{\langle R_g^2\rangle_{\mathrm{bulk}}}}$, ratio between the height of the slit and the root-mean-square gyration radius of rings in bulk (*i.e.*, no confinement) conditions. (iii) M, total number of simulated chains in the melt. (iv) $\langle b\rangle$, mean bond length. Notice that the values for $\langle b\rangle$ between the bulk and the confined rings are all very close to each other, with a slight increase as confinement decreases.

Simulations are based on the kinetic Monte Carlo (kMC) algorithm introduced in Chapter 5 in which the Topology-*preserving* moves (see Sec. 2.1.2) are complemented with the Topology-*changing* moves (see Sec. 5.2.3) which induce random strand crossings between nearby polymer filaments at a tunable rate which we set to 10^4 kMC elementary steps as in the previous chapters.

Finally, ring polymers are subject to slit confinement. This particular form of constraint is imposed by forcing the chains to move on the fcc lattice, with periodic boundary conditions on the xy-plane and hard boundaries in the z-direction placed in $z = 0$ and $z = \mathrm{H}$. We vary the height of the box, H, to study different confinement regimes, while adjusting the lateral box sides $L_x = L_y$ to keep density constant. The degree of confinement is quantified by the ratio $\hat{\mathrm{H}} = \mathrm{H}/\sqrt{\langle R_g^2\rangle_{\mathrm{bulk}}}$, expressing the ratio between the height of the slit H and the root-mean-square gyration radius (Eq. (2.11)), $\sqrt{\langle R_g^2\rangle_{\mathrm{bulk}}}/a = \sqrt{49.66}$ of randomly knotted and concatenated rings in bulk conditions (Chapter 6).

We investigate system's behavior from highly confined ($\hat{\mathrm{H}} \simeq 0.30$) to mildly confined

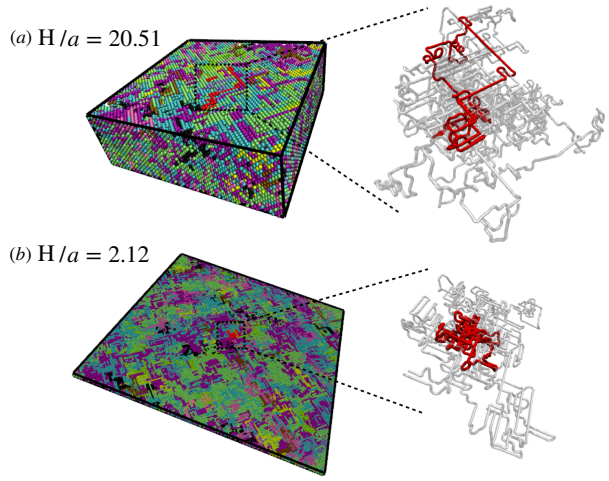

Figure 7.1: Ring melt conformations under slit-confinement. The figure illustrates the two extreme cases of mild ($\mathrm{H}/a = 20.51$, panel (a)) and tight ($\mathrm{H}/a = 2.12$, panel (b)) confinement, where H is the thickness of the slit and a the lattice unit (see Sec. 7.2 for details). On the left part of each panel, the full melt is shown with each ring in a different color to ease the visualization. On the corresponding right part, a zoom-in view of a typical ring conformation (in red) alongside the neighboring rings (in faint grey) which the red ring is linked to (see Sec. 7.3.2).

($\hat{\mathrm{H}} \simeq 2.91$) regimes and systematically compare the results with the corresponding values in bulk. Wherever appropriate, we have also compared the systems here with melts of unknotted and non-concatenated rings in bulk described in Chapter 3.

We simulate $M \simeq 420$ chains, comprising a total of $N \times M \simeq 134400$ monomers, with M slightly adjusted to maintain a constant density (see Table 7.1 for specific numbers). Typical melt conformations (with corresponding zoom-in views of a single-ring and the neighbors which it is linked to) for the two situations of mild ($\mathrm{H}/a = 20.51$) and tight ($\mathrm{H}/a = 2.12$) confinement are shown in Fig. 7.1 (panel (a) and (b), respectively).

To assess meaningful chain statistics we follow the same protocol of the previous chapters simulating the systems long enough in order to obtain plateaus (see Fig. C.1 in Appendix C) in the single monomer mean square displacement in the centre of mass reference (Eq.(2.19)), g_2. Consequently, the time to reach the plateau correspond to the portion of the trajectory which has been removed from the computation of the relative observables.

7.2.2 Notation

As for rings' metric properties, for some observables $\mathcal{O}$ which can be expressed as a function of monomers' coordinates we study separately the contributions $\mathcal{O}_\perp$ and $\mathcal{O}_\parallel$, respectively perpendicular (or, transverse) and parallel to the plane of the slit (which coincides with the xy-plane see Sec. 7.2.1).

As for rings' topological properties, we follow the same pipeline described in Chapter 6 for the topological analysis of the polymer melts. In referring to a given knot or link we employ the same convention used in the previous chapters, namely, the Rolfsen convention [149].

7.3 Results

7.3.1 Single-chain properties

Rings' size and shape

First, we characterize the impact of slit confinement on the size and shape of the rings. To this purpose, for each ring of the system we compute the 3×3 symmetric gyration tensor $Q_{\alpha\beta}$ (see Eq. (2.13). We recall that the mean values of the eigenvalues of Q ordered in descending order, $\langle \lambda_1^2 \rangle \geq \langle \lambda_2^2 \rangle \geq \langle \lambda_3^2 \rangle$, quantify the mean spatial elongations of the polymers on the corresponding principal axes, while the mean value of the trace of Q, $\langle \mathrm{tr} Q \rangle = \sum_{\alpha=1}^{3} \langle \lambda_\alpha^2 \rangle$, is equal to the mean-square gyration radius Eq. (2.11), $\langle R_g^2 \rangle$ of the chain.

The results for $\langle R_g^2 \rangle$ and the perpendicular and parallel components, $\langle R_{g,\perp}^2 \rangle$ and $\langle R_{g,\parallel}^2 \rangle$, are reported in Fig. 7.2. As H decreases, the transverse component $\langle R_{g,\perp}^2 \rangle$ decreases (green curve in Fig. 7.2(a)) as expected. Conversely, the parallel component $\langle R_{g,\parallel}^2 \rangle$ grows with confinement (red curve in Fig. 7.2(a)) because the ring is forced to spread along the plane of the slit. Together, these two effects produce a characteristic non-monotonic behavior in the overall $\langle R_g^2(\hat{\mathrm{H}}) \rangle$ (blue curve in Fig. 7.2(a)) with the minimum attained around $\hat{\mathrm{H}} \simeq 0.7$, *i.e.* where confinement effects are expected to become more pronounced. Interestingly, for high confinement ($\hat{\mathrm{H}} \lesssim 0.3$), the rings are markedly larger than the bulk reference (blue dotted curve in Fig. 7.2(a)). In a previous study [192] of randomly concatenated rings under slit confinement, the non-monotonic behavior was also observed but the swelling compared to the bulk state was not seen. We attribute this discrepancy to the fact that, in the previous work, rings without excluded volume were considered which could have favored more compact conformations.

Beyond average values, we have also computed the corresponding probability distributions, $P(R_g)$, $P(R_{g,\perp})$ and $P(R_{g,\parallel})$, and represented each of them (see Fig. 7.2, panels (b)

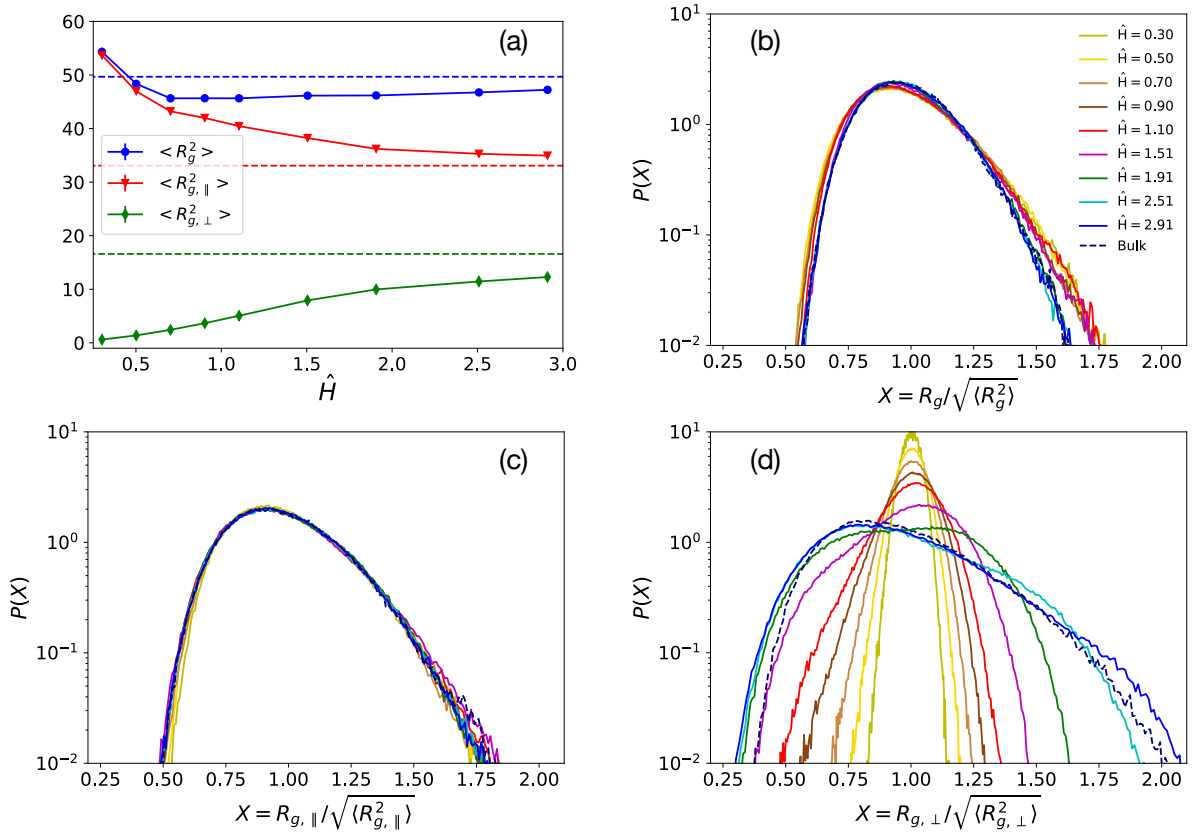

Figure 7.2: (a) Ring mean-square gyration radius ($\langle R_g^2 \rangle$) with its parallel ($\langle R_{g,\parallel}^2 \rangle$) and transverse ($R_{g,\perp}^2$) components as a function of the degree of confinement $\hat{\mathrm{H}}$. The dashed lines are for the values of the bulk system (*i.e.*, no confinement). Error bars are smaller than the symbols size. (b, c, d) Scaling plots for, respectively, distribution functions of the ring gyration radius ($P(R_g/\sqrt{\langle R_g^2 \rangle})$) and of its parallel ($P(R_{g,\parallel}/\sqrt{\langle R_{g,\parallel}^2 \rangle})$) and transverse ($P(R_{g,\perp}/\sqrt{\langle R_{g,\perp}^2 \rangle})$) components, at different degrees of confinement $\hat{\mathrm{H}}$ (see legend in panel (b)). The dashed line in each panel corresponds to the reference distributions in bulk conditions.

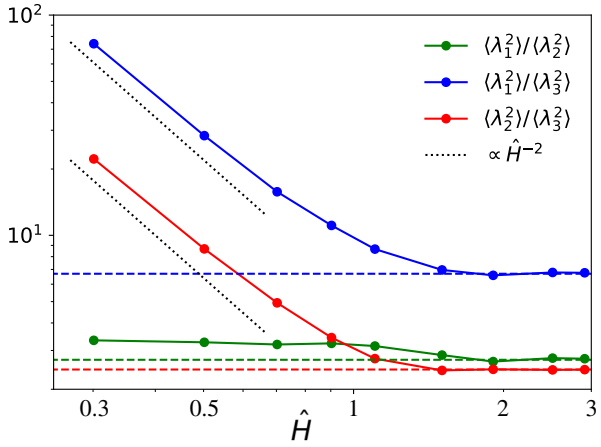

Figure 7.3: Ratios between the mean eigenvalues ($\langle\lambda_1^2\rangle$, $\langle\lambda_2^2\rangle$ and $\langle\lambda_3^2\rangle$) of the ring gyration tensor Q (Eq. (2.13)) as a function of the degree of confinement $\hat{\mathrm{H}}$ (see Sec. 7.2.1 for definition). Dotted lines ($\sim \hat{\mathrm{H}}^{-2}$) describe the behavior under strong slit-confinement, in agreement with the blob-like picture *à la* de Gennes (see Sec. 7.3.1 for details). Dashed horizontal lines correspond to the bulk reference values of the three ratios.

to (d)) in the corresponding scaled variable to ease comparison. While the distributions of the parallel component of the gyration radius are fundamentally unaffected by confinement (Fig. 7.2(c)), the ones of the normal components (see Fig. 7.2(d)) undergo a significant change in shape as the confinement becomes stronger, in particular becoming more peaked. Together these changes produce an interesting effect on the distributions of the full gyration radius (Fig. 7.2(b)), which are characterized by higher tails for the systems under confinement. This suggests that, under confinement, rings assume more heterogeneous sizes.

We study then rings' shapes and anisotropies by looking at the ratios: (i) $\langle\lambda_1^2\rangle/\langle\lambda_2^2\rangle$, (ii) $\langle\lambda_1^2\rangle/\langle\lambda_3^2\rangle$ and (iii) $\langle\lambda_2^2\rangle/\langle\lambda_3^2\rangle$. The first ratio indicates the elongation or "asphericity" of the ring mean shape, while the other two measure the extent to which rings become effectively flat due to slit confinement.

Results are shown in Fig. 7.3, where it is clear that at mild confinement $\hat{\mathrm{H}} \gtrsim 1.5$ rings attain the shame shape of the bulk ones. Conversely, for higher confinement ($\hat{\mathrm{H}} \lesssim 0.7$) the ratios to the smallest eigenvalues (blue and red curves in Fig. 7.3) are described by the same characteristic power-law behavior $\sim \hat{\mathrm{H}}^{-\alpha}$ with $\alpha = 2$ (dotted lines). This exponent can be derived [193] by the following simple blob scaling argument *à la* de Gennes [194, 195]: for tight confinement and since rings obey ideal statistics [1, 3] owing to strand crossings, we do expect $\langle\lambda_3^2\rangle \sim \mathrm{H}^2 \sim a^2 g_{\mathrm{H}}$ while $\langle\lambda_1^2\rangle \sim \langle\lambda_2^2\rangle \sim \mathrm{H}^2(N/g_{\mathrm{H}})$ where g_{H} is the mean number of monomers spanning a distance of the order of H. Together these two relations imply $\alpha = 2$,

i.e. rings' flattening is indeed compatible with the scaling picture. At the same time (ratios $\langle\lambda_1^2\rangle/\langle\lambda_2^2\rangle$, green curve), the polymers maintain an elongated shape.

Bond-vector correlation function

We investigate now in more detail how the folding of polymer chains is affected by confinement by looking at the bond-vector correlation function (see Eq.(2.15)) , $c(\ell)$, as a function of the polymer contour length ℓ.

As discussed in the chapter 3, this quantity gives useful insight when applied to bulk $3d$ melts of unknotted and non-concatenated rings, in particular, as it was shown there, its distinct anti-correlation is a symptom of the double folding of the polymer chains at the entanglement scale (dot-dashed line in Fig. 7.4(a) and 3.8). In contrast (dashed line in Fig. 7.4(a) and 6.3), bulk $3d$ melts of randomly knotted and concatenated rings exhibit normal exponential decay behavior and are not characterized by double folding, hence the anti-correlation is absent.

To investigate the impact of confinement on chain folding, we have computed $c(\ell)$ for the confined rings. Results (Fig. 7.4) exhibit several noteworthy effects. Firstly (Fig. 7.4(a)), for confined rings at small ℓ, $c(\ell)$ decays more slowly than the bulk counterpart. This is reflected (Fig. 7.4(b)) in the increase of the mean-cosine of the angle between consecutive bond vectors, $\langle\cos(\theta)\rangle$, as confinements increases: in other words, confined rings are slightly stiffer than the bulk reference and this confinement-enhanced stiffness grows with the confinement. At the same time, $c(\ell)$ develops a characteristic anti-correlation that exhibits non-monotonic dependence on $\hat{\mathrm{H}}$: in particular the deepest minimum occurs at $\hat{\mathrm{H}} \simeq 0.7$, *i.e.* the same value at which the gyration radius (Fig. 7.2(a)) attains its minimum value. Moreover, the minimum itself disappears at the highest level of confinement. This peculiar behavior can be explained by considering the individual contributions of the parallel and transverse components of $c(\ell)$. $c_{\parallel}(\ell)$ does not exhibit any minima (Fig. 7.4(c)), while $c_{\perp}(\ell)$ displays a minimum for all values of $\hat{\mathrm{H}}$ (Fig. 7.4(d)). The mismatch in the values of ℓ, at which $c_{\perp}(\ell)$ is minimum while $c_{\parallel}(\ell) \simeq 0$, causes the non-monotonicity of the full $c(\ell)$. The latter goes to zero for similar values of ℓ for all $\hat{\mathrm{H}}$, demonstrating that correlations grow mildly with the confinement. In contrast, $c_{\perp}(\ell)$ shows a minimum for ℓ close to the thickness of the slit H (Fig. 7.4(d), inset). This is due to the back-folding of the polymer filaments induced by the hitting with the impenetrable walls of the slit: of course this effect is more pronounced under strong confinement conditions, *i.e.* for $\mathrm{H}/\ell_K \leq 1$. Thus the minima in $c(\ell)$ appear when H has similar value to the correlation length of $c_{\perp}(\ell)$, indicating the competition between these two length scales.

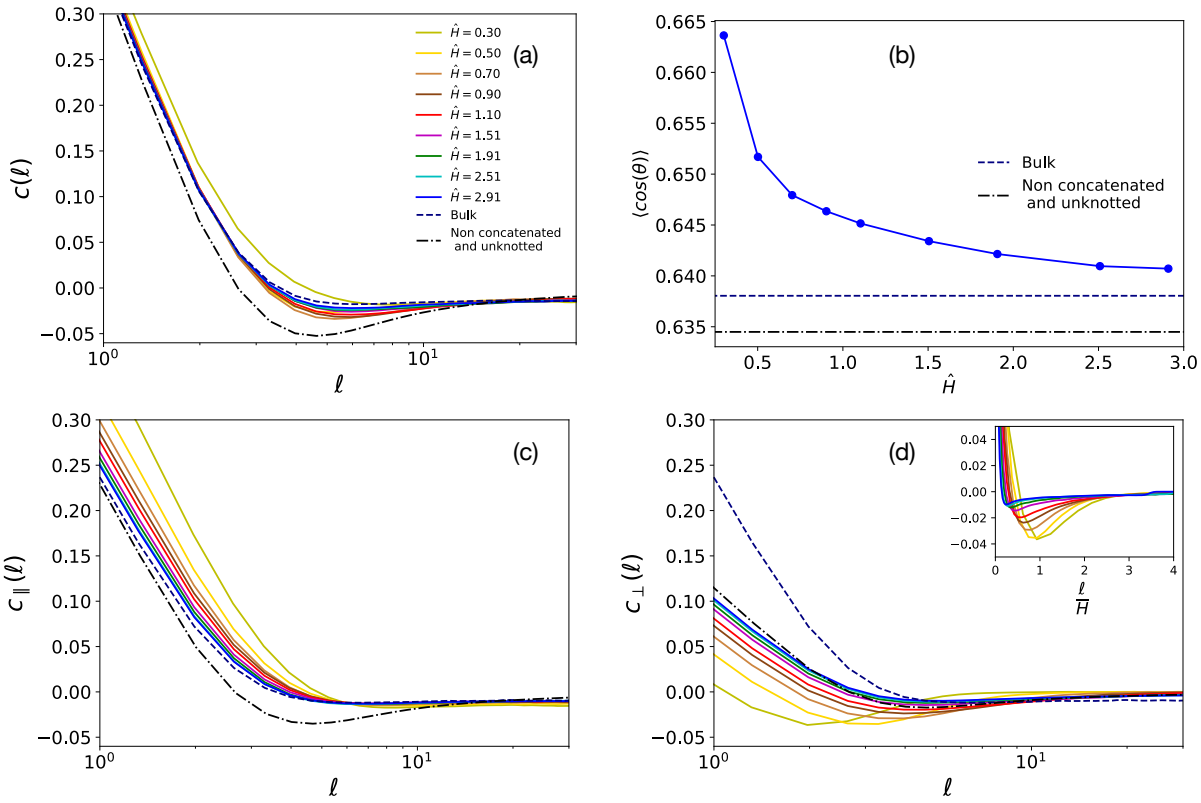

Figure 7.4: (a) $c(\ell)$, bond-vector correlation function as a function of the contour length distance ℓ. Colors are for different confinements, dashed and dot-dashed lines are for bulk melts and melts of non-concatenated and unknotted rings (see legend). (b) $\langle\cos(\theta)\rangle$, mean cosine value between two consecutive bonds along the chain as a function of the degree of confinement $\hat{\mathrm{H}}$. (c) $c_\parallel(\ell)$, contribution to the bond-vector correlation function in the xy-plane parallel to the slit. (d) $c_\perp(\ell)$, contribution to the bond-vector correlation function orthogonal to the plane of the slit; in the inset the same quantity is represented as a function of the ring contour length normalized by the slit thickness, ℓ/H. Colors and symbols in panels (c) and (d) are as in panel (a).

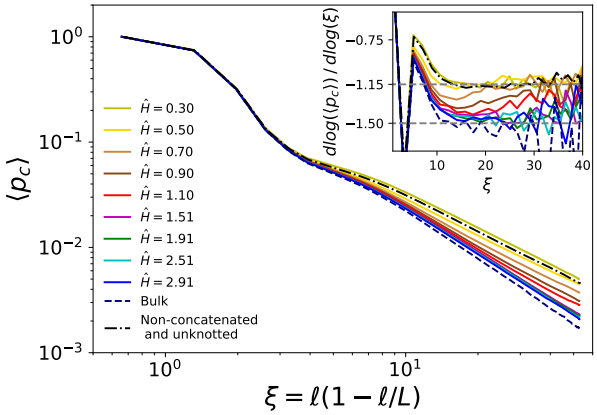

Figure 7.5: Mean contact probabilities, $\langle p_c \rangle$ (Eq. (2.16)), as a function of $\xi = \ell\,(1 - \ell/L)$ where ℓ is the contour length separation between monomers and L is ring total contour length. Colors are for different confinements, dashed and dot-dashed lines are for bulk melts and melts of non-concatenated and unknotted rings (see legend). Inset: local differential exponent $\equiv \frac{d\log\langle p_c \rangle}{d\log\xi}$.

Contact probability

As just shown, confinement alters the metric properties of the polymers. Then, it is natural to expect that the consequent reorganization of the chains modifies the intra-chain polymer interactions. To test this hypothesis, we compute the mean contact probability between two monomers at contour length separation $\ell = n\langle b \rangle$ (see Eq.(2.16)), $\langle p_c(\ell) \rangle$.

Results are shown in Fig. 7.5, where $\langle p_c \rangle$ is plotted, as in the previous chapters, against the "effective" variable $\xi = \ell(1 - \ell/L)$ in order to reduce [130] finite-size effect due to the ring geometry. First, one can notice that in bulk systems, as we let rings perform strand crossings, long-distance contacts decrease (dashed line) with respect to melts of non-concatenated and unknotted rings (dot-dashed line). In contrast, confinement leads to an increase in the tail of the mean contact probability compared to the bulk reference. Notably, at $\hat{\mathrm{H}} = 0.30$, the tail's slope is slightly less steep than in the non-concatenated state.

To get more insight, it is interesting to look at the exponent controlling the asymptotic power-law decay, $\langle p_c \rangle \simeq \xi^{-\gamma}$ (Fig. 7.5, inset). In bulk, strand-crossing rings attain ideal statistics characterized by $\gamma \simeq 1.5$, as confirmed by our previous findings (see Fig 5.4 in Chapter 5). In contrast, confinement leads to a decrease in γ which becomes close to the same asymptotic value as the non-concatenated state, $\gamma \simeq 1.15$. Based on mean-field arguments [38], $\gamma = d\nu$ where d is space dimension and ν is the metric exponent of the chain relating [5, 14] the chain mean linear size to the number of monomers (*i.e.*, $\langle R_g^2 \rangle \sim N^{2\nu}$). Strand-crossing rings

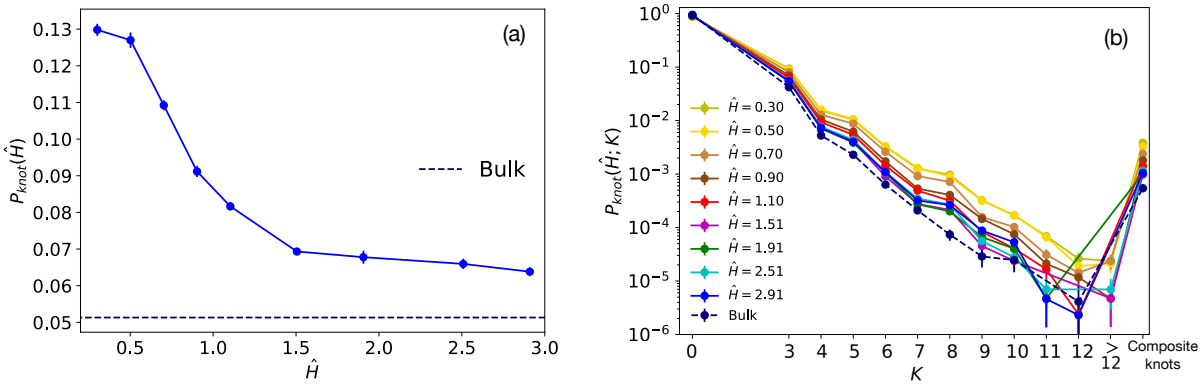

Figure 7.6: (a) $P_{\rm knot}(\hat{\rm H})$, ring knotting probability (Eq. (7.1)) for knots with K crossings and as a function of the degree of confinement $\hat{\rm H}$. The dashed line correspond to the value for the bulk melt. (b) $P_{\rm knot}(\hat{\rm H}; K)$, probability of finding a knot with crossing number K. Colors are for different confinements, the dashed is for bulk melts (see legend). $K = 0$ correspond to the unknot and $P_{\rm knot}(\hat{\rm H}; K = 0) = 1 - P_{\rm knot}(\hat{\rm H})$ is its corresponding probability. Knots with > 12 crossings cannot be distinguished by *Topoly* [173]. Composite knots are knots made up by 2 or more irreducible knots.

in bulk exhibit ideal statistics with $\nu = 1/2$ [1] and they are characterized by $\gamma = \frac{3}{2}$ in three dimensions. In confined systems, however, the rings cannot fold freely in three dimensions, effectively reducing the dimensionality of the system and resulting in a decrease in γ.

Knots statistics

In our kMC algorithm two filaments from the same chain can cross and this event may induce the formation of a knot along the chain. Characterization of knots spectra in confined systems have been addressed so far mostly for isolated chains [151, 193, 196], while less results are available for confined systems at melt conditions. To fill this gap, we have investigated the occurrence of knots by computing the Jones polynomial of each ring of our systems and, for simplicity, we present our results based on the number of irreducible crossings (denoted by K). Specifically, we have computed the probability, $P_{\rm knot}(\hat{\rm H}; K)$, of finding a knot with K irreducible crossings at given confinement degree $\hat{\rm H}$ and the *cumulative* knotting probability:

$$P_{\rm knot}(\hat{\rm H}) = \sum_{K=3}^{\infty} P_{\rm knot}(\hat{\rm H}; K)\,, \tag{7.1}$$

which gives the probability that a ring in the melt contains a knot (of any type).

As shown in Fig. 7.6(a), $P_{\rm knot}(\hat{\rm H})$ grows with the confinement and reaches the maximum value of $\simeq 0.13$ for the smallest $\hat{\rm H}$, resulting in an increase of $\simeq 130\%$ compared to bulk

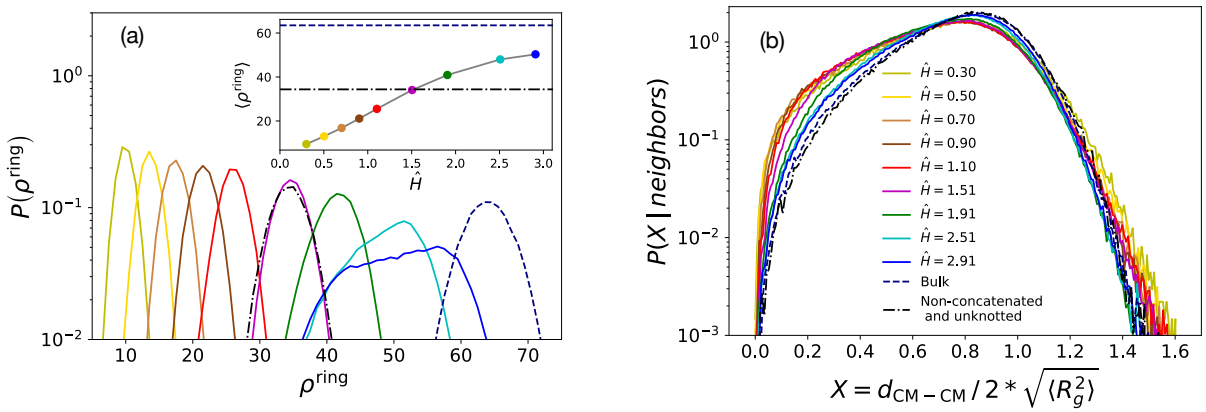

Figure 7.7: (a) Distribution function, $P(\rho^{\mathrm{ring}})$, of the the number of neighbors per chain ρ^{ring}. Inset: mean number of neighbors per ring, $\langle\rho^{\mathrm{ring}}\rangle$. (b) Distribution function of the distances between the centres of mass of neighbour chains, $P(d_{\mathrm{CM-CM}} \mid \mathrm{neighbours})$, as a function of the variable normalized to twice the root mean-square gyration radius, $2\sqrt{\langle R_g^2\rangle}$, of the rings. Colors are for different confinements, dashed and dot-dashed lines are for bulk melts and melts of non-concatenated and unknotted rings (see legend).

reference (dashed line). Both in bulk and in confinement, the most common knot type is the simplest one, namely the *trefoil* knot 3_1. Overall (Fig. 7.6(b)), more complex knots are much less probable for all $\hat{\mathrm{H}}$ values, yet their abundance increases with confinement, see Fig. 7.6(b) for $P_{\mathrm{knot}}(\hat{\mathrm{H}}; K)$ and Fig. C.2 in Appendix C for the relative population of knot types with K crossings.

In conclusion, our analysis points out that confinement enhances the probability of knot formation, yet the overall occurrence of knots (*i.e.*, P_{knot}) remains relatively low ($\lesssim 0.13$).

7.3.2 Chain-chain correlations

Chain neighbours

The increase of the long-range intra-chain contacts seen in Fig. 7.5 may be indicative of the fact that confinement reduces the overlap between distinct chains or, in other words, ring-ring contacts should decrease.

To test this hypothesis, we introduce the variable for the number of neighbors of ring i $(i = 1, 2, ..., M)$,

$$\rho_i^{\mathrm{ring}} \equiv \sum_{\substack{j=1 \\ j \neq i}}^{M} \Theta\left(2\sqrt{\langle R_g^2\rangle} - |\vec{r}_{\mathrm{CM},i} - \vec{r}_{\mathrm{CM},j}|\right) , \tag{7.2}$$

where $\Theta(x)$ is the Heaviside step function, $\langle R_g^2 \rangle$ is the mean square gyration radius of the system, and $\vec{r}_{\mathrm{CM},j}$ represents the centre of mass position of the j-th ring. According to Eq. (7.2), two rings are defined as "neighbor" whenever the spatial distance between their centres of mass is smaller than the twice the root mean-square gyration radius of the system.

We have measured the distribution function of ρ^{ring}, $P(\rho^{\mathrm{ring}})$, and its mean value, $\langle \rho^{\mathrm{ring}} \rangle$, at different confinements and we study these quantities in relation to the distribution of spatial distances between the centres of mass $d_{\mathrm{CM-CM}}$ for neighboring rings, $P(d_{\mathrm{CM-CM}} \,|\, \mathrm{neighbors})$.

Results are shown in Fig. 7.7, from which it is evident (panel (a)) that $\langle \rho^{\mathrm{ring}} \rangle$ decreases as confinement increases, with $\langle \rho^{\mathrm{ring}} \rangle$ being always smaller with respect to the bulk reference (dashed line) and even smaller (for the tighter confinements $\hat{\mathrm{H}} \lesssim 1.5$) with respect to the non-concatenated and unknotted case (dot-dashed line). At the same time (panel (b)), the distributions of spatial distances $d_{\mathrm{CM-CM}}$ demonstrate that neighboring chains tend to overlap more with each other under stronger confinement.

Taken all together, we can motivate the reason why the inter-chain contacts decrease in terms of the geometry of the slit. First, confinement can prevent the formation of stacked conformations along the transverse direction (see Fig. C.3 in Appendix C), and this surely reduces the inter-chain contacts. Moreover, we observe that, by reducing the width of the slit, inter-ring distances tend to increase and this is an effect due to the increasing asymmetry of the slit as confinement increases (see Fig. C.4 in Appendix C).

Links

The reduction of inter-chain contacts should also have consequences on the *linking* properties of the confined systems. To explore this aspect, we adopt the approach described in Chapter 6 and compute: (a) $\langle n_{\mathrm{2link}}(|\mathrm{GLN}|) \rangle$, the mean number of two-chain links per ring with at absolute Gauss linking number $|\mathrm{GLN}|$, and (b) $\langle n_{\mathrm{3link}} \rangle$, the mean number of distinct three-chain links per ring with given chain topology. Results for $\langle n_{\mathrm{2link}}(|\mathrm{GLN}|) \rangle$ are summarized in panel (a) of Fig. 7.8. We notice that ring-ring links are mostly Hopf-like (*i.e.*, with $|\mathrm{GLN}| = 1$) and that confinement reduces the extent to which the rings are linked, in agreement with the reported trend of neighbors per ring (Fig. 7.7). In general, the participation in more complex links decreases exponentially but the rate of decay depends on the level of confinement in the system. Chains under stronger confinement are characterized by a slower decay, which can be attributed to the fact that neighboring chains penetrate each other more (see Fig. 7.7(b)). Additionally, links with $|\mathrm{GLN}| = 0$ (*i.e.*, the so-called Whitehead links) have been found between those with $|\mathrm{GLN}| = 2$ and $|\mathrm{GLN}| = 3$ at all confinements. We further classify these links by computing their Jones polynomial and determining their relative

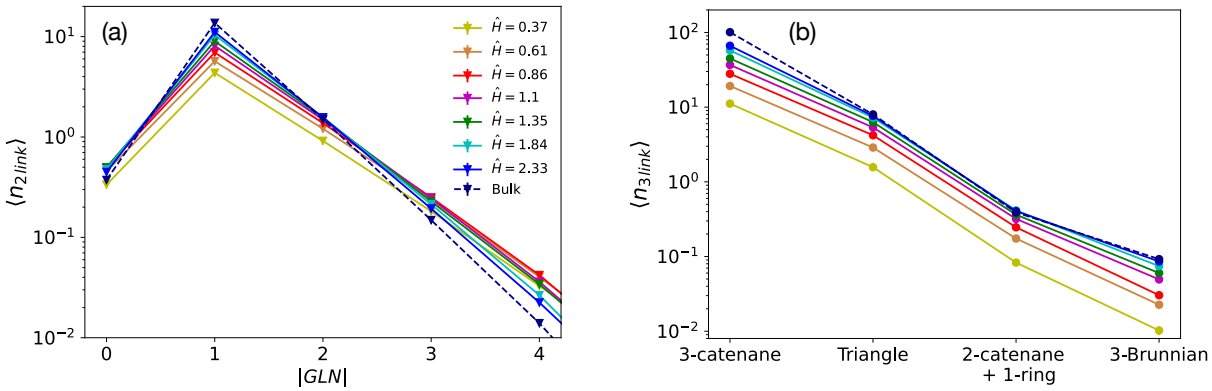

Figure 7.8: (a) $\langle n_{2\text{link}}(|\text{GLN}|)\rangle$, mean number of links per ring with absolute Gauss linking number $|\text{GLN}|$. (b) $\langle n_{3\text{link}}\rangle$, mean number of different three-chain linked structures per ring. Different colors are for the different confinements, the dashed line is for the bulk system.

abundances (panel (a) in Fig. C.5 in Appendix C). We found that, even in this case, rings under stronger confinement form more complex links with greater ease.

To examine three-chain links, it is necessary to distinguish between two distinct groups of links: those that can be reduced to two-chain links and irreducible ones as done in Chapter 6. As in the previous chapter, the first group include: (a) *poly(3)catenanes*, chains made of three rings in which two non-concatenated rings are connected to a common ring, and (b) *triangles*, triplets of rings which are all pairwise concatenated. Both (a) and (b) can be detected via pairwise linking. Instead, irreducible three-chain links cannot be detected via pairwise linking and can be further divided in two sub-types: (c) *poly(2)catenane+1-ring*, structures made of a poly(2)catenane plus another ring which is not directly concatenated (in a pairwise manner) to any of the other two, and (d) *Brunnian* links, non-trivial links which become a set of trivial links whenever one component ring is unlinked from the others (the so called *Borromean* conformation, the link 6_2^3, constitutes the easiest example of this kind).

By resorting to the shrinking method described in Chapter 6, we have detected links belonging to the last two classes and computed $\langle n_{3\text{link}}\rangle$ for the different types of three-chain links (Fig. 7.8(b)). It is clear from $\langle n_{3\text{link}}\rangle$ that links organize onto a network made almost entirely via pairwise concatenation both in bulk and in confinement. Irreducible three-chain links are much more rare and decrease with the degree of confinement, for this reason the next analysis relative to polymer networks and entanglements has been performed by neglecting these three-chain links contribution. A detailed topological classification of these structures has been reported in Fig. C.5(b) in Appendix C, and even in this case three-chain links with higher crossings seem to be more likely for more confined systems.

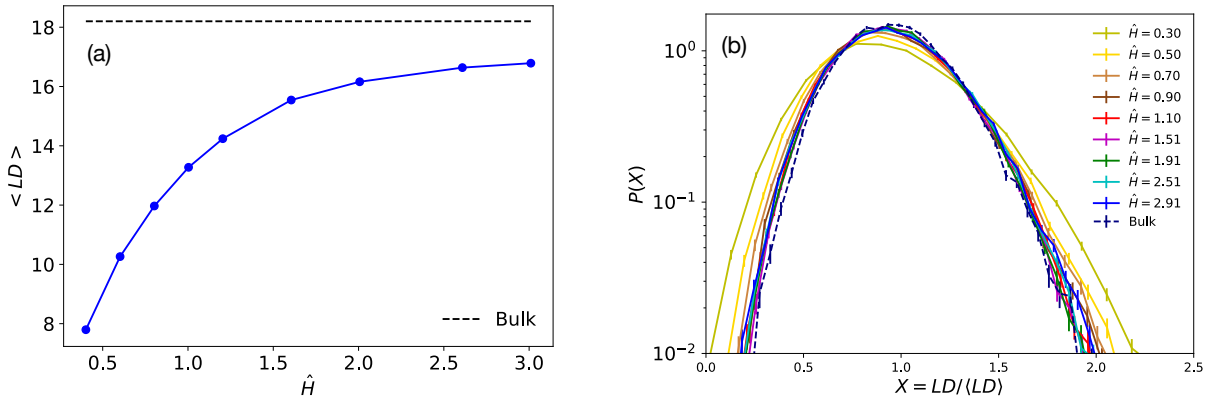

Figure 7.9: (a) Mean linking degree, $\langle \mathrm{LD} \rangle$, as a function of the confinement. The horizontal dotted line represents the bulk value. (b) Distribution functions, $P(\mathrm{LD})$, of the linking degree as a function of the variable normalized to the corresponding mean value $\langle \mathrm{LD} \rangle$. Different colors are for the different confinements, the dashed line is for the bulk system.

Polymer network and entanglements

Concatenated rings give rise to a fully connected polymer network as seen in Chapters 5 and 6. To characterize this network, we use the linking degree, LD_i, of ring i,

$$\mathrm{LD}_i = \sum_{j=1}^{M} \chi_{ij}\, C_{ij}\,, \tag{7.3}$$

previously introduced in Chapter 6. Here the sum runs over the total number of chains in the melt, and where C_{ij} is the $M \times M$ matrix expressing the concatenation status between rings i and j, as defined in Eq.(6.3):

$$C_{ij} = \begin{cases} 0\,, & \text{if } i = j \\ 1\,, & \text{if } i \neq j \textit{ and} \text{ form a two-chain link} \\ 0\,, & \text{otherwise} \end{cases} \tag{7.4}$$

The "weight" factor χ_{ij} takes into account the "complexity" of two-chain links: $\chi_{ij} = |\mathrm{GLN}|$ or $= \frac{K}{2}$ depending on whether $\mathrm{GLN} \neq 0$ or $\mathrm{GLN} = 0$ respectively, with K representing the number of crossings of the link.

This quantity is of special interest as we have showed in the previous chapter that the mean value $\langle \mathrm{LD} \rangle \equiv \langle \frac{1}{M} \sum_{i=1}^{M} \mathrm{LD}_i \rangle$ is directly connected to the entanglement length of the melt, N_e, via the relation $\langle \mathrm{LD} \rangle = N/N_e$ of the systems. To complement this analysis, we have also computed the distribution of the values LD at the single ring level, $P(\mathrm{LD})$, which

gives us information about the heterogeneity of the network.

Results are presented in Fig. 7.9. $\langle \mathrm{LD} \rangle$ (panel (a)) decreases as a function of the confinement, up to a reduction of $\simeq 60\%$ with respect to bulk conditions. Then, by looking at the distribution functions (panel (b)) of the linking degree as a function of $X = \mathrm{LD}/\langle \mathrm{LD} \rangle$, we see that the curves at mild confinements display the same behavior for bulk conditions. Conversely, tails become stronger for more confined systems. This is in agreement with the behaviour seen for the distribution functions of the sizes of the rings (Fig. 7.2(b)), where the tails are higher for stronger confinements. Indeed, fluctuations of ring size may impact on concatenation, since smaller rings will be less concatenated having less possibility to reach other rings, while bigger rings can host more contacts and consequently more concatenations.

To sum up, the resulting polymer networks tend to be less concatenated and, at the same time, more heterogeneous as the confinement become stronger, with the last effect in line with the fluctuations on the rings' sizes.

7.4 Discussion and conclusions

Our findings illustrate the impact that slit confinement has on the spatial structure of randomly concatenated and knotted ring polymers in melt conditions.

At the single-chain level, our investigation shows that as rings flatten with increasing confinement they tend to adopt more elongated conformations. At the same time, rings become slightly more rigid with the confinement, a tendency captured by the increase of the correlation ($\langle \cos(\theta) \rangle$, Fig. 7.4(b)) between consecutive bonds along the chain. We have also demonstrated that the competition between the Kuhn length of the polymers, ℓ_K, and the height of the slit, H, induces a non-monotonous behavior on the bond-vector correlation function, $c(\ell)$ (see Fig. 7.4(a, c, d)). In general, the impact of confinement on ring conformations becomes particularly pronounced with respect to the formation of long intra-chain contacts as the slit narrows (see Fig. 7.5), resulting in more compact rings. Finally, these changes have significant repercussions on the knotting probability which increases with the confinement, and for which we register an increase of $\simeq 130\%$ compared to the bulk value (see Fig. 7.6(a)).

The effects of slit confinement on the inter-chain statistics is similarly noteworthy. Specifically, as the level of confinement increases, the average number of neighbors per ring, $\langle \rho^{\mathrm{ring}} \rangle$, experiences a considerable decrease (see Fig. 7.7(a)). This is directly connected to the decrease of the mean linking degree, $\langle \mathrm{LD} \rangle$, which displays a total reduction of $\simeq 60\%$ with respect to bulk conditions.

This finding has relevant implications. Being $\langle \mathrm{LD} \rangle$ directly related to the mean number of entanglement strands per ring (see Chapter 6) its decrease as confinement grows means that,

at fixed monomer density, confinement alone may alter the entanglement properties of the system making N_e effectively bigger. This would explains recent findings [197, 198] showing that for both linear chains and rings in two-dimensional melts the resulting dynamical quantities display a quite surprising Rouse-like behavior [5, 14] which, ultimately, points towards the effective irrelevance of entanglement effects due to inter-chain interactions. Along the same lines, it is worth recalling that the elastic plateau modulus G_0, which quantifies the stress-strain relationship of polymeric materials, is related [5] to the total number of entanglement strands of the melt, $G_0 \propto \frac{NM}{N_e}$. In other words our results imply that, as confinement grows, the resulting polymer network becomes softer (G_0 decreases), revealing a fundamental connection existing between geometric confinement, topology and the mechanical properties of the stored network. Interestingly, this connection appears to be not limited to only polymer melts but it seems to be a quite general feature appearing in other notable classes of soft materials like, *e.g.*, DNA nanostar hydrogels [199].

We conclude by proposing a possible experimental realization of the systems studied in this work. As discussed in the Introduction, a first experiment [190] on slit-confined kinetoplast DNA – a naturally-occurring catenated network of DNA rings – at different degrees of confinement has already been performed. However, there the topology of the kinetoplast was maintained fixed since the study was focussing on the shape and size rearrangements of the network once placed under confinement. Our predictions here could be tested in a relatively simple variant of this experiment in the following way: as in Krajina *et al.* [93], it would be sufficient to introduce suitable amounts of the enzyme topoisomerase-II and, by doing so, promoting cut-and-resealing events in the system that would reshape the DNA network topology. Then, again as described in [93], by probing the system through microrheology, it should be possible to measure the mechanical properties of the catenated network and verify the predicted softening under confinement.

Chapter 8

The role of entanglement for melts of active polymers

In this chapter, we present some preliminary results in the context of active polymer systems[1]. Active polymers are a new class of polymeric systems that do not obey the classic law of equilibrium statistical mechanics as they are characterized by some mechanism that breaks the detailed balance condition. In this work, we focus on polymer systems subject to non-conservative tangential forces, and we compare the static and dynamical properties of an isolated active linear chain and active linear chains in melt. We show progressive similarity in numerous observables between these two systems as the activity increases. Interestingly, we find that, at high activity, entanglements appear to become less relevant for the dynamic properties of the melt.

The chapter is structured as the following: in Sec. 8.1 I introduce and talk about the relevance and recent results obtained in the new field of active polymers. In Sec. 8.2, I present details about the polymer model and simulation employed for the work. Then in Sec. 8.3 and Sec. 8.4 I present and discuss the main results of the work and we provide potential new outlines worth exploring in the future. Additional figures have been included in the Appendix D.

8.1 Introduction

Active matter consists of systems whose fundamental units can transduce energy into persistent movement leading to very different features with respect to the passive counterparts [200, 201]. Examples of such systems abound in nature, from the macroscopic scale, where we observe the coordinated flight of bird flocks or fish shoals [202], to the sub-cellular

[1]The present work is in collaboration with Dr. Emanuele Locatelli from the University of Padova.

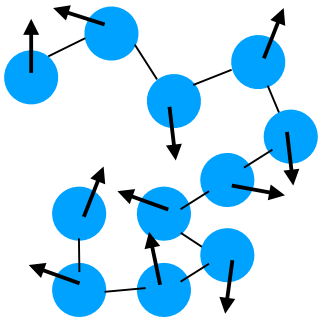

Figure 8.1: Sketch of a polymer made up of active Brownian particles. In this model, monomers are subject to a force (black arrows in the figure) with constant modulus and with direction performing rotational diffusion.

level, as seen in the dynamic behavior of the cytoskeleton within cells [200, 201].

Of late, significant attention has focused on a specific subset of active matter – *active polymers* [203, 204]. This interest arises from their biological relevance, as many biological systems feature molecular motors, which serve as prototypical examples of active matter by converting energy from chemical reactions into motion along biological filaments, such as DNA or RNA. For instance, DNA polymerase [205] traverses DNA strands during replication, while ribosomes [205] actively synthesize proteins by sliding along RNA filaments. Experimentally anomalous diffusion of chromatin loci have been observed [206] and showed to be caused by non-equilibrium processes related to enzymatic activity. Remarkably, experimental efforts have already engineered active polymer chains [207–209]. Consequently, the comprehension of the non-equilibrium statistical mechanics governing active polymer systems poses an important challenge.

Notably, significant progress has been achieved in theoretically and computationally characterizing isolated active linear and ring polymers [203, 204, 210–213]. Most of these works have concentrated on single-chain systems, exploring various implementations of activity. As a first example, polymers made up by *Active Brownian Particles* (ABP) have been considered [203, 204] (see Fig. 8.1). In this case, activity is introduced through a propulsive force with constant modulus and with direction performing rotational diffusion. Conformational and dynamical properties of such systems have been studied in the absence of excluded volume interactions analytically within the framework of the Rouse model [5]. Flexible polymers, for instance, exhibit a monotonous swelling with increasing activity, while semiflexible polymers, characterized by large persistence lengths, display an initial contraction followed by a subsequent swelling, eventually approaching the behavior of their flexible counterparts. In terms of dynamics, these polymers demonstrate activity-dependent persistent motion and asymptoti-

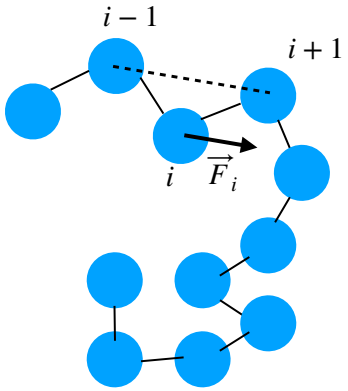

Figure 8.2: Sketch of a polymer subject to active tangential forces. Each bead i is subject to the active force $\vec{F}_i$ (see Eq. 8.1), which is parallel to the vector $\vec{r}_{i+1} - \vec{r}_{i-1}$. In this chapter, we consider polymers subject to this active force.

cally enhanced diffusivity. Remarkably, the diffusion coefficient remains independent of polymer size, representing a stark departure from the scaling of the diffusion coefficient, $D \sim N^{-1}$ [5], for passive polymers.

Inspired by biology and in particular by the action of molecular motors, as kinesin motors [214], DNA and RNA polymerases [215], which, while sliding, exert forces on the backbone of biological filaments, activity has been taken into account also in the form of non-conservative tangential forces applied to the monomers of the polymer chain (see Fig. 8.2) [211–213, 216, 217]. For these systems, analytical results have been obtained in the absence of excluded volume interactions for both linear chains [216] and polymer rings [217]. Intriguingly, these studies have revealed that, for both linear chains and polymer rings, conformational properties remain unaffected by the level of activity. This is in contrast with simulations of self-avoiding active polymers done by Locatelli and collaborators [211–213], *i.e.,* where static properties are heavily dependent on activity. Linear chains [211, 213] shrink as a function of the activity. Polymer rings [212] are characterized by a complex phase behavior as a function of their sizes and the level of activity featuring a region in which polymers collapse. In terms of dynamics, in the absence of interactions linear chains exhibit an increase in polymer diffusivity in line with ABP polymers. Conversely, polymer rings demonstrate intriguing new dynamics, featuring an enhanced rotational motion. Self-avoiding active polymers, in the context of linear chains, exhibit dynamical behavior akin to their ideal counterparts, whereas rings in the collapsed state manifest arrested dynamics. It is worth noting that these investigations highlight the important role of interactions within non-equilibrium systems.

However, few studies, and all restricted to the limit of small activity [220–222] have

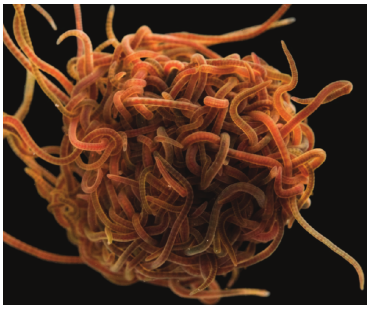

Figure 8.3: A system of entangled worms. Depending on the external conditions, *e.g.*, light and temperature, worms can aggregate forming a blob and can perform directed locomotion. These systems have been modelled as a solution of active linear chains subjected to tangential forces [218].Image adapted from [219]

focused on the case of entangled polymer systems, a feature which, as discussed in the first chapter, is relevant in many contexts as in chromatin organization [37]. Concurrently, the interest in such systems has grown due to recent experiments [223–225] involving systems of living worms (see Fig.8.3), which serve as excellent models for investigating entangled active polymers [219].

For these reasons, this chapter aims to investigate the features of active polymer melts, drawing comparisons with the extensively studied case of isolated chains. First, we will introduce the polymer model and simulation details used for this work in Sec. 8.2. Subsequently, we will show results, by first focusing on static quantities Sec. 8.3.1. Then we will show how entanglement is affected by activity, and by presenting the results on the dynamics Sec. 8.3.3., we demonstrate that it becomes irrelevant to the chains' relaxation process. Finally, the chapter will conclude by discussing the results and proposing potential avenues for further exploration in this evolving field.

8.2 Model and Methods

Differently from the previous chapters, here we employ off-lattice molecular dynamics simulations (see Sec. 2.1.1) to explore and compare the properties of isolated linear self-avoiding active polymers and melts of linear active polymers. The choice of the off-lattice model is because we want to use the well-established polymer model (see Sec. 8.2.1), developed by Locatelli (collaborator of this work), which already served to characterize the behavior of isolated self-avoiding active linear chains [211] and isolated self-avoiding active ring polymers [212].

8.2.1 The polymer model

Chain connectivity and monomer-monomer interactions in melts of linear chains are accounted for by readaptating the classical polymer model by Kremer and Grest [35] (see Sec. 2.1.1). Specifically, the interaction parameter, ϵ, appearing in the purely repulsive LJ potential (see Eq. (2.4)), is changed to $\epsilon = 20\, k_B T$ (against the standard $\epsilon = 1\, k_B T$). Consequently, the spring constant, κ, entering in the FENE bond (see Eq. 2.5) takes the value: $\kappa = 30\epsilon/\sigma^2 = 600\, k_B T/\sigma^2$. The choice of the new parameters makes the FENE bond (Eq. 2.5) stronger and in this way strand-crossings between chains are avoided even in the presence of active tangential forces [212].

Finally, polymer activity is taken into account by imposing that the i-th monomer of each chain of spatial coordinates $\vec{r}_i$ (for $i = 2, ..., N-1$, with N being the total number of monomers of a single chain) is subject to an active force $\vec{F}_i$ [211]:

$$\vec{F}_i = f_a \frac{\vec{r}_{i+1} - \vec{r}_{i-1}}{|\vec{r}_{i+1} - \vec{r}_{i-1}|}\,, \tag{8.1}$$

of constant magnitude f_a and instantaneous orientation directed along the tangent to the polymer chain at $\vec{r}_i$. Notice that, the first and last monomers are (conventionally [211]) excluded by the active perturbation because those monomers have only one, instead of two, neighbor along the chain.

Following the literature [211] the activity is aptly expressed in terms of the so-called Péclet number $\mathrm{Pe} \equiv f_a \sigma / k_B T$ which reflects the strength of the activity *vs.* thermal fluctuations. Here, we work at different Pe's by varying the parameter f_a. More specifically, we have considered $f_a = 1, 5, 10, 20$ corresponding to $\mathrm{Pe} = 1, 5, 10, 20$. At the same time, we have also considered the corresponding *passive* case with $f_a = 0$.

8.2.2 Simulation details

We consider monodisperse melts of M linear polymer chains, each chain being made of N monomers. Specifically, up to $N = 400$ we consider systems resulting in a total of $M \times N = 100000$ monomers: $(M, N) = (1000, 100)$, $(500, 200)$ and $(250, 400)$. Additionally, we simulate systems with $N = 800$ comprising a total of $M \times N = 200,000$ monomers, corresponding to $M = 250$ chains. As in the original work by Kremer and Grest [35], we maintain a fixed monomer density of $\rho = 0.85\sigma^{-3}$ for all values of N.

As mentioned in the introduction, we compare simulation results for active polymer melts with those for isolated self-avoiding active polymers. For the latter case, we simulate the same systems as described above, but we turn off the inter-chain excluded volume interactions. This allows us to effectively simulate replicas of isolated linear chains.

The static and kinetic properties of chains are studied using fixed-volume and constant-temperature Molecular Dynamics (MD) simulations (see Sec. 2.1.1) with implicit solvent and periodic boundary conditions. We integrate the equations of motion using the Velocity Verlet algorithm, with elementary time step with $\Delta t = 0.01\,\tau_{\rm MD}$ in the case of passive polymers ($\mathrm{Pe} = 0$) and $\Delta t = 0.001\,\tau_{\rm MD}$ for all the other cases to prevent strand-crossings. We set $m = \sigma = \kappa_B T = 1$ as the units of mass, length, and energy, respectively, then, the unit of time is $\tau_{MD} = \sigma(m/k_B T)^{1/2} = 1$. Finally, we employ the standard Langevin thermostat with friction coefficient $\gamma = 20\,\tau_{MD}^{-1}$ (see Eq. 2.1). The choice of the value of γ ensures to study the system in the overdamped regime [226]. Simulations are performed using the LAMMPS package [111].

8.2.3 Choice of initial configurations and check for equilibration

Preparation of melts of linear chains poses no technical problem: up to $N = 400$, chains are initially arranged inside the simulation box and the system is passively (*i.e.*, active forces at this stage are turned off) let towards equilibration (*i.e.*, chains are diffusing from their original positions for several times their own size). For the case with $N = 800$, we have first prepared the system on the lattice and let it partially equilibrate using the kinetic-monte carlo algorithm employed in the previous chapters of this Thesis, then we have let the system evolve off-lattice. Being the system highly entangled for the polymer size considered, we did not manage to equilibrate the system properly, yet the results showed in this chapter have been checked to be independent of the initial conditions[2].

These (partially-)equilibrated conformations are the starting point for the production runs of systems with active force ($\mathrm{Pe} \geq 0$).

8.3 Results

8.3.1 Single-chain properties

Rings' size and shape

Initially, we investigate how activity impacts polymer sizes and shapes. In terms of sizes, we examine the scaling behavior of the mean square end-to-end distance, $< R_{ee}^2 >$ (see Eq. 2.9) and of the mean-square gyration radius $< R_g^2 >$ (see Eq. 2.11). Concerning shapes, as in the previous chapter 7, we compute the 3×3 instantaneous symmetric gyration tensor $Q_{\alpha\beta}$ (see

[2]For the preparation of the initial conditions, we have employed the conventional Kremer-Grest potential parameters (see Sec. 2.1.1), specifically, $\epsilon = 1\ k_B T$ and $\kappa = 30\ k_B T/\sigma^2$.

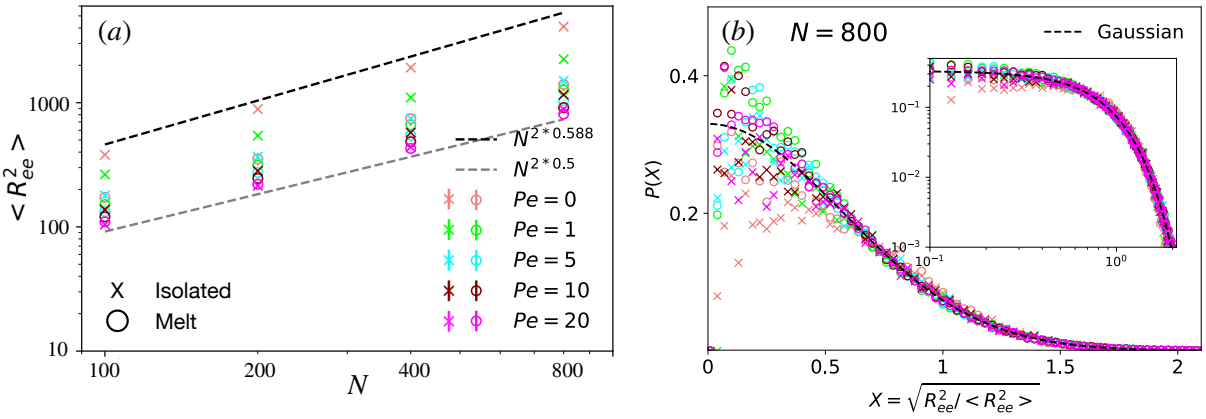

Figure 8.4: (a) Scaling of the mean squared end-end distance, $< R_{ee}^2 >$, as a function of the polymer size, N, for the different Pe compared with the passive case ($Pe = 0$), for isolated ($\times$ symbol) and linear chains in the melt ($\circ$ symbol). (b) Distribution functions of the rescaled end-end distance, $P\left(\sqrt{R_{ee}^2/ < R_{ee}^2 >}\right)$, for both isolated and linear chains in the melt compared with the Gaussian distribution. Color code as in panel (a).

Eq. (2.13)) and we analyse the mean values of its eigenvalues.

Results for $< R_{ee}^2 >$ are reported in Fig. 8.4, and similar results for $< R_g^2 >$ are reported in Appendix in Fig. D.1. The passive case ($Pe = 0$) behaves as expected, isolated linear chains exhibit swelling compared to chains within the melt, with their sizes scaling differently. Specifically, the scaling exponent for isolated chains is $\nu = 0.588$ [5], while in the melt, linear chains follow random walk statistics [5] and their sizes scale with $\nu = 0.5$ (see Fig.8.4 (a)). Notably, in both systems, as Pe grows, the polymers crumple, a feature already seen for isolated active linear chains [211]. Remarkably, at high Peclet number $\simeq 10/20$, across all considered polymer lengths N, $< R_{ee}^2 >$ for both isolated and melt cases converge to similar values. Moreover, at high activity, the scaling of $< R_{ee}^2 >$ appears to align with ideal behavior, exhibiting a scaling exponent of $\nu = 0.5$ for both cases. Similar trends and dependencies on activity are also evident in the mean square gyration radius, R_g^2, as illustrated in Fig. D.1 in the appendix.

By the fact that single chains and chains in melt attain the same average sizes, we have explored the distribution of the end-end distances for both systems so to check whether this correspondence extended beyond the average level. Results are presented in Fig.8.4 (b) for N=800 and in Fig.D.2 for all the other sizes. Notably, distinct deviations from the Gaussian distribution describing ideal polymers are evident in both systems at low Peclet numbers. However, as the Peclet number increases, these distributions begin to align closely. This outcome implies that at elevated activity levels, around $\mathrm{Pe} \simeq 10/20$, at least concerning

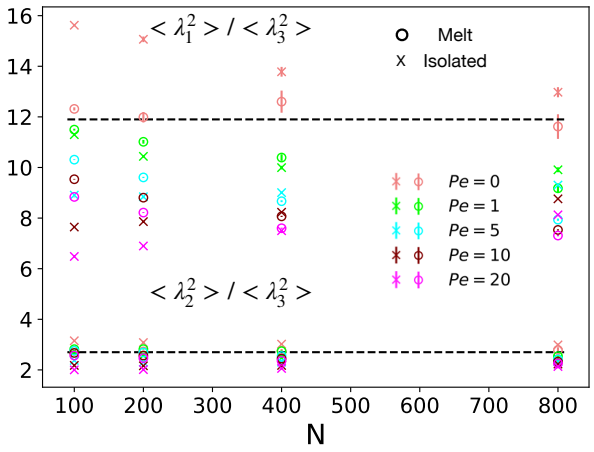

Figure 8.5: Ratios between the first two mean eigenvalues $< \lambda_1^2 >$, $< \lambda_2^2 >$ and the smallest one $< \lambda_3^2 >$. Black dashed lines correspond to the asymptotic values of the ratios, respectively 11.9 and 2.7, for equilibrium chains in melt obtained in [44].

$< R_{ee}^2 >$, whether a chain is isolated or in melt appears to have a minimal impact on its extension.

The crumpling of polymer chains induced by activity points to a significant reorganization in terms of polymer conformations, and this transformation is, to some extent, summarized by the ratios of the eigenvalues of the gyration tensor Q: $< \lambda_1^2 > / < \lambda_3^2 >$ and $< \lambda_2^2 > / < \lambda_3^2 >$. Results are contained in Fig. 8.5. Ratios for the passive case of linear chains in the melt are fairly in agreement with previous measurements obtained for the same system [44], respectively 11.9 and 2.7, which in turn are quite near the ratios one would obtain from a random walk, respectively 12 and 3 [44]. Instead, isolated linear chains are less spherical in the passive case, *i.e., the ratios are bigger respect to the melt*. As activity increases, the ratios decrease for both systems. However, even at $\mathrm{Pe} = 20$, the difference between the two systems persists, with active isolated chains appearing less spherical. Intriguingly, while linear chains in the melt display a decreasing trend in the ratio $< \lambda_1^2 > / < \lambda_3^2 >$ with N, single chains, at high activity levels ($Pe \geq 10$), exhibit an increase in this ratio with increasing polymer length. This implies that longer isolated chains are less spherical than their shorter counterparts.

In summary, both isolated chains and chains in the melt undergo a reduction in size as activity increases, and for $\mathrm{Pe} \geq 10$, their mean-square end-to-end distances, $< R_{ee}^2 >$ (and $< R_g^2 >$), converge to nearly identical values. This correspondence also holds for their distribution functions. However, when it comes to polymer shapes, quantified by the ratios of the eigenvalues of the gyration tensor (see Fig. 8.5), linear chains in the melt tend to adopt more spherical conformations compared to their isolated counterparts. Nevertheless, both

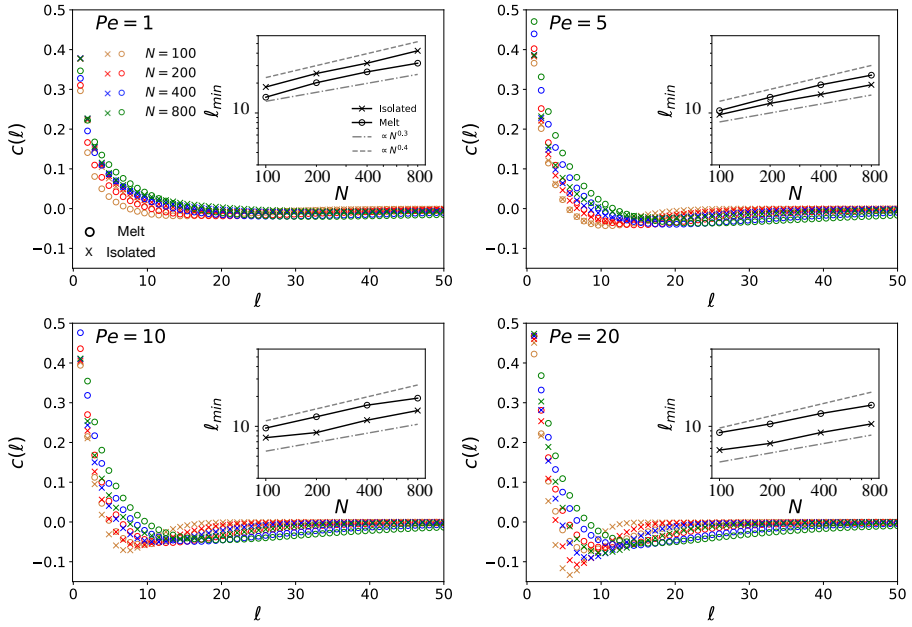

Figure 8.6: $c(\ell)$, bond-vector correlation function as a function of the contour length distance ℓ for all the $Pe > 0$ considered and polymer sizes simulated for both isolated ($\times$ symbol) and melt ($\circ$ symbol) cases. Insets display the position of the minima, ℓ_{min}, of $c(\ell)$ as a function of the polymer size N

systems become progressively spherical as activity increases.

Tangent correlation function and internal distances

The mean-square end-to-end distance, $< R^2_{ee} >$, provides a global measure of the polymer extension but cannot reveal multi-scale information, which, as we will see in this section, contains a more complex pattern with respect to the one shown so far. To this end, we have computed the tangent-tangent correlation function (see Eq. (2.15)), $c(\ell)$, as a function of contour length distance[3], ℓ, since, as demonstrated in the previous chapters, it may offer valuable insights into polymer folding at various length scales. Simultaneously, we have calculated the mean square internal distance between monomers[4], $< R^2(\ell) >$, as a function of ℓ. While $< R^2(\ell) >$ inherently contains the information of $< R^2_{ee} >$, as $< R^2\,(L = N\langle b\rangle) >=< R^2_{ee} >$, it also offers details regarding the scaling of the distances at different length scales. Particularly significant is the local logarithmic derivative, $\nu(\ell)$, which can be extracted from $< R^2(\ell) >$. This observable informs us about how polymer size scales locally with ℓ (Eq. (2.12)).

[3]As in the previous chapters (see Eq. (2.15)), $\ell \equiv n\langle b\rangle$, with n representing the distance in monomer units and $\langle b\rangle$ the average bond length.

[4]It is worth mentioning that $c(\ell)$ and $R^2(\ell)$ are deeply connected being $c(\ell) = \frac{d^2 R^2(\ell)}{d\ell^2}$ [122].

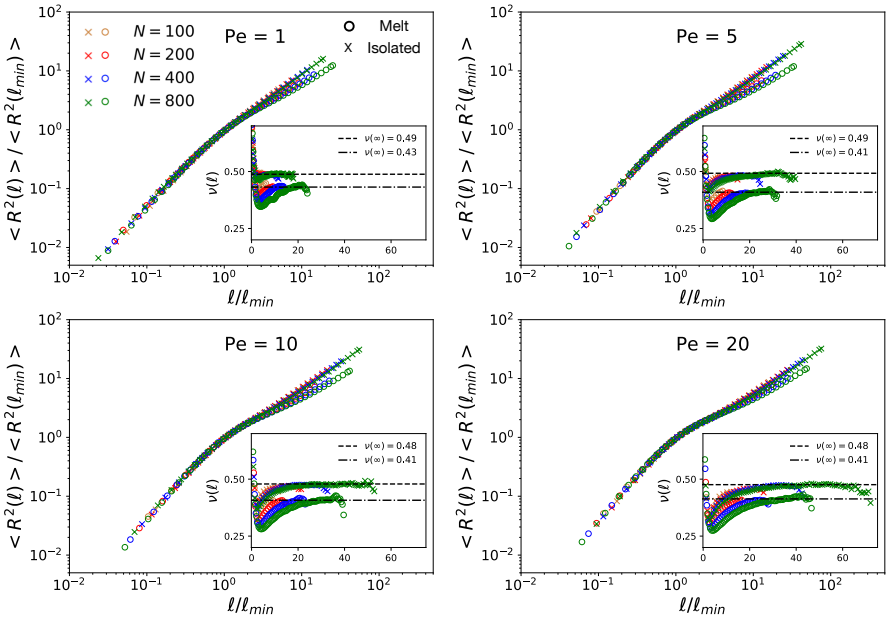

Figure 8.7: Mean-square internal distance, $R^2(\ell)$, as a function of the contour length distance along the polymer chain ℓ for all the $\mathrm{Pe} > 0$ considered and the polymer sizes, N, simulated for both isolated ($\times$ symbol) and melt ($\circ$ symbol) systems.

Results for $c(\ell)$ are presented in Fig. 8.6 for the different $Pe \geq 1$ studied for both isolated and melt systems. The passive case is illustrated in Fig. D.3 (a) in the Appendix D. In all the active cases, $c(\ell)$ exhibits an anti-correlation pattern at characteristic length scales denoted as ℓ_{min}. The value of ℓ_{min} depends on both Pe and the polymer size N and varies depending on whether the chain is isolated or within the melt. As activity increases, ℓ_{min} decreases, reaching values approximately around $\simeq 10\sigma$ for $\mathrm{Pe} = 20$. Notably, isolated chains display a smaller ℓ_{min} compared to chains in the melt. This suggests that linear chains, whether isolated or in the melt, tend to fold into loops (see Chapter 3) at a characteristic contour-length of ℓ_{min}, with isolated chains forming smaller loops. Even if the minima are deeper for isolated chains, the correlation decays more rapidly compared to chains in the melt. This indicates that larger loops are more prevalent in the case of chains in the melt, aligning with the observation that these chains tend to be more spherical (see Fig. 8.5) compared to their isolated counterparts[5]. Moreover, ℓ_{min} exhibits slow power-law growth as N^{α} (see inset in Figure 8.6), with α within the range $0.3 < \alpha < 0.4$ for all the investigated values of Pe.

Results for $< R^2(\ell) >$ are presented for the active cases in Fig. 8.7 and Fig. D.4, and for the passive case in Fig. D.3 (b). First, by considering the size-dependent typical scale

[5]Furthermore, it is important to note that the anti-correlation pattern and dependencies of $c(\ell)$ on the polymer size N is a feature completely absent in the passive case (see Fig. D.3).

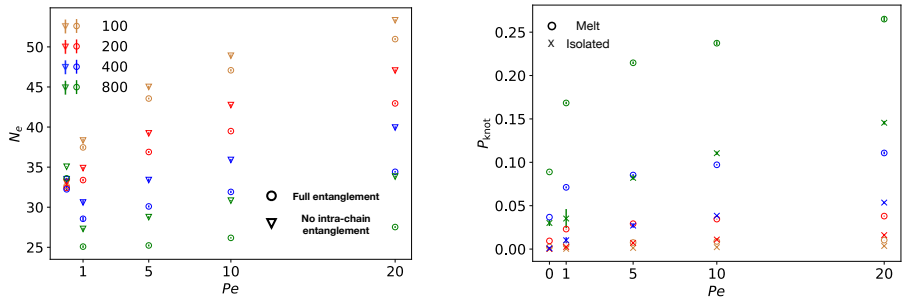

Figure 8.8: (a) Entanglement length, N_e, as a function of Pe for all the N considered. Employing the Z1 algorithm, we estimate N_e considering ($\circ$ symbols) or not ($\triangledown$ symbols) the effect of inter-chain entanglements. (b) Knotting probability, P_{knot}, for both the isolated ($\times$ symbols) and melt ($\circ$ symbols) case as a function of Pe, for all the N considered.

of the loop, ℓ_{min}, we have rescaled the $< R^2(\ell) >$ by the typical size of the loop given by $< R^2(\ell_{min}) >$ and plotted the ratio as a function of ℓ/ℓ_{min}. By rescaling by these factors, all the curves for both isolated and melt systems collapse for all[6] N up to $\ell/\ell_{min} \simeq 1$. Initially, both systems display a regime for $\ell \ll \ell_{min}$ for which the chains are more persistent than a random walk being $\nu(\ell) > 0.5$ (see inset of Fig. 8.7). Then, at $\ell/\ell_{min} \simeq 1$, the looping, already highlighted by $c(\ell)$, gets manifested with a surprisingly low value of ν which further diminishes with increasing activity. Asymptotically, $\ell/\ell_{min} \gg 1$, the curves of the two systems deviate attaining different asymptotic values for $\nu(\infty)$ (see inset of Fig. 8.7). Interestingly, these asymptotic values appeared to be independent of the activity level from $Pe \gtrsim 5$. Specifically, we find $\nu(\infty) = 0.48$ for single chains, and $\nu(\infty) = 0.41$ for chains in melt, in both cases the result is independent of N.

This finding may appear at odds with the observations in Fig. 8.4, where both systems displayed a scaling behavior of $< R^2_{ee} > \sim N$ at high Peclet values. However, it is crucial to recognize that the differences between the global and local-scale analyses can be attributed to the size-dependent properties of the polymer chains (see Figs. 8.6 and D.4). Indeed, the scaling of $< R^2_{ee} >$ as a function of the polymer's size, N, is also influenced by the subtle dependence of ℓ_{min} on N (Fig. 8.6). Moreover, it is worth mentioning that these features arise due to the presence of activity, since for passive systems the polymer's size does not alter the local static properties of the polymer chain (see Fig. D.3).

[6]Note that, without the rescaling, the curves are not universal and depend on N on almost the whole range of ℓ (see Fig. D.4).

8.3.2 Entanglement and topology

The influence of activity on the conformational properties of polymers in melt naturally prompts the question of how interactions among the chains are affected too. As shown in the first chapter (see Sec. 1.2.2), the properties of a polymer chain in melt are well described by the tube model of Edwards [13, 14]. According to this model, all the interactions between a reference chain and all the other chains in the melt are effectively summarized by an effective tube-like region constraining the motion of the test chain. The size of the tube is given by the tube diameter, d_T, which in turn depends (see Eq. (1.2)) on the entanglement length N_e. In this section, we explore how entanglement, and in particular N_e, is affected by the activity.

To this end, as in Chapters 6, we apply the Z1+ algorithm [174] to compute N_e as a function of Pe both with and without accounting for intra-chain entanglements (knots). Moreover, to complement this analysis and to understand the extent of intra-chain entanglement, we have also computed the probability of finding a chain to be knotted. To this purpose, as in Chapter 6, we compute the Jones polynomials associated with the polymers using the Python package[7] Topoly [173]. While, for the entanglement properties, we analyze just the linear chains in the melt, for the knotting probabilities we also study the isolated case and compare the two systems.

The results are presented in Fig. 8.8. In the passive case, for all N, N_e falls within the range of $30 \lesssim N_e \lesssim 35$, with only slight differences between the estimates accounting or not the intra-chain entanglements. Turning on the activity makes N_e first drop, *i.e.*, chains are more entangled with respect to the passive case (except polymers of size $N = 100$), and then raise again with Pe. Notably, for the longest size considered, $N = 800$, we find that N_e results to be lower with respect to the passive case, even at $\mathrm{Pe} = 20$. This behavior is surprising because, given that the chains shrink with activity, one would expect that active chains would interpenetrate less. Yet, we recall that active linear chains assume quite different conformations with respect to the passive case which may lead to different entanglement behavior. In particular, it could be that while forming loops, chains get entangled with other chains forming links, which, as previously established in Chapter 6, are responsible for entanglement in the melt. Anyway, we do not dig further into the matter as we show in the next section 8.3.3 that entanglements become irrelevant for the chains' relaxation dynamics in the presence of activity.

Additionally, two other notable effects are worth mentioning. First, unlike the passive case, there is a substantial dependence of N_e on N, which aligns with previous observations regarding the size dependence of structural polymer properties in the active case. Second, a

[7] See caption of Fig. 6.10 for more details on how knots in open chains are detected in Topoly.

clear distinction emerges between the estimates of N_e when considering or not knots, absent in the passive case, which becomes particularly evident at high Pe. This observation aligns with the increasing knotting probability, P_{knot}, as a function of Pe for all N (see Fig. 8.8 (b)). Notably, for $N = 800$, we observe an increase in P_{knot} of $\simeq 300\%$ at $Pe = 20$ respect to the equilibrium value ($Pe = 0$). Overall, in both systems, activity enhances P_{knot}, with linear chains in the melt exhibiting a significantly higher propensity for knotting compared to the isolated case.

8.3.3 Dynamics

Finally, we focus on how the activity influences the dynamics of the polymer chains. Previous works have demonstrated that the diffusion of isolated linear chains is enhanced by the action of active tangential forces [211, 216, 226]. This enhancement is reflected in the mean square displacement of the center of mass (Eq. (2.18)), g_3, exhibiting first a ballistic regime, proportional to t^2, up to the decorrelation time, denoted as τ_{relax}, of the end-end vector, $\vec{R}_{ee}$. Beyond this initial regime, it follows an asymptotic diffusive behavior with a diffusion coefficient, D, that increases with Pe and is independent of the chain length, N, in contrast with the passive case dependence of $D \sim N^{-1}$ [5].

As in the previous studies, we focus on g_3 (see Eq.(2.18)) and we estimate τ_{relax} from the condition:[8] $g_3(\tau_{relax}) \equiv < R_{ee}^2 >$. Finally, we also extract the diffusion coefficient, D, from the asymptotic behavior of g_3.

The results are presented in Fig. 8.9. Interestingly, when we divide g_3 by $< R_{ee}^2 >$ and plot it as a function of the reduced time $x = \tau_{MD}/\tau_{relax}$, all the curves, for both isolated and melt chains, collapse onto the same master curve. The universal dynamics is characterized by a first regime, $x \leq 1$, in which chains undergo a ballistic regime, after which diffusion takes over. This result is quite surprising, in particular for the melt systems. Indeed, according to the tube model, for $\tau_{MD} < \tau_{relax}$, dynamics is expected to be sub-diffusive, *i.e.*, $g_3 \sim t^{1/2}$, as a result of the constrained diffusion of the chain along the tube. The absence of such regime and the universality of the dynamics suggests that the dynamics is entirely governed by the time-scale τ_{relax} and its associated length-scale $< R_{ee}^2 >$. Consequently, it implies that entanglement becomes irrelevant for the chain's relaxation dynamics when chains are subject to tangential forces, which is in stark contrast to the passive case for which entanglement significantly affects the chain's dynamics [5, 14]. Enforcing the last point, we observe that τ_{relax} scales almost linearly with N in both systems (see inset of Fig. 8.9), which again deviates

[8] This choice is based on the fact that when the chain moves over distances comparable to its end-end distance, the end-end vector should decorrelate.

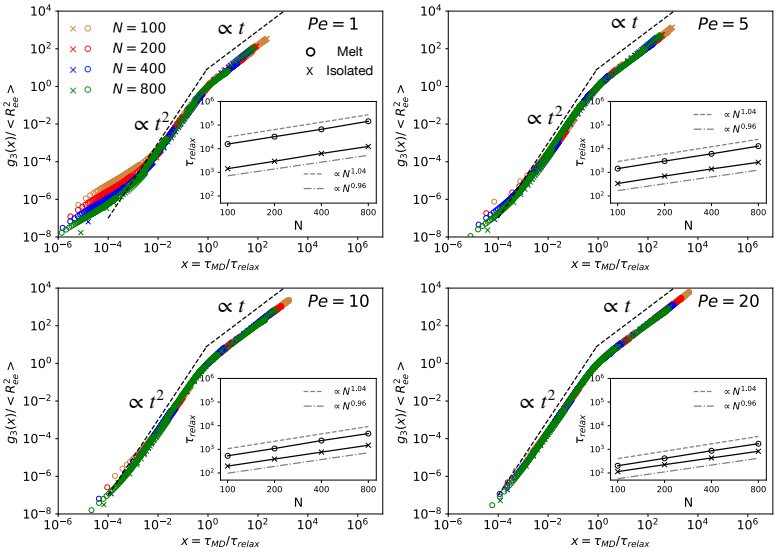

Figure 8.9: Mean square displacement of the centre of mass, g_3, for all the N considered, with $\times$-symbols corresponding to single-chain systems and $\circ$-symbols to chains in the melt. Each panel corresponds to a value of Pe. Here, the mean-square displacement, g_3, of any system is divided by the corresponding $< R^2_{ee} >$ and plotted as a function of τ_{MD}/τ_{relax}, with τ_{relax} defined as: $g_3(\tau_{relax}) =< R^2_{ee} >$.

significantly with the slow relaxation in passive melts, *i.e.*, $\tau_{relax} \propto N^3$ [5, 14]. Yet, it is worth noting that τ_{relax} for melts of active chains differs for a prefactor from the single chain's one. However, these differences decrease with Pe.

To conclude this analysis, we present the results regarding the asymptotic diffusion coefficient, D, reported in Fig. 8.10. First, we find that activity enhances the diffusion of both systems, with D becoming independent of N. In both systems, D grows as a power-law in Pe, denoted as $D \sim \mathrm{Pe}^{\alpha}$. For single chain and chains in the melt we find[9] a value of $\alpha_{isolated} = 0.54 \pm 0.05$ and $\alpha_{melt} = 1.05 \pm 0.03$, respectively. The fact that D grows more rapidly as a function of Pe for melts of chains, in comparison to single chains, aligns with the decrease in the difference of τ_{relax} between the two systems as Pe increases (see insets of Fig. 8.9).

Taken together, these results suggest that the dynamics becomes universal, independent of whether chains are isolated or in melt. In particular, entanglement, which is fundamental in the passive case, might enter at most in the prefactors of the quantities characterizing such dynamics as in the case of τ_{relax} and D.

[9]The estimates on the exponents have been obtained by separately performing power-law fits for all N, and then by averaging over the N-dependent exponents. The error is the standard deviation of those exponents.

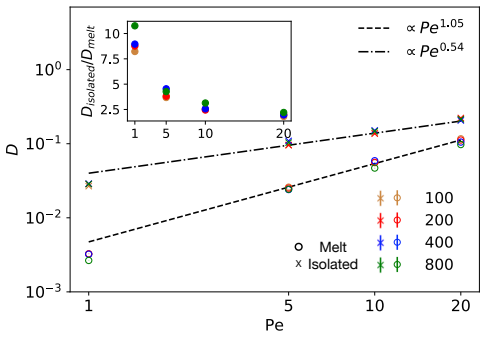

Figure 8.10: Asymptotic diffusion coefficient, D, as a function of Pe for all the N considered and for both systems of isolated chains ($\times$ symbols) and chains in the melt ($\circ$ symbols). The exponents of the plotted power-laws have been obtained by separately performing power-law fits for all N, and then by averaging over the N-dependent exponents. Inset shows the ratio between the diffusion coefficient of the two systems, $D_{isolated}/D_{melt}$, as a function of Pe for all the N considered.

8.4 Discussion and Conclusions

In this chapter, we have investigated the impact of activity on the conformational and dynamical properties of linear chains in the melt and compared these results with the behavior of isolated linear chains.

Regarding conformational properties, we have demonstrated that chains in the melt exhibit a size reduction, similar to the isolated case. Intriguingly, at high activity levels (Peclet number $Pe \geq 10$), chains of both systems converge to similar sizes, as evidenced by both $< R_{ee}^2 >$ (see Fig. 8.4 (a)) and by $< R_g^2 >$ (see Fig. D.1). Moreover, once we look at the scaling of these global observables, both systems exhibit random walk scaling.

However, when exploring multi-scale observables like $c(\ell)$ and $R^2(\ell)$, we find a more intricate pattern. Notably, we observe deviations from random walk statistics, particularly for the formation of loops (see Fig. 8.6) within the chains. Moreover, the asymptotic exponent ν extracted from $R^2(\ell)$ deviates from the random walk value of $\nu = 1/2$. While the deviation is small for single chains as we find $\nu \simeq 0.48$, chains in the melt deviate significantly reaching a value of $\nu \simeq 0.41$.

Turning to the dynamics, we find that both systems remarkably exhibit the same dynamics (see Fig. 8.9) governed by the time-scale τ_{relax}, which scales linearly with N. The values of τ_{relax} for the two systems differ by a prefactor that decreases with Pe, and for $\mathrm{Pe} = 20$, the prefactor is $\simeq 2$. At long times, $\tau \gg \tau_{relax}$, both systems diffuse with a diffusion coefficient, D, which increases with Pe (see Fig. 8.10) and is independent on N. As for τ_{relax}, the dif-

ference in D between the two systems becomes smaller with Pe. In summary, our findings suggest that multi-chain interactions, such as entanglements, become negligible when chains are subjected to tangential active forces. These results align with experimental observations [224] on active worms, which showed a decrease in system viscosity with activity, and a milder dependence on concentration compared to passive entangled systems.

To conclude, this chapter offers insights into how activity influences generic entangled polymeric systems. These findings lay the groundwork for more complex models of active entangled polymer systems. For instance, one can consider non-uniform active forces to model regions of chromosomes with varying levels of activity inside the nucleus [227]. Additionally, future studies could explore the dynamics of chains where only one chain's end is subjected to active forces, akin to the activity observed in the heads of active worms [218]. Finally, out-of-equilibrium rings in the melt have been studied [43], there the non-equilibrium is due to the mixed composition of rings made up of monomers with different mobilities. The asymmetry, as demonstrated, leads to a transition into a glassy state. Thus, it would be interesting to understand whether this phenomenon is universal or dependent upon the specific mechanisms employed to induce non-equilibrium conditions within the system.

Conclusions

In this Thesis, I have investigated the role of topology and entanglement in the physics of ring polymers in melt conditions. First, I have focused on the role of permanent topological constraints, which are fundamental in the physics of chromatin organization, by studying melts of non-concatenated and unknotted polymer rings. Then, inspired by the recent realizations of topologically complex polymer assemblies, I have focused on melts of polymer rings with unconstrained topology, exploring the relations between several polymer parameters, such as the polymer contour length and its bending rigidity, and the topology of the systems. Finally, deviating from the main theme of the Thesis, I have explored the physics of active linear polymers in melt conditions.

In detail, we have studied the following problems:

- In Chapter 3, we have studied the properties of melts of non-concatenated and unknotted polymer rings at varying bending rigidity. In particular, we have characterized the conformational properties of such systems addressing the apparent contradiction between the postulated double-folding of the rings and the formation of threadings, which implies that rings must be open. Based on extensive numerical simulations, we showed that most of the threadings are localized at scales smaller than the tube diameter, d_T, while rings double fold on and above the entanglement length, N_e. This explains why large-scale ring features are well accounted for by the lattice-tree models. Additionally, through an analysis of the mean polymer shapes, we have established a scaling relationship between the largest and smallest eigenvalues of the gyration tensor, which is in quantitative agreement with the lattice-tree theory of Grosberg. Finally, we have characterized the dynamics of these systems and observed that most aspects are well accounted by both the lattice tree and the fractal loopy globule models. However, we have shown that threadings can cause divergence in the relaxation time of a partially immobilized system. This observation cannot be explained by these models, highlighting the necessity of incorporating threadings for an accurate description of ring dynamics.

- The aim of Chapter 5 was to create a model suitable for the description of systems

like the recently synthesized Olympic DNA networks. To this end, we have developed a polymer lattice model with Monte Carlo dynamics which integrates the strand-crossing mechanism, allowing for the manipulation of ring topologies. Then, we applied this model to studying melts of polymer rings with different contour lengths. We have shown that rings with unconstrained topology (allowing for strand-crossing) swell and attain ideal statistics. We also have characterized the topology of the melt. At the single-chain level, we have found that knots are rare even for long entangled chains ($N/N_e \simeq 10$). As for links, we have focused on the characterization of the resulting network of concatenated rings. We have found that rings form a fully connected network when, on average, each ring is connected to more than two other rings, which occurs at $N/N_e \gtrsim 2$. As for the dynamics, we have shown the presence of two dynamical regimes depending on the interplay between the inverse of the strand crossing rate, λ_{SC}^{-1}, and the self-diffusion time of untangled rings, τ_d. When $\lambda_{SC}^{-1} < \tau_d$, strand-crossing rings relax faster, and their diffusion is enhanced with respect to the untangled case, consistent with experimental available observations. Conversely, for $\lambda_{SC}^{-1} > \tau_d$, the strand-crossing mechanism slows down ring dynamics, a prediction that could be experimentally tested.

- In Chapter 6, we have addressed the problem of the relationship between entanglement and topology in polymer melts. To this end, we have exploited rings with unconstrained topology as model systems to represent ideal polymer melts. First, we have analysed the topology and entanglement of the networks of polymer rings as a function of polymer length and bending rigidity. In particular, we have developed an algorithm that can detect "topological interactions" at any order and we have applied it for the detection of knots, 2-chain links, and 3-chain links. In parallel, we have estimated N_e of these systems using the Z1 algorithm. Finally, we have shown that the number of entanglements per chain, N/N_e, is recovered by the ring mean linking degree, $\langle \mathrm{LD} \rangle$, demonstrating that the topology of the melt is directly linked to its entanglement. Moreover, we have shown that 2-chain links contribution to $\langle \mathrm{LD} \rangle$ is sufficient to match the estimates of N/N_e, indicating that higher-order links have negligible influence on the entanglement properties of the melts.

- In Chapter 7, motivated by recent experiments performed on the Kinetoplast DNA at varying degree of confinement, we have investigated how geometric constraints can affect the structural and topological properties of melts of strand-crossing rings. Specifically, we have explored systems experiencing a range of slit confinements, from highly confined to mildly confined regimes. We have found that geometric constraints affect deeply both single-chain and many-chain properties. Notably, as the level of confinement increases,

the resulting network becomes less interconnected. We argue that this observation suggests the potential use of confinement as a mean to fine-tune the mechanical properties of Olympic networks. In particular, confinement can bias the synthesis process towards the creation of softer networks.

- In Chapter 8, motivated by the relevance of active polymers in modeling biological systems, we have explored how activity, under the form of non-conservative tangential forces, affects the properties of melts of linear chains in comparison with the single-chain case. Interestingly, we have observed that the two systems exhibit striking similarity when focusing on global properties, such as $< R_{ee}^2 >$. However, employing a multi-scale analysis, we have revealed differences between the two, prominently manifesting in the form of a distinct scaling exponent, ν. Finally, we have found that active chains in melt do not display any indication of reptation and their dynamics is similar to the one of active single chains. In this regard, we have shown that the differences between the two systems, in the relaxation time, τ_{relax}, and in the asymptotic diffusion coefficient, D, decrease with increasing activity. All these observations point towards the fact that entanglement becomes less important with increasing activity.

In conclusion, in my PhD work, I have used computer simulations to address fundamental questions regarding the spatial and dynamic behaviors of melts of ring polymers. The physics of these systems is of crucial interest in the design and synthesis of soft materials with non-conventional mechanical properties while, at the same time, it displays intriguing connections to the biophysics of chromosome behavior in cell nuclei.

Expanding from the results presented in this Thesis, several questions remain to be addressed. In particular, the integration of the role of ring-ring inter-threadings is pivotal to a faithful understanding of the mechanisms behind rings' dynamics, yet most of its aspects remain unclear. From the perspective of topological materials, several predictions, such as the confinement-induced softening or the relationship between rings' dynamics and strand-crossing rates, have been obtained and it would be interesting to test them experimentally. Finally, in the context of active polymers, there are a lot of possible directions to be explored: as an example, active processes shape chromatin organization and its transcription, then it would be interesting to construct realistic polymer models of chromatin that can account for these non-equilibrium effects.

Acknowledgments

Here comes the most interesting part of any PhD Thesis: the Acknowledgments.

First, I would like to thank my supervisor, Prof. Angelo Rosa, for his constant guidance and patience. Thank you for helping and mentoring me at every stage of this long path.

After all the years I spent in Trieste, SISSA has become a second home to me. Here, I have met many people whom I can call friends. In particular, I would like to thank Giuseppe, Jack, Pierluigi, Piero, Sara, and Saman for all the happy moments spent during these years. Also, I want to thank all the people I played with in the SISSA Soccer Team, with a special mention to Hayato and Maskio. Thank you because I had a lot of fun even if we were not so (just to use a euphemism) successful. Finally, my time in Trieste wouldn't have been the same without the constant presence of Betta and all the spritz and pizza we had in Barcola (we basically invented this).

Before Trieste, I enjoyed my time in Trento, where I met many friends. In particular, I would like to thank Jack (again), with whom I shared many hours of studying, countless hours of YouTube videos, and much more (like your wedding). Then I would like to thank Elena, even if we don't see each other much, every time we meet it's always as when we were in Trento.

It has been a while since I lived in Ostra, yet I am always happy to come back, and this is for all the old and good friends I have there. In particular, I would like to thank Matteo. Even if we are distant most of the time, I know I can count on you for anything.

Infine, vorrei ringraziare la mia famiglia, i miei genitori, mia sorella e la sua nuova famiglia, e i miei nonni. Se sono qui, è sicuramente anche grazie a voi.

Infine, vorrei ringraziare Francesca, con la quale ho condiviso qualsiasi momento vissuto negli ultimi (tanti :)) anni. Non vedo l'ora di passarne altrettanti e più insieme.

Appendix A

Supplementary material of Chapter 5

N	M	$T_{\mathrm{run}}\,[\tau_{\mathrm{MC}}]$	$\tau_d\,[\tau_{\mathrm{MC}}]$	N	M	$T_{\mathrm{run}}\,[\tau_{\mathrm{MC}}]$	$\tau_d\,[\tau_{\mathrm{MC}}]$
Ideal rings				Melts of untangled rings			
40	100	$\simeq 6.0 \cdot 10^6$	$\simeq 7.0 \cdot 10^3$	40	5120	$\simeq 2.0 \cdot 10^6$	$\simeq 1.0 \cdot 10^4$
80	100	$\simeq 6.0 \cdot 10^6$	$\simeq 7.0 \cdot 10^3$	80	2560	$\simeq 2.0 \cdot 10^6$	$\simeq 3.0 \cdot 10^4$
160	100	$\simeq 6.0 \cdot 10^6$	$\simeq 1.0 \cdot 10^4$	160	1280	$\simeq 2.0 \cdot 10^6$	$\simeq 2.0 \cdot 10^5$
320	100	$\simeq 9.0 \cdot 10^6$	$\simeq 4.0 \cdot 10^4$	320	640	$\simeq 4.0 \cdot 10^6$	$\simeq 7.0 \cdot 10^5$
640	200	$\simeq 1.5 \cdot 10^7$	$\simeq 2.0 \cdot 10^5$	640	320	$\simeq 1.5 \cdot 10^7$	$\simeq 3.0 \cdot 10^6$
Melts of rings with strand crossings				Melts of permanently catenated rings			
40	5120	$\simeq 2.0 \cdot 10^6$	$\simeq 1.0 \cdot 10^4$	40	5120	$\simeq 2.0 \cdot 10^6$	$\simeq 1.0 \cdot 10^4$
80	2560	$\simeq 2.0 \cdot 10^6$	$\simeq 3.0 \cdot 10^4$	80	2560	$\simeq 2.0 \cdot 10^6$	$\simeq 5.0 \cdot 10^4$
160	1280	$\simeq 2.0 \cdot 10^6$	$\simeq 1.0 \cdot 10^5$	160	1280	$\simeq 7.0 \cdot 10^6$	$\simeq 5.0 \cdot 10^5$
320	640	$\simeq 5.0 \cdot 10^6$	$\simeq 6.0 \cdot 10^5$	320	640	$\simeq 9.8 \cdot 10^7$	–
640	320	$\simeq 1.4 \cdot 10^7$	$\simeq 2.0 \cdot 10^6$	640	320	$\simeq 1.9 \cdot 10^8$	–

Table A.1: Computational cost of MC runs. In interacting systems (melts) M is the total number of chains, whereas for ideal systems with no excluded volume interactions it represents the number of single independent runs. (i) T_{run}: length of the single MC run. (ii) τ_d: ring self-diffusion time. Values for permanently catenated rings with $N = 320$ and $N = 640$ are not defined because the corresponding time mean-square displacements of the centre of mass ($g_3(\tau)$, Eq. (2.18)) attain the characteristic plateaus for stacked dynamics (see Fig. 5.8(c)). $\tau_{\mathrm{MC}} = N \cdot M$ is the Monte Carlo time unit (see Sec. 5.2.4 for details).

N	$\langle R_g^2\rangle/a^2$	$P_{\rm knot}$	N	$\langle R_g^2\rangle/a^2$	$P_{\rm knot}$
	Ideal rings			Melts of untangled rings	
40	3.178 ± 0.002	–	40	3.3334 ± 0.0004	–
80	6.284 ± 0.006	–	80	6.361 ± 0.003	–
160	12.52 ± 0.02	–	160	11.88 ± 0.02	–
320	24.9 ± 0.1	–	320	21.9 ± 0.1	–
640	50.0 ± 0.3	–	640	38.1 ± 0.5	–
	Melts of rings with strand crossings			Melts of permanently catenated rings	
40	3.5093 ± 0.0005	0	40	3.521 ± 0.004	–
80	7.088 ± 0.004	$1 \cdot 10^{-3}$	80	7.10 ± 0.01	–
160	14.30 ± 0.02	$6 \cdot 10^{-3}$	160	14.36 ± 0.07	–
320	28.6 ± 0.1	$3 \cdot 10^{-2}$	320	29.3 ± 0.3	–
640	57.6 ± 0.4	$9 \cdot 10^{-2}$	640	59 ± 1	–

Table A.2: Single-chain properties in melts of N-monomer rings. (i) $\langle R_g^2\rangle$: ring mean-square gyration radius, expressed in lattice units. (ii) $P_{\rm knot}$: mean knotting probability per chain (only for melts of rings with strand crossings).

N	GLN_0	$\langle\mathcal{L}\rangle$	$p_{\rm link}$
40	0.164 ± 0.004	0.376 ± 0.001	$(7.32 \pm 0.02) \cdot 10^{-5}$
80	0.22 ± 0.01	1.143 ± 0.003	$(4.46 \pm 0.01) \cdot 10^{-4}$
160	0.29 ± 0.01	2.754 ± 0.004	$(2.153 \pm 0.003) \cdot 10^{-3}$
320	0.36 ± 0.01	5.77 ± 0.01	$(9.00 \pm 0.02) \cdot 10^{-3}$
640	0.46 ± 0.01	10.92 ± 0.08	$(3.29 \pm 0.02) \cdot 10^{-2}$

Table A.3: Network properties in melts of N-monomer rings with strand crossings. (i) GLN_0: decay length for the probability distribution function of the Gauss linking number, $P(N;\mathrm{GLN}) \sim e^{-|\mathrm{GLN}|/\mathrm{GLN}_0(N)}$ (see Fig. 5.6 and Fig.A.1 in Appendix A). (ii) $\langle\mathcal{L}\rangle$: mean number of chains linking to a single ring. (iii) $p_{\rm link}$: mean fraction of pairs of linking rings.

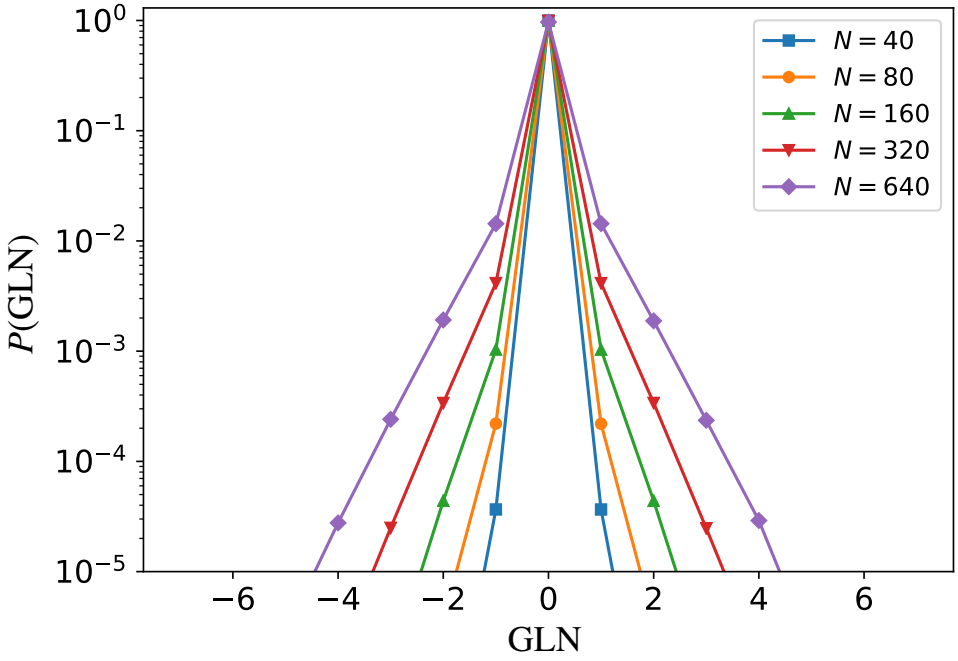

Figure A.1: Probability distribution function, $P(\mathrm{GLN})$, of the Gauss linking number GLN between pairs of N-monomer rings. The function is perfectly symmetric around $\mathrm{GLN} = 0$, which validates the numerical approach (based on Ref. [155]) used to detect GLN.

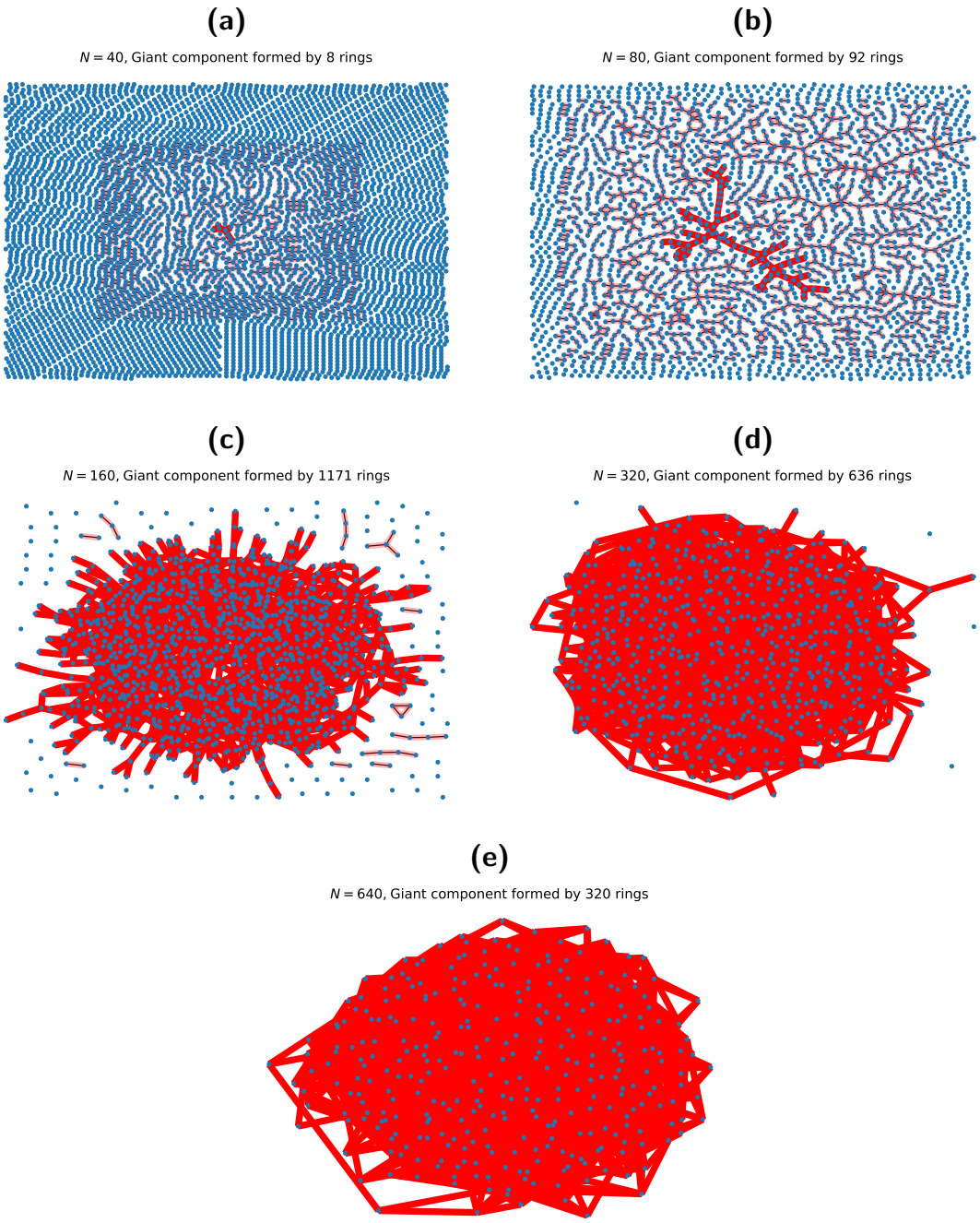

Figure A.2: Examples of typical network structures for melts of N-monomer rings with unconstrained topology. Clusters definition, detection and visualization have been perfomed by using the Python *Networkx* package by Hagberg, Schult and Swart [228]. In each panel, blue dots represent rings and light-red lines represent links between pairs of rings. Thick-red paths identify the largest clusters of each network. Each picture represents a single snapshot, taken on the corresponding trajectory of the system.

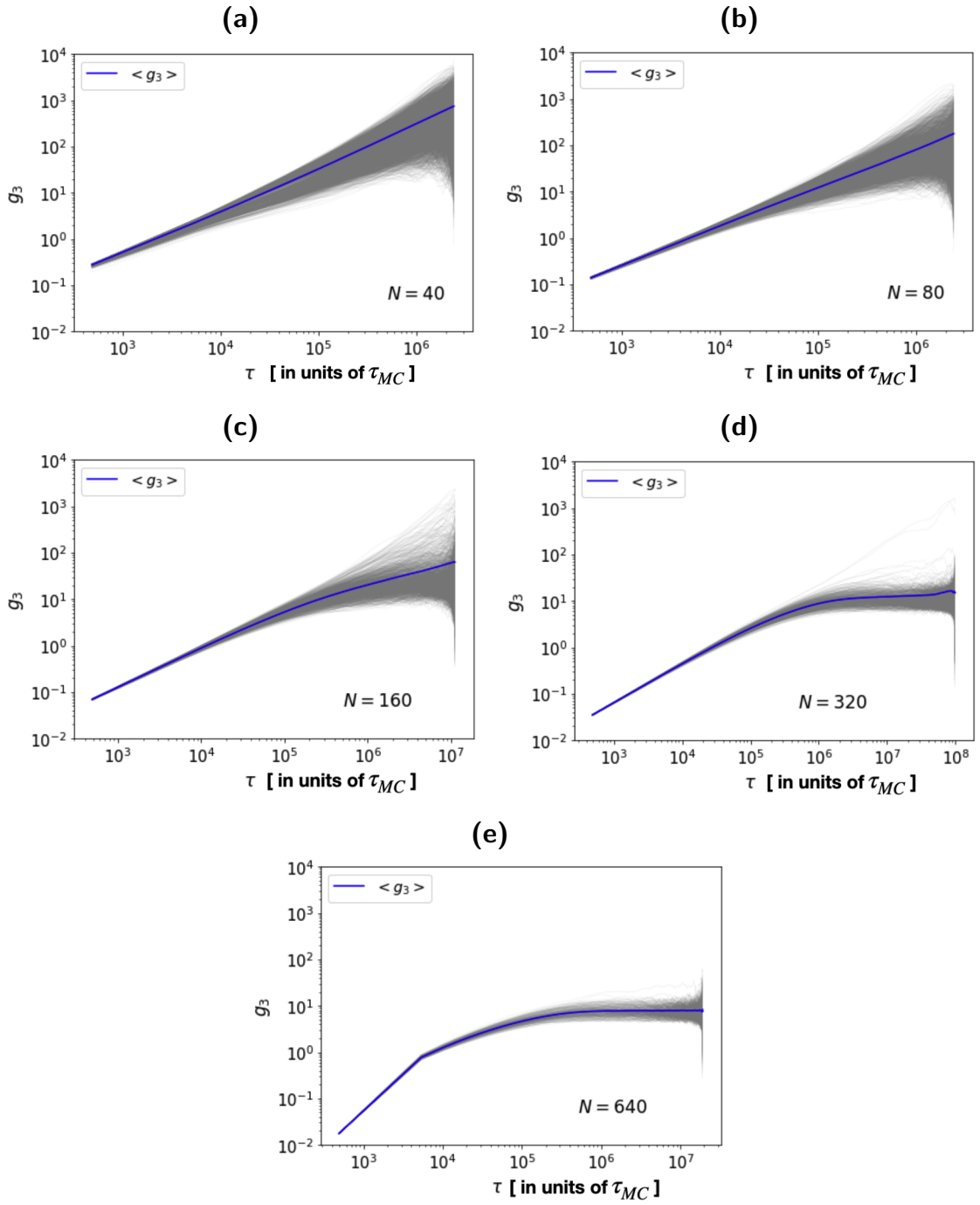

Figure A.3: Time mean-square displacement of the chain centre of mass, $g_3(\tau)$, in melts of permanently catenated N-monomer rings. Gray lines are for displacements of single rings, the blue line is the average over the entire ensemble of rings.

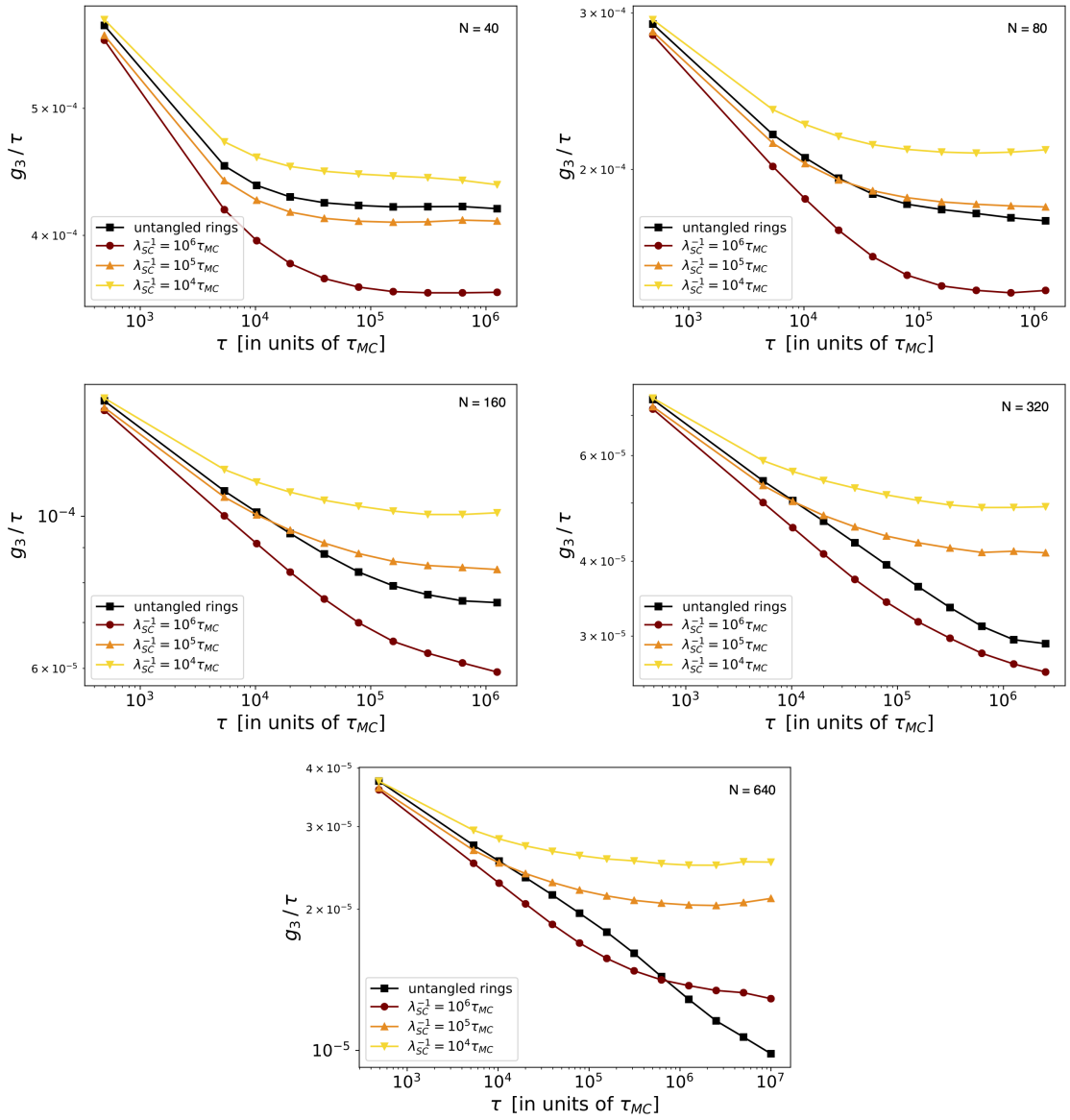

Figure A.4: Time mean-square displacement of the centre of mass of N-monomer rings, $g_3(\tau)/\tau$, normalized to time τ. Results for ring melts with unconstrained topology at different SC rates λ_{SC} (see legends) are compared to melts of untangled rings.

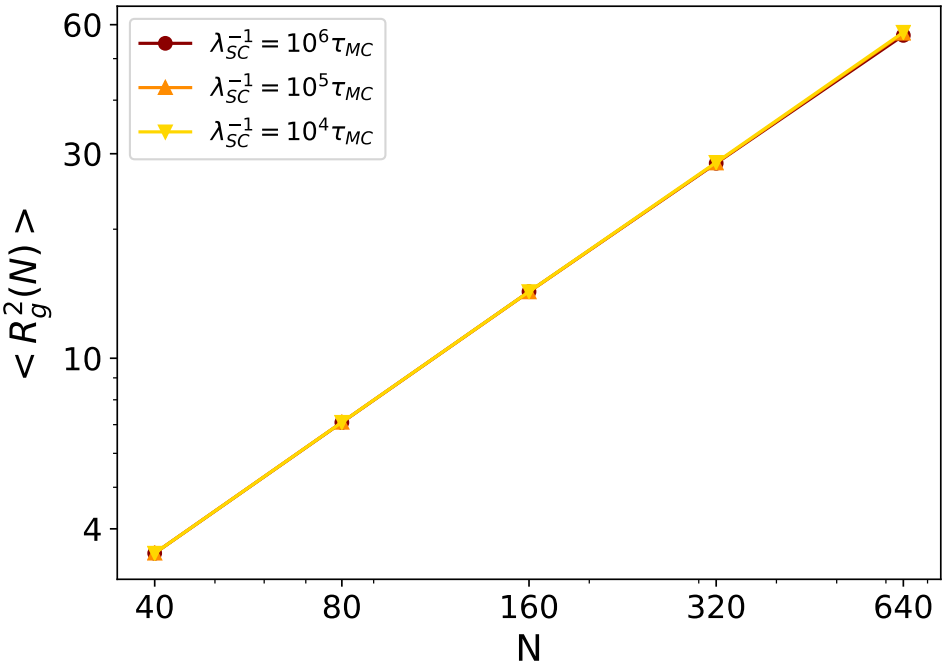

Figure A.5: Mean-square gyration radius, $\langle R_g^2(N) \rangle$, of ring polymers as a function of the number of bonds, N. Results for ring melts with unconstrained topology at different SC rates λ_{SC} (see legend).

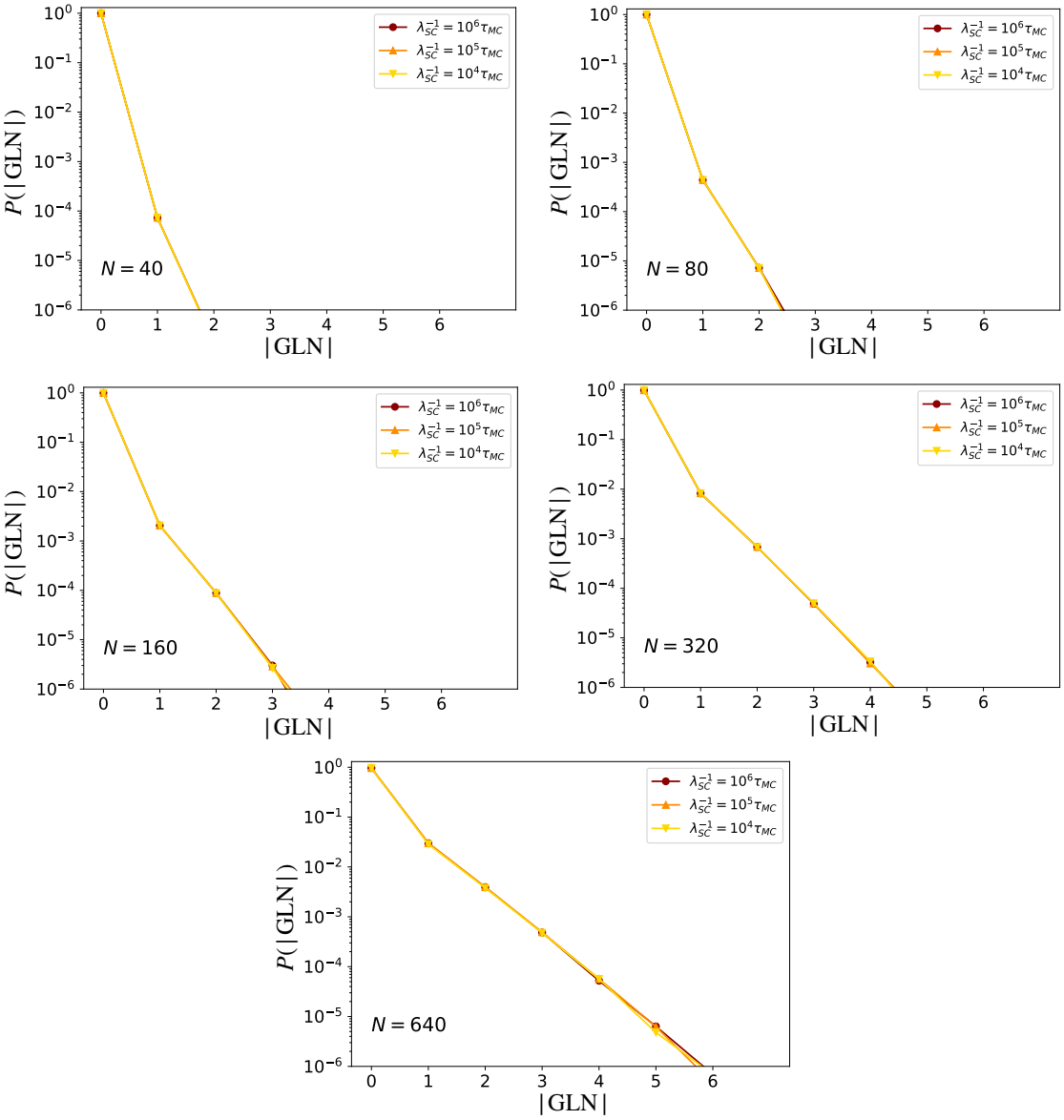

Figure A.6: Probability distribution function, $P(|\mathrm{GLN}|)$, of the absolute value of the Gauss linking number $|\mathrm{GLN}|$ between pairs of N-monomer rings. Results for ring melts with unconstrained topology at different SC rates λ_{SC} (see legend).

Appendix B

Supplementary material of Chapter 6

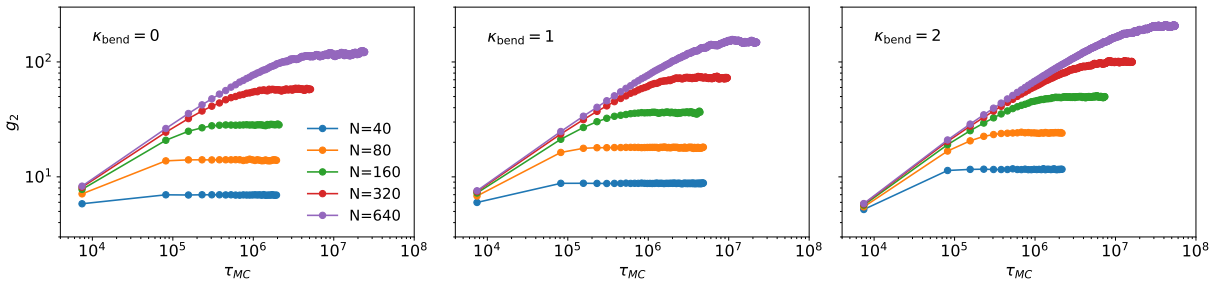

Figure B.1: Single monomer mean square displacement, $g_2(\tau_{MC})$, in the centre of mass reference frame (Eq. (2.19)) for all the polymer's sizes, N, and for the three κ_{bend} considered in Chapter 6.

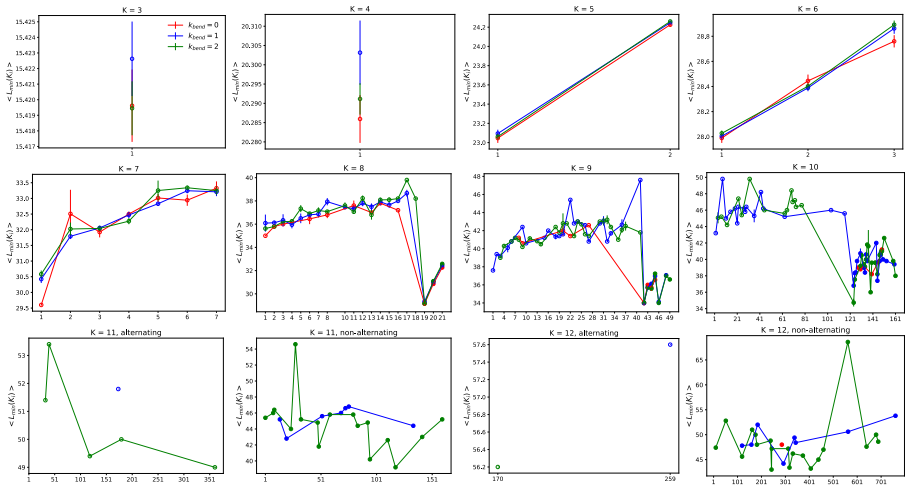

Figure B.2: Average ring minimal contour length (with error bars), $\langle L_{\min}(K_i)\rangle$, computed for each knot type. The labels on the x-axis are for each possible knot at the given K; for $K \geq 9$, the labels (starting from 1) appear with regular spacing for reasons of space (except the panel "$K = 12$, alternating" where only two knots have been detected). As in Figs. 6.6 and 6.7 in Chapter 6, empty/full circles are for alternating/non-alternating knots. As in the rest of the Thesis (see Sec. 4.1) knots with $K \leq 10$ crossings are named according to the Rolfsen's convention, while knots with $K = 11$ and $K = 12$ crossings are conventionally [173] split into alternating, $K_{\mathrm{a\_i}}$, and non-alternating, $K_{\mathrm{n\_i}}$, ones with the ordered index $i \geq 1$ in both cases. Data with no error bars are for rare knot types, which occur only once in the generated melt conformations. The results shown here are for rings with $N = 640$ monomers and different values of the bending stiffness, κ_{bend}.

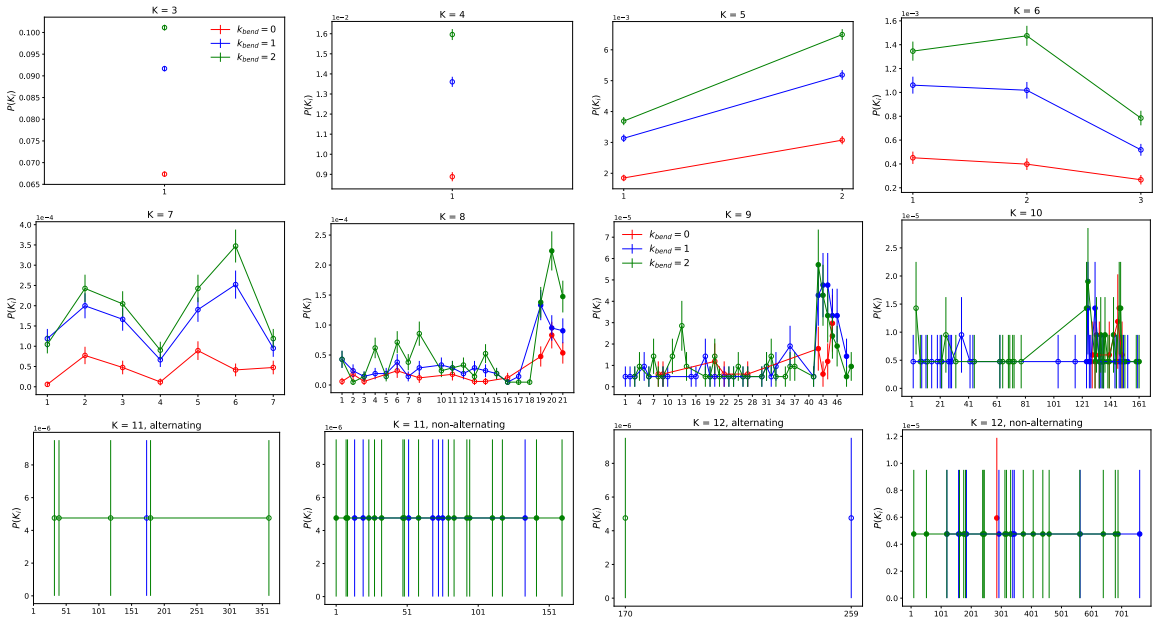

Figure B.3: Fractional population (with error bars), $P(K_i)$, computed for each knot type. Notice that the values on each y-axis have to be multiplied by the power-law reported on the top left corner of the corresponding panel. Symbols, labels and notation are as in Fig. B.2. Large error bars are due to the limited size of the relative sample.

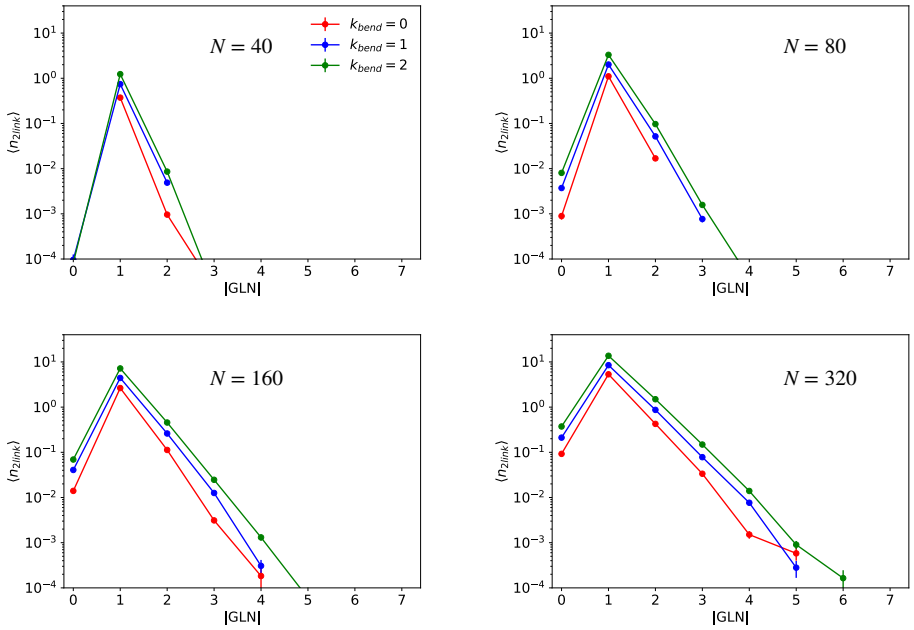

Figure B.4: $\langle n_{\rm 2link}(|{\rm GLN}|)\rangle$, mean number of 2-chain links per ring with absolute Gauss linking number $|{\rm GLN}|$. Results for rings with N monomers (to be compared to the results for $N = 640$ reported in the l.h.s. panel of Fig. 6.6 in Chapter 6).

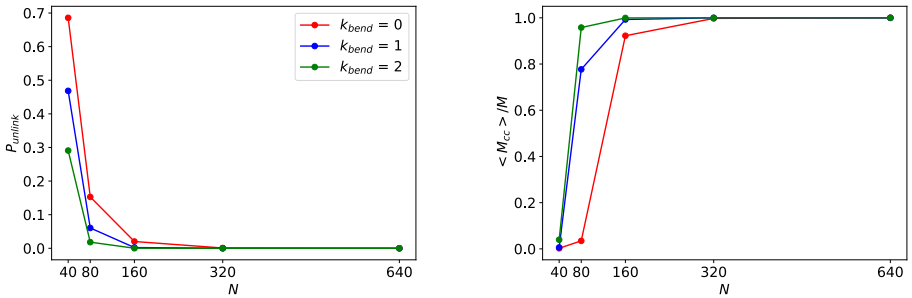

Figure B.5: (Left) Probability, $P_{\rm unlink}$, that a ring is *not* concatenated to any other ring of the system as a function of N and $\kappa_{\rm bend}$. (Right) Mean fraction of rings, $\langle M_{\rm cc}\rangle/M$, belonging to the *largest connected component* of chains in the melt as a function of N and $\kappa_{\rm bend}$.

Appendix C

Supplementary material of Chapter 7

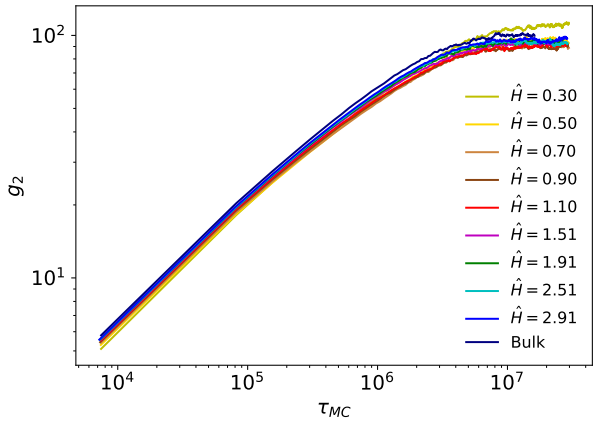

Figure C.1: Single monomer mean square displacement, $g_2(\tau_{MC})$, in the centre of mass reference (Eq. (2.19)), for the different values of slit-confinement, $\hat{\mathrm{H}}$, and the bulk reference considered in Chapter 7.

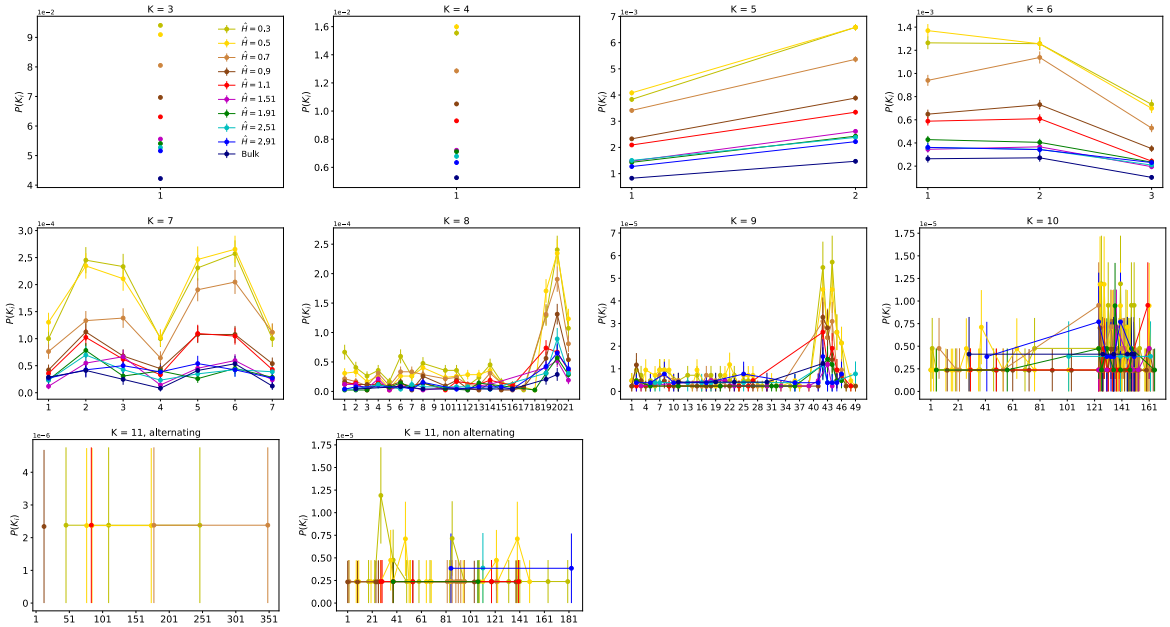

Figure C.2: Fractional population of each knot type – named according to the Rolfsen convention [149] – at fixed number of crossings K and for the different values of confinement $\hat{\mathrm{H}}$ and in bulk conditions (see legend). For $K = 11$, knots are categorized according the Hoste-Thistlethwaite table [229] that split them in *alternating* (K_{a_i}) and *non-alternating* ones (K_{n_i}), with the index i used to enumerate the rings separately within each group. Large relative error bars are due to the limited size of the sample (notice that the values of each y-axis have to be multiplied by the power-law reported on the top left corner of the corresponding panel).

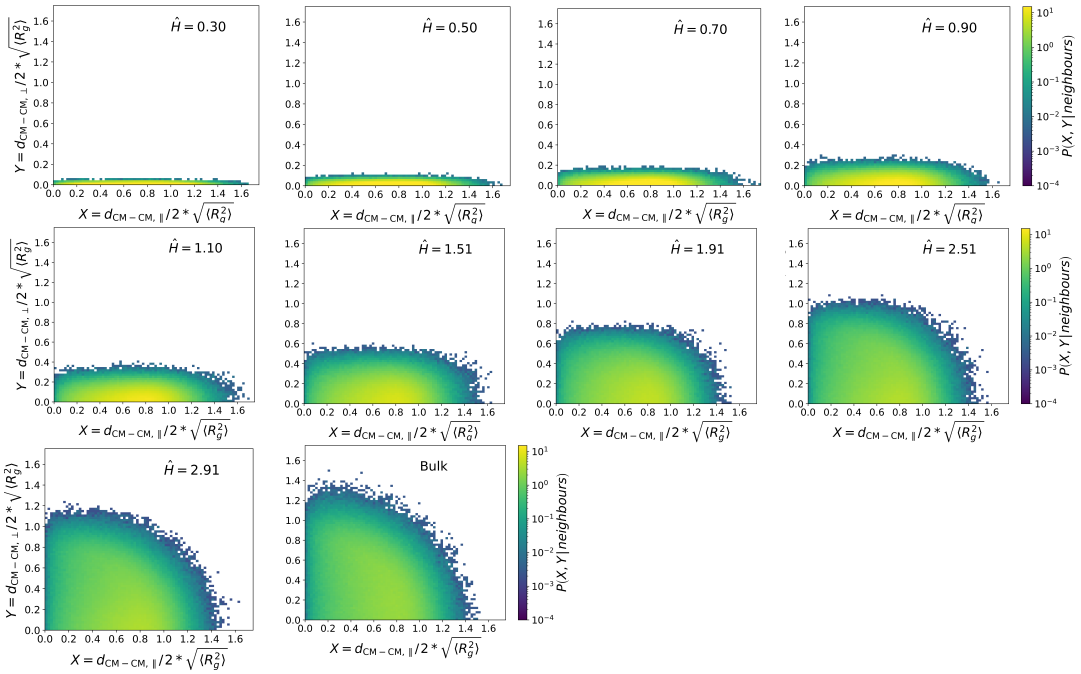

Figure C.3: Contour plots for the joint distribution function of the slit-parallel and slit-transverse (or, slit-perpendicular) components of the distances between the centres of mass of neighboring rings $P(d_{\mathrm{CM-CM},\parallel}, d_{\mathrm{CM-CM},\perp} \mid \mathrm{neighbors})$. Distances have been rescaled by the corresponding root-mean-square gyration radius of the rings.

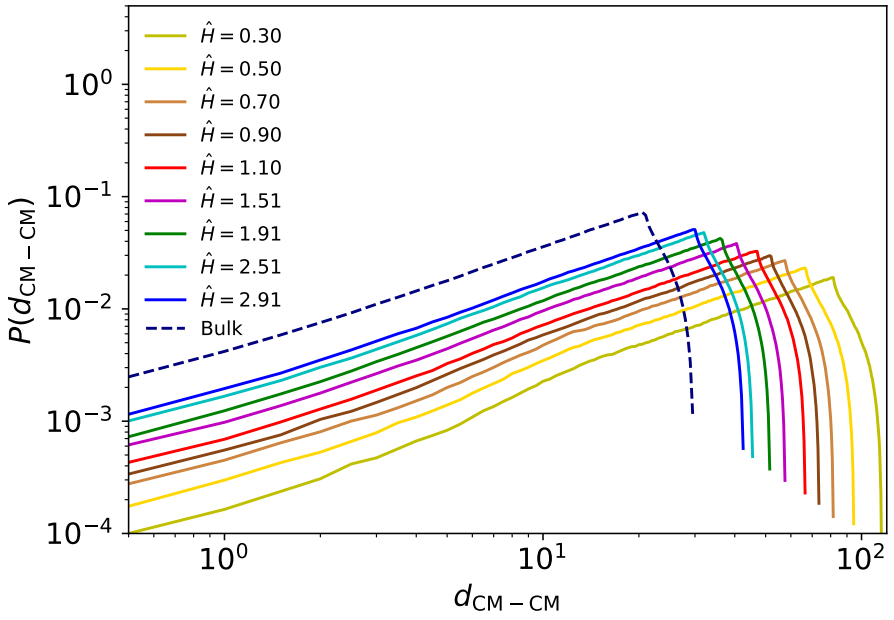

Figure C.4: Distribution functions of the distances between the rings' centres of mass, $P(d_{\mathrm{CM-CM}})$.

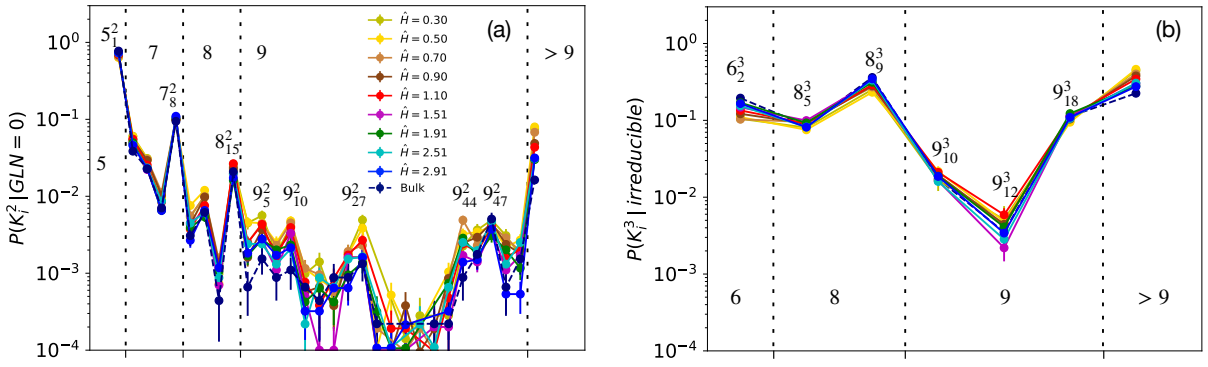

Figure C.5: (a) $P(K_i^2|\mathrm{GLN} = 0)$, fractional population of two-chain links K_i^2 (termed according to the Rolfsen convention [149]) having $\mathrm{GLN} = 0$. Labels have been put for links corresponding to peaks of the distributions. (b) $P(K_i^3|\text{irreducible})$, fractional population of three-chain links K_i^3 (also termed according to the Rolfsen convention [149]) belonging to the poly(2)catenane+1-ring and Brunnian classes (see main text for details). *Topoly* fails [173] recognizing links with > 9 crossings, so these lack categorization. In both panels, vertical dotted lines delimit areas of links at fixed number of crossings K.

Appendix D

Supplementary material of Chapter 8

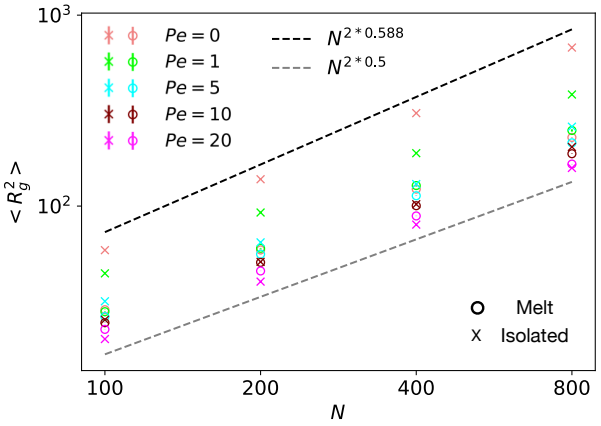

Figure D.1: Mean-square gyration radius, $< R_g^2 >$, as a function of N for all the value of Peclet, Pe, considered for both isolated chains ($\times$ symbol) and in the melt ($\circ$ symbol).

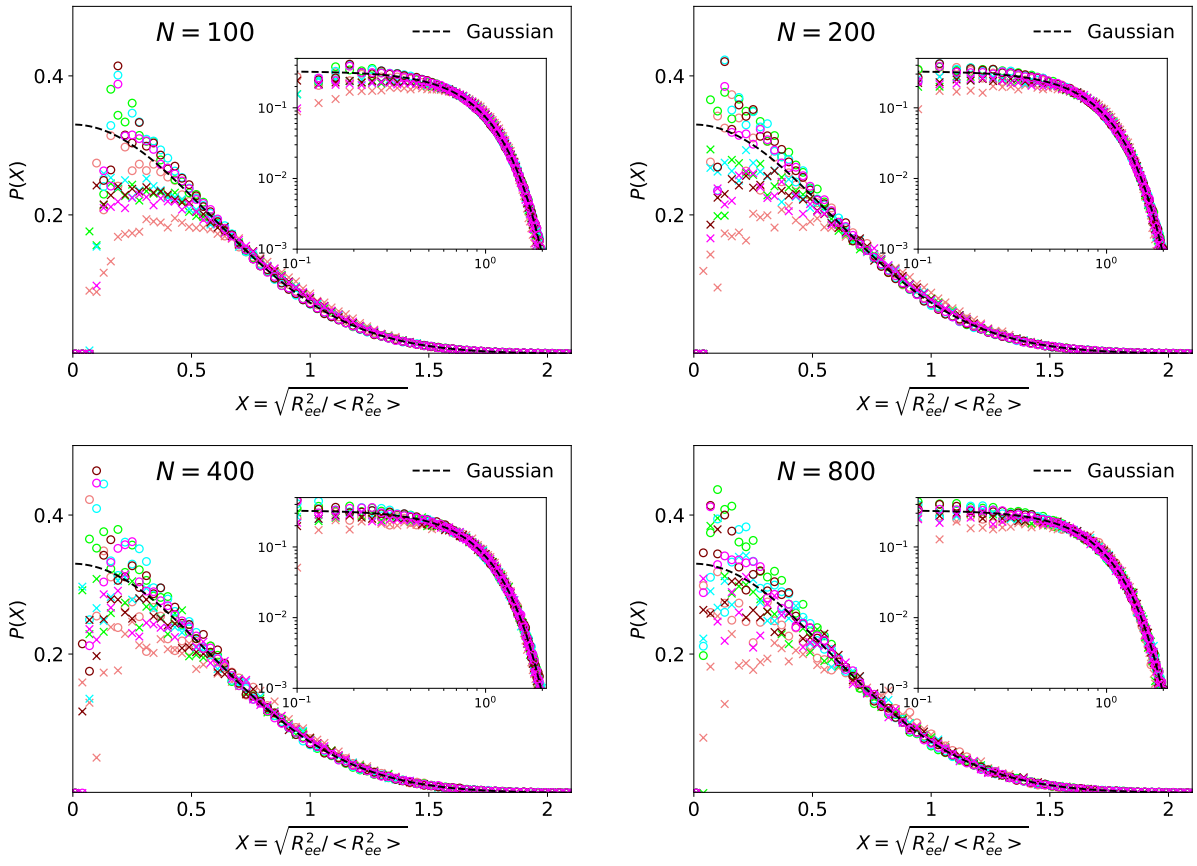

Figure D.2: Distribution functions of the rescaled end-end distance, $P\left(\sqrt{R_{ee}^2 / < R_{ee}^2 >}\right)$, for both isolated and linear chains in the melt for all the N considered compared with the Gaussian distribution. The same legend of Fig. D.1 applies here.

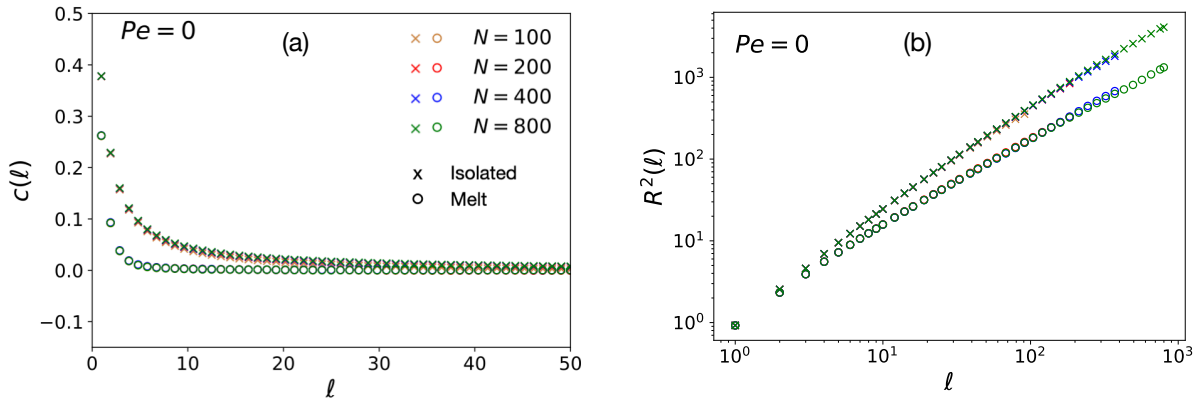

Figure D.3: (a) Tangent-tangent correlation function, $c(\ell)$, as a function of contour distance ℓ, for all the polymer's sizes, N, simulated for both isolated chains ($\times$ symbol) and in the melt ($\circ$ symbol) at $\mathrm{Pe} = 0$ (passive case). (b) Mean-square internal distance $R^2(\ell)$, as a function of contour distance ℓ for all the N simulated for both isolated chains and in the melt at $\mathrm{Pe} = 0$.

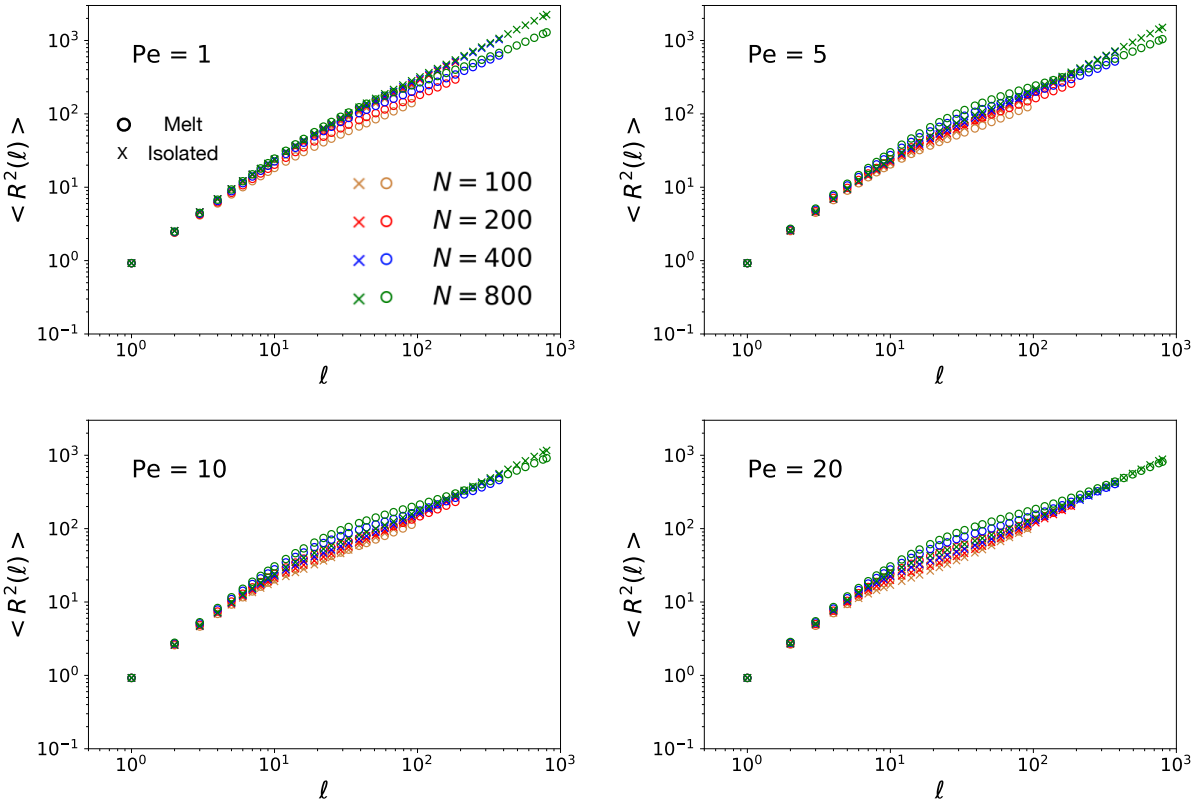

Figure D.4: Means square internal distance, $R^2(\ell)$, as a function of ℓ, for all the $\mathrm{Pe} > 0$ considered and the polymer sizes, N, simulated for both isolated ($\times$ symbol) and melt ($\circ$ symbol) systems.

Bibliography

1. Ubertini, M. A. & Rosa, A. Computer simulations of melts of ring polymers with non-conserved topology: A dynamic Monte Carlo lattice model. *Phys. Rev. E* **104,** 054503 (2021).
2. Ubertini, M. A., Smrek, J. & Rosa, A. Entanglement length scale separates threading from branching of unknotted and non-concatenated ring polymers in melts. *Macromolecules* **55,** 10723–10736 (2022).
3. Ubertini, M. A. & Rosa, A. Topological Analysis and Recovery of Entanglements in Polymer Melts. *Macromolecules* (2023).
4. Ubertini, M. A. & Rosa, A. Spatial Organization of Slit-Confined Melts of Ring Polymers with Nonconserved Topology: A Lattice Monte Carlo Study. *Macromolecules* (2023).
5. Rubinstein, M. & Colby, R. H. *Polymer Physics* (Oxford University Press, New York, 2003).
6. Deutsch, J. Equilibrium size of large ring molecules. *Physical Review E* **59,** R2539 (1999).
7. Flory, P. J. Thermodynamics of high polymer solutions. *The Journal of chemical physics* **10,** 51–61 (1942).
8. Huggins, M. L. Theory of solutions of high polymers1. *Journal of the American Chemical Society* **64,** 1712–1719 (1942).
9. Edwards, S. The size of a polymer molecule in a strong solution. *Journal of Physics A: Mathematical and General* **8,** 1670 (1975).
10. Kremer, K. Statics and dynamics of polymeric melts: a numerical analysis. *Macromolecules* **16,** 1632–1638 (1983).
11. Kremer, K. & Grest, G. S. Dynamics of entangled linear polymer melts: A molecular-dynamics simulation. *The Journal of Chemical Physics* **92,** 5057–5086 (1990).

12. Shaffer, J. S. Effects of chain topology on polymer dynamics: Bulk melts. *The Journal of chemical physics* **101,** 4205–4213 (1994).

13. Edwards, S. The statistical mechanics of polymerized material. *Proceedings of the Physical Society* **92,** 9 (1967).

14. Doi, M. & Edwards, S. F. *The Theory of Polymer Dynamics* (Clarendon, Oxford, 1986).

15. Edwards, S. Statistical mechanics with topological constraints: I. *Proceedings of the Physical Society* **91,** 513 (1967).

16. Edwards, S. Statistical mechanics with topological constraints: II. *Journal of Physics A: General Physics* **1,** 15 (1968).

17. Iwata, K. & Edwards, S. F. New model of polymer entanglement: Localized Gauss integral model. Plateau modulus G_N, topological second virial coefficient A_2^θ and physical foundation of the tube model. *J. Chem. Phys.* **90,** 4567–4581 (1989).

18. Everaers, R. & Kremer, K. Topological interactions in model polymer networks. *Phys. Rev. E* **53,** R37–R40 (1996).

19. Michalke, W., Lang, M., Kreitmeier, S. & Göritz, D. Simulations on the number of entanglements of a polymer network using knot theory. *Phys. Rev. E* **64,** 012801 (2001).

20. Likhtman, A. E. The tube axis and entanglements in polymer melts. *Soft Matter* **10,** 1895–1904 (2014).

21. Caraglio, M., Micheletti, C. & Orlandini, E. Physical Links: defining and detecting interchain entanglement. *Scientific Reports* **7,** 1156 (2017).

22. Bobbili, S. V. & Milner, S. T. Simulation study of entanglement in semiflexible polymer melts and solutions. *Macromolecules* **53,** 3861–3872 (2020).

23. Lin, Y. Number of entanglement strands per cubed tube diameter, a fundamental aspect of topological universality in polymer viscoelasticity. *Macromolecules* **20,** 3080–3083 (1987).

24. Kavassalis, T. A. & Noolandi, J. New view of entanglements in dense polymer systems. *Physical review letters* **59,** 2674 (1987).

25. Semenov, A. N. Dynamics of concentrated solutions of rigid-chain polymers. Part 1. Brownian motion of persistent macromolecules in isotropic solution. *Journal of the Chemical Society, Faraday Transactions 2: Molecular and Chemical Physics* **82,** 317–329 (1986).

26. Odjik, T. On the statistics and Dynamics of Confined or Entangled Stiff Polymers, 1983. *Macromol* **16,** 1340.

27. Everaers, R. *et al.* Rheology and microscopic topology of entangled polymeric liquids. *Science* **303,** 823–826 (2004).

28. Kröger, M. Shortest multiple disconnected path for the analysis of entanglements in two-and three-dimensional polymeric systems. *Computer Physics Communications* **168,** 209–232 (2005).

29. Everaers, R. *et al.* Rheology and Microscopic Topology of Entangled Polymeric Liquids. *Science* **303,** 823 (2004).

30. Sukumaran, S. K., Grest, G. S., Kremer, K. & Everaers, R. Identifying the primitive path mesh in entangled polymer liquids. *Journal of Polymer Science Part B: Polymer Physics* **43,** 917–933 (2005).

31. Uchida, N., Grest, G. S. & Everaers, R. Viscoelasticity and primitive path analysis of entangled polymer liquids: From F-actin to polyethylene. *J. Chem. Phys.* **128,** 044902 (2008).

32. Ferrari, F. Topologically linked polymers are anyon systems. *Physics Letters A* **323,** 351–359 (2004).

33. Halverson, J. D., Lee, W. B., Grest, G. S., Grosberg, A. Y. & Kremer, K. Molecular dynamics simulation study of nonconcatenated ring polymers in a melt. II. Dynamics. *J. Chem. Phys.* **134,** 204905 (2011).

34. De Gennes, P.-G. Reptation of a polymer chain in the presence of fixed obstacles. *The journal of chemical physics* **55,** 572–579 (1971).

35. Kremer, K. & Grest, G. S. Dynamics of entangled linear polymer melts: A molecular-dynamics simulation. *J. Chem. Phys.* **92,** 5057–5086 (1990).

36. Colby, R. H., Fetters, L. J. & Graessley, W. W. The melt viscosity-molecular weight relationship for linear polymers. *Macromolecules* **20,** 2226–2237 (1987).

37. Rosa, A. & Everaers, R. Structure and Dynamics of Interphase Chromosomes. *Plos Comput. Biol.* **4,** e1000153 (2008).

38. Halverson, J. D., Smrek, J., Kremer, K. & Grosberg, A. Y. From a melt of rings to chromosome territories: the role of topological constraints in genome folding. *Rep. Prog. Phys.* **77,** 022601 (2014).

39. Bolzer, A. *et al.* Three-dimensional maps of all chromosomes in human male fibroblast nuclei and prometaphase rosettes. *PLoS biology* **3,** e157 (2005).

40. Lo, W.-C. & Turner, M. S. The topological glass in ring polymers. *EPL (Europhysics Letters)* **102,** 58005 (2013).

41. Michieletto, D. & Turner, M. S. A topologically driven glass in ring polymers. *Proc. Natl. Acad. Sci. USA* **113,** 5195–5200 (May 2016).

42. Michieletto, D., Nahali, N. & Rosa, A. Glassiness and Heterogeneous Dynamics in Dense Solutions of Ring Polymers. *Phys. Rev. Lett.* **119,** 197801 (19 2017).

43. Smrek, J., Chubak, I., Likos, C. N. & Kremer, K. Active topological glass. *Nature Communications* **11,** 26 (2020).

44. Halverson, J. D., Lee, W. B., Grest, G. S., Grosberg, A. Y. & Kremer, K. Molecular dynamics simulation study of nonconcatenated ring polymers in a melt. I. Statics. *J. Chem. Phys.* **134,** 204904 (2011).

45. Brereton, M. G. & Vilgis, T. A. The statistical mechanics of a melt of polymer rings. **28,** 1149–1167 (1995).

46. David Moroz, J. & Kamien, R. D. Self-avoiding walks with writhe. *Nuclear Physics B* **506,** 695–710 (1997).

47. Kholodenko, A. L. & Vilgis, T. A. Some geometrical and topological problems in polymer physics. *Physics Reports* **298,** 251–370 (1998).

48. Kung, W & Kamien, R. D. Topological constraints at the Theta-point: Closed loops at two loops. *Europhysics Letters (EPL)* **64,** 323–329 (2003).

49. Ferrari, F., Paturej, J., Piątek, M. & Zhao, Y. Knots, links, anyons and statistical mechanics of entangled polymer rings. *Nuclear Physics B* **945,** 114673 (2019).

50. Cates, M. E. & Deutsch, J. M. Conjectures on the statistics of ring polymers. *J. Phys. France* **47,** 2121–2128 (1986).

51. Khokhlov, A. R. & Nechaev, S. K. Polymer chain in an array of obstacles. *Physics Letters A* **112,** 156–160 (1985).

52. Rubinstein, M. Dynamics of Ring Polymers in the Presence of Fixed Obstacles. *Phys. Rev. Lett.* **57,** 3023–3026 (24 1986).

53. Obukhov, S. P., Rubinstein, M. & Duke, T. Dynamics of a Ring Polymer in a Gel. *Phys. Rev. Lett.* **73,** 1263–1266 (9 1994).

54. Obukhov, S., Johner, A., Baschnagel, J., Meyer, H. & Wittmer, J. P. Melt of polymer rings: The decorated loop model. *EPL (Europhysics Letters)* **105,** 48005 (2014).

55. Ge, T., Panyukov, S. & Rubinstein, M. Self-Similar Conformations and Dynamics in Entangled Melts and Solutions of Nonconcatenated Ring Polymers. *Macromolecules* **49,** 708–722 (2016).

56. Frank-Kamenetskii, M., Lukashin, A. & Vologodskii, A. Statistical mechanics and topology of polymer chains. *Nature* **258,** 398–402 (1975).

57. Grosberg, A. Y. Annealed lattice animal model and Flory theory for the melt of non-concatenated rings: towards the physics of crumpling. *Soft Matter* **10,** 560–565 (2014).

58. Gutin, A. M., Grosberg, A. Y. & Shakhnovich, E. I. Polymers with annealed and quenched branchings belong to different universality classes. *Macromolecules* **26,** 1293–1295 (1993).

59. Rosa, A. & Everaers, R. Ring Polymers in the Melt State: The Physics of Crumpling. *Phys. Rev. Lett.* **112,** 118302 (11 2014).

60. Smrek, J. & Grosberg, A. Y. Understanding the dynamics of rings in the melt in terms of the annealed tree model. *Journal of Physics: Condensed Matter* **27,** 064117 (2015).

61. Brás, A. R. *et al.* Compact structure and non-Gaussian dynamics of ring polymer melts. *Soft matter* **10,** 3649–3655 (2014).

62. Goossen, S. *et al.* Molecular scale dynamics of large ring polymers. *Physical review letters* **113,** 168302 (2014).

63. Kruteva, M., Allgaier, J., Monkenbusch, M., Porcar, L. & Richter, D. Self-Similar Polymer Ring Conformations Based on Elementary Loops: A Direct Observation by SANS. *ACS Macro Lett.* **9,** 507–511 (2020).

64. Müller, M, Wittmer, J. & Cates, M. Topological effects in ring polymers: A computer simulation study. *Physical Review E* **53,** 5063 (1996).

65. Brown, S. & Szamel, G. Structure and dynamics of ring polymers. *The Journal of chemical physics* **108,** 4705–4708 (1998).

66. Müller, M., Wittmer, J. P. & Cates, M. E. Topological effects in ring polymers. II. Influence of persistence length. *Phys. Rev. E* **61,** 4078–4089 (4 2000).

67. Vettorel, T., Grosberg, A. Y. & Kremer, K. Statistics of polymer rings in the melt: a numerical simulation study. *Physical biology* **6,** 025013 (2009).

68. Schram, R. D., Rosa, A. & Everaers, R. Local loop opening in untangled ring polymer melts: a detailed "Feynman test" of models for the large scale structure. *Soft Matter* **15,** 2418–2429 (11 2019).

69. Smrek, J. & Grosberg, A. Y. Minimal Surfaces on Unconcatenated Polymer Rings in Melt. *ACS Macro Lett.* **5,** 750–754 (2016).

70. Lang, M. Ring Conformations in Bidisperse Blends of Ring Polymers. *Macromolecules* **46,** 1158–1166 (2013).

71. Smrek, J., Kremer, K. & Rosa, A. Threading of Unconcatenated Ring Polymers at High Concentrations: Double-Folded vs Time-Equilibrated Structures. *ACS Macro Lett.* **8,** 155–160 (2019).

72. Kruteva, M. *et al.* Self-Similar Dynamics of Large Polymer Rings: A Neutron Spin Echo Study. *Phys. Rev. Lett.* **125,** 238004 (23 2020).

73. O'Connor, T. C., Ge, T., Rubinstein, M. & Grest, G. S. Topological Linking Drives Anomalous Thickening of Ring Polymers in Weak Extensional Flows. *Phys. Rev. Lett.* **124,** 027801 (2 2020).

74. Sumners, D. & Whittington, S. Knots in self-avoiding walks. *Journal of Physics A: Mathematical and General* **21,** 1689 (1988).

75. Duplantier, B. Linking numbers, contacts, and mutual inductances of a random set of closed curves. *Communications in mathematical physics* **82,** 41–68 (1981).

76. Pohl, W. F. *The probability of linking of random closed curves* in *Geometry Symposium Utrecht 1980: Proceedings of a Symposium Held at the University of Utrecht, The Netherlands, August 27–29, 1980* (2006), 113–126.

77. Orlandini, E. & Whittington, S. G. Statistical topology of closed curves: Some applications in polymer physics. *Reviews of modern physics* **79,** 611 (2007).

78. Orlandini, E. & Micheletti, C. Topological and physical links in soft matter systems. *Journal of Physics: Condensed Matter* **34,** 013002 (2021).

79. Orlandini, E, Van Rensburg, E. J., Tesi, M. & Whittington, S. Random linking of lattice polygons. *Journal of Physics A: Mathematical and General* **27,** 335 (1994).

80. Hirayama, N., Tsurusaki, K. & Deguchi, T. Linking probabilities of off-lattice self-avoiding polygons and the effects of excluded volume. *Journal of Physics A: Mathematical and Theoretical* **42,** 105001 (2009).

81. Michieletto, D., Marenduzzo, D. & Orlandini, E. Is the kinetoplast DNA a percolating network of linked rings at its critical point? *Phys. Biol.* **12,** 036001 (2015).

82. Lang, M., Fischer, J. & Sommer, J. U. Effect of Topology on the Conformations of Ring Polymers. *Macromolecules* **45,** 7642–7648 (2012).

83. Lang, M., Fischer, J., Werner, M. & Sommer, J.-U. Swelling of Olympic Gels. *Phys. Rev. Lett.* **112,** 238001 (23 2014).

84. Lang, M., Fischer, J., Werner, M. & Sommer, J.-U. Olympic Gels: Concatenation and Swelling. *Macromol. Symp.* **358,** 140–147 (2015).

85. Fischer, J., Lang, M. & Sommer, J.-U. The Formation and Structure of Olympic Gels. *J. Chem. Phys.* **143,** 243114 (2015).

86. Wu, Q. *et al.* Poly[n]catenanes: Synthesis of molecular interlocked chains. *Science* **358,** 1434 (2017).

87. Hart, L. F. *et al.* Material properties and applications of mechanically interlocked polymers. *Nat. Rev. Mater.* **6,** 508–530 (2021).

88. Rauscher, P. M., Schweizer, K. S., Rowan, S. J. & de Pablo, J. J. Dynamics of poly [n] catenane melts. *The Journal of Chemical Physics* **152,** 214901 (2020).

89. Rauscher, P. M., Schweizer, K. S., Rowan, S. J. & De Pablo, J. J. Thermodynamics and structure of poly [n] catenane melts. *Macromolecules* **53,** 3390–3408 (2020).

90. Dehaghani, Z. A., Chubak, I., Likos, C. N. & Ejtehadi, M. R. Effects of topological constraints on linked ring polymers in solvents of varying quality. *Soft Matter* **16,** 3029–3038 (2020).

91. Chiarantoni, P. & Micheletti, C. Effect of Ring Rigidity on the Statics and Dynamics of Linear Catenanes. *Macromolecules* **55,** 4523–4532 (2022).

92. Circular Polycatenanes: Supramolecular Structures with Topologically Tunable Properties. *Physical Review Letters* **129,** 227801 (2022).

93. Krajina, B. A., Zhu, A., Heilshorn, S. C. & Spakowitz, A. J. Active DNA Olympic Hydrogels Driven by Topoisomerase Activity. *Phys. Rev. Lett.* **121,** 148001 (14 2018).

94. Cremer, T. & Cremer, C. Chromosome territories, nuclear architecture and gene regulation in mammalian cells. *Nat. Rev. Genet.* **2,** 292–301 (2001).

95. Brahmachari, S. & Marko, J. F. Chromosome disentanglement driven via optimal compaction of loop-extruded brush structures. *Proc. Natl. Acad. Sci. USA* **116,** 24956–24965 (2019).

96. Champoux, J. J. DNA Topoisomerases: Structure, Function, and Mechanism. *Annu. Rev. Biochem.* **70,** 369–413 (2001).

97. Sikorav, J. L. & Jannink, G. Kinetics of chromosome condensation in the presence of topoisomerases: a phantom chain model. *Biophys. J.* **66,** 827–837 (1994).

98. De Gennes, P.-G. *Scaling Concepts in Polymer Physics* (Cornell University Press, Ithaca, 1979).

99. Raphaël, E., Gay, C. & de Gennes, P. G. Progressive construction of an "Olympic"gel. *Journal of Statistical Physics* **89,** 111–118 (1997).

100. Renger, H. C. & Wolstenholme, D. R. The Form and Structure of Kinetoplast DNA of Crithidia. *J. Cell Biol.* **54,** 346 (1972).

101. Shapiro, T. A. & Englund, P. T. The structure and replication of kinetoplast DNA. *Annual review of microbiology* **49,** 117–143 (1995).

102. Klotz, A. R., Soh, B. W. & Doyle, P. S. Equilibrium structure and deformation response of 2D kinetoplast sheets. *Proc. Natl. Acad. Sci. USA* **117,** 121 (2020).

103. Everaers, R., Karimi-Varzaneh, H. A., Fleck, F., Hojdis, N. & Svaneborg, C. Kremer–Grest models for commodity polymer melts: linking theory, experiment, and simulation at the Kuhn scale. *Macromolecules* **53,** 1901–1916 (2020).

104. Grest, G. S. & Kremer, K. Molecular dynamics simulation for polymers in the presence of a heat bath. *Physical Review A* **33,** 3628 (1986).

105. Svaneborg, C. & Everaers, R. Characteristic time and length scales in melts of Kremer–Grest bead–spring polymers with wormlike bending stiffness. *Macromolecules* **53,** 1917–1941 (2020).

106. Kremer, K. & Binder, K. Monte Carlo simulation of lattice models for macromolecules. *Computer Physics Reports* **7,** 259–310 (1988).

107. Carmesin, I & Kremer, K. The bond fluctuation method: a new effective algorithm for the dynamics of polymers in all spatial dimensions. *Macromolecules* **21,** 2819–2823 (1988).

108. Deutsch, H. & Binder, K. Interdiffusion and self-diffusion in polymer mixtures: A Monte Carlo study. *The Journal of chemical physics* **94,** 2294–2304 (1991).

109. Hugouvieux, V., Axelos, M. A. V. & Kolb, M. Amphiphilic Multiblock Copolymers: From Intramolecular Pearl Necklace to Layered Structures. *Macromolecules* **42,** 392–400 (2009).

110. Rubinstein, M. Discretized model of entangled-polymer dynamics. *Phys. Rev. Lett.* **59,** 1946–1949 (17 1987).

111. Thompson, A. P. *et al.* LAMMPS-a flexible simulation tool for particle-based materials modeling at the atomic, meso, and continuum scales. *Computer Physics Communications* **271,** 108171 (2022).

112. Schram, R. D. & Barkema, G. T. Simulation of ring polymer melts with GPU acceleration. *J. Comput. Phys.* **363,** 128–139 (2018).

113. Schram, R. D., Barkema, G. T. & Schiessel, H. On the stability of fractal globules. *J. Chem. Phys.* **138,** 224901 (2013).

114. Olarte-Plata, J. D., Haddad, N., Vaillant, C. & Jost, D. The folding landscape of the epigenome. *Physical biology* **13,** 026001 (2016).

115. Ghosh, S. K. & Jost, D. How epigenome drives chromatin folding and dynamics, insights from efficient coarse-grained models of chromosomes. *PLoS computational biology* **14,** e1006159 (2018).

116. Gitchev, T., Zala, G., Meister, P. & Jost, D. 3DPolyS-LE: an accessible simulation framework to model the interplay between chromatin and loop extrusion. *Bioinformatics* **38,** 5454–5456 (2022).

117. Abdulla, A. Z., Tortora, M. M., Vaillant, C. & Jost, D. Topological constraints and finite-size effects in quantitative polymer models of chromatin organization. *bioRxiv,* 2023–06 (2023).

118. Metropolis, N., Rosenbluth, A. W., Rosenbluth, M. N., Teller, A. H. & Teller, E. Equation of state calculations by fast computing machines. *The journal of chemical physics* **21,** 1087–1092 (1953).

119. Huang, K. *Statistical mechanics* (John Wiley & Sons, 2008).

120. Alim, K. & Frey, E. Shapes of semiflexible polymer rings. *Physical review letters* **99,** 198102 (2007).

121. Wittmer, J. *et al.* Long range bond-bond correlations in dense polymer solutions. *Physical review letters* **93,** 147801 (2004).

122. Wittmer, J. *et al.* Intramolecular long-range correlations in polymer melts: The segmental size distribution and its moments. *Physical Review E* **76,** 011803 (2007).

123. Lieberman-Aiden, E. *et al.* Comprehensive Mapping of Long-Range Interactions Reveals Folding Principles of the Human Genome. *Science* **326,** 289–293 (2009).

124. Zhang, Y. *et al.* Spatial organization of the mouse genome and its role in recurrent chromosomal translocations. *Cell* **148,** 908–921 (2012).

125. Sakaue, T. Ring Polymers in Melts and Solutions: Scaling and Crossover. *Phys. Rev. Lett.* **106,** 167802 (16 2011).

126. Halverson, J. D., Grest, G. S., Grosberg, A. Y. & Kremer, K. Rheology of Ring Polymer Melts: From Linear Contaminants to Ring-Linear Blends. *Phys. Rev. Lett.* **108,** 038301 (3 2012).

127. Rosa, A. & Everaers, R. Computer simulations of melts of randomly branching polymers. *J. Chem. Phys.* **145,** 164906 (2016).

128. Michieletto, D. On the tree-like structure of rings in dense solutions. *Soft Matter* **12,** 9485–9500 (2016).

129. Dell, Z. E. & Schweizer, K. S. Intermolecular structural correlations in model globular and unconcatenated ring polymer liquids. *Soft Matter* **14,** 9132–9142 (2018).

130. Rosa, A. & Everaers, R. Conformational statistics of randomly branching double-folded ring polymers. *Eur. Phys. J. E* **42,** 1–12 (2019).

131. Michieletto, D. & Sakaue, T. Dynamical Entanglement and Cooperative Dynamics in Entangled Solutions of Ring and Linear Polymers. *ACS Macro Lett.* **10,** 129–134 (2021).

132. Ghobadpour, E., Kolb, M., Ejtehadi, M. R. & Everaers, R. Monte Carlo simulation of a lattice model for the dynamics of randomly branching double-folded ring polymers. *Phys. Rev. E* **104,** 014501 (1 2021).

133. Kapnistos, M. *et al.* Unexpected power-law stress relaxation of entangled ring polymers. *Nat. Mater.* **7,** 997–1002 (2008).

134. Pasquino, R. *et al.* Viscosity of Ring Polymer Melts. *ACS Macro Lett.* **2,** 874–878 (2013).

135. Iwamoto, T. *et al.* Conformations of Ring Polystyrenes in Bulk Studied by SANS. *Macromolecules* **51,** 1539–1548 (Feb. 2018).

136. Huang, Q. *et al.* Unexpected Stretching of Entangled Ring Macromolecules. *Phys. Rev. Lett.* **122,** 208001 (2019).

137. Wang, J. & Ge, T. Crazing Reveals an Entanglement Network in Glassy Ring Polymers. *Macromolecules* **54,** 7500–7511 (2021).

138. Smrek, J. Unraveling entanglement. *Journal Club for Condensed Matter Physics.* doi:10.36471/jccm_january_2022_03. https://doi.org/10.36471/jccm_january_2022_03 (2022).

139. Ashcroft, N. W. & Mermin, N. D. *Solid State Physics* (Saunders College Publishing, New York, 1976).

140. Uchida, N., Grest, G. S. & Everaers, R. Viscoelasticity and primitive path analysis of entangled polymer liquids: From F-actin to polyethylene. *J. Chem. Phys.* **128,** 044902 (2008).

141. Fudenberg, G., Abdennur, N., Imakaev, M., Goloborodko, A. & Mirny, L. A. Emerging Evidence of Chromosome Folding by Loop Extrusion. *Cold Spring Harb. Symp. Quant. Biol.* **82,** 45–55 (2017).

142. Tu, M. Q. *et al.* Unexpected Slow Relaxation Dynamics in Pure Ring Polymers Arise from Intermolecular Interactions. *ACS Polymers Au* (2023).

143. Micheletti, C., Marenduzzo, D. & Orlandini, E. Polymers with spatial or topological constraints: Theoretical and computational results. *Physics Reports* **504,** 1–73 (2011).

144. Mai, D. J. & Schroeder, C. M. Single polymer dynamics of topologically complex DNA. *Current Opinion in Colloid & Interface Science* **26,** 28–40 (2016).

145. Arsuaga, J. *et al.* DNA knots reveal a chiral organization of DNA in phage capsids. *Proceedings of the National Academy of Sciences* **102,** 9165–9169 (2005).

146. Valdés, A., Segura, J., Dyson, S., Martínez-García, B. & Roca, J. DNA knots occur in intracellular chromatin. *Nucleic acids research* **46,** 650–660 (2018).

147. Graessley, W. W. & Pearson, D. S. Stress–strain behavior in polymer networks containing nonlocalized junctions. *The Journal of Chemical Physics* **66,** 3363–3370 (1977).

148. Adams, C. C. *The knot book* (American Mathematical Soc., 1994).

149. Rolfsen, D. *Knots and links* (AMS Chelsea Publishing, 2003).

150. Alexander, J. W. Topological invariants of knots and links. *Transactions of the American Mathematical Society* **30,** 275–306 (1928).

151. Micheletti, C., Marenduzzo, D. & Orlandini, E. Polymers with spatial or topological constraints: Theoretical and computational results. *Phys. Rep.* **504,** 1–73 (2011).

152. Jones, V. F. in *Fields Medallists' Lectures* 448–458 (World Scientific, 1997).

153. Tubiana, L., Polles, G., Orlandini, E. & Micheletti, C. KymoKnot: A web server and software package to identify and locate knots in trajectories of linear or circular polymers. *Eur. Phys. J. E* **41,** 72 (2018).

154. Bonato, A., Marenduzzo, D., Michieletto, D. & Orlandini, E. Topological gelation of reconnecting polymers. *Proc. Natl. Acad. Sci. USA* **119,** e2207728119 (2022).

155. Klenin, K. & Langowski, J. Computation of writhe in modeling of supercoiled DNA. *Biopolymers* **54,** 307–317 (2000).

156. Kim, Y. S. *et al.* Gelation of the genome by topoisomerase II targeting anticancer agents. *Soft Matter* **9,** 1656–1663 (5 2013).

157. Shaffer, J. S. Effects of chain topology on polymer dynamics: Bulk melts. *J. Chem. Phys.* **101,** 4205–4213 (1994).

158. Shaffer, J. S. Effects of chain topology on polymer dynamics: Configurational relaxation in polymer melts. *J. Chem. Phys.* **103,** 761–772 (1995).

159. Brown, S., Lenczycki, T. & Szamel, G. Influence of topological constraints on the statics and dynamics of ring polymers. *Phys. Rev. E* **63,** 052801 (5 2001).

160. Carmesin, I. & Kremer, K. The bond fluctuation method: a new effective algorithm for the dynamics of polymers in all spatial dimensions. *Macromolecules* **21,** 2819–2823 (Sept. 1988).

161. Paul, W., Binder, K., Heermann, D. W. & Kremer, K. Crossover scaling in semidilute polymer solutions: a Monte Carlo test. *J. Phys. II France* **1,** 37–60 (1991).

162. Tanaka, M., Iwata, K. & Kuzuu, N. High-precision computer simulations of entangled polymer chains: 1. Determination of entanglement parameters of bond-fluctuation model. *Comput. Theor. Polym. S.* **10,** 299–308 (2000).

163. Auhl, R., Everaers, R., Grest, G. S., Kremer, K. & Plimpton, S. J. Equilibration of long chain polymer melts in computer simulations. *J. Chem. Phys.* **119,** 12718–12728 (2003).

164. Minato, T. & Hatano, A. On the distribution function of the square radius of gyration of a ring chain. *J. Phys. Soc. Japan* **42,** 1992–1996 (1977).

165. Grosberg, A. Y. Critical Exponents for Random Knots. *Phys. Rev. Lett.* **85,** 3858–3861 (18 2000).

166. Lee, E. & Jung, Y. Slow Dynamics of Ring Polymer Melts by Asymmetric Interaction of Threading Configuration: Monte Carlo Study of a Dynamically Constrained Lattice Model. *Polymers* **11,** 516 (2019).

167. Marko, J. F. & Siggia, E. D. Stretching DNA. *Macromolecules* **28,** 8759–8770 (Dec. 1995).

168. Kavassalis, T. A. & Noolandi, J. New View of Entanglements in Dense Polymer Systems. *Phys. Rev. Lett.* **59,** 2674–2677 (1987).

169. Svaneborg, C. & Everaers, R. Characteristic Time and Length Scales in Melts of Kremer–Grest Bead–Spring Polymers with Wormlike Bending Stiffness. *Macromolecules* **53,** 1917–1941 (2020).

170. Kremer–Grest Models for Commodity Polymer Melts: Linking Theory, Experiment, and Simulation at the Kuhn Scale. *Macromolecules* **53,** 1901–1916 (2020).

171. Lin, Y. H. Number of entanglement strands per cubed tube diameter, a fundamental aspect of topological universality in polymer viscoelasticity. *Macromolecules* **20,** 3080–3083 (1987).

172. Jones, V. F. R. A polynomial invariant for knots via von Neumann algebras. *Bulletin of the American Mathematical Society* **12,** 103–111 (1985).

173. Dabrowski-Tumanski, P., Rubach, P., Niemyska, W., Gren, B. A. & Sulkowska, J. I. Topoly: Python package to analyze topology of polymers. *Briefings in Bioinformatics* **22,** bbaa196 (2021).

174. Kröger, M., Dietz, J. D., Hoy, R. S. & Luap, C. The Z1+ package: Shortest multiple disconnected path for the analysis of entanglements in macromolecular systems. *Computer Physics Communications* **283,** 108567 (2023).

175. Shanbhag, S. & Kröger, M. Primitive path networks generated by annealing and geometrical methods: Insights into differences. *Macromolecules* **40,** 2897–2903 (2007).

176. Karayiannis, N. C. & Kröger, M. Combined molecular algorithms for the generation, equilibration and topological analysis of entangled polymers: Methodology and performance. *International Journal of Molecular Sciences* **10,** 5054–5089 (2009).

177. Hoy, R. S., Foteinopoulou, K. & Kröger, M. Topological analysis of polymeric melts: Chain-length effects and fast-converging estimators for entanglement length. *Phys. Rev. E* **80,** 031803 (2009).

178. Sumners, D. W. & Whittington, S. G. Knots in self-avoiding walks. *Journal of Physics A: Mathematical and General* **21,** 1689 (1988).

179. Van Rensburg, E. J. J. & Whittington, S. G. The knot probability in lattice polygons. *Journal of Physics A: Mathematical and General* **23,** 3573 (1990).

180. Coronel, L., Orlandini, E. & Micheletti, C. Non-monotonic knotting probability and knot length of semiflexible rings: the competing roles of entropy and bending energy. *Soft matter* **13,** 4260–4267 (2017).

181. Tubiana, L. *et al.* Comparing equilibration schemes of high-molecular-weight polymer melts with topological indicators. *Journal of Physics: Condensed Matter* **33,** 204003 (2021).

182. Katritch, V. *et al.* Geometry and physics of knots. *Nature* **384,** 142–145 (1996).

183. Klotz, A. R. & Maldonado, M. The ropelength of complex knots. *Journal of Physics A: Mathematical and Theoretical* **54,** 445201 (2021).

184. Tzoumanekas, C. & Theodorou, D. N. Topological Analysis of Linear Polymer Melts: A Statistical Approach. *Macromolecules* **39,** 4592–4604 (2006).

185. Everaers, R. Topological versus rheological entanglement length in primitive-path analysis protocols, tube models, and slip-link models. *Phys. Rev. E* **86,** 022801 (2 2012).

186. Wu, Q. *et al.* Poly [n] catenanes: Synthesis of molecular interlocked chains. *Science* **358,** 1434–1439 (2017).

187. Hart, L. F. *et al.* Material properties and applications of mechanically interlocked polymers. *Nature Reviews Materials* **6,** 508–530 (2021).

188. Lang, M., Fischer, J. & Sommer, J.-U. Effect of topology on the conformations of ring polymers. *Macromolecules* **45,** 7642–7648 (2012).

189. Lang, M., Fischer, J., Werner, M. & Sommer, J.-U. Swelling of Olympic gels. *Phys. Rev. Lett.* **112,** 238001 (2014).

190. Soh, B. W. & Doyle, P. S. Equilibrium Conformation of Catenated DNA Networks in Slitlike Confinement. *ACS Macro Letters* **10,** 880–885 (2021).

191. Chen, J., Rauch, C. A., White, J. H., Englund, P. T. & Cozzarelli, N. R. The topology of the kinetoplast DNA network. *Cell* **80,** 61–69 (1995).

192. D'Adamo, G., Orlandini, E & Micheletti, C. Linking of ring polymers in slit-like confinement. *Macromolecules* **50,** 1713–1718 (2017).

193. Micheletti, C. & Orlandini, E. Numerical study of linear and circular model DNA chains confined in a slit: metric and topological properties. *Macromolecules* **45,** 2113–2121 (2012).

194. De Gennes, P. Large Scale Organisation of Flexible Polymers. *Israel Journal of Chemistry* **14,** 154–159 (1975).

195. Daoud, M *et al.* Solutions of flexible polymers. Neutron experiments and interpretation. *Macromolecules* **8,** 804–818 (1975).

196. Tesi, M., van Rensburgs, E. J., Orlandini, E & Whittington, S. Knot probability for lattice polygons in confined geometries. *Journal of Physics A: Mathematical and General* **27,** 347 (1994).

197. Kim, J., Kim, J. M. & Baig, C. Intrinsic chain stiffness in flexible linear polymers under extreme confinement. *Polymer* **213,** 123308 (2021).

198. Kim, J., Kim, J. M. & Baig, C. Intrinsic structure and dynamics of monolayer ring polymer melts. *Soft Matter* **17,** 10703–10715 (2021).

199. Palombo, G., Weir, S., Michieletto, D. & Fosado, Y. A. G. Topological Elasticity in Physical Gels with Limited Valence. *arXiv preprint arXiv:2308.09689* (2023).

200. Ramaswamy, S. The mechanics and statistics of active matter. *Annu. Rev. Condens. Matter Phys.* **1,** 323–345 (2010).

201. Marchetti, M. C. *et al.* Hydrodynamics of soft active matter. *Reviews of modern physics* **85,** 1143 (2013).

202. Vicsek, T. & Zafeiris, A. Collective motion. *Physics reports* **517,** 71–140 (2012).

203. Winkler, R. G., Elgeti, J. & Gompper, G. Active polymers—Emergent conformational and dynamical properties: A brief review. *Journal of the Physical Society of Japan* **86,** 101014 (2017).

204. Winkler, R. G. & Gompper, G. The physics of active polymers and filaments. *The journal of chemical physics* **153** (2020).

205. Alberts, B. *et al.* in *Molecular Biology of the Cell. 4th edition* (Garland science, 2002).

206. Weber, S. C., Spakowitz, A. J. & Theriot, J. A. Nonthermal ATP-dependent fluctuations contribute to the in vivo motion of chromosomal loci. *Proceedings of the National Academy of Sciences* **109,** 7338–7343 (2012).

207. Dreyfus, R. *et al.* Microscopic artificial swimmers. *Nature* **437,** 862–865 (2005).

208. Biswas, B. *et al.* Linking catalyst-coated isotropic colloids into "active" flexible chains enhances their diffusivity. *ACS nano* **11,** 10025–10031 (2017).

209. Nishiguchi, D., Iwasawa, J., Jiang, H.-R. & Sano, M. Flagellar dynamics of chains of active Janus particles fueled by an AC electric field. *New Journal of Physics* **20,** 015002 (2018).

210. Isele-Holder, R. E., Elgeti, J. & Gompper, G. Self-propelled worm-like filaments: spontaneous spiral formation, structure, and dynamics. *Soft matter* **11,** 7181–7190 (2015).

211. Bianco, V., Locatelli, E. & Malgaretti, P. Globulelike conformation and enhanced diffusion of active polymers. *Physical review letters* **121,** 217802 (2018).

212. Locatelli, E., Bianco, V. & Malgaretti, P. Activity-induced collapse and arrest of active polymer rings. *Physical Review Letters* **126,** 097801 (2021).

213. Foglino, M. *et al.* Non-equilibrium effects of molecular motors on polymers. *Soft Matter* **15,** 5995–6005 (2019).

214. Sanchez, T., Chen, D. T., DeCamp, S. J., Heymann, M. & Dogic, Z. Spontaneous motion in hierarchically assembled active matter. *Nature* **491,** 431–434 (2012).

215. Alberts, B *et al.* Molecular Biology of the Cell Taylor & Francis. *New York* (2002).

216. Philipps, C. A., Gompper, G. & Winkler, R. G. Tangentially driven active polar linear polymers—An analytical study. *The Journal of Chemical Physics* **157** (2022).

217. Philipps, C. A., Gompper, G. & Winkler, R. G. Dynamics of active polar ring polymers. *Physical Review E* **105,** L062501 (2022).

218. Nguyen, C. *et al.* Emergent collective locomotion in an active polymer model of entangled worm blobs. *Frontiers in Physics* **9,** 734499 (2021).

219. Deblais, A. *et al.* Worm Blobs as Entangled Living Polymers: From Topological Active Matter to Flexible Soft Robot Collectives. *arXiv preprint arXiv:2305.00353* (2023).

220. Tejedor, A. R. & Ramirez, J. Reptation of active entangled polymers. *Macromolecules* **52,** 8788–8792 (2019).

221. Tejedor, A. R. & Ramirez, J. Dynamics of entangled polymers subjected to reptation and drift. *Soft matter* **16,** 3154–3168 (2020).

222. Tejedor, A. R., Carracedo, R. & Ramírez, J. Molecular dynamics simulations of active entangled polymers reptating through a passive mesh. *Polymer* **268,** 125677 (2023).

223. Deblais, A, Maggs, A., Bonn, D & Woutersen, S. Phase separation by entanglement of active polymerlike worms. *Physical Review Letters* **124,** 208006 (2020).

224. Deblais, A., Woutersen, S. & Bonn, D. Rheology of entangled active polymer-like T. tubifex worms. *Physical Review Letters* **124,** 188002 (2020).

225. Ozkan-Aydin, Y., Goldman, D. I. & Bhamla, M. S. Collective dynamics in entangled worm and robot blobs. *Proceedings of the National Academy of Sciences* **118,** e2010542118 (2021).

226. Fazelzadeh, M., Irani, E., Mokhtari, Z. & Jabbari-Farouji, S. Effects of inertia on conformation and dynamics of tangentially driven active filaments. *Physical Review E* **108,** 024606 (2023).

227. Goychuk, A., Kannan, D., Chakraborty, A. K. & Kardar, M. Polymer folding through active processes recreates features of genome organization. *Proceedings of the National Academy of Sciences* **120,** e2221726120 (2023).

228. Hagberg, A., Schult, D. & Swart, P. Exploring Network Structure, Dynamics, and Function Using Networkx. *Proceedings/Talk - Scipy,* 1–5 (2008).

229. Hoste, J., Thistlethwaite, M. & Weeks, J. The first 1,701,936 knots. *Math. Intelligencer* **20,** 33–48 (1998).